Automatic Optical Coherence Tomography Imaging Analysis for Retinal Disease Screening

Md Akter Hussain

Submitted in total fulfilment of the requirements of the degree of

Doctor of Philosophy

School of Computing and Information Systems
THE UNIVERSITY OF MELBOURNE

August 2017

Abstract

The retina and the choroid are two important structures of the eye and on which the quality of eye sight depends. They have many tissue layers which are very important for monitoring the health and the progression of the eye disease from an early stage. These layers can be visualised using Optical Coherence Tomography (OCT) imaging. The abnormalities in these layers are indications of several eye diseases that can lead to blindness, such as Diabetic Macular Edema (DME), Age-related Macular Degeneration (AMD) and Glaucoma. If the retina and the choroid are damaged there is little chance to recover normal sight. Moreover, any damage in them will lead to blindness if no or late treatment is administered. With eye diseases, early detection and treatment are more effective and cheaper. Biomarkers extracted from these tissue layers, such as changes in thickness of the layers, will note the presence of abnormalities called pathologies such as drusen and hyper-reflective intra-retinal spots, and are very effective in the early detection and monitoring the progression of eye disease. Large scale and reliable biomarker extraction by manual grading for early detection is infeasible and prone to error due to subjective bias and are also cost ineffective. Automatic biomarker extraction is the best solution. However, OCT image analysis for extracting biomarkers is very challenging because of noisy images, low contrast, extremely thin retinal layers, the presence of pathologies and complex anatomical structures such as the optic disc and macula. In this thesis, a robust, efficient and accurate automated 3D segmentation algorithm for OCT images is proposed for the retinal tissue layers and the choroid, thus overcoming those challenges. By mapping OCT image segmentation problem as a graph problem, we converted the detection of layer boundaries to the problem of finding the shortest paths in the mapped graph. The proposed method exploits layer-oriented small regions of interest, edge pixels from

canny edge detections as nodes of the graph, and incorporates prior knowledge of the structures into edge weight computation for finding the shortest path using Dijkstra's shortest path algorithm as a boundary of the layers. Using this segmentation scheme, we were able to segment all the retinal and choroid tissue layers very accurately and extract eight novel biomarkers such as attenuation of the retinal nerve fibre layer, relative intensity of the ellipsoid zone, thickness of the retinal layers, and volume of pathologies i.e. drusen, etc. In addition, we demonstrated that using these biomarkers provides a very accurate (98%) classification model for classifying eye patients into those with normal, DME and AMD diseases which can be built using a Random Forest classifier.

The proposed segmentation method and classification method have been evaluated on several datasets collected locally at the Center for Eye Research Australia and from the public domain. In total, the dataset contains 56 patients for the evaluation of the segmentation algorithms and 72 patients for the classification model. The method developed from this study has shown high accuracy for all layers of the retina and the choroid over eight state-of-the-art methods. The root means square error between manually delineated and automatically segmented boundaries is as low as 0.01 pixels. The quantification of biomarkers has also shown a low margin of error from the manually quantified values. Furthermore, the classification model has shown more than 98% accuracy, which outperformed four state-of-the-art methods with an area under the receiver operating characteristic curve (AUC) of 0.99. The classification model can also be used in the early detection of diseases which allows significant prevention of blindness as well as providing a score/index for the condition or prediction of the eye diseases. In this thesis, we have also developed a fully automated prototype system, OCTInspector, for OCT image analysis using these proposed algorithms and methods.

Declaration

This is to certify that

1. the thesis comprises only my original work towards the PhD degree,

2. due acknowledgement has been made in the text to all other material used,

3. the thesis is less than 100,000 words in length, exclusive of tables, maps, bibliographies and appendices.

_____

Md Akter Hussain, August 2017

Acknowledgements

I praise Allah (the Creator and the Sustainer of the Worlds), the Most Gracious, the Most Merciful, for blessing me with the opportunity, courage, and intellect to undertake this research.

I would like to express my gratitude to my supervisor, Prof. Ramamohanarao (Rao) Kotagiri, for his patient guidance, constant support, helpful criticisms, valuable suggestions and commendable support for the completion of my thesis. I am profoundly indebted to my co-supervisor Dr. Alauddin Bhuiyan for his constant guidance and insightful advice as an experienced researcher in the field of imaging. They have given me the freedom to explore research challenges of my choice and guided me when I felt lost. I am grateful to Prof. Robyn Guymer and Prof. Chi D. Luu for their guidance relating to eye research and for providing me with access to the data from the Center for Eye Research Australia (CERA). I would also like to thank Prof. Andrew Turpin for his support and encouragement and his advice as the chair of my Advisory Committee. I am also thankful to Prof. Smith, R. Theodore and Prof. Hiroshi Ishikawa, New York University, for their guidance and provision of data. I would like to thank Juan Sepulveda and Dr. Fumi Tanabe for helping me in reviewing the manual segmentation of OCT images. I would like to thank Gregory Rowe and my friends Shamir Bhuiyan and Nur Azam for proofreading the thesis.

I am grateful to the University of Melbourne for the financial and logistic support throughout the tenure of my postgraduate research. I would like to thank the Head of the Department Prof. Justin Zobel and all the staff of the Faculty of IT for their support and encouragement.

I would also like to thank my friends Nahian, Muzammel, Rasel, Rezuwan, colleagues

Preface

The thesis has nine chapters and the major chapters are 2, 3, 4, 5, 6 and 7.

Chapter 2 is based on the following publication:

Md Akter Hussain, Alauddin Bhuiyan and Ramamohanarao Kotagiri, *Progress on Analysing OCT imaging on Retina and Choroid: A Review" (To be submitted).*

Chapter 3 is based on the following publications:

Md Akter Hussain, Alauddin Bhuiyan, Andrew Turpin, Chi D Luu, R Theodore Smith, Robyn H Guymer and Ramamohanarao Kotagiri, *"Automatic Identification of Pathology Distorted Retinal Layer Boundaries Using SD-OCT Imaging." IEEE Transactions on Biomedical Engineering 64.7 (2017): 1638-1649.*

Md Akter Hussain, Alauddin Bhuiyan and Ramamohanarao Kotagiri. *"Retinal Cross Sectional Layer Segmentation using Optical Coherence Tomography." 2nd Annual Doctoral Colloquium, The University of Melbourne. 2014.*

Chapter 4 is based on the following publications:

Md Akter Hussain, Alauddin Bhuiyan, Hiroshi Ishikawa, R Theodore Smith, Joel S. Schuman and Ramamohanarao Kotagiri. *"An Automated Method for Choroidal Thickness Measurement from Enhanced Depth Imaging Optical Coherence Tomography Images", Computerized Medical Imaging and Graphics. (Under review)*

Kokroo, Aushim, Alauddin Bhuiyan, Md Akter Hussain, Ramamohanarao Kotagiri, Meleha Ahmad and Theodore Smith. *"Validation of an Automated Software for*

Choroidal Thickness (CTh) Measurement." Investigative Ophthalmology and Visual Science 57, no. 12 (2016): 5954-5954.

Md Akter Hussain, Alauddin Bhuiyan and Ramamohanarao Kotagiri. *"Automatic Detection of Choroid-Sclera Interface in EDI-OCT Images." 4th Annual Doctoral Colloquium, The University of Melbourne. 2016.*

Chapter 5 is based on the following publication:

Md Akter Hussain, Alauddin Bhuiyan, Chi D. Luu, Robyn H. Guymer, Hiroshi Ishikawa, Joel S. Schuman and Ramamohanarao Kotagiri. *"A robust and reliable 3D segmentation Method for the retinal layers from Optical Coherence Tomography imaging", Computer Methods and Programs in Biomedicine. (Under review)*

Chapter 6 is based on the following publications:

Md Akter Hussain, Alauddin Bhuiyan, Chi D. Luu, Robyn H. Guymer, Hiroshi Ishikawa, Joel S. Schuman and Ramamohanarao Kotagiri. *"Novel Automatic Approach of Computing Eight Biomarkers for Retinal and Neuropathy Diseases in Macula and ONH Centred SD-OCT Imaging" (To be submitted)*

Md Akter Hussain, Alauddin Bhuiyan and Ramamohanarao Kotagiri. *"Disc segmentation and BMO-MRW measurement from SD-OCT image using graph search and tracing of three bench mark reference layers of retina." Image Processing (ICIP), 2015 IEEE International Conference on. IEEE, 2015.*

Md Akter Hussain, Alauddin Bhuiyan and Ramamohanarao Kotagiri. *"Automatic Retinal Minimum Distance Band (MDB) Computation from SD-OCT Images." Digital Image Computing: Techniques and Applications (DICTA), 2015 International Conference on. IEEE, 2015.*

Chapter 7 is based on the following publication:

Md Akter Hussain, Alauddin Bhuiyan, Chi D. Luu, Robyn H. Guymer, Hiroshi Ishikawa, R Theodore Smith, Joel S. Schuman and Ramamohanarao Kotagiri. *"Clas-*

sification of Healthy and Diseased Retina Using SD-OCT Imaging and Random Forest Algorithm" (To be submitted)

Table 1: List of abbreviations in lexicographical order.

AD	Anisotropic Diffusion	ICG	IndoCyanine Green
AMD	Age-related Macular Degeneration	ILM	Internal Limiting Membrane
aprxONL	the approximate locations of ONL	INL	Inner Nuclear Layer
aprxRNFL	the approximate locations of RNFL	IPL	Inner Plexiform Layer
aprxRPE	the approximate locations of RPE	IZ	Interdigitation Zone
aprxTRL	the approximate locations of Three Reference Layers	LBP	Local Binary Pattern
AUC	An Area Under the receiver operator characteristics Curve	MDB	Minimum Distance Band
BM	Bruch's membrane	MUE	Mean Unsigned Error
BMO	Bruch Membrane Opening	MZ	Myoid Zone
BMO-MRW	Bruch Membrane Opening Minimum Rim Width	nGA	nascent Geographic Atrophy
BoW	Bag-of-word	OCT	Optical Coherence Tomography
Cc	Choriocapillaris	OCV	Outer Choroidal Vessel
CED	Canny Edge Detection	ONH	Optic Nerve Head
CERA	Centre for Eye Research Australia	ONL	Outer Nuclear Layer
CFP	Colour Fundus Photography	OPL	Outer Plexiform Layer
CNV	Choroidal Neovascularization	OSL	Outer Segment Layer
CSI	Choroid Sclera Interface	PCA	Principle Component Analysis
CTh	Choroidal Thickness	PL	Photoreceptor Layer
CV	Choroidal Vessel	PS-OCT	Polarization-Sensitive Optical Coherence Tomography
CWS	Cotton Wool Spots	RBC	the complex of the RPE/ BM/ Choriocapillaris)
DC	Dice Coefficient	RMSE	Root Mean Square Error
DIN	Depth-based Intensity Normalization	RNFL	Retinal Nerve Fiber Layer
DME	Diabetic Macular Edema	ROI	Region Of Interest
DR	Diabetic retinopathy	RPE	Retinal pigment epithelium
EDI-OCT	Enhanced Depth Imaging Optical Coherence Tomography	SA	Simulated Annealing
ELM	External Limiting Membrane	Sch	Suprachoroid
EZ	Ellipsoid Zone	SD-OCT	Spectral Domain Optical Coherence Tomography
FA	Fluorescein Angiography	SEAD	Symptomatic Exudate-Associated Derangement
GA	Geographic Atrophy	SLO	Scanning Laser Ophthalmoscopy
GCL	Ganglion Cell Layer	SR	Stable Reference
GT	Ground Truth	SS-OCT	Swept Source Optical Coherence Tomography
HRC	Hyper-Reflective Complex	TD-OCT	Time Domain Optical Coherence Tomography
HRS	Hyper-Reflective intra-retinal Spots	TRL	Three Reference Layers
ICC	Interclass Correlation Coefficient	VMT	vitreomacular traction

Contents

List of Figures

List of Tables

Chapter 1

Introduction

Life expectancy is increasing and vision needs to be preserved to maintain a good quality of life for individuals. Consequently, vision loss is an alarming issue for the ageing population. The top three common eye diseases which result in irreversible vision loss are Diabetic Macular Edema (DME), Age-related Macular Degeneration (AMD) and glaucoma. These diseases often remain undiagnosed or are only diagnosed late and can cause permanent loss of vision which is impossible to reverse [7, 8, 12, 13]. DME mainly affects diabetic patients and the prevalent cases of DME are expected to grow to over 300 million (globally) within the next few years [14]. AMD and glaucoma affect mainly aged people. AMD affects nearly 35% of adults who are over 80 years of age; glaucoma accounts for 9-12% of all cases of blindness. The number of AMD and glaucoma patients are expected to increase by approximately 150% over the next few years due to an increase in the ageing population [7, 13]. As a consequence, a large proportion of the world's health budget needs to be spent on screening, diagnosis and treatment of these diseases. The costs for individuals suffering from such diseases can be enormous. Therefore, early detection and treatment of those diseases can save vision, money and provide a better quality of life for individuals.

Our visual system involves both the eyes and brain. The eye has many parts or structures such as lens, retina, choroid, sclera. The light comes through the lens of the eye and falls onto the retina which converts the light into an electrical signal for passing to the brain that processes the signal to make sense to us. The choroid is located under the retina and its main purposes are to provide oxygen, nutrition to the retina and to absorb

excess light to protect the retina. The retina has many substructures such as optic disc, blood vessels (artery and vein), macula as shown in colour fundus image, Fig. 1.1. Colour fundus image can only show the surface of the retina and can provide a detailed image of the retina substructures' surface. The retina has ten different layers of tissue as shown in Fig. 1.2. The functions of these layers are discussed in Chapter 2 (Section 2.2.1.4). The cross sectional view of these tissue layers can be observed using Optical Coherence Tomography (OCT) imaging: each slice is known as a B-scan (see Fig 1.2) [7]. High resolution and the speed of the OCT technology also allow constructing a 3-Dimensional (3D) view of the retina by capturing and combining multiple OCT images. Since the choroid is located under the retina, it is not as easy to observe from the outside as the retina. However, advances in OCT imaging technology allow capturing the cross-section of not only retinal tissue layers but also the choroid as shown in Fig. 1.2. OCT imaging can capture the retina and the choroid structures in detail and can extract biomarkers from these structures for understanding and monitoring the progression of eye diseases. Ophthalmologists have found some morphological changes such as variation in layers' thickness in the retina and the choroid and the presence of cysts (a risk factor for DME), and drusen (a risk factor for AMD) due to these eye diseases before there is any noticeable deterioration in vision experienced by the individual [15–18]. The morphological changes noticed for eye diseases are listed in Table 1.1.

Research studies associated with understanding the progression of the diseases required analyses of large numbers of OCT images and quantifying many potential biomarkers. Traditional methods of quantifying biomarkers involving humans are no longer feasible or cost-effective on large-scale datasets as high-resolution images from OCT imaging create a huge volume of images. For example, it is possible to collect up to 400 OCT images per person for both eyes every 3 months [24]. Moreover, human grading is prone to inaccuracy, more grading variability and subjective bias. On the other hand, automatic grading will allow more consistent and effective measurements on a very large scale and consequently may give an opportunity to gain a new reliable insight into many eye diseases [7, 8]. This has given impetus to building automatic tools for segmentation of the retinal layer from OCT images since 1995. Some segmentation methods have been pro-
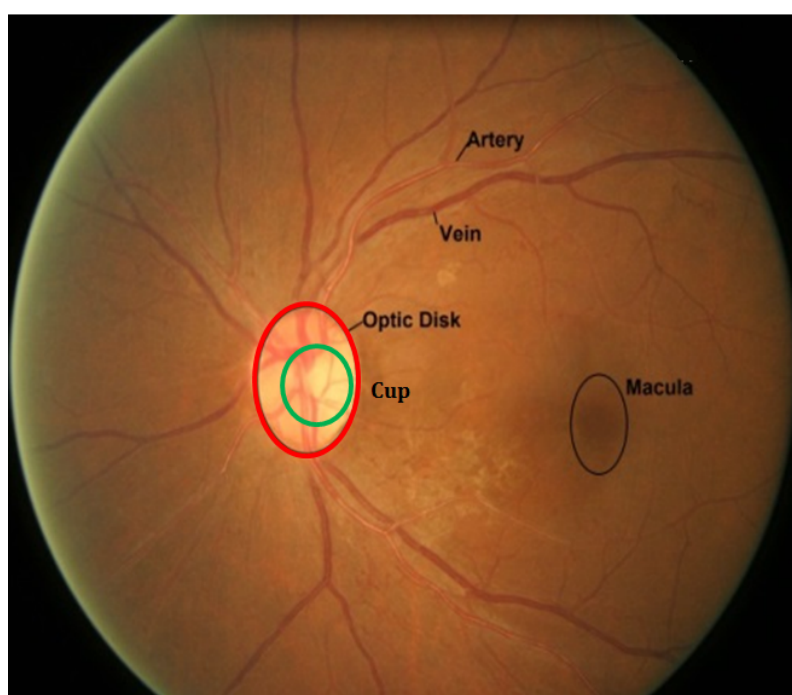
Figure 1.1: A surface image of the retina using Colour Fundus Photography with outlining the major components/substructures of the retina.
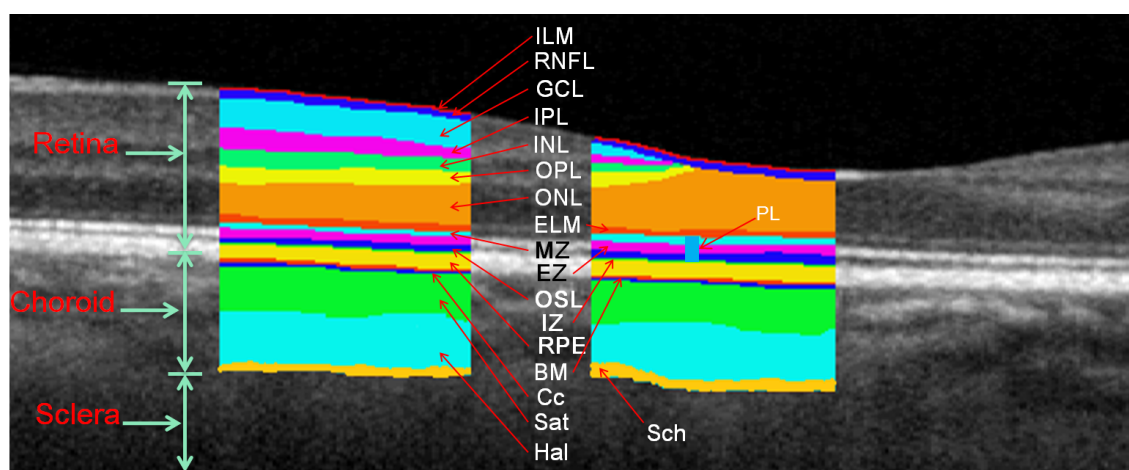
Figure 1.2: A cross section of the retina and the choroid using Optical Coherence Tomography (OCT) imaging, slice is known as B-scan. Outlining the layers of the retina and the choroid in the image. Details of these layers are discussed in Chapter 2 (section 2.2.1.4).

posed to enhance the clinical benefit of the OCT such as detecting and quantifying the pathologies and layer thicknesses. However, none of the methods are capable of segmenting layers with good accuracy in all conditions due to different challenges found in

Table 1.1: Association of the biomarkers with eye diseases.

Biomarkers	Association of the biomarkers with the eye disease
Layer Thickness	RNFL, GCL, and IPL layers of the retina were significantly thinner in eyes with glaucoma - approximately 20% less width than age-matched normal eyes ($p < 0.001$) [17]. Mean retinal thickness was reduced significantly in early AMD patients, approximately 10% ($p = 0.008$) than age-matched normal eyes [19].
Quantification value of Hyper-Reflective intra-retinal Spots (HRS)	The presence of HRS is a characteristic finding of the various stages of DME and is a key risk factor for the development of more advanced stages of DME [18].
Quantification value of Drusen	The presence of large macular drusen ($125\,\mu$m) is a characteristic finding of the early stages of AMD and is a key risk factor for the development of more advanced stages [20].
Cup-disc ratio	A cup-disc ratio more than 0.5 is a risk indicator of glaucoma [15].
Bruch's membrane opening - minimum rim width (BMO-MRW)	The visual sensitivity of glaucoma patients is significantly correlated to the BMO-MRW ($r = 0.32, p < 0.001$), which has a higher correlation than RNFL Thickness [21]. BMO-MRW in normal patients is $307 \pm 84.3\,\mu$m whereas early glaucoma patients have $211 \pm 60.5\,\mu$m [22].
Minimum distance Band (MDB)	The correlation coefficient between the MDB and cup-disc ratio are -0.88 and -0.56 for MDB value and area respectively with $p < 0.05$ which means MDB is highly correlated to glaucoma like cup-disc ratio [12].
Attenuation Coefficient of the RNFL	The severity label of glaucoma increases with decreasing the RNFL's attenuation coefficient [23]. Schoot et al. [23] found a significant structure-function relationship between the attenuation coefficient and the visual field's mean defect.
Reflectivity value of EZ layer	Early AMD patients have an average value of 1.73, and the control patients have an average value of 2.27 [16].

RNFL: Retinal Nerve Fiber Layer; GCL: Ganglion Cell Layer; IPL: Inner Plexiform Layer; EZ: Ellipsoid Zone

OCT images. Such challenges include: unpredictable changes in the retina and choroid due to pathologies and anatomical structures such as optic disc, macula; inconsistent contrasts in the homogeneous areas due to noise and imaging technology. Considering these essential requirements, in this study, an automatic 3D segmentation method for the retinal layers and the choroid from OCT images is proposed. Since OCT technology can show morphological changes of the retina and the choroid due to eye diseases, it is possible to design a classification model of eye diseases and its severity using this morphologi-

cal information. There are some methods proposed for the classification of diseases based on texture analysis of OCT images [1,25]. There is only one method available for the classification of diseases from clinically defined morphological changes, where biomarkers are extracted manually and results show excellent accuracy [26]. Therefore, in this study, novel methods have been developed for detecting pathologies such as drusen and extracting biomarkers such as changes of the layer thickness. Using these clinically derived biomarkers automatically, a classification model has been designed for identifying eye diseases that showed excellent accuracy.

1.1 Research objectives

This research aims to develop an automatic segmentation algorithm for the retinal layers and the choroid which can be utilised to quantify clinically derived biomarkers. Furthermore, this project aims to quantify pathologies, such as inner retinal lesion (e.g. HRS) and outer retinal lesion (e.g. drusen). In particular, this research addresses the following problems: 1) automating 3D segmentation of the retinal layer and the choroid; 2) quantifying biomarker related to DME, AMD, and glaucoma, and 3) developing a retinal OCT-based classification model for classifying the eye diseases into DME, AMD and normal.

1.1.1 Automated 3D Segmentation algorithm for the retinal layer and the choroid

The main goal of this study is to develop an automatic method for segmenting the retinal layers and the choroid from OCT images. An automated method will help ophthalmologists to conduct large-scale early detection and to monitor eye diseases. Manual segmentation of the retinal layers and the choroid is very expensive and time-consuming because OCT technology provides high-resolution images with a large number of slices (B-scans). Just one individual may have 400 OCT images for both eyes. Moreover, the quality of the manual segmentation is prone to inaccuracy, higher grading variability, and subjective bias and fatigue. Therefore, it is highly desirable to develop an accurate and robust automatic method for the segmentation of the retinal layers, the choroid and pathologies

of the retina as well as to provide their quantified values. However, that is a challenging task due to the uneven anatomical structure of the retina, unpredictable changes due to pathologies and inconsistent contrasts in homogeneous areas because of noise [8]. In the last two decades, a large number of studies have been done to develop an automatic tool to resolve this problem. However, none of the methods has performed well for the retinal layer segmentation as the accuracy of these methods is highly dependent on dataset due to the presence of various pathologies. Therefore, we need to develop an improved automatic segmentation method for retinal layers and choroid that can work reliably under various disease conditions and eye anatomical structures.

OCT images are contaminated by additive and speckle noises [27]. As a result, a homogeneous area can show uneven contrasts. Moreover, the intensity values decrease deterministically with growing imaging depth across layers due to the absorption and scattering of light in the retina and the choroid tissues which make detecting the choroid a challenging task. The structure of the retina is also different in the different regions of the retina such as optic disc and macula, as shown in Fig. 1.1 and also becomes more unpredictable in the presence of the pathologies such as geographic atrophy (GA) and drusen [8]. The presence of varying blood vessel sizes makes an unpredictable pattern in the Optic Nerve Head (ONH) region, another name of optic disc [8]. These properties make it difficult to segment ONH region. Additionally, the choroid differs largely from the retina, where large blood vessels and the structure of the choroid make an uneven pattern throughout the region. Thus, developing a robust method for segmenting the retinal layer and the choroid to handle those difficulties is a big challenge. Therefore, an automatic and robust method is required for handling the noise, intensity inconsistencies, different anatomical regions (the presence/absence of the ONH and/or macula), unpredictable changes due to the presence of pathologies, etc. to find accurate positions of the retinal layers and the choroid.

1.1.2 Biomarkers quantification

The goal of the retinal layer automatic segmentation is to extract biomarkers for the prediction of eye diseases. Such an automated system would enable large scale studies. It

can also help to establish new biomarkers by analysing their correlation with eye diseases. To extract reliable biomarkers, a segmentation method should be able to detect the pathologies with high accuracy. That detection is very challenging due to unpredictable positions, shapes, and sizes of the pathologies. Biomarker extraction also involves all ten retinal layers that need to be detected properly. The retinal layers' detection in the diseased eye is more challenging due to unpredictable thickness variations in the layers and loss of the retinal layers. Consequently, thin layers become more challenging to detect accurately. Therefore, this thesis investigates the development of robust algorithms for accurate extraction of biomarkers.

1.1.3 Development of classification model for eye diseases

Prediction of eye diseases from OCT images is an important problem. It can help early detection of eye diseases and be able to calibrate the severity of the disease. Consequently, many research schemes have been suggested for designing a classification model. Most methods classify the diseases based on the texture of the OCT images. Since textures could misguide the model due to changes of the dataset and the presence of multi-type pathologies and noise, they are prone to error and thus a model based on the clinically-driven parameters is required [28]. To produce a robust classification method for an eye disease, we need to address the following: (a) accurate measurement of biomarkers; (b) selection of appropriate machine-learning algorithm, and (c) computation of the optimal hyper-parameters for the chosen machine-learning algorithms.

1.2 Thesis contributions

The contributions of this thesis are: a) To develop an efficient and accurate automatic method of segmenting all ten retinal layers and the choroid; b) Quantifying the biomarkers including segmenting the pathologies; and c) Classification of eye diseases; with addressing three important research problems as mentioned in the previous section.

In addition to the above contributions, we have developed a fully automated software system for OCT image segmentation, biomarkers extraction and classification. The

system is designed to manually correct any part of the automated segmentation. This functionality helps the system to continually improve its accuracy; corrected images can be used in the learning process. The details of each contribution are presented in the following subsections.

1.2.1   Automated 3D Segmentation algorithm for the retinal layer and the choroid

A robust and effective automatic method has been proposed for segmentation of the retinal layers and the choroid from the Spectral Domain Optical Coherence Tomography (SD-OCT) images or higher-resolution OCT images such as Enhanced Depth Imaging OCT (EDI-OCT) and Swept Source OCT (SS-OCT). The proposed method seamlessly works in the presence or absence of the ONH and/or macula. The proposed method also works in the presence or absence of pathologies and morphological changes due to disease. The segmentation of boundaries is achieved by modelling the problem as the shortest path graph problem. The edge pixels found from a Canny Edge Detection Algorithm form the nodes. The slope similarity to a reference line and node's non-associativity (pixels not satisfying associated layer property) to the layer along spatial distances of the nodes are used for the computation of the graph edge weight. The edge weight is computed by addressing pathologies, macula and ONH related structural change of the retina. Since the choroid is considerably different from the retina, where large blood vessels and the structure of the choroid make the region uneven in the distribution of intensity, the approach of detecting retinal layers is not suitable for the Choroid-Sclera Interface (CSI) - the outer boundary of the choroid. A novel method has been proposed to normalise the intensity of the choroid region for providing an even distribution of the background. Finally, the CSI boundary is detected using a similar segmentation algorithm that is used for retinal layers; however, edge weights incorporate the effect of imaging technology and the anatomy of the choroid. Moreover, the tissues of the retina and the choroid are continuous in adjacent B-scans when the distance between the adjacent scans are very close. Therefore, very small changes of the boundaries from one B-scan to an adjacent B-scan are expected. This information helps to obtain correct boundaries where 2D automatic segmentation fails due to the presence of noise or various tissue

structures or pathologies. The method first detects the boundaries sequentially in the order of high contrast and the maximum gradient intensity to low contrast and minimum gradient intensity of the boundaries. This approach helps detect the low-contrast boundaries in a small Region of Interest (ROI), since ROI is defined using the already detected boundaries and adjacent B-scans. The reduction of the ROI helps to improve the accuracy and efficiency of the detection even in the presence of pathologies. Due to the differences among the patterns of ONH boundaries, the top boundary of the retina is detected by utilising approximate ONH region in the edge weight. Following this, ONH is detected by using the top boundary and three patterns (the absence of layers, dissimilar layer positions, and intensity pattern) of the ONH in the SD-OCT image. This method is evaluated using five datasets from four sources including two public datasets, which consists of 56 subjects where 55 are macula-centred volumes and one is ONH-centred SD-OCT. In those datasets, 36 subjects are AMD and glaucoma patients, and 20 subjects are healthy. Three different graders trace the boundaries for different datasets that serve as a gold standard for the automatic segmentation evaluation. In total, eight state-of-the-art methods (six methods are for retinal layer segmentation while the others are for the CSI segmentation) and the proposed method has been used to compare the accuracy of the automatic methods. The proposed method has also been shown to outperform the other eight state-of-the-art methods on every dataset.

1.2.2 Biomarkers quantification

In this study, a novel framework has also been proposed for measuring biomarkers that are already defined by ophthalmologists for retinal structures using SD-OCT images. A total of eight biomarkers are of interest to ophthalmologists. These are: retinal structural thickness; three morphological parameters of ONH; the volume of the pathologically altered tissue (lesion of the inner and outer retina); the relative intensity of the Ellipsoid Zone, and attenuation coefficients of the Retinal Nerve Fibre Layer. These are very significant for early screening of glaucoma, DME and AMD. The proposed 3D segmentation method delivers its primary goal of detecting the layers in any circumstances - for example, in the presence of pathologies or distorted layers due to disease. Furthermore, an

automated method for detecting pathologies (such as drusen and HRS) using the thickness of the layers and intensity profiling has been developed. The same protocol has been followed as defined by the previous studies that introduced these biomarkers when computing them on SD-OCT images that resulted in low margins of error between manual and automatic grading of the biomarkers. Two AMD patients (having a total of 98 B-scans) have been used for the evaluation of the quantified values of the biomarkers; one glaucoma patient (total 200 B-scans) and one DME patient (total 97 B-scans). The automatic method achieved F1-scores of 0.79 and 0.70 for a HRS of the inner retina and drusen respectively, using manual grading as a gold standard. The mean error of the biomarkers' quantified value is as low as 0.06.

1.2.3 Development of classification model for eye diseases

In this study, the first automatic method of clinically-derived features-based classification method of eye diseased patients from SD-OCT images has been proposed. The patients are classified into DME, AMD and normal. Total ten features have been used for developing the model of eye-disease classification. Ten features are comprised with the thickness of the retina and retinal layers, the volume of the pathologies such as drusen and HRS, curviness of the boundaries of the retinal layers. The classification model is then designed based on Random Forest. Experimental results with two datasets of 45 (a public dataset, 15 DME, 15 AMD and 15 normal) and 72 (combining the public and local datasets, 15 DME, 28 AMD and 29 normal) show the SD-OCT volumes have very good classification accuracy. The proposed method has achieved a high level of accuracy compared to the existing four state-of-the-art methods.

1.2.4 OCTInspector: A Complete Automated System for OCT Image Analysis

Although the proposed automatic segmentation shows excellent performance in segmenting the retinal layers and choroid, it can occasionally fail in some places and require manual correction. Therefore, we have provided a very efficient manual editing facility. This uses the same graph representation as the automatic method but reduces the ROI

by the use of mouse pointer and clicks. The manual correction is made consistent by the use of nearby edge-pixels instead of the exact position of the user's clicks. The system also provides an option to visualise any set of combination of the layers, sub-structures and pathologies in 3D as well as in enface image (frontal sections of retinal OCT scans, also called C-scan OCT). It also computes selected biomarkers that have been proposed in this thesis.

1.3   Thesis organisation

The rest of this thesis is organised as follows.

Chapter 2: Background

This chapter presents the background knowledge of the biological properties of the retina and the choroid. Following that, the major pathologies and disease manifestation in the retina and the choroid are discussed. The imaging technologies of the retina and the choroid are briefly presented. We also discuss various OCT technologies and imaging procedures. Finally, a literature review on the existing computer-aided segmentation methods for the retinal layers, the choroid, and pathologies; and classification model based on SD-OCT images are presented.

Chapter 3: 2D Segmentation (2DS) Algorithm for the Detection of Retinal Layers

This chapter presents an automatic 2D segmentation (2DS) algorithm of the four significant boundaries of the retina that are distorted in the presence of pathologies (such as drusen) for the macula-centred SD-OCT image. This is the initial work towards developing the proposed 3D segmentation method. This chapter proposes a noise-reduction approach using anisotropic diffusion and Weiner filter. Then, an algorithm for finding the three reference layer positions approximately using prior knowledge of intensity and position of them has been proposed. Following that, the procedure of the boundary detection by constructing graph is discussed. Finally, performance evaluation and comparison between automated methods is presented.

Chapter 4: 2D Segmentation (2DS) Algorithm for the Detection of the Choroid-Sclera Interface

In this chapter, an automated 2D segmentation (2DS) algorithm of choroid segmentation from EDI-OCT images is presented. A novel intensity-normalisation technique that is based on the depth of the choroid is used to equalise the intensity of all non-vessel pixels in the choroid region. Extension of the 2DS algorithm developed in Chapter 3 for the CSI is described. This method is tested on 190 B-scans of 10 subjects against manual segmentation by two expert graders and two state-of-the-art automated methods.

Chapter 5: 3D Segmentation (3DS) Algorithm for the detection of the retinal layers and the Choroid-Sclera Interface

In this chapter, an automated 3D segmentation (3DS) method of the retinal layers and the choroid from OCT images is presented. The previously- proposed 2D segmentation methods have been utilised in the 3D segmentation method. The selection of small layer-specific regions of interest from adjacent B-scans makes the method efficient, accurate and robust. The method on 250 B-scans from 10 (8 normal and 2 AMD) subjects has been evaluated by comparing the boundary positions and layer thicknesses marked by one grader. The performance of the proposed method has been compared with five state-of-the-art methods and the proposed method showed a significant improvement in accuracy.

Chapter 6: The Optic Nerve Head Detection and Eight Prominent Biomarkers Extraction

In this chapter, a proposal is made for a unified method of segmenting ONH from SD-OCT images that allow segmenting the retinal layers seamlessly in ONH or other regions. Furthermore, an automatic method of quantifying retinal biomarkers after segmenting pathologies, such as drusen and HRS, is proposed. Finally, eight clinically-useful biomarkers of the retinal diseases are computed automatically using a defined protocol by ophthalmologists. A low margin of error between manual and automatic grading of the biomarkers is found.

Chapter 7: Classification model of Diseased patients

In this chapter, an automatic method of classification of SD-OCT images for identification of patients into three different classes (DME, AMD and Normal) is proposed. This classification model is designed based on ten features using Random Forest. Exper-

imental results have been used with two datasets including a public dataset. Classification of three classes (DME, AMD and normal) and two classes (diseased and normal) is performed and compared with state-of-the-art methods and using many classification methods.

Chapter 8: OCTInspector: A Complete Automated System for OCT Image Analysis

In this chapter, the features and functionality of the OCTInspector are presented.

Chapter 9: Conclusion and Future Research Direction

This chapter summarises the contributions of this thesis and discusses possible areas for future research.

Chapter 2

Background

This chapter presents background knowledge of this research including the anatomy, the imaging technology and ending with identifying the research work done on the Optical Coherence Tomography (OCT) imaging of the retina and the choroid. This chapter is based on the following publication:

Md Akter Hussain, Alauddin Bhuiyan and Ramamohanarao Kotagiri. *"Progress on Analysing OCT imaging on Retina and Choroid: A Review". (To be submitted).*

2.1 Introduction

The eye is the main organ of the human visual system. The light enters the eye, the retina converts it into an electric signal and sends it to the brain for us to make sense [8]. The retina is thus called an extension of the brain. The choroid protects the retina from the harm of excess light as well as supplying nutrition [29]. The retina and the choroid are two structures of the eye and constructed by different tissues. They also have different substructures, such as an optic disc in the retina that contains nerve cells which transfer the electric signals to the brain. Consequently, many eye diseases and other systemic diseases such as strokes manifest themselves in the retina, the choroid and their substructures [30]. Eye diseases include ocular diseases, such as macular degeneration and glaucoma, which are the most significant causes of blindness in the developed world [7, 13]. Systemic diseases include diabetic retinopathy from diabetes, hypertensive retinopathy from cardiovascular disease, and multiple sclerosis [14]. Consequently, for the past few decades, ophthalmologists prefer to diagnose eye diseases by investigating the retinal

tissue structure and the choroid. With proper techniques, the retina is visible through the pupil and is accessible non-invasively for imaging. Since the choroid is behind the retina, it is not as easy as the retina to visualise from the outside. However, advances in imaging technology (e.g. spectral domain optical coherence tomography) permit them to be viewed with high resolution. Therefore, ophthalmologists are keenly interested in image-based diagnoses for the eye diseases due to accuracy and the ability to monitor disease progression.

Many non-invasive techniques are available for two-dimensional (2D) imaging of the retina such as Colour Fundus Photography (CFP) and InfraRed (IR). [7, 8]. More invasive techniques such as Fluorescein Angiography (FA) and IndoCyanine Green (ICG) angiography that require dye injection, are used for imaging functional retina and choroid. However, advance-imaging technology, Spectral Domain Optical Coherence Tomography (SD-OCT) allows non-invasive procedures to obtain proper 3-Dimensional (3D) images of the retinal tissue structure. Enhanced depth imaging mode of SD-OCT technology can image choroid with high resolution [31]. Using biomarkers, for example, are where tissues or pathologies from the images are used for diagnosis of eye diseases and their progression. Extracting biomarkers requires segmentation of the OCT image for identifying tissue structures of the retina, choroid and optic disc. Segmentation can be performed either manually or automatically. Manual segmentation is generally trustworthy due to expert human grading but it is time-consuming, expensive and can be unreliable for large-scale imaging [7, 8]. The problem becomes even more difficult with high-resolution images. Also, manual segmentation is prone to inaccuracy, more grading variability and subjective bias of the graders. As a result, manual segmentation is infeasible in practice. These limitations demand automatic segmentation methods. Therefore, many attempts have been made for segmenting the various structures of the retina and the choroid [7,8,25]. Automatic segmentation is very cheap and fast and can be employed for diagnosis and monitoring of progression of eye diseases. However, segmentation of OCT images is a challenging task due to the presence of noise, pathologies and different anatomical structures captured in the image. The noise in the images makes for uneven distribution of the intensity of retinal tissue structures. Diseased eyes have different

types of pathologies that severely affect the tissue structures. Therefore, researchers have found the segmentation of the structures is very challenging. Some automatic methods succeeded in segmenting accurately high quality and fine image but performed poorly in the diseased eyes where accurate segmentation is most desired. In this chapter, we will review automatic segmentation of different structures and sub-structures of the retina and the choroid. In a nutshell, this review will cover the following topics.

- Diseases manifestation in the retina and the choroid

- Imaging based Diagnosis method of the retina and the choroid

- Biomarkers of the retina and the choroid including pathologies from OCT image

- Image analysis techniques based on OCT technology for:

  - Detection of retinal and choroidal layers;

  - Detection of pathologies;

  - Extraction of biomarkers;

  - Prediction of eye diseases using classification models.

2.2   Eye, Retina and Choroid

The eye and the brain constitute the human vision system. Figure 2.1 is a cross-section through the eye showing its major structures [32]. A ray of light passes through the cornea, the anterior chamber, the pupil, the lens and the vitreous, and is then focused on the retina [8]. The choroid, the sclera and the retinal pigment epithelium of the retina absorb any excess light and thus protect the eye from harmful light. The light is focused on 125 million receptors, called rods and cones, in the photoreceptor layer of the retina [33]. These receptors are nerve cells and, when the light hits the receptors, they emit electrical signals which are passed to the brain. The brain processes the signal and makes sense of the image. In the following subsection, we will look at the retina and the choroid in detail.
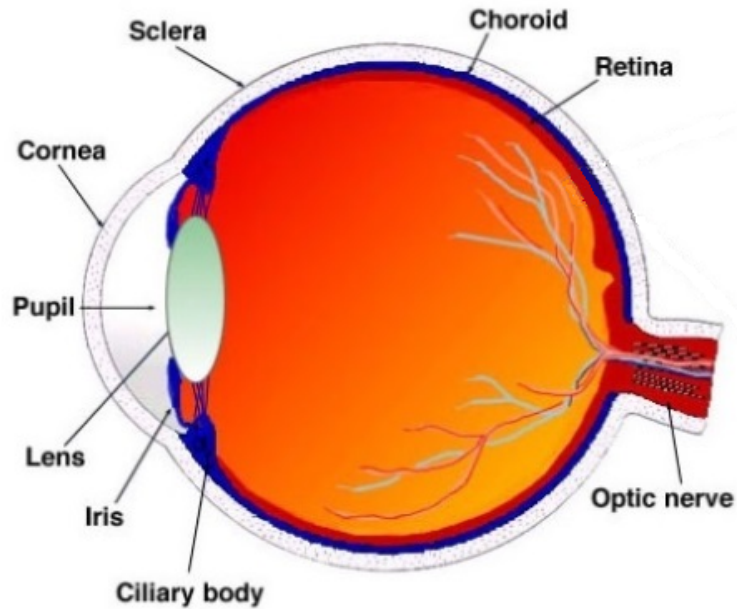
Figure 2.1: The human eye [1].

2.2.1   The retina

The retina is the inner part of the eye and a central entity of vision [33]. The major components of the retina are optic disc, macula and blood vessels as shown in Fig. 2.2. Different types of tissue cells comprise the retina, which is divided into ten layers [34, 35]. The following section elaborates on these components and the layers of the retina.

2.2.1.1   The optic disc

The optic disc is called a blind spot because it has no light-sensitive rods or cones tissues. It is also known as Optic Nerve Head (ONH) [15]. In the CFP image, the optic disc is brightest in intensity as shown in Fig. 2.2. In the OCT image, the optic disc region is shown as a fall in layers due to the absence of retinal tissues. In the optic disc, there is a pink neuro-retinal rim containing the nerve fibres and a central pale area (cup) devoid of nerve fibres, shown in Fig. 2.2 (red circle and cup enclosed rim is by the green circle).
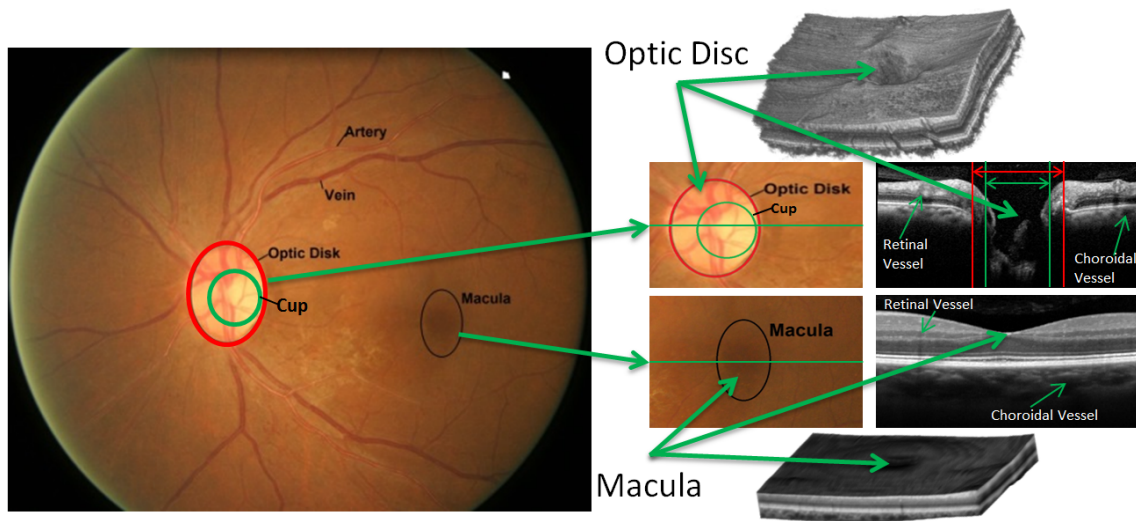
Figure 2.2: Colour Fundus Photography (CFP) Image of a portion of the retina where optic disc, cup, macula, artery and vein are shown. The cross-section of the optic disc and macula (along a green line at the elongated CFP image) displayed at the right of the corresponding CFP image captured by SD-OCT technology. The 3D view of the optic disc and macula-centred images illustrated at the top and bottom are constructed by multiple SD-OCT scans.

This cup-to-disc ratio is a vital biomarker for retinal diseases such as glaucoma [15].

2.2.1.2   The macula

The macula or macula lutea is an oval-shaped highly-pigmented yellow spot near the centre of the retina [36]. It is the densest area of cones and rods in the retina. The macula is thus responsible for the central, high-resolution and colour vision as well as contributing to the highest visual acuity of vision. Any damage to the macula or fovea hampers the central vision and this disease is called macular degeneration. The macula is represented as black in the fundus image and a small pit (due to the absence of retinal ganglion tissues) in the SD-OCT image, shown in Fig. 2.2.

2.2.1.3   The blood vessel

The blood vessels carry oxygen and carbon dioxide. There are two categories of the carrier, the Artery, the oxygen-rich blood carrier, and the Vein, the carbon dioxide-rich

blood carrier [37]. Arteries look a brighter red in the fundus photography and narrower than veins as shown in Fig. 2.2. The thinnest artery and vein, called capillaries, connect to each other to exchange nutrients and wastes.

2.2.1.4   The retinal tissue layers

The retina is composed of several types of tissue layers for building up the vision system. The tissues are divided into ten layers [34]. The OCT technology allows visualising the cross-section and the tissue layers of the retina as shown in Fig. 2.3. A short description of retinal layers (below) is based on [35, 38].

- Internal Limiting Membrane (ILM): A boundary between the retina and the vitreous body.

- Retinal Nerve Fibre Layer (RNFL): A layer of the axonal fibres from the ganglion cells.

- Ganglion Cell Layer (GCL): It contains the nuclei of ganglion cells, the axons of which become the optic nerve fibres that carry the generated signal to the brain.

- Inner Plexiform Layer (IPL): A layer of synapses between ganglion cells and amacrine cells and the axons of bipolar cells.

- Inner Nuclear Layer (INL): A layer of the cell bodies and nuclei of the integrator neurones.

- Outer Plexiform Layer (OPL): A layer of the synaptic portions of the rod and cone cells.

- Outer Nuclear Layer (ONL): A layer of the nuclei of rod and cone cells.

- External Limiting Membrane (ELM): Inter-cellular junctions between photoreceptor cells.

- Photoreceptor Layer (PL): A layer of light sensitive element rods and cones that convert light into electrical signals. Divided into three sub-layers: Myoid Zone (MZ), Ellipsoid Zone (EZ) and Outer Segment Layer (OSL).

- Retinal Pigment Epithelium Layer (RPE): A layer of cuboidal cells impregnated with melanin and responsible for providing essential nutrition to and waste removal from the photoreceptor cells. There is a small band top of the RPE layer where the interdigitation occur, and termed as the interdigitation zone (IZ).
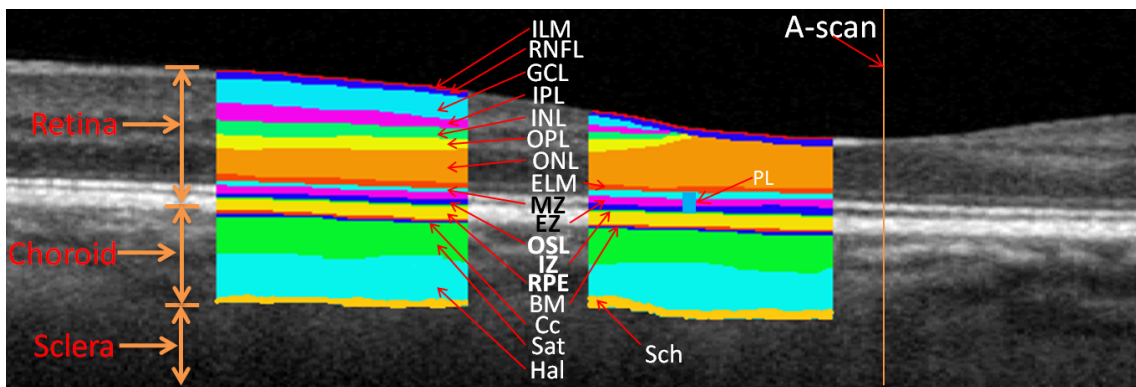
Figure 2.3: The layers of the retina and the choroid, and the sclera.

2.2.2 The choroid

The choroid is a collection of vascular tissues located behind the retina and before the sclera. It is also known as choroidea or choroid coat. Recent improvements in OCT technology such as Enhanced Depth Imaging (EDI)-OCT can capture the cross-section of the choroid in high resolution as shown in Fig. 2.3. It provides oxygen and metabolic support to the outer retina and optic nerve. The blood supply of the retina is primarily ($\sim 65\%$) through the choroid and secondarily ($\sim 35\%$) through the retinal vasculature which lies on top of the retina. It has melanin, a dark coloured pigment, which helps to absorb the excess light penetrating the retina [29]. Anatomically, choroidal vessels and stroma are the two major components of the choroid. The choroidal stroma is comprised of melanocytes, fibroblasts, immune cells, neurones, and ground substance that contribute to choroid thickness [39]. The boundary between the choroid and the sclera is called the Choroid-Sclera Interface (CSI).

2.2.2.1 The Choroidal Layers

The structure of the choroid is divided into five layers, and they are briefly described in [39, 40]. Illustration of the layers is provided in Fig. 2.3.

- Bruch's membrane (BM): The innermost layer of the choroid that separates the retina and the choroid.

- Choriocapillaris: The Choriocapillaris (Cc) is adjacent to Bruch's membrane and is comprised of small fenestrated capillaries (small vessels). These micro-vessels connect the artery and vein and exchange nutrients and wastes.

- Sattler's layer (Sat): It is next to Choriocapillaris and is a layer of medium diameter of blood vessels.

- Haller's layer (Hal): This is the outermost layer of the choroid and consists of the larger diameter blood vessels.

- Suprachoroidea (Sch): The suprachoroid is a transitional zone between choroid and sclera.

2.3 Visualisation of the pathologies in the retina and the choroid

There are many forms of pathologies found in the retina and the choroid [7, 8]. They are formed due to malfunction of the cells and aging and are responsible for many diseases mentioned in the earlier section. Figure 2.4 shows different pathologies that can be observed using CFP and OCT images. The quantification of biomarkers such as volume, shape, and intensity of the pathologies are important for diagnosis of disease and its progression. A brief description of a few pathologies found in the retina and choroid that have a strong correlation with the occurrence of eye diseases is presented in the following subsections.

2.3.1 Cotton Wool Spots/Soft Exudate

Cotton Wool Spots (CWS) appear as fluffy white patches in CFP images and swollen RNFL layer in SD-OCT image as shown in Fig. 2.4 (a) [41]. When there is reduced axonal transport within the nerves because of the ischemia (blood blockage), then it causes damage to the nerve fibres by swelling the surface layer of the retina.

2.3.2 Hard Exudate

Hard exudates are largely made up of extracellular lipid that has leaked from abnormal retinal capillaries [42]. In CFP images, it looks distinct yellow-white and in SD-OCT, white at the inner retina as shown in Fig. 2.4 (b).

2.3.3 Drusen

The exchange of nutrients and wastes by the RPE slows down and waste accumulates under the RPE forming yellowish deposits called drusen as shown in Fig. 2.4 (c) [7]. As the RPE continues to slow its transportation of nutrients and wastes, the overlying photoreceptors become damaged, up to causing legal blindness.

2.3.4 Geographic Atrophy (GA)

Characterised by sharply delineated areas of severe depigmentation or apparent absence of the RPE, through which larger choroidal vessels are more easily seen, with a minimum diameter of 175 μm as shown in Fig. 2.4 (d) [7].

2.3.5 Hyper-Reflective intra-retinal Spots (HRS)

The HRS have been recently hypothesised as different pathogenetic origin by some authors [2]. HRS may represent sub-clinical features of lipoprotein extravasation that act as precursors of hard exudates. They were not observed on clinical examination, fundus photography, or fluorescein angiography, due to their small size [2]. However, they were observed by SD-OCT image as shown with yellow arrow signs in Fig. 2.4 (e). Eyes with

Diabetic Macular Edema (DME) patients have HRS in the outer retina (53.7%) and in the inner retina (99.1%).

2.3.6   Choroidal Neovascularization (CNV)

CNV refers to the proliferation of new choroidal vessels either under the RPE or breaking through the RPE mainly in the macula region area as shown in Fig 2.4 (f). It leads to destruction of the photoreceptors due to exudative damage (fluid, lipids, and blood, ultimately leading to fibrous scarring) [3]. As a result, objects in that portion of the visual field may appear wavy or distorted. The natural course of CNV is rapidly deteriorating acuity, scarring of the pigment epithelium and permanent visual loss or blindness.
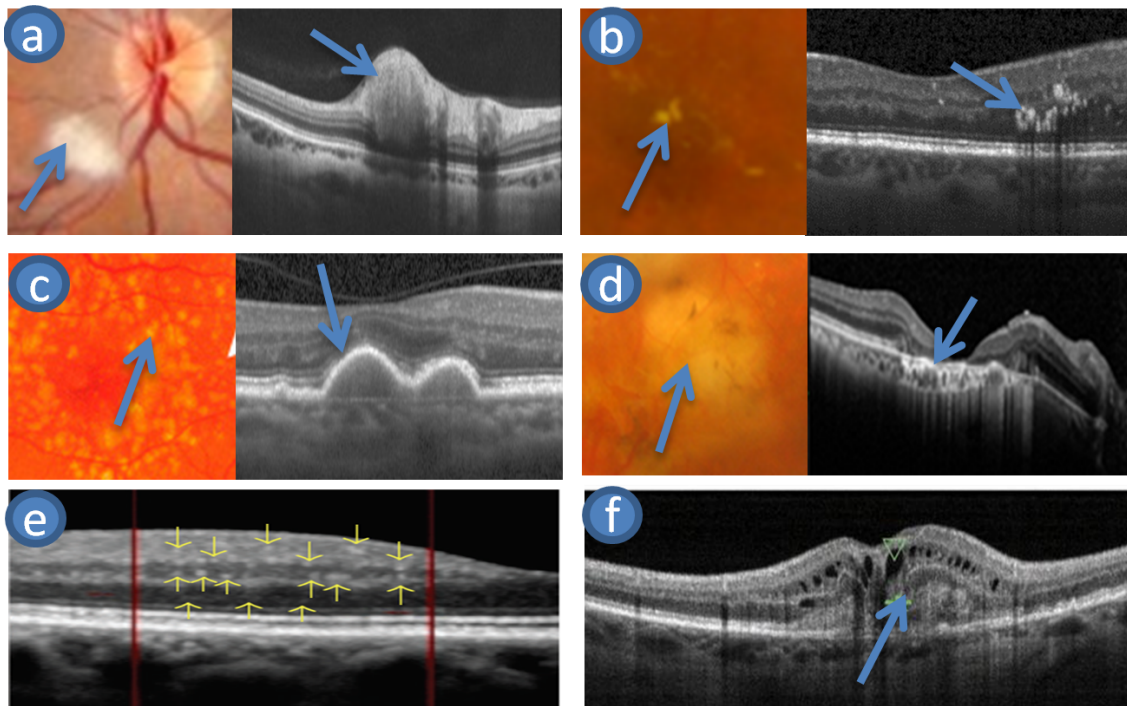
Figure 2.4: Pathologies shown in CFP (left) and SD-OCT (right) images. (a) Cotton wool spots / Soft Exudates[1]; (b) Hard Exudate [1]; (c) drusen; (d) Geographic Atrophy; (e) Hyper-Reflective intra-retinal Spots (HRS) (it is not visible in CFP) [2]; (f) Choroidal neovascularization (it is not visible in CFP) [3]. Arrow sign indicated the pathologies.

[1] http://www.octmd.org/findings/ischemia/cotton-wool-spot/

2.4 Diseases manifestation in the retina and the choroid

Eye diseases such as glaucoma and Age-related Macular Degeneration (AMD) tend to manifest clear signs in the retina and the choroid long before an individual notices a change in their vision [7,8,12]. Many deadly diseases or strokes also manifest signs in the retina and the choroid at an early stage before showing any visible symptoms in another part of the body. Figure 2.5 provides examples of many diseases' effects on vision. A brief overview of the most prevalent diseases studied through the retina and choroid analysis is as follows.
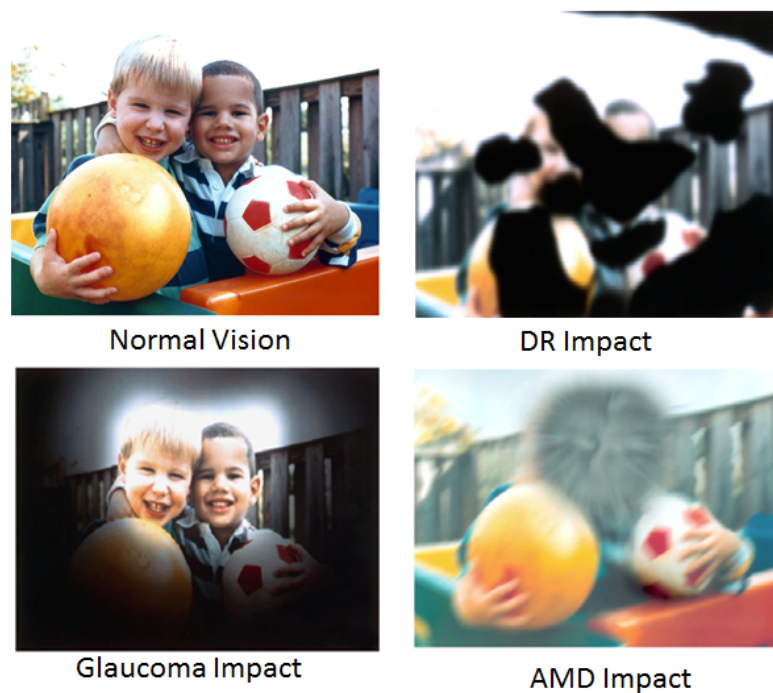
Figure 2.5: Examples of diseases' effects on vision[1] .

_____
[1] https://www.nei.nih.gov/

2.4.1 Diabetic Retinopathy (DR)

Diabetic Retinopathy (DR) is also known as diabetic eye disease and Fig. 2.5 shows its impact on vision. It can eventually lead to blindness and is a leading cause of blindness

in the world. It affects up to 80 percent of all patients who have had diabetes for 20 years or more. The blindness due to this disease can be prevented at least 90% by regularly monitoring the retina and early diagnosis [8, 43].

2.4.2   Age-related Macular Degeneration (AMD)

Age-related Macular Degeneration (AMD) is the most common cause of vision loss in the world and is a growing public health problem; Fig. 2.5 illustrates the impacts of AMD. AMD is the cause of blindness for 54% of all legally blind Americans, and the estimated annual cost burden is estimated as $30 billion [8]. The prevalence of AMD is expected to increase by 1.5 fold over the next ten years [7]. RPE detachments, sub-retinal or sub-RPE neovascular membranes, scar tissue, sub-retinal haemorrhages and related hard exudates (lipids) are its typifications [44]. AMD has two forms: dry and wet. Dry AMD is the initial form of AMD and wet AMD is the advanced form of AMD.

2.4.3   Glaucoma

Glaucoma is also one of the leading causes of blindness and its impact on vision is shown in Fig. 2.5. Early diagnosis and optimal treatment have been shown to minimise the risk of visual loss due to glaucoma. Mostly, this disease affects the ONH region that destroys side vision. Ophthalmologists are interested in the disc condition such as colour, cupping size (as a cup-to-disc ratio), swelling, haemorrhages and any other unusual anomalies that help to track and estimate the severity the disease [8]. The number of glaucoma patients worldwide is expected to increase by $\sim$1.5 fold over the next few years due to an increase in the ageing population [7, 13].

2.4.4   Cardiovascular Disease

Cardiovascular disease manifests itself in the retina in many ways. For example, hypertension and atherosclerosis cause changes in the ratio between the diameter of retinal arteries and veins, known as the A/V ratio. A decrease in the A/V ratio, i.e. thinning of the arteries and widening of the veins, is associated with an increased risk of stroke and

myocardial infarction [8].

2.4.5 Central Nervous System (CNS) Diseases

Anatomically and developmentally, the retina is acknowledged as an extension of the central nervous system (CNS) [45]. RNFL layer thinning is a symptom of many CNS diseases such as Stroke, Multiple Sclerosis, Alzheimer and Parkinson diseases [45]. Retinal ganglion cell layer loss is another symptom of Alzheimer and Multiple Sclerosis. Degeneration of optic nerve is a symptom of stroke. RNFL thickness was only significantly thinner in the nasal quadrant in migraineurs compared to the control group [46].

2.5 Diagnosis method of the retina and the choroid

Retinal imaging is the main approach to diagnosing these diseases. The first retinal imaging was done in 1823 [8], and in 1910, the fundus camera was developed by Gullstrand. This can capture the retina photographically in 2D. With the invention of OCT 3D, retinal structural imaging was made possible [7, 8]. Table 2.1 reports the significant features of the imaging technology of the Retina and Choroid. Since this paper focuses on OCT technology, only this technology is explained in the following section.

2.5.1 Optical Coherence Tomography (OCT) imaging technology

Huang et al. [9] introduced Optical Coherence Tomography (OCT) with micrometre resolution and capable of cross-sectional imaging in 1991 for retina *in-vivo*. From then on, OCT imaging became a powerful clinical apparatus for monitoring retinal cross-sectional structure in patients. The principle of OCT is the estimation of the depth by measuring the time of flight of a specific backscatter using the principle of low coherence interferometry, also called white light interferometry [8]. The most common interferometer for the OCT system is a simple Michelson interferometer [10]. In OCT, a 50/50 beam splitter splits a low coherent light source into two parts. One part of the light is sent to a mirror located at a specific distance used as a reference beam, and the other part is sent to the sample (i.e. tissues of the retina). The reflected light from the mirror (reference beam)

Table 2.1: Significant features of the imaging technology of the retina and the choroid based on [7–11].

	Technology		Significant Features
Oph‡	Direct Oph‡		Most common use is for a routine physical examination. Shows an upright and 15 times magnified of a small portion of the interior of the eye.
	Indirect Oph‡		Allows a wider view even if cataracts cloud the lens. Shows reversed and up to 5 times magnified of a small portion of the eye interior.
Fundus photography (FP)	Red-free photography		Use a filter for better contrast of the pathologies and others, for example; a green filter ∼540-570 nm is used to block out red wavelengths of light. Superior to colour photography in the progression assessment of the DR.
	Colour FP		Visualisation of the retinal surface is better with colour information.
	Stereo FP		Allows photographs in different view angles that can be used to create a 3D image. It gives better information about surface characteristics of the retina.
	Hyper-spectral imaging		Can construct a 3D data cube for multivariate data analysis. Two ways of separating spectral: Dispersive Optics (a prism) and interferometers.
	Infrared Imaging		Can acquire the RPE/BM and detect drusen through small pupils, blood, or sub-retinal fluid, etc. The light 820 nm wavelength is used with an SLO for acquiring the image. Cannot define leakage or intra-retinal fluid.
	SLO†	Confocal SLO	Has a high degree of spatial sensitivity, thus useful in monitoring and diagnosis of glaucoma, macular and other retinal degeneration.
		Adaptive optics SLO	For improving image quality, confocal SLO is updated with adaptive optics technology and removes optical aberrations from images.
	Ang•	F.Ang°	Can capture a sequence of images of the retina and the choroid that show the movement of blood over time. It utilises blue excitation light of ∼490 nm and fluoresces a yellow light of ∼530 nm.
		ICG.Ang⋆	The dye, indocyanine green (ICG) fluorophore, is used for deeper photography such as for choroidal diseases. It utilises near-infrared diode laser of 805 nm.
Optical Coherence Tomography (OCT)	TD-OCT		Lower speed, accuracy and resolution than SD-OCT. Maintains sensitivity regardless of scanning depth.
	SD-OCT		Higher speed, accuracy and resolution. Maintains sensitivity with higher speeds but loses sensitivity with increased scanning depth.
	SS-OCT		Combines the advantages of standard TD and SD-OCT while simpler than SD-OCT. Since it uses a longer wavelength, it has the potential to image choroid much better than conventional SD-OCT.

‡ Oph: Ophthalmoscope; † SLO: scanning laser ophthalmoscopy; • Ang: Angiography; ° F.Ang: Fluorescein Angiography; ⋆ ICG.Ang: indocyanine green Angiography; TD-OCT: Time Domain OCT; SD-OCT: Spectral Domain OCT; SS-OCT: Swept Source OCT;

and the sample occur interference (non-zero cross-correlation) when their flight times are equal ("equal" means a difference of less than a coherence length), being zero everywhere else because of the low coherence property. The coherence is a measurement of the correlation of physical quantities (i.e. phase and frequency). Two wave sources will be perfectly coherent while they are within a constant phase difference and same frequency. The low coherence means the waves have a profound difference in the phase difference and frequency. Those reflected lights are recombined at the beam splitter. A photodetector collects half of the combined light in the detection arm of the interferometer. Half of the light is returned towards the source and lost. The interference pattern converted into an intensity that represents the amount of backscatter from the image location [8]. Equation (2.1) and (2.2) tells that coherence of the light is inversely proportional to the depth: that is, the less coherent the light, the narrower the peak in the cross-correlation with the reference mirror.

$$I = k_r I_s + k_s I_s + 2\sqrt{(k_r I_s) \cdot (k_s I_s)} \cdot Re\{\gamma(\tau)\} \tag{2.1}$$

Where k_r and k_s are two equalisation coefficients for splitting ratio equally for the reference mirror and sample, respectively, I_s the intensity of the source light, and $\gamma(\tau)$ is the complex degree of coherence which is (2.2).

$$\gamma(\tau) = exp\left[-\left(\frac{\pi\Delta v\tau}{2\sqrt{ln2}}\right)^2\right] \cdot exp\left(-i2\pi v_0\tau\right) \tag{2.2}$$

where v_0 is the centre of the wavelength of the light source (I_s) and Δv is the width of I_s in the frequency domain.

The interference pattern of the light from each single scan point recorded as a depth profile of the sample called A-Scan is shown in Fig. 2.3. By scanning and combining a series of these axial depth scans linearly across the sample, it creates a cross-section called B-scan as shown in Fig. 2.2 and 2.3. Similarly, a combination of the multiple cross-sections (B-scans) in a linear fashion gives a 3D volumetric image of the sample as shown in Fig. 2.2. A face imaging at an acquired depth is possible by slicing the 3D volume at that depth called C-scan or enface image or surface image, which provides the interpretation

that is similar to fundus images or images scanning by laser ophthalmoscopes.

In developing the OCT system, its goal was to maximise the number of A-scans per unit of time because a higher A-scan per unit of time will reduce the motion artefacts, increase patient comfort, and achieve high image resolution. As a result, time domain OCT (the first version of the OCT technology) is obsolete by frequency domain-based OCT. The frequency domain technique uses a Fourier-transform analysis according to the Wiener-Khintchine theorem to get the depth position [10]. Removing the mirror improves imaging speed dramatically. The basic version of frequency domain-based OCT is called Spectral Domain OCT (SD-OCT). SD-OCT is not sensitive enough to capture the outer limit of the choroid in better resolution. An updated version of SD-OCT called Enhanced Depth Imaging OCT (EDI-OCT) moved the zero delay line (a point at which echoes occur and have peak sensitivity) and image averaging from multiple scans [47]. There are some more variations in the frequency domain that can provide the flow velocity, changes in the probe light's wavelength spectrum, or the polarisation properties of tissues as in Doppler OCT, spectroscopic OCT, and Polarization-Sensitive (PS) OCT, respectively [44]. A newer version called Swept Source OCT (SS-OCT) was developed by combining some of the advantages of standard TD and SD-OCT. SS-OCT has several advantages over SD-OCT such as increased sensitivity through the full imaging depth, decreased fringe washout, better axial resolution over a broad imaging range and higher detection efficiencies. Also, being a longer wavelength, it has the potential to image choroid much better than conventional SD-OCT [39].

2.6   Retinal and Choroidal OCT imaging

A high-resolution 3D image of the retina and choroid can be captured using the OCT technology non-invasively in real time. Ten layers and membranes of the retina are identifiable by the position and intensity level in the OCT image, as shown in Fig. 2.3. The five layers of the choroid is illustrated in an EDI-OCT image in Fig. 2.3. OCT technology allows imaging at a new dimension of the retina and the choroid for diagnosis purposes, called enface image. The enface image is a surface of the image comprising any com-

bination of the layers, such as average intensity along A-scan of the RPE layer. Figure
2.6 shows an example of the contrast of images from its original and the enface image
which encompassed the MZ/OSL Boundary and shows more clear geographic atrophy
than colour fundus photography [4].
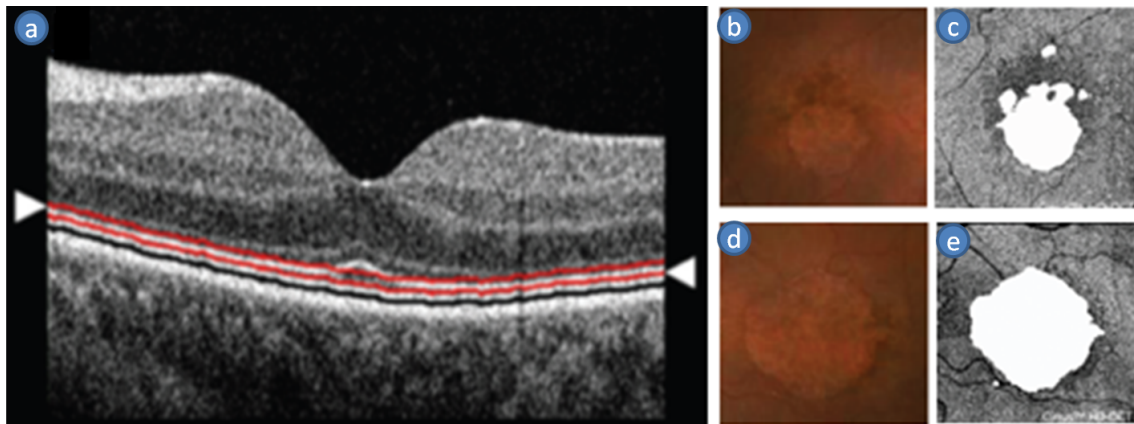
Figure 2.6: (a) SD-OCT B-Scans and (c) and (e) are Enface images of (b) and (d) CFP im-
ages respectively. The atrophic regions (white) in the enface image is much clearer than
CFP images [4]. The red lines showing the outer and inner segmentation lines (arrow-
heads in a) are used to generate the enface.

2.6.1   Pathology Quantification through the OCT image

With advanced imaging techniques of OCT technology, much more info is available to
analyse and assess the clinical relevance of the new information such as volumetric infor-
mation about pathologies. [7,8]. We next briefly discuss some pathologies quantification
for the retinal disease progression and diagnosis.

2.6.1.1   Quantification value of the drusen

The morphological features such as distinctness, individual size, total area, volume and
number of the drusen used as critical biomarkers of early AMD progression. The pres-
ence of macular large (greater than 125 μm) drusen is a particular finding of non-exudative
disease and is a key risk factor for the development of more advanced stages [20].

2.6.1.2 Quantification value of OCT defined Geographic Atrophy

Geographic Atrophy (GA) appears in advanced stages of non-exudative AMD and is increasingly the leading cause of vision loss in patients [49]. In OCT image, it is also known as OCT defined GA. The morphological features such as distinctness, individual size, total area, volume and number of GA are used as the hallmark of advanced non-exudative (dry) AMD where only OCT allows computation of volumetric information [4].

2.6.2 Biomarkers computed through the OCT image

With advanced imaging techniques of OCT technology, much more info is available to analyse and assess the clinical relevance of the new information such as retinal layer thickness and volumes, etc. [7,8]. We next briefly discuss some biomarkers for the retinal disease progression and diagnosis.

2.6.2.1 Layer thickness

The thickness of the retinal layer and choroid is a significant biomarker for the retinal and other diseases such diabetes, AMD, glaucoma, CNS diseases and cardiovascular diseases. For example, the RNFL, GCL and IPL layers were significantly ($p < 0.001$) thinner in a glaucoma eye - approximately 20% less than normal eyes [17]. The choroidal thickness correlates negatively with age [48] but shows no changes in early AMD [19].

2.6.2.2 Cup-Disc ratio

A widely-used and very vital hallmark and crucial structural indicator for assessing the presence and progression of glaucoma is a cup-disc ratio. The ratio of optic disc cup and neuroretinal rim surfaces is called a cup-disc ratio. The normal cup-disc ratio is defined as 0.5 [50]. In glaucomatous eyes, the death of nerve fibres causes the size of the cup to increase and thus the cup-to-disk ratio also increases.

2.6.2.3 Bruch's Membrane Opening-Minimum Rim Width (BMO-MRW)

The end point of the Bruch's membrane at the ONH is called a Bruch's membrane opening (BMO). So the minimum distance between BMO and ILM is referred to as the BMO-minimum rim width (BMO-MRW), as shown in Fig. 2.7, a strongly correlated biomarker for glaucoma. The visual sensitivity of Glaucoma patients significantly corresponds to the BMO-MRW ($r = 0.32, p < 0.001$), which has higher correlation than RNFL Thickness and BMO-MRW volume ($r = 0.26, p < 0.001$) [21]. BMO-MRW in normal patients is 307 $\pm$ 84.3 μm whereas early glaucoma patients have 211 $\pm$ 60.5 μm [22].
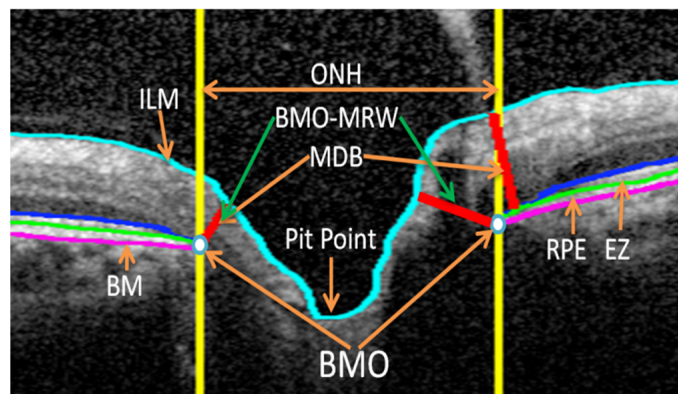
Figure 2.7: Example of BMO-MRW and MDB.

2.6.2.4 Minimum Distance Band (MDB)

The MDB is the circular band and computed by the minimum distance between ONH surface and RPE as shown in Fig. 2.7. It is a strongly correlated biomarker for glaucoma and also a parameter of the optic disc. Moreover, the correlation coefficient between the MDB and cup-disc ratio are -0.88 and -0.56 for MDB value and area respectively with $p < 0.05$ which means MDB has a profound correlation to a glaucoma-like cup-disc ratio [12].

2.6.2.5 Attenuation Coefficient of the RNFL

It is a normalisation technique of the OCT strength where it reduces the artefact and error due to media opacities, the power of the incident light beam, and the intermediate

tissue before reaching the deeper tissues. By increasing the severity label of glaucoma, RNFL's attenuation coefficient decreases. There is also a significant structure-function relationship between the attenuation coefficient and the visual field's mean defect [23]. An example of the attenuation coefficient of the RNFL is shown in Fig. 2.8. Schoot et al. [43] suggested the attenuation coefficient of the RNFL from the RNFL and RPE signal for each A-scan using the following formula.

$$\mu_{RNFL} = \frac{log\left(\frac{R}{\beta} + 1\right)}{2d} \tag{2.3}$$

Where R denotes the ratio of the RNFL and the RPE for an A-scan, d denotes the thickness of the RNFL, and β is 2.3.
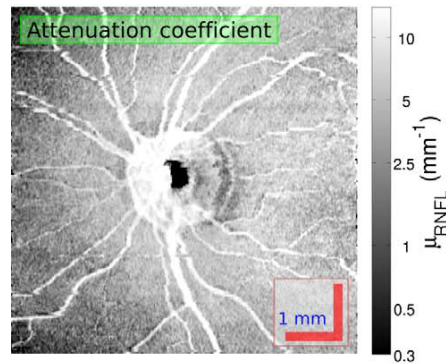
Figure 2.8: An example of the attenuation coefficient of the RNFL [5].

2.6.2.6 Relative intensity of the second reflective band (EZ layer)

The first reflective band is ELM and second reflective band is EZ. The ratio between the peak intensity of the EZ and ELM defines the relative intensity value of the second reflective band. The control patients average 2.27 where early AMD patients have 1.73 ratio value of the relative intensity of the second reflective band [16].

2.7 Retinal and Choroidal OCT image analysis

Image processing for the OCT expands in many dimensions such as layer detection, ONH detection, blood vessel detection, choroid detection and pathologies detection [7,8,10,51]. The abnormalities and layers of the retina and choroid are the main focus to be detected by the OCT images. Some segmentation methods have been proposed since 1995 to enhance the clinical benefit of the OCT, such as detecting and quantifying the pathologies and layers. However, none of those methods are capable of segmenting layers with good accuracy in all conditions due to different challenges in the OCT image. In the following subsections, we will describe the difficulties that need to be met for successful OCT image processing, followed by the detailed background.

2.7.1 The challenges in the OCT image processing

The challenges of the retinal images come from image technology and structure of the retina. Due to image acquisition technology and reality, OCT images are contaminated by additive and speckle noises. The structure of the retina is also different in various areas such as the optic disc and macula, and the image also becomes more unpredictable in the presence of the pathologies such as GA or drusen [7, 8, 10, 52]. More details of the challenges are as follows.

- Noise: The OCT images usually have two types of noises: additive and speckle. These decrease the contrast of the layers' boundary and eventually decrease the quality of the image. As a consequence, noise increases the difficulties of boundary identification and other abnormalities detection. It is a major problem for poor image segmentation.

- Intensity Variation within an area: Intensity of the homogeneous region decreases deterministically with increasing the imaging depth due to the methodology of the OCT technology. Variations are produced by absorption and scattering of light in the retinal tissue.

- Optical shadows and low optical contrast: Since haemoglobin absorption of light

is high, the retinal blood vessels create optical shadows and generate low optical contrast. This will also misguide the detection algorithm that needs to address the issue and will require extra effort for accurate detection.

- Irregularities in Anatomical Structural: The retinal layers present varying thicknesses and generally provide weak contrasts. Moreover, the anatomical structure of the retina is not the same for the entire region such as macula and optic disc, as shown in Fig. 2.2.

- Irregular shaped of pathologies: The presence of pathologies such as macular holes, retinal detachments, geographic atrophy and drusen in the retina and the choroid creates non-uniform morphological changes in the layers as shown in Fig. 2.4. As a result, the difficulties and challenges of the identification of the layers' boundaries are severe.

2.7.2   Pre-processing methods on the OCT images

De-noising Optical Coherence Tomography (OCT) image data was an active area of research until a few years ago, before high resolution of OCT images was introduced [53]. Our study observes that the traditional standard image de-noising and filtering techniques have been used for pre-processing of the retinal images. In Table 2.2, we have reported several noise reduction methods used by researchers for OCT image processing.

2.7.3   Detection of the retinal layers or boundaries

Most research on retinal OCT image analysis were on the retinal layer segmentation since the OCT invention. Some studies have reported semi-automatic and automatic methods of the retinal layers segmentation in all kinds of OCT images. A simple threshold technique to complex machine learning and graph search approach has been used for detecting layers in 2D and 3D imaging [7, 8, 10, 52]. Approaches include thresholding, edge detecting, active contour method, machine learning and graph-based multi-surface segmentation. However, these methods do not perform well on noisy images, thin layer,

Table 2.2: The noise reduction methods on OCT images.

Mth	Type	Aims & Researchers
None	TD	**RL:** Ishikawa et al. [54], Tan et al. [17]
	SD	**RL:** Fuller et al. [55], Ahlers et al. [56], Yazdanpanah et al. [57], Fabritius et al. [58], Yang et al. [59], Vermeer et al. [60], Kafieh et al. [61], Antony et al. [62], Tian, et al. [63]; **CL:** Zhang et al. [64] , Hu et al. [65], **SEADs:** Dolejsi et al. [66], **PED:** Ahlers et al. [56] **Drusen:** Baumann et al. [44] **GA:** Baumann et al. [44], Hu et al. [67], **ONH:** Abramoff et al. [68] **RV:** Dittrich et al. [37], Hu et al. [69], Hu et al. [70], Hu et al. [71], Kafieh et al. [72]; **CV:** Zhang et al. [64], Kajic et al. [73]
	EDI	**CL:** Danesh et al. [74]
Mean Filter	TD	**RL:** Huang et al. [75], Ishikawa et al. [76]
	SD	**RL:** Chiu et al. [77], Chiu et al. [78], Ehnes et al. [79], **CL:** Chen et al. [80], **ONH:** Lee et al. [81], Miri et al. [82]
	PS	**CL:** Torzicky et al. [83], Duan et al. [84]
	EDI	**CL:** Tian et al. [85], Alonso-Caneiro et al. [86]
Median Filter	TD	**RL:** George et al. [87], Koozekanani et al. [88], Shahidi et al. [89], Boyer et al.[90], Baroni et al. [91], Zang et al. [92],**ONH:** Herzog et al. [93], Zang et al. [92]
	SD	**RL:** Srinivasan et al. [94], Tolliver et al. [95], Tan et al. [96], Tumlinson et al. [97], Koprowski et al. [98], Lu et al. [99], Mayer et al. [100], Lang et al. [101], Ehnes et al. [79],**ONH:** Lee et al. [81], **RV:** Lee et al. [102]
Gauss. Filter	TD	**RL** Baroni et al. [91], **FFR:** Fernandez et al. [103]
	SD	**RL:** Chiu et al. [77], Chiu et al. [78],**RV:** Guimaraes et al. [104]
	EDI	**CL:** Mazzaferri et al. [105]
AD Filter	TD	**RL:** Gregori et al. [106], Haeker et al. [107], Garvin et al. [108],**FFR:** Fernandez et al. [103]
	SD	**RL:** Mujat et al. [109], Garvin et al. [110], Antony et al. [111], Ghorbel et al. [112], Antony et al. [113], Song et al. [51], Dufour et al. [114], Rossant et al. [115], Duan et al. [116] **SEADs:** Chen et al. [117] **Drusen:** Yi et al. [118], **ONH:** Antony et al. [119], **RV:** Niemeijer et al. [120], **CV:** Duan et al. [121]
Others	TD	**RL:** (CDF) Fernandez et al. [103], (WPB) Bagci et al. [122], (LPF) Hee et al. [123]
	SD	**RL:** (WPB) Bagci et al. [122], (AVK) Mishra et al. [124], (DTCW) Kajic et al. [125], (BF) Lu et al. [99], Shi et al. [126]; (WT) Lee et al. [127], (STD) Niu et al. [128], (LPF) Mayer et al. [129], Farsiu et al. [130], Lang et al. [101], **SEAD:** (WT) Quellec et al. [131], **PED:** (BF) Shi et al. [126], **Drusen:** (BF) Chen et al. [132], **GA:** (BF) Chen et al. [49],**RV:** (STD) Wu et al. [133], (BEM) Pilch et al. [134], (LPF) Wehbe et al. [135]
	EDI	**CL:** (WF) Tian et al. [85], Beaton et al. [136], (BM3D) Vupparaboina et al. [137]

The first column gives the method that researchers used and the second column identifies the type of OCT used. The third column lists the aim of the research and the researchers. Text colours of the researchers represent 1D (red), 2D (green) and 3D (blue) segmentation methods. The reported formats of the third column are as follows. 1) X: a, b, c, ... means the aim of the researchers a, b, and c is to detect X. 2) X: (Y) a, b, ... means the objective of the researchers a and b is to detect the X using Y filter.

AD: Anisotropic Diffusion; AVK: an Adaptive Vector-valued Kernel function; BEM: a general Bayesian Estimation based Method; BF: Bilateral Filter; BM3D: Block-Matching and 3D filtering; CL: Choroidal Layer; CDF: Complex Diffusion Filter; CV: Choroidal Vessel; DTCW: Dual-tree Complex Wavelet; FFR: Fluid-Filled Regions; Gauss.: Gaussian; GA: OCT defined Geographical Atrophy; LPF: Low Pass Filter; Mth: Methods; ONH: Optic Nerve Head; PED: Pigment Epithelial Detachments; RL: Retinal Layer; RV: Retinal Vessel; SEAD: Symptomatic Exudate-Associated Derangement; STD: Sparse 3-D Transform-Domain collaborative filter; Type: OCT Types; WF: Wiener Filter; WPB: Wedge-shaped Pass Band; WT: Wavelet Transformation.

presence of pathologies etc. of the retina [116]. Poor performance of current automatic detection algorithms for segmenting the retinal layers show there is a strong need for a robust algorithm to diagnose and monitor eye diseases.

The layer tracking methods are categorised into two groups: Layer segmentation of normal or healthy subjects' images and Layer segmentation in the presence of pathology [8,10,52]. For the first category, some methods propose using active contour, graph-based and machine learning approaches for the identification of the retinal layer boundaries. On the other hand, for Category Two, very few methods have been published [8]. Hee et al. [123] proposed an automatic method for computing retinal thickness on finding peaks in 1-D using kernel and threshold. Since then, many methods have been published on 2D and 3D segmentation. Ruggeri et al. [138] published the first 3D segmentation method for Rodent OCT imaging which segments ILM-RNFL, IZ-RPE, and RBC boundaries. Table 2.3 reports all the main methods of layer segmentation including the types of the OCT images used. A short description of the methods are provided in the following subsections.

2.7.3.1 Thresholding techniques:

Several methods proposed in the early years of the OCT imaging analysis are based on the direct thresholding technique. These methods are prone to noise, are less accurate and hence not very useful. In Table 2.3, we report some of the threshold-based methods and here we briefly describe some significant methods.

Hee et al. [123] proposed a method for measuring the thickness of the retina and RNFL layer using a simple threshold on the intensity value. It was the first report of OCT image processing and quantitative information. George et al. [87] proposed using dual thresholding for measuring thickness and volume of the retina and choriocapillaris structures. Unfortunately, very little information is available about this system. Since fixed thresholding is unreliable, an adaptive thresholding-based method of detecting ONH was proposed by Herzog et al. [93]. They applied 1-D kernel named Marr-Hildreth operator in each column of the OCT B-scan and defined the edges of the boundary using an optimal threshold that was found from analysing smoothness constraints. They eval-

Table 2.3: The segmentation methods for various structures of the retina and the choroid from OCT images.

MM	Type	Aims & Researchers
Thresholding	TD	**RL:** Hee et al. [123], George et al. [87], **ONH:** Herzog et al. [93]
	SD	**RL:** Szkulmowski et al. [139], **CL:** Vupparaboina et al. [137], **ONH:** Moupagiatzis et al. [140]; **RV:** Wehbe et al. [135], Dittrich et al. [37], Kafieh et al. [72] **CV:** Zhang et al. [64], Kajic et al. [73], Duan et al. [121]
	PS	**RL:** Gotzinger et al. [141]; **CL:** Torzicky et al. [83]
Peak Finding	TD	**RL:** Huang et al. [75], Ishikawa et al. [54], Shahidi et al. [89], Ishikawa et al. [76],Fernandez et al. [103], Baroni et al. [91], Tan et al. [17],
	SD	**RL:** Srinivasan et al. [94], Ahlers et al.[56], Tan et al.[96], Tumlin et al.[97], **PED** Ahlers et al.[56]
Edge Based	TD	**RL:** Koozekanani et al. [88], Boyer et al. [90], Baroni et al. [91], Bagci et al. [122]
	SD	**RL:** Bagci et al. [122], Tolliver et al. [95], Yang et al. [59], Niu et al. [128]
Line Fitting	SD	**CL:** Zhang et al. [64], **Drusen:** Farsiu et al. [130], Toth et al. [142], Baumann et al. [44], Gregori et al. [143], Iwama et al. [144], Chen et al. [132]; GA: Baumann et al. [44], **ONH:** Zang et al.[92]
Active Contour	TD	**FFR:** Fernandez et al. [103]
	SD	**RL:** Mujat et al. [109], Farsiu et al. [130], Mishra et al. [124], Yazdanpanah et al. [57], Koprowski et al. [98], Ghorbel et al [112], Rossant et al. [115], Toth et al. [142]], Mayer et al. [100], Dufour et al. [114], **GA:** Chen et al. [49], Hu et al. [67] , **RV:** Pilch et al. [134]
UC	SD	**RL:** (OTSU) Fabritius et al. [58]; (K-means) Kafieh et al. [61]; (FCM) Mayer et al. [129], **RV:** (K-means) Wu et al. [133]
Machine learning	SD	**RL:** (SVM) Fuller et al. [55], Vermeer et al. [60]; (RF) Lang et al. [101], Antony et al. [62] , (AAM) Kajic et al. [125], **CL:** (AAM) Kajic et al. [145], **ONH** (k-NN) Abramoff et al. [68], Miri et al. [82], Lee et al. [81]; **RV** (SVM) Guimaraes et al. [104], (BA) Xu et al. [36], (k-NN) Niemeijer et al. [120], Hu et al. [69], Hu et al. [70], Hu et al. [71], Garvin et al. [146]
Graph Method	TD	**RL:** (MFMC) Haeker et al. [107], Garvin et al. [108]
	SD	**RL:** (MFMC) Garvin et al. [110], Antony et al. [111], Lee et al. [127], Antony et al. [113], Song et al. [51], Lang et al. [101], Dufour et al. [114], Antony et al. [62], Shi et al. [126], Zang et al. [92], (SPA) Chiu et al. [77], Yang et al. [59], Chiu et al. [78], Ehnes et al. [79], Tian, et al. [63], Duan et al. [116]; **CL:** (MFMC) Chen et al. [80]; (SPA) Kajic et al. [145], Hu et al. [65], **SEAD:** (MFMC) Quellec et al. [131], Dolejsi et al. [66], Chen et al. [117]; **PED:** (MFMC) Shi et al. [126], **ONH:** (MFMC) Antony et al. [119]; (SPA) Hu et al. [147], Hu et al. [148] RV: (MFMC) Lee et al. [102], Hu et al. [69],
	EDI	**CL:** (MFMC) Danesh et al. [74]; (SPA) Tian et al. [85], Alonso-Caneiro et al. [86], Beaton et al. [136], Mazzaferri et al. [105]
	PS	**CL:** (SPA) Duan et al. [84]

The first column gives the main method that researchers used and the second column identifies the type of OCT used. The third column lists the aim of the research and the researchers. Text colours of the researchers represent 1D (red), 2D (green) and 3D (blue) segmentation methods. The reported formats of the third column are as follows. 1) X: a, b, c, ... means the aim of the researchers a, b, and c is to detect X. 2) X: (Y) a, b, ... means the objective of the researchers a and b is to detect the X using Y method.

AAM: Active Appearance Model; BA: Boosting Algorithm; CL: Choroidal Layer; CV: Choroidal Vessel; EM: Energy Minimisation; FCM: Fuzzy C-means Clustering; FFR: Fluid-Filled Regions; GA: OCT defined Geographic Atrophy; k-NN: k-Nearest Neighbour Classifier; MFMC: Max-Flow-Min-Cut (closed set); MM: Main Methods; ONH: Optic Nerve Head; PED: Pigment Epithelial Detachments; RF: Random Forest; RL: Retinal Layer; RV: Retinal Vessel; SEAD: Symptomatic Exudate-Associated Derangement; SPA: Shortest Path Algorithm (minimum cost finding); SVM: Support Vector Machine; Type: OCT Types; UC: Unsupervised Clustering.

uated their method's performance qualitatively. Szkulmowski et al. [139] proposed a semi-automatic method for identifying two boundaries of the retinal layers using multiple thresholding on intensity and variance with manual intervention. Gotzinger et al. [141] proposed an automated method for RPE layer detection from PS-OCT images using thresholding in the degree of polarisation uniformity. They showed qualitative results instead of any quantitative analysis. However, these methods are subjective and can suffer from low accuracy in the presence of noise.

2.7.3.2   Peak finding or Edge detection methods:

Since thresholding methods are less accurate and unreliable, researchers have proposed sets of rules that describe properties such as highest gradient value and peak finding or edge detection-based methods for detecting the retinal layers. Several methods have been proposed (see Table 2.3) and here we discuss some of them.

Huang et al. [75] proposed an automated method for measuring the thickness of the retina and the choroid. It was the first reported using hereditary retinal degeneration in animals from TD-OCT imaging. A computer algorithm based on signal amplitude and slope was used to locate the signal features of transitions, peaks, valleys and plateau-like regions which defined the positions of the layers. Later, Ishikawa et al. [76] proposed a method for detecting six boundaries of the retinal layers from TD-OCT images. They used a cut-off threshold value by analysing reflectivity histogram of each A-scan. If adjacent A-scans had disruption, they recomputed the cut-off threshold value for reflectivity threshold, peak width and peak height for the segmentation algorithm. They showed layer thicknesses were significantly greater in normal than in glaucomatous eyes using 47 subjects. Fernandez et al. [103] proposed a method based on a peak-finding algorithm for detecting seven boundaries of the retinal layers and tested on 72 OCT scans with AMD and glaucoma patients. They computed structure coherence matrix from original image intensity using a diffusion tensor for finding peaks. Local maximum characteristic and the first derivative changes sign from either positive to negative or from negative to positive are used for finding the peaks and the edges of boundaries. The algorithm can detect the boundaries reasonably well in almost the entire macula, except for the region

where the layer structure is distorted by the presence of abnormal fluid (cyst). They also offered semi-automatic correction of the automatic detection. Srinivasan et al. [94] proposed a modified version of Koozekanani et al. [88] to detect six boundaries of the retinal layers using peak finding on a complex matrix that is formed by zero crossing, intensity etc. They tested their method on 43 normal subjects and found an error in eccentricity varying from -4 to 1 μm.

These techniques are not sufficient to determine the retinal layers with an acceptable accuracy and are still prone to error due to noise and pathologies in the image. Many methods have used peak or edge detection for finding potential regions, or nodes of a graph for layers and a graph search method for finding the layers. These schemes are described in later sections.

2.7.3.3 Active contour method:

An active contour method is an energy-minimising problem where deformable splines are influenced by constraint and image forces that pull it towards object contours and internal forces that resist deformation. Several methods have been proposed using this method and these are reported in Table 2.3. The major drawbacks to this approach are computational inefficiency and poor accuracy in the presence of noise and pathologies. Some important methods based on an active contour algorithm are described below.

Mujat et al. [109] proposed a method of segmenting RNFL layer using deformable splines (snake algorithms) from SD-OCT images. They initialised the snake algorithms and defined the external force field by detecting a boundary approximately based on the threshold of a filtered image and a gradient image. The algorithm detects the boundaries with reasonable accuracy in 350 frames within an SNR range of 31-44 dB, except for a few isolated places. Later, a semi-automatic method for segmenting six boundaries of the retina based on ChanVese's energy-minimising active contour was proposed by Yazdanpanah et al. [57] from 20 rats' SD-OCT images. The noise was added synthetically to evaluate segmentation method for showing the robustness of the method and achieved an average Dice similarity coefficient of 0.85. The minimisation of an energy function consisting of gradient and local smoothing terms based segmentation method for three

boundaries of the retinal layers was proposed by Mayer et al. [100]. They achieved a mean unsigned error (MUE) per A-Scan of 2.9 μm on glaucomatous eyes, and 3.6 μm on healthy eyes. Ghorbel et al. [112] proposed a method for segmenting nine boundaries of the retinal layers using Active contours, Markov random fields, and a Kalman filter. They detected approximate locations of hyper-reflective complex (lower bright layers) using k-means clusters. These approximate locations were used to initialise the active contour for detecting the boundaries. A large dataset of 700 subjects had been used for evaluating their method and the study achieved MUE nearly 3 pixels. Recently, a modified active contours or snakes-based nine boundaries of the retinal layers segmentation algorithm was proposed by Rossant et al. [115]. They called this modified active contours as parallel double snakes are good in detecting the deformable models, which are nearly parallel lines. The parallel double snakes simultaneously grow two contours and minimise an energy function which attracts these contours towards high image gradients and enforces the approximate parallelism between them. The segmentation achieved a similarity index of above 0.87, sensitivity between 0.85 and 0.93, and specificity between 0.84 and 0.94.

2.7.3.4   Unsupervised clustering:

A few methods have been proposed based on unsupervised clustering such as k-means clustering, OTSU clustering and Fuzzy C-means clustering for the retinal layers detection, as shown in Table 2.3. The clustering was used either directly on the image intensity or gradient, or on a modified matrix such as Eigen values or a combination of intensity, gradient or other textural information. A brief description of those significant methods follows.

Mayer et al. [129] proposed an automatic method for segmenting RNFL layer using Peaks finding and Fuzzy C-means clustering. For each peak in the image, they defined feature vectors which were constructed with pixel positions, intensities, gradient values etc. These feature vectors were clustered with fuzzy C-means clustering used to define the boundaries. They used Median and Gaussian filter in post-processing to reduce error. They evaluated with 12 SD-OCT B-scans and found border positions errors within 2 pix-

els range for 98% ILM-RNFL boundary and 72% RNFL-GCL boundary. OTSU clustering was used to segment two boundaries of the retinal layers by Fabritius et al. [58] from SD-OCT images. They incorporated 3D intensity information to improve the intensity-based segmentation without massive pre-processing of the OCT image. More than 99% and 97% of depth scans had a smaller error for ILMRNFL and IZ-RPE in normal and ARMD patients respectively. Kafieh et al. [61] created a diffusion map using Eigen-values and functions decomposition from SD-OCT image intensities. A K-means cluster was applied in a sequential order on that diffusion map to find 11 boundaries of the retinal layers. The overall MUE of border positions (BPs) in (mean $\pm$ SD) was 7.56 ± 2.95 μm. The method relies on regional image texture and demonstrates robustness in the low contrast between boundaries.

The methods that use unsupervised clustering as their main approach suffer from less accuracy due to noise, pathologies, and devices from where OCT is obtained. They are also subjective. There are several methods using clustering as intermediate steps for reducing the search space to improve accuracy and layer detection by the graph search method described in a later section.

2.7.3.5 Machine learning and pattern recognition technique:

A few methods proposed using a different type of machine-learning and pattern recognitions (supervised clustering) technique such as support vector machine, Random Forest, and k-NN classifier, as shown in Table 2.3. A brief description of some significant works on the machine-learning technique for the retinal layers detection follows.

The first machine-learning approach based on support vector machine for the retinal layers detection was proposed by Fuller et al. [55]. They proposed a semi-automatic method for detecting three boundaries (ILM-RNFL, MZ-EZ, RBC) of the retinal layers using a Multi-resolution Hierarchical support vector machine from SD-OCT images where the features were formed by scalar intensity, gradient, spatial location, mean of the neighbours and variance of the pixels in manually drawn regions. They evaluated their method with four subjects and found the average boundary position error is around four pixels with a standard deviation of six pixels. An active appearance model-based segmentation

method was proposed by Kajic et al. [125] with the aim of detecting nine boundaries of the retinal layers from SD-OCT images. They had used shape and texture information of the images as features for training and detecting phase of the machine-learning algorithm. They evaluated a large dataset of 466 B-scans from 17 subjects. The method showed a difference of only 2.6% against the inter-observer variability. Another support vector machine-based retinal layers segmentation algorithm was proposed by Vermeer et al. [60]. They used eight features constructed by the intensity and gradient distribution for detecting five boundaries of the retinal layers. They evaluated the method in 18 subjects, and root mean square errors (RMSEs) for the first and last boundary of the retina were between 4 and 6 μm, while the errors for intra-retinal interfaces were between 6 and 15 μm.

2.7.3.6   Graph search method:

Most of the efficient and accurate methods published use a different type of graph search such as max-flow-min-cut, minimum-cost closed set and the shortest path algorithms (see Table 2.3). Several improved optimal 3-D graph search approaches (including fluctuating feasibility constraints [43] and soft constraints [44, 45]) were designed for detecting numerous surfaces: these significantly improved the segmentation accuracy. A few methods defined different constraints or coefficient of graph edge weight using machine-learning or other optimisation techniques such as Simulated Annealing [62, 101]. Brief descriptions of some significant works on the graph search method for retinal layers detection are described next.

A group from Iowa University published several algorithms using a max-flow-min-cut algorithm for detecting the retinal layers. Haeker et al. [107], first from the Iowa group, proposed a method of detecting two boundaries of the retinal layers from TD-OCT images. In 3D, the boundaries form surfaces of the retinal layers. Haeker et al. detected each surface of the layers as a minimum s-t cut from a geometric graph constructed from edge/regional information and a priori-determined surface constraints. An updated version of that work, a multilayer segmentation using a minimum-cost closed set in a geometric 3-D graph, was suggested by Garvin et al. [108] for detecting six boundaries of the

retinal layers from TD-OCT images. It was the first reported approach for an automated 3D segmentation of intra-retinal layers. A total of 24 eyes from 12 subjects were used for evaluation purposes and found an overall mean unsigned border positioning error of 6.1±2.9 μm. They applied the same method for SD-OCT images as well [109] and found that an overall mean unsigned border positioning error of the boundaries was 5.69 ± 2.41 μm in 13 subjects. This group published several methods for improving the segmentation of the ONH, retinal layers in both macula and ONH centred images and released a software package which is available on request for research purposes [149]. Antony et al. [62] (another work of their group) proposed a segmentation method based on a minimal cost closed set graph problem for segmenting seven boundaries of the retinal layers; where Random Forest was used to define the parameters of the cost function for the graph. Haar, Gabor, Gaussian, Steerable filters and intensity features are used to train the system and form the cost function. The overall unsigned border position errors observed when using the recommended configuration of the graph-theoretic method was 6.45 ± 1.87 μm, 3.35 ± 0.62 μm and 9.75 ± 3.18 μm for the human, mouse and canine sets of images, respectively.

Chiu et al. [77] proposed a method to detect eight boundaries of the retinal layers from SD-OCT images using the shortest path-finding algorithm. Their edge weights of graph nodes were computed with vertical gradient information of the pixels where each pixel formed a node. They evaluated ten healthy images and found the overall mean and standard deviation for the border positions errors in percentage were 0.26% and 0.09% respectively. An updated version of their work [78] was published for detecting pathological distorted boundaries from the retina. In this updated version, they included distance of the nodes in the computation of edge weights and detected three boundaries distorted for drusen and geographic atrophy. In total, 220 B-scans from 20 patients were used for evaluation purposes, and the mean unsigned error for the reproducibility of the whole retina and RPEDC volumes were $0.28\% \pm 0.28\%$ and $1.60\% \pm 1.57\%$, respectively.

Lang et al. [101] proposed a segmentation method using Random Forest and a max-flow-min-cut algorithm. The Random Forest was used to create a probability map using 27 features of spatial awareness, local and context-aware features. A Graph max-flow-

min-cut was applied on that map to find the boundaries of the layers. In total, 35 subjects of healthy and diseased eyes were used to evaluate the method and the mean unsigned boundary position error for the dataset in mean $\pm$ SD is $3.38 \pm 4.10 \mu m$. There are no differences in performance for the healthy or MS subjects. They share their system publicly as a whole software package, named AURA tools [150].

Dufour et al. [114] proposed a method for identifying six retinal layer boundaries using the energy minimisation and solved by a graph-based multi-surface segmentation algorithm, an extended version of Song et al. [51]. They added the use of soft constraint for the regularisation of the distances between two simultaneously segmented surfaces; a total of 50 B-scan segments were manually processed for evaluation. An extensive evaluation showed a mean unsigned segmentation error of $3.05 \pm 0.54 \ \mu m$ over all datasets. Their system is publicly available [151].

Tian et al. [63] have proposed a method using a graph shortest path approach: OCTRIMA-3D. They flatten the image based on a reference boundary. Gradient information and already detected boundaries are used to choose the region of interest. Biasing and Masking are used to increase the contrast of the low contrast boundary. Finally, a Dijkstra shortest path is used to find the retinal boundary. The graph weight computation is similar to the method proposed by Chiu et al. [77]. They evaluated the method on two datasets including Chiu et al.'s [77] dataset. They showed their method is superior to the Iowa and Dufour methods. The average unsigned error of border positions was about 1 pixel (i.e., 4 μm for this image set).

Duan et al. [116] computed a distance map using a fast sweeping algorithm: the geodesic curve is then detected using a discretised gradient descent. The geodesic curve is the shortest path where the geodesic distance between nodes is smallest. They showed the method was better than four state-of-the-art methods on their local and public dataset.

2.7.4 Detection of the choroid and its layers

The EDI-OCT and SS-OCT technology (with a greater penetration signal, i.e. it reaches below the retina) offers the cross-sectional image of the choroid which gives an opportunity to compute the choroidal thickness. Recent reports have demonstrated a suc-

cessfully automated measurement of choroid thickness (CTh) in healthy and pathologic states from optical coherence tomography (OCT) images [31, 80, 152]. Some studies have reported semi-automatic and automatic methods of choroid segmentation in different types of OCT images such as PS-OCT, SD-OCT and EDI-OCT [65,80,85,145]. Approaches include thresholding, machine-learning and graph-based multi-surface segmentation. However, these methods have limitations for the variable size, noisy image, presence vessels, etc. of the choroid [80]. The lack of robustness and accuracy of the automatic choroid detection (the choroid is defined by the RBC and CSI boundaries) and the need for an automatic algorithm for monitoring and diagnosis of choroidal diseases is still the subject of active research to develop a robust, reliable and more accurate automatic system for the measurement of CTh. We have reported the main methods used by researchers in Table 2.3 and a brief description of the important method of detecting the choroid is follows.

Zhang et al. [64] proposed threshold-based choroidal layers and a vessel detection algorithm from SD-OCT images. They created a tensor matrix for each voxel containing local directionality and shape information. A multi-scale Hessian matrix analysis was applied and created a vesselness map from where voxels were defined as vessel using an experimentally- determined threshold. They found average dice coefficient of the reproducibility is 0.78 ± 0.08 on 24 normal subjects. Kajic et al. [145] proposed a neural network and Active Appearance Model-based algorithm for detecting the choroid outer boundary, also known as a CSI from SD-OCT images. They evaluated 871 manually segmented cross-sectional scans from 12 eyes with pathologies and AMD. The average error rate for identifying the CSI was 13%. Vupparaboina et al. [137] proposed an automated method for detecting choroid using thresholding on a structural similarity (SSIM) index, tensor voting, and Eigenvalue analysis of the Hessian matrix. The thickness error was 9.15 μm. Chen et al. [80] proposed a method for detecting choroid using thresholding, graph max-flow-min-cut, and the energy minimisation technique. They computed a gradual intensity distance image from where nodes were defined. The edge weights were computed using a complex form of the distances between nodes. Then a 2D graph search method with curve smooth constraints obtained the CSI positions. They evalu-

ated 212 High Definition (HD)-OCT images from 110 eyes in 66 patients. The mean CTh difference and overlap ratios are 6.72 μm and 85.04%, respectively, and thus superior to the method of Tian et al. [85], a graph shortest path-based choroid detection method.

2.7.5   Detection of the Optic Disc/ Optic Nerve Head/ Cup and Rim

The hallmark of glaucoma is cupping of the optic disc. Currently, CFP is used as a gold standard to compute the cup-disc ratio. With the introduction of SD-OCT imaging, it is possible to extract new information from the optic disc such as a 3D structure. Consequently, many researchers try to find the ONH from OCT images and compute as biomarkers for the Glaucoma progression including cup-disc ratio, MDB, and BMO-MRW. Herzog et al. [93] devised the first automatic method to detect ONH from TD-OCT using an adaptive thresholding approach. Many other methods have since been published for other OCT modality such as SD-OCT to get the 3D structure of the ONH. Markov model, k-NN classifier, Graph Search: max-flow-min-cut, line fitting on the detected retinal layers boundaries (for example BM) are used to detect the border of the ONH as shown in Table 2.3. Miri et al. [82] had been used a multi-modal approach (OCT + CFP) for ONH detection. A brief description of optic disc or ONH detection is described next.

The method proposed by Herzog et al. [93] is the first published work on the ONH detection from TD-OCT image which used adaptive threshold and edge detection. Their method was based on edge maximisation and smoothness constraints to choose an optimal threshold to automatically extract the ONH. The method also detected retinal boundaries from axial OCT scans through ONH but did not provide any performance evaluation other than the demonstration of some output segmented images. In 2009, Abramoff et al. [68] proposed a method of detecting ONH cup and rim by combining a multi-scale 3D graph search algorithm and a voxel column classification algorithm using a k-NN classifier. Ten features consisting of distances and intensities with respect to surface of the retinal layers were used for the classifier. This study showed a high correlation between automatic segmentation results and results of glaucoma experts. Lee et al. [81] also proposed an improved technique based on similar methodology using graph search

combined with a k-NN classifier. They employed contextual information combined with a convex hull based fitting procedure to segment the ONH cup and rim. They achieved accuracy with an unsigned error for the cup detection of 0.076 ± 0.026 mm and the neuroretinal rim of 0.061 ± 0.026 mm. Hu et al. [148] developed a graph-based method for the automated segmentation of the cup and ONH from OCT datasets. The method detected the location of blood vessels, as they are quite large in the ONH. They found correlations of the linear cup-to-disc area ratio, disc area, rim area and cup area between manual and automatic detection which were 0.85, 0.77, 0.69, and 0.83, respectively. Moupagiatzis et al. [140] detected ONH based on thresholding and some morphological operations with sensitivity 0.89 and specificity 0.98. Miri et al. [82] proposed a multi-modal imaging approach using both SD-OCT and CFP images for detecting ONH using k-Nearest Neighbour (k-NN) classifier and Iterative Closed Point registration. A total of 33 features are extracted from both modalities and a k-NN classification approach is used to classify the pixels as cup, rim or background. They showed that multi-modal imaging approach gains more accuracy over uni-modal imaging approach (i.e. only SD-OCT) (97.8% versus 95.2%; $p < 0.05$; paired t-test). Antony et al. [119] described a segmentation method for detecting ONH from SD-OCT image using a Random Forest classifier. They used individual feature significances to select 20 features for the classifier to classify pixels as ONH. They found the 3D Euclidean distance of the Neural Canal Opening was $55.29 \pm 33.97 \; \mu m$.

2.7.6 Detection of pathologies and extracting the biomarkers

The main goal of the automatic segmentation of the OCT image analysis is to help ophthalmologists to diagnose eye diseases. For clinical purposes, the automatic image processing system must also be able to handle images with pathologies. Many researchers developed methods for detecting layers of OCT images consisting of pathologies, and many pathologies such as drusen and geographic atrophy, hyper-reflective intra-retinal spots were considered. A few researchers also detected a combination of those pathologies called Symptomatic Exudate-Associated Derangement (SEAD). SEADs are the main retinal manifestations of AMD, including intra-retinal fluid, sub-retinal fluid and pig-

ment epithelial detachment [66,117]. The active contour method, line fitting on the layer position, peak finding, max-flow-min-cut and support vector machine are used to detect the pathologies listed in Table 2.3. A summary of the important methods of detecting pathologies and quantifying biomarkers is presented.

Gregori et al. [106] proposed a method for detecting three boundaries of the retinal layers and pathologies such as a cyst and drusen, using an iterative boundary detection algorithm. Unfortunately, this is a proprietary algorithm of Carl Zeiss Meditec and is not described in detail. In total, 40 B-scans were used to evaluate the method, and qualitative analysis shows ILM and RPE were identified correctly for 37 scans. They also showed the intraclass correlation coefficient was > 0.99 for both area and volume measurements of drusen in [143]. Farsiu et al. [130] proposed a method for detecting drusen and pigment epithelial detachments etc. using a deformable snake algorithm and fitting fourth order polynomial line in the RPE layer position from SD-OCT images. They evaluated on OCT data from six AMD eyes (a total of 228 SDOCT B-scans) and qualitatively claimed good results. They allowed semi-automatic correction using a user interface. Chen et al. [132] also proposed a method for detecting drusen using line fitting on the RPE layer and found more than 0.90 correlation coefficient between automatic and manual on 143 SD-OCT volumetric images from 143 eyes in 99 patients with AMD

Dolejsi et al. [66] proposed a semi-automatic method for detecting SEADs from SD-OCT images using a conventional Graph Cut (maximum flow) algorithm. They proposed a regularisation energy term for Graph Cut that incorporates manual interventions. They showed a correlation of 0.97 and reproducibility mean error was 0.12 mm^3 on 25 SD-OCT B-scans of AMD patients. Quellec et al. [131] also proposed an automatic method for detecting SEADs including 11 boundaries of the retinal layers. It is a multi-scale 3-D graph search technique where the intensity value of the image constructs the cost function. The overall Mean Unsigned Surface Positioning Errors of SEADs in mean $\pm$ Standard Deviation is 5.75 ± 1.37 μm on 91 SD-OCT volumes from 39 (13 normal + 26 with pathology) subjects. Chen et al. [117] also proposed a method to detect SEADs using a probability constraint combined graph search graph cut method. They used approximate positions of the SEADs as candidate SEADs which were detected using a

supervised voxel classification approach, where features of voxel are constructed with textural, structural and positional information. In the second stage, a cost function is defined using the surface of the layers and candidate SEADs in a graph search graph cut method for detecting the SEADs. They showed a true positive volume fraction was 86.5% on 15 SD-OCT images of 15 subjects with exudative AMD.

Chen et al. [49] proposed a semi-automatic method for detecting geographic atrophy from SD-OCT images using a geometric active contour model. After estimating RPE layer positions, a projection image was generated where the presence of GA can be identified. A geometric active contour model is used for the segmentation of the GA on the projected images incorporating the shape and size of GA information in the edge weight cost function. The mean overlap ratios between automatic detection and manually drawn were 72.60% on 101 SD-OCT scans from 68 eyes in 64 patients. Hu et al. [67] proposed a semi-automatic method to detect geographic atrophy from SD-OCT images using a level setbased approach in the partial OCT projection image. Seed points of the GA for level set initialisation were chosen manually and a propagation speed image was generated by the mapping of the gradient magnitude of the partial OCT projection image. The area correlation was 0.96 ($P < 0.001$) on 20 macular volumes of 20 subjects with GA.

There are many automatic methods for detecting the optic disc or ONH from OCT images. Only a few extend their work towards cup detection and cup-disc ratio computation. The first work, by Boyer et al. [90] showed the correlation coefficient between manual and their algorithm to be 0.8 for cup diameter and 0.9 for disc diameter. Abramoff et al. [68] detected ONH using graph search and computed the cup-disc ratio with 0.93 correlation coefficient between manual and automatic detection. Lee et al. [81] used k-NN classifier for a cup and disc detection and found an unsigned error for the optic disc cup of 0.076 ± 0.026 mm and the neuroretinal rim of 0.061 ± 0.026 mm.

Some biomarkers are only able to extract from OCT images such as changes of the layer thickness, Bruch's membrane opening minimum rim width, minimum distance band. Our study found only Antony et al. [119] compute this parameter automatically. They reported that their measurements are not significantly different from the manual computation. Tan et al. [96] showed the thickness of the retinal layers as biomarkers for

the retinal diseases where Peak intensity finding performed layer segmentation. They performed disease correlation with the layer thickness and showed a reduction in thickness of inner retinal layers in glaucoma patients tracing 310 eligible eyes from 178 participants.

2.7.7   Classification model for diseased eye detection

Another interesting field of the OCT image processing is to classify normal and different eye diseased patients. Most of the research conducted features are created from image texture analysis using template matching and Local Binary Pattern (LBP) etc. Features are reduced using principal component analysis (PCA), Bag-of-Words, etc. Only one researcher, Fraccaro et al. [26] used retinal structure information and pathologies to create the features vector and to classify the images into normal and diseased. The classification methods have been developed using different types of machine-learning approach. Fraccaro et al. show Random Forest algorithms perform better than One-rule, Decision Tree, Logistic Regression, AdaBoost, and Support vector machines.

Liu et al. [153] proposed a method for macular pathology detection in OCT images using Local Binary Patterns (LBP) and gradient information as attributes. The method starts by aligning and flattening the images, and then a 3-level multi-scale spatial pyramid is created. From each level of the pyramid, edge and LBP histograms extracted in each block. These histograms are used to form a global descriptor. The principal component analysis is used to reduce the dimension of the global descriptor. Finally, a two-class, non-linear support vector machine is used to train the system and to classify the SD-OCT volume into normal macula and three macular pathologies (macular hole, macular edema and AMD). They used 193 volumes from 136 subjects for training the system and 58 volumes from 37 subjects for testing the system. The cross-validation area under the receiver operating curve (AUC) on the development dataset was 0.976, 0.931, 0939, and 0.938, and the AUC result on the holdout testing set was 0.978, 0.969, 0.941, and 0.975, for identifying normal macula, macular hole, maculae edema and AMD, respectively.

Albarrak et al. [154] proposed a decomposition-based approach for classifying the patients into normal or AMD. After de-noising the image, they flattened the image and

cropped an interest of volume for extracting 192 histogram bins as features using a normal LBP histogram and a Histogram of Oriented Gradients (HOG) for LBP-TOP on XY, XZ, and YZ planes. A Bayesian network classifier was then used to categorise the subjects. The proposed technique was evaluated using a ten-fold cross validation to 140 volumetric OCT images and demonstrated a promising performance with the best AUC value of 94.4%.

Srinivasan et al. [1] proposed a classification method to distinguish DME, AMD and normal SD-OCT volumes. After de-noising the image using the sparsity-based block matching and 3D-filtering, the image is flattened based on an estimated RPE layer position and the region of interest is cropped to extract features for the classifier. The features are extracted for each slice of a volume using HOG and a linear Support Vector Machines for classification. On a dataset of 45 patients equally subdivided into the three classes above, this method leads to a correct classification rate of 100%, 100% and 86.67% for DME, AMD, and normal patients, respectively.

Venhuizen et al. [155] also proposed a method for OCT images classification into AMD and normal patients using the Bag-of-Words (BoW) models. The method selected the key points in each B-scan from where textons are extracted around each key point. The dimension of the texton is reduced by using the PCA and create a codebook using k-means clustering. The obtained codebook from the training represents each OCT volume as a feature vector occurrence histogram. Finally, Random Forest with a maximum of 100 trees is used for the classifier. The method achieved an AUC of 0.984 with a dataset of 384 (269 AMD, 115 control) OCT volumes.

Fraccaro et al. [26] proposed a method for AMD and Normal Patients classification from SD-OCT images using various machine-learning approaches and showed Random Forest perform best compared to all other methods. They used manual segmentation of the drusen and other pathologies from 912 volumes of 487 patients. They tested Decision Tree, Logistic Regression, AdaBoost, Support vector machine and Random Forest algorithms. Regarding AUC, Random Forests, logistic regression and AdaBoost, they showed a mean performance of (0.92), followed by SVM and decision trees (0.90). Lemaitre et al. [14] proposed a method for automatic classification of patients into DME and normal

subjects from SD-OCT volumes. Their method was based on LBP features to describe the texture of OCT images and dictionary learning using the BoW models. The images were divided into local patches and extracted a dense set of LBP descriptors. They extracted 3D-LBP features from the entire OCT volume and used a Random Forest classifier. They used two datasets from two different sources and consisted of 32 (16 DME and 16 Normal) volumes from SERI and 30 (15 DME and 15 Normal) from Srinivasan et al. [1]. They achieved approximately 87% sensitivity and 75% specificity over the two datasets. Sidibe et al. [25] proposed a classification model for DME patients by modelling the appearance of normal OCT images with a Gaussian Mixture Model (GMM) and detecting abnormal OCT images as outliers. The classification of an OCT volume was based on the number of detected outliers. They used the same dataset as Lemaitre et al. [14] and showed a better output than both Lemaitre et al. and Venhuizen et al. [155]. They achieved a sensitivity and a specificity of 100% and 80% on the DUKE dataset [1].

2.8 Conclusions

Retinal and Choroidal imaging have developed quite rapidly over the past few decades. At the same time, image analysis becomes crucial in the care and progression of retinal disease in patients. In this review, we have described current ocular imaging modalities and their respective strengths for extracting different pathological information. We have also described current methods of detecting layers of the retina and the choroid from OCT images. We have also discussed OCT image processing images with pathologies, biomarker quantification and eye diseases classification. We have reviewed the methodologies, datasets, accuracy of the methods based on OCT image analysis. We have also discussed the pre-processing methods for reducing noise from the OCT image for detecting the layers more accurately.

Chapter 3

2D Segmentation (2DS) Algorithm for the Detection of Retinal Layers

This chapter presents a novel 2D segmentation method for segmenting four boundaries of the retinal layers in the presence of the pathologies from Spectral Domain Optical Coherence Tomography (SD-OCT) images. This chapter is based on following publications:

Md Akter Hussain, Alauddin Bhuiyan, Andrew Turpin, Chi D Luu, R Theodore Smith, Robyn H Guymer and Ramamohanarao Kotagiri, *"Automatic Identification of Pathology Distorted Retinal Layer Boundaries Using SD-OCT Imaging." IEEE Transactions on Biomedical Engineering 64.7 (2017): 1638-1649.*

Md Akter Hussain, Alauddin Bhuiyan and Ramamohanarao Kotagiri. *"Retinal Cross Sectional Layer Segmentation using Optical Coherence Tomography." 2nd Annual Doctoral Colloquium, The University of Melbourne. 2014.*

3.1 Introduction

Many researchers are increasingly using Spectral Domain Optical Coherence Tomography (SD-OCT) images for finding new biomarkers (for example thickness of the individual retinal layers) for early detection of Age-related Macular Degeneration (AMD) risk factors due to its ability to provide high resolution cross-sectional details of the retina [7, 8, 156]. Extraction method of the biomarkers (thickness of layers, the presence and size of drusen etc.) from the retinal SD-OCT image needs first the identification of the boundaries of the retinal layers in the presence of pathology [78].The retina has ten lay-

ers shown in Fig. 3.1 (top), details are in Chapter 2 (Section 2.2.1.4). The literature reviews of retinal layers segmentation are described in (Section 2.7.3). However, currently available automatic segmentation algorithms show poor performance for the segmentation of the retinal layers boundaries in the presence of pathology or morphological changes in the retina due to various diseases (please see the performance evaluation section 3.7). The morphological structure of the retinal layers such as Retinal Nerve Fiber Layer (RNFL), Photoreceptor Layer (PL) and Retinal Pigment Epithelium (RPE) are largely affected by the pathology of VitreoMacular Traction (VMT), drusen and OCT defined atrophy. The associated boundaries of these layers (RNFL, PL and RPE) are ILM-RNFL, MZ-EZ, IZ-RPE and RBC (ILM: Internal Limiting Membrane; MZ: Myoid Zone; EZ: Ellipsoid Zone; IZ: Interdigitation Zone, RBC: the complex of the RPE/BM/Choriocapillaris). RBC is the boundary between retina and choroid is defined by the retinal pigment epithelium (RPE), Bruch's Membrane (BM) and choriocapillaris [145]. Motivated by this, we have developed a robust effective automatic method for identification of these four important boundaries: ILM-RNFL, MZ-EZ, IZ-RPE and RBC in the presence of the pathology as shown in Fig. 3.1 (bottom). The significance of these four retinal boundaries can be summarised as follows:

- The change of retina thickness (ILM-RNFL to RBC) is one important biomarker for the retinal diseases such as AMD and Glaucoma [157].

- The role of VMT as shown by red arrow in Fig. 3.2 (a) is still unclear and needs further study [158]. Reliable identification of the ILM-RNFL boundary can also help determining the presence and the size of VMT.

- The IZ-RPE and RBC boundaries can determine the presence, location and size of drusen (as shown in Fig. 3.2 (red marks in a-d, f)), the most important biomarker for the retinal diseases such as AMD [20, 159].

- The identification of MZ-EZ, IZ-RPE and RBC boundaries can determine the presence, location and size of the OCT defined atrophy, an important biomarker for the retinal diseases such as advanced AMD as shown by red ellipse in Fig. 3.2 (e-f) [49].
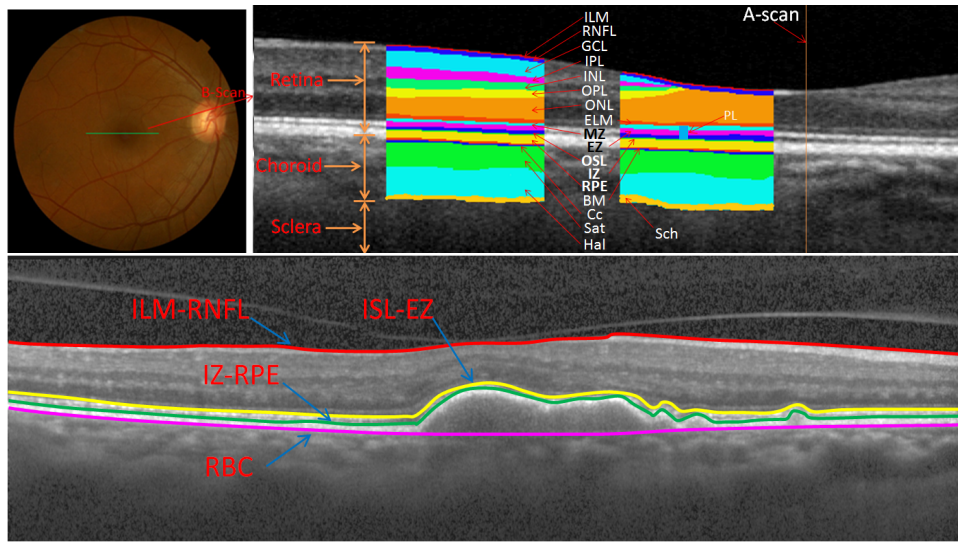
Retinal Layers: **ILM**: Internal Limiting Membrane; **RNFL**: Retinal Nerve Fiber Layer; **GCL**: Ganglion Cell Layer; **IPL**: Inner Plexiform Layer; **INL**: Inner Nuclear Layer; **OPL**: Outer Plexiform Layer; **ONL**: Outer Nuclear Layer; **ELM**: External Limiting Membrane; **PL**: Photoreceptor Layer; **RPE**: Retinal pigment epithelium.
IZ: Interdigitation Zone, a layer which is not always distinguishable even in the normal eyes.
PL is comprised with three segments and they are MZ + EZ + OSL **MZ**: Myoid Zone; **EZ**: Ellipsoid Zone; **OSL**: Outer Segment Layer;
RBC: The complex of the RPE/BM/choriocapillaris;

Figure 3.1: A Colour Fundus Photography image showing the retinal surface (top left) and a macula centre SD-OCT B-scan image (top right), a portion of the cross section across green line (top left image), defining the layers in the SD-OCT B-scan image. Proposed segmented boundaries are delineated in an SD-OCT image (bottom).
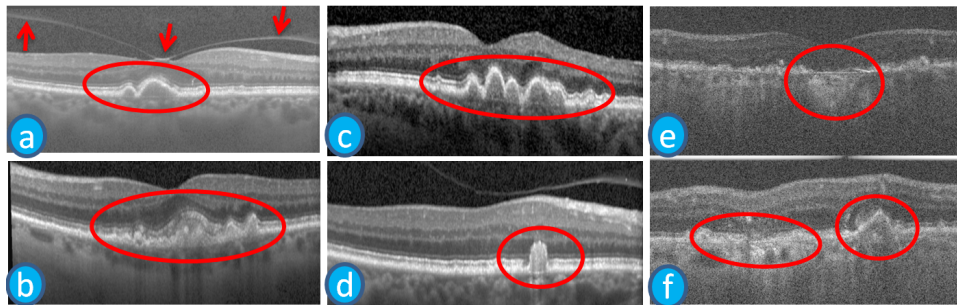
Figure 3.2: SD-OCT B-Scan images of the retina showing VMT, Drusen and OCT defined atrophy: (a) depicts drusen (red ellipse) and VMT (red arrow sign); (b, c, and d) contain drusen, distortion of layers and morphological changes in each image; (e) contains OCT defined atrophy; the left red ellipse of (f) is OCT defined atrophy and layers loss and the right red ellipse of (f) is drusen and layer loss.

In this chapter, we propose a robust automatic method to identify four significant boundaries of retinal layers in the presence of three common pathologies: VMT, drusen, and OCT defined atrophy. Our proposed algorithm uses a constrained search space

within an SD-OCT image and boundary specific intensity profiling of pixels that are labelled by the Canny edge detection algorithm [160] as edge pixels in determining boundaries accurately. We identify the boundaries by mapping the image-processing problem into the shortest path problem of weighted graph. In the mapped problem, the nodes of the graph represent the edge pixels. The edge weight between the nodes is determined using the pixel's distance, slope similarity to a reference and non-associativity of the layers, which is designed to overcome the effect of pathology on the boundary determination. Pixels associated with the shortest path forms the boundary. We utilise the approximate locations of three reference layers (TRL) for providing guidance in determining the optimum search space for the layer-boundaries. The boundaries are determined sequentially one after the other and sequence order is ILM-RNFL, RBC, MZ-EZ and IZ-RPE. We address the challenges associated with the identification of these layer-boundaries, which are as follows.

- The SD-OCT images of the retina usually have noise such as additive and speckle, which increases the difficulties of boundary identification.

- The retinal layers have varying thicknesses and generally weak contrast.

- The presence of pathologies in the retina creates unpredictable morphological changes in the layers. As a result, the identification of boundaries becomes more difficult and challenging. Some of the changes are as follows:

  - Drusen changes the structure of layers unpredictably. For example, the RPE and Photoreceptor layers as shown in Fig. 3.2 (a-f). Since, these layers are very thin, it is very difficult to identify the MZ-EZ, IZ-RPE and RBC boundaries.

  - The presence of OCT defined atrophy decreases the contrast between the PL and RBC as shown in Fig. 3.2 (e, f). As a result, the boundaries become invisible which makes it very difficult to identify the IZ-RPE and RBC boundaries.

  - The ILM-RNFL boundary is hard to identify while VMT is severe (larger VMT), since VMT has similar gradient pattern and is located immediately next to the ILM-RNFL boundary.

The rest of the chapter is organised as follows. The details of the proposed method is described in Section 3.2, 3.3 and 3.4. Sections 3.5, 3.6 and 3.7 comprise the validation methods, experimental setup and performance evaluation respectively. The novelty of our proposed algorithm is discussed in section 3.8. Finally, Section 3.9 concludes the chapter.

3.2   Proposed Method

Our method detects and identifies retinal ILM-RNFL, MZ-EZ, IZ-RPE and RBC boundaries from retinal SD-OCT B-scan images even in the presence of pathology. The steps involved in our method are shown in Fig. 3.3. In Step 1, we reduce the additive and speckle noise in the image by applying Wiener and Anisotropic Diffusion (AD) filters. The benefit of using both of these filters is that they remove the impulse noise while preserving the layer boundary position [161, 162]. In Step 2, we compute the approximate locations of three reference layers (*aprxTRL*) using their relative positions and pixel intensities. We refer to each of the *aprxTRL* as approximate RNFL (*aprxRNFL*), approximate ONL (*aprxONL*) and approximate RPE (*aprxRPE*). Following this, the *aprxTRL* are used as reference layers to detect the ILM-RNFL boundary. ILM-RNFL boundary is easily identifiable compared to other boundaries due to its high contrast. For this reason, we focus on identifying the ILM-RNFL boundary first. This also helps reducing the search space for computing the other boundaries. In Step 4, we refine the location of *aprxTRL* to increase the accuracy of identification of other layer boundaries. In Step 5, the RBC boundary is identified using the refined *aprxTRL* layers. Now, the search region is reduced to within the ILM-RNFL and RBC boundaries. This reduced search space helps us to identify the MZ-EZ boundary more accurately (Step 6). Finally, the IZ-RPE boundary is identified by searching between the MZ-EZ and RBC boundaries (Step 7). We note that IZ-RPE and RBC are the most difficult boundaries of the retina due to their low contrast and potential distortion by drusen and OCT defined atrophy. These boundary-oriented search spaces give an excellent accuracy even in the presence of the pathology and show better performance than the existing methods. We have used a stochastic optimization method,
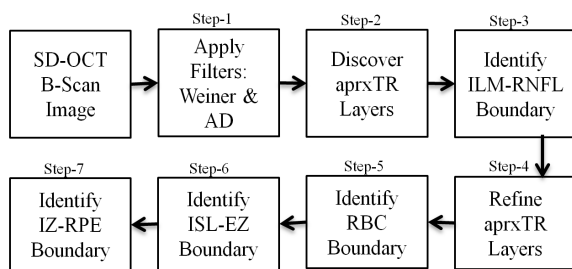
Figure 3.3: Flow diagram of the proposed method

Simulated Annealing (SA) [163] for approximating the global optimum for finding each constant parameter for our method, more details are presented in Section 3.6. Details of the boundary detection method are presented in the following subsections.

3.2.1   Noise removal by Wiener & Anisotropic Diffusion (AD) Filters

The SD-OCT images are affected by the intrinsic speckle noise, which reduces the quality of the image. Consequently, the identification of boundaries becomes very difficult and inaccurate [10]. Image de-noising is essential for accurate tracking of the boundaries. A traditional linear smoothing filter (for example, Averaging or Gaussian) blur or displace the semantically meaningful edges in the image [164] and are not suitable. Non-linear smoothing filters (for example, Wiener Filter and Anisotropic Diffusion (AD) filter etc.) can remove speckle and additive noise without disturbing the location of the edges. Thus, we have applied the Wiener Filter and Anisotropic Diffusion filter for removing noise and smoothing the image.

The Wiener Filter removes additive noise and inverts blurring simultaneously [162]. It minimises the overall mean square error in the process of inverse filtering and noise smoothing. The orthogonality principle implies that the Wiener filter in Fourier domain can be expressed as follows [162]:

$$W(x,y) = \frac{H^*(x,y)S_{xx}(x,y)}{|H(x,y)|^2 S_{xx}(x,y) + S_{nn}(x,y)} \tag{3.1}$$

where $S_{xx}(x,y)$ and $S_{nn}(x,y)$ are power spectra of the original image and the additive noise respectively, $H(x,y)$ is the blurring filter (low pass filter) and $H^*(x,y)$ is the

conjugate of the blurring filter.

Anisotropic Diffusion (AD) is a non-linear filter [161]. It can successfully smooth noise while preserving the region boundaries and small structures within the image, a very essential feature for SD-OCT B-scan image analysis. The AD filter can be expressed as follows.

$$AD(x,y,t) = \frac{\delta I(x,y,t)}{\delta t}$$
$$= div[g(\|\Delta I(x,y,t)\|)\Delta I(x,y,t)]$$

(3.2)

where t is the iteration time, $\Delta I(x,y,t)$ is the gradient image at iteration t, $g(.)$ is the conductance function and div is the divergence function. At $t = 0, I(x,y,0)$ represents the original image.

The conductance function is chosen to satisfy two different conditions. Firstly, in a uniform region where diffusion is maximal, $lim_{x\to 0}g(x) = 1$ must hold. Secondly, for across edges where diffusion is minimal, $lim_{x\to \alpha}g(x) = 0$ must hold so that the diffusion is stopped. We use the efficient conductance functions proposed by [161] as follows.

$$g(x) = \frac{1}{1+(\frac{x}{K})^2}$$

(3.3)

where K is the gradient magnitude threshold that controls the rate of the diffusion and serves as a soft threshold between the image gradients as attributed to noise and edges.

In our method, we have used Wiener filter with two iterations using 3×15 and 3×17 windows, these window sizes were found using SA. Since images have different resolution in the x and y-axis (that is, boundaries are horizontally expanded) we choose a rectangular window size to smooth the image and reduce noise. Following this, the AD filter is applied twice with $K = 32$, the numbers of first and second iteration are 8 and 3 which were determined using SA.
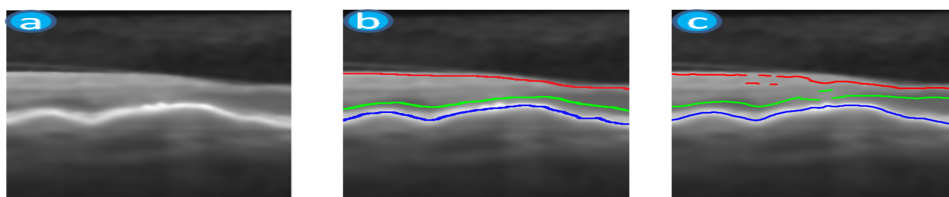
Figure 3.4: The TRL approximate detection: (a) is a smooth and a cropped portion of the retinal SD-OCT B-Scan; (b) manually delineated TRL; and (c) automatically discovered *aprxTRL* by our proposed method (red, green and blue lines represent the RNFL, ONL and RPE layer locations respectively).

3.2.2   Discover approximate locations of Three Reference Layers (*aprxTRL*)

To locate the boundaries, we utilise three layers (RNFL, ONL and RPE) location; two of them (RNFL and RPE) have the highest and one of them (ONL), has the lowest intensity in the retinal layers. The ONL layer is located in between RNFL and RPE layers as shown in Fig. 3.4 where red, green and blue lines represent the position of RNFL, ONL and RPE layers respectively. Due to their extremes of intensities in the retinal layers, they are easy to locate approximately, and we refer them as three references layers (TRL) because they are used to locate and bound the region of interest (ROI) and detect the boundaries. Since the approximate locations of the *aprxTRL* are easily detectable, we use them for narrowing the search space for boundary locations. For example, the ILM-RNFL boundary should be above the *aprxRNFL* layer.

We discover the approximate location of the TRL using column-wise (A-scan) intensity profiling. If we analyze the intensity profile of an A-scan, a low region surrounded by two high spikes will be found as shown in Fig. 3.5 (a). The two high spikes are the RNFL and RPE layer position and the low position is the ONL layer (red, green and blue dots define the RNFL, ONL and RPE layer position respectively). Since the SD-OCT images have noise and pathology, the intensity profile of the A-scan does not always follow the same pattern. The pattern can differ substantially from the case shown in Fig. 3.5 (b), where the RNFL layer has less brightness than the non-RNFL region (VMT) marked by a red arrow sign in the Fig. 3.5 (c). Thus simply focusing on using only the two highest intensity values for finding the position of the RNFL and RPE layers can lead to errors. For this reason, simultaneous consideration of the ONL layer with the RNFL and RPE

layers can reduce the probability of error. To find the position of the RNFL, ONL and RPE, an ideal signal is simulated and shown in Fig. 3.5 (d). This can be used as a model to fit to the actual signal along A-scan where two spikes and the low position represent the approximate location of the RNFL, RPE and ONL layers.

We use intensity value of those three layers pixels for finding the best fitting of the ideal signal (as shown in Fig. 3.5 (d)) to the original signal (intensity profile) along A-scan. The three pixels that have maximum $I(RNFL) + I(RPE) - I(ONL)$, the intensity of the corresponding layer pixels, are considered the best match.

$$C_{rn,rp,on} = \arg\max_{rn,rp,on}(I_{rn} + I_{rp} - I_{on}) \qquad (3.4)$$

This is formulated in (3.4) where C is the position of the three pixels that represent the approximate locations of RNFL, ONL and RPE layers. In (3.4), the indexes rn, rp, and on represent the position of RNFL, RPE and ONL layers respectively in the A-Scan. The relative position $(rn < on < rp)$ of the layers is also incorporated in (3.4) using the indexes for increasing accuracy. The TRL do not overlap each other rather they have varying relative distance such as RNFL and ONL layers have less distance at the center of the macula than other region of the retina. For finding the approximate location, we apply a constant relative distance constraint at the indexes in (3.4) which improve the robustness and accuracy. We add constraints $minRNO < on - rn < maxRNO$; and $minRPO < rp - on < maxRPO$; in the indexes of (3.4) where $maxRNO, maxRPO, minRNO$ and $minRPO$ are the maximum and minimum distance of RNFL and RPE layers from ONL layer. Since the retinal thickness is between 300 and 500 μm [9],we have chosen $maxRNO = maxRPO = 200\mu m(\approx 50pixels)$ and $minRNO = minRPO = 40\mu m(\approx 10pixels)$, since our dataset contains $1pixel \approx 4\mu$m.

Since, we are interested in the approximate location of TRL instead of exact boundary positions; we have more flexibility to smooth the images for getting more accurate position of the *aprxTRL*. As a result, we apply a Gaussian filter on the Wiener and AD filtered image to remove local noise. This smooth image is only used to find the *aprxTRL* and not for the accurate identification of boundaries. The Gaussian filter with a 10×10 window and 0.5 standard deviation is applied on the image. Now using (3.4), the constraints, and
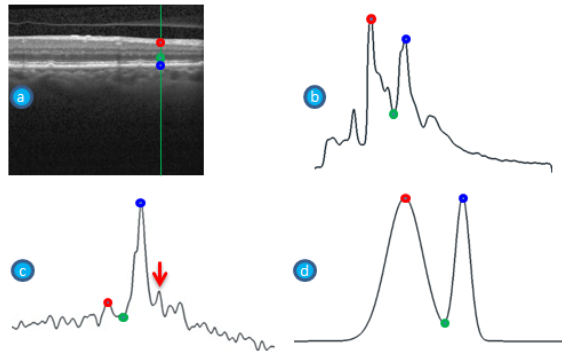
Figure 3.5: (a) A B-scan image showing one A-scan as a green line; (b) the intensity profile of the A-scan in (a) (green line on a); (c) is an A-scan from a different image, showing a different pattern of intensity profile; and (d) is used to fit to the actual signal for finding the *aprxTRL*. The red, green and blue circles define the RNFL, ONL and RPE layer positions respectively. The arrow sign on (c) indicates that pixels under RPE have higher intensity than the RNFL layer.

the Gaussian smooth image (I), we find the *aprxTRL*. Then these *aprxTRL* are used to identify the retinal layer boundaries as described in the following section.

3.2.3 General model for the identification of the four retinal layer Boundaries

The flow diagram for identifying a boundary of our proposed method is shown in Fig. 3.6 and Algorithm 1 provides the pseudo code. We utilise the *aprxTRL* for selecting the region of interest for any particular boundary. The *aprxTRL* give a smaller search space compare the whole image, reducing errors due to noise, pathology and poor contrast. Moreover, the pixels with peak intensity gradient (edge pixels) are considered rather than all image pixels for the identification of boundary. This provides the robustness and increases the efficiency of the method. The Canny edge detection algorithm is used to find edge pixels [160]. Then edge pixels are filtered using the information of the boundary position and intensity gradient [77]; for example, the edge pixels with positive intensity gradient and above *aprxRNFL* layer are considered for the identification of ILM-RNFL boundary. These selected pixels are called candidate pixels. The contiguous (within 3×3 neighbourhood) candidate pixels are grouped based on the number of pixels (that is, if there are more than *np* contiguous pixels, where *np* is a parameter, then split them so that the number becomes less than *np*) and called a pixel-group as shown in Fig. 3.7 (f), each
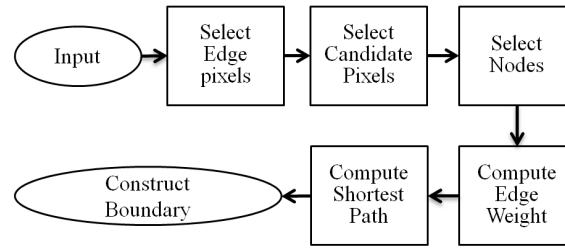
Figure 3.6: Flow diagram for identifying a boundary in our proposed method.

colour represents different pixel-group.

The end pixels of each pixel group form nodes in a graph, since we model the boundary identification problem as a graph shortest path problem. Large pixel groups can be misleading when pathology and/or noise causes mixing of two boundaries as shown in Fig. 3.2. We can avoid such difficulties by splitting pixel groups that are longer than the threshold *np* as shown in Fig. 3.7 (f). The edge weight is computed based on the node distance, slope discontinuity and non-association to the layers. The non-association value is computed using the boundary anatomical knowledge such as the candidate pixels with positive intensity gradient, closest and above *aprxRNFL* layer have high association (i.e. low non-association) to the ILM-RNFL boundary than other pixels.

Algorithm 1 2DS Algorithm for a boundary of retinal layers

Input: B-scan Image, required already detected boundary.
Output: Boundary position.
  1: Apply noise reduction filter.
  2: Find the ROI using already detected boundary.
  3: Apply Canny Edge Detection Algorithm and ROI to find the candidate pixels.
  4: Form pixel groups and their end pixels are labels as nodes. Form fully connected graph.
  5: Compute edge weights of the graph.
  6: Find the shortest path using Dijkstra's algorithm.
  7: Apply extrapolation for finding the boundary position using the pixels on the shortest path.

In Fig. 3.7, we pictorially show the procedure of finding MZ-EZ boundary as an example of the identification of the boundary by our proposed method. Figure 3.7 (a) shows an SD-OCT B-scan image. The edge pixels are shown in Fig. 3.7 (b). To form candidate pixels, edge pixels with positive intensity gradient are considered (Fig. 3.7 (c)) and the

region of interest is defined from the *aprxONL* layer to the RBC (Fig. 3.7 (d)). These candidate pixels are grouped so that no group has more than a certain number of pixels (*np*) as in Fig. 3.7 (e) (the red region of (d) magnified with pixel groups formed with $np = 15$). Then the end points (black rectangle in the coloured pixels) of each pixel group form the nodes in the graph as shown in Fig. 3.7 (e). The graph representing edge pixels-groups of Fig. 3.7 (e) is shown in Fig. 3.7 (f). To make it is clear, Fig. 3.7 (f) shows only partial graph and it does not show edges coming into the graph and leaving the graph to its neighbouring edge pixel-groups; Then graph edge weights are computed by incorporating the continuity of the node position by computing distance, slope discontinuity and non-association to a boundary. The weight computation method is described in the following sections. Finally, Dijkstra's shortest path algorithm is applied to the weighted graph to find the target boundary. We pick the pixel-groups of corresponding nodes of the shortest path and construct the boundary as shown in Fig. 3.7 (g). Then, the remaining non-connected pixels of the boundary are connected using extrapolation to produce a continuous line. Figure 3.7 (h) shows an example of the constructed boundary in the image.

3.3   Edge weight computation & Boundary construction

The weight of the edge between nodes *a* and *b* is computed as the sum of three components:

$$\omega_{a,b} = \phi_{a,b} + \psi_{a,b}^r + \gamma_{a,b} \tag{3.5}$$

where

$\phi_{a,b}$ represents the spatial distance between pixels *a* and *b*, and is high when *a* and *b* are not near each other in the image;

$\psi_{a,b}^r$ represents slope between *a* and *b* relative to an already determined reference line (r), and is high when the slope is not similar to the reference; and

$\gamma_{a,b}$ represents how well the pixel group containing *b* matches pre-defined properties
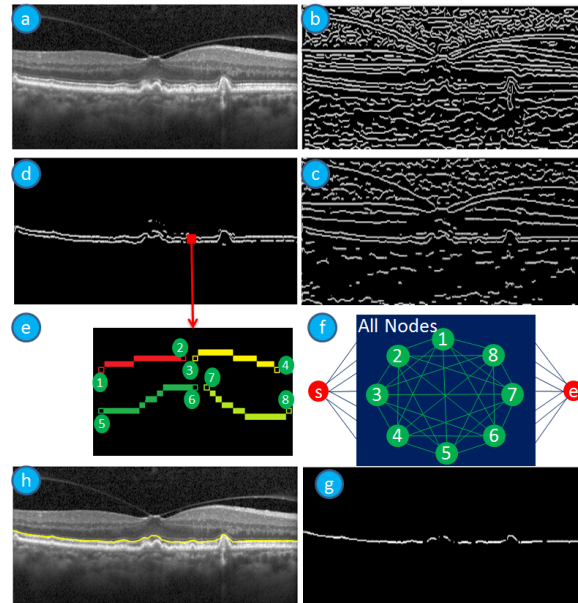
Figure 3.7: An example of MZ-EZ boundary detection steps: (a) the input SD-OCT B-Scan image; (b) the edge Image after applying Canny edge detection; (c) the edge pixels having positive intensity gradient; (d) candidate pixels; (e) a magnified image of the red region of (d), each colour represents different pixels-groups, and black circles represent the end pixels and node of the graph; (f) An example of the fully connected graph representation of the boundary detection problem (s and e is two special node added automatically for defining the start and destination for the shortest path algorithm). (g) corresponding pixel-groups obtained from the shortest path algorithm; and (h) the MZ-EZ Boundary (yellow line).

of pixels forming the boundary, and is high when pixels do not conform to that property.

3.3.1 The weight for the spatial distance ($\phi_{a,b}$)

The weight for the spatial distance ($\phi_{a,b}$) is computed as

$$\phi_{a,b} = \begin{cases} 0 & \text{, if } a = b \\ \alpha_0 & \text{, if } a \text{ \& } b \text{ in the same pixel-group} \\ \alpha_1|a_x - b_x|^2 + \\ \alpha_2|a_y - b_y|^2 + & \text{, otherwise} \\ \alpha_3|\frac{a_y - b_y}{a_x - b_x}|^2 \end{cases} \tag{3.6}$$

where α_1, α_2, and α_3 are three parameters, and a_x, a_y, b_x and b_y are the coordinate position of nodes a and b. $\alpha_0 = 0.0001$ is found using SA.

The three parameters α_1, α_2, and α_3 are linked with horizontal, vertical and diagonal distance respectively. The values of these coefficients are defined based on prior knowledge of the boundary being detected. For example, we put more cost on the vertical (α_2) and diagonal (α_3) distances for the RBC as it is flat, and usually not distorted by the pathologies we are studying.

Specific settings for α_1, α_2 and α_3 for each boundary are discussed in Section 3.4.

3.3.2   The weight for the slope similarity to a reference ($\psi^r_{a,b}$)

The boundaries of the retinal layers are horizontally aligned, even though they may have sudden deviations (spikes) due to pathology or morphological structure of the retina (as shown in Fig. 3.2). While the spatial distance $\phi_{a,b}$ rewards pixels that are close to each other, it may lead to boundaries that are not the same shape as their neighbouring boundaries. The term $\psi^r_{a,b}$ corrects for this, giving high weights to pixel pairs that have a slope that is dissimilar to the given reference line r (for example, one of the *aprxTRL* boundaries), and low weights to slopes that are similar to r. This may also have the effect of causing a and b to incorrectly merge with another boundary, which is why we introduce the third component $\gamma_{a,b}$ described in the next section.

$$\psi^r_{a,b} = |(r(a_x) - a_y) - (r(b_x) - b_y)| \tag{3.7}$$

where $r(x)$ is the y value of the reference boundary r at x-coordinate x.

Figure 3.8: An example of the computation of the weight for finding the slope disconti-nuity (ψ).

For example, in Fig. 3.8, the red line is r and the white pixels are candidates for a boundary. Let us choose four pixels as four nodes a (green pixel), b (red pixel), c (pink pixel) and d (blue pixel). The vertical yellow lines represent the distance between nodes to the r along an A-scan. In this example, the signed distance between nodes and r is

$$
\begin{aligned}
d_a &= (r(a_x) - a_y) = 126 - 121 = 5 \\
d_b &= (r(b_x) - b_y) = 4, \\
d_c &= (r(c_x) - c_y) = -4 \text{ and} \\
d_d &= (r(d_x) - d_y) = -5. \\
\text{Hence, } \psi^r_{a,b} &= |d_a - d_b| = 1, \\
\psi^r_{a,c} &= |d_a - d_c| = 9 \text{ and} \\
\psi^r_{c,d} &= |d_c - d_d| = 1,
\end{aligned}
$$

so the two segments joining ab and cd are closer in slope to r than the segment ac, as expected.

3.3.3 The weight for the layer's non-associativity ($\gamma_{a,b}$)

For each boundary, one or more properties of pixel groups for that boundary is defined. In particular, a count of the pixels that satisfy the properties is used to decrease the weight of the edge between a and b. For example, pixels in the ILM-RNFL boundary should be above the *aprxRNFL* layer, thus when computing this boundary, a count of pixels above
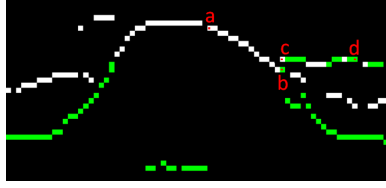
Figure 3.9: An example of the computation of the weight for finding the layer's non-associativity (γ).

the *aprxRNFL* for each pixel group is used. In general,

$$\gamma_{a,b} = \sum_i (1 + E_b - f_{b,i})^{p_i} \tag{3.8}$$

where E_b is the number of pixels in the pixel-group containing node b, i is 1 to total number of property, $f_{b,i}$ is the number of associated pixels for i^{th} property in the pixel group containing node b, and p_i is a parameter to control the influence of each property. Thus when many pixels satisfy property i, $f_{b,i}$ is close to E_b and so the total weight is near to zero. On the other hand, when there are not many pixels that satisfy property i, $f_{b,i}$ is small relative to E_b and $\gamma_{a,b}$ is large.

The idea is further illustrated in Fig. 3.9, which shows candidate pixels for computing the MZ-EZ boundary. Each pixel is colour coded according to their satisfaction of Property 1: closeness to the *aprxRPE* layer. For each A-scan (column in the image), there is one white pixel that is close to the *aprxRPE* layer (not shown) while the green pixels do not satisfy this property. Also shown, two pixel groups which contain four nodes a, b, c and d (the end points of the each pixel groups is the graph node). The pixel group with nodes a and b has $E_b = 15$ pixels, and $f_{b,1} = 14$ pixels satisfying Property 1 (white pixels); while the pixel group with nodes c and d has $E_c = 12$ pixels, and $f_{c,1} = 5$ white pixels. Thus, $\gamma_{a,b} = (1 + 15 - 14)^p = 2^p$, and $\gamma_{a,c} = (1 + 12 - 5)^p = 8^p$. No matter the value of $p > 0$, it can be seen that the edge from a to b will have a lower weight than the edge from a to c which is correct as that edge has more pixels that obey Property 1 (closer to *aprxRPE*).

For each boundary, properties are chosen based on the retinal structure, nearby *aprxTRL*, intensity profile and boundary gradient. We note that there could be multiple properties for a particular boundary: all are described in Section 3.4.
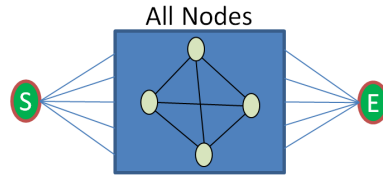
All Nodes

Figure 3.10: The start and end nodes are specially and automatically handled in our method. Only horizontal distances are considered to compute the edge weight for all nodes to start and end nodes.

3.3.4 Selection of start and end node points

We create two special nodes in the graph, the start and the end, which are given x coordinates of 0 and one more than the width of B-scan respectively. Each of these special nodes is connected to all other nodes in the graph, with an edge weight of

$$\omega_{a,b} = (a_x - b_x)^2$$

where a is the start or end node, and b is any other node in the graph. This is shown in Fig. 3.10, and is the same procedure for all boundaries.

3.3.5 Boundary construction from the shortest path

After adding the start and end nodes with computing their weight, shortest path between the two is computed using Dijkstra's shortest path algorithm [165]. Since, start and end nodes are found automatically by our method, these two nodes are removed from the shortest path for the final boundary. Next, the pixel-groups of the corresponding nodes of the shortest path are extracted from the candidate pixels list and the remaining non-connected pixels are joined using extrapolation. Since, remaining noise (the Wiener and AD filter cannot remove noise completely) creates unwanted spikes in the boundary, we apply Gaussian smoothing on the boundary as a final step.

3.4 Identification of four boundaries

This section describes each boundary identification method including defining the coefficients and properties for the edge weight computation. The constant coefficients for each boundary are determined using Simulated Annealing and more details will be found in Section 3.6. The method of boundary identification is described according to the flow diagram of boundary identification which is found in Fig. 3.6.

3.4.1 Identification of ILM-RNFL boundary

ILM-RNFL boundary is the first boundary to be identified by our proposed method. *Select Edge pixels:* Canny edge detection algorithm is applied with standard deviation $\sqrt{2}$ and threshold value 0.1 for finding the edge pixels. *Select Candidate pixels:* The edge pixels with non-positive intensity gradients are removed. The remaining edge pixels which are closest and above the *aprxRNFL* layer are considered as the initial candidate pixels. Pixels that are connected to initial candidate pixels are also included to form the candidate pixels. *Select Nodes:* Pixel-groups are formed from $np = 25$ contiguous pixels, and end pixels of each pixel-groups are taken as the nodes in the graph. *Compute Edge Weight:* The three coefficients of (3.6) for computing spatial distance (ϕ) for this boundary are set to $\alpha_1 = 1, \alpha_2 = log_2(|a_y - b_y|)$ and $\alpha_3 = 2.5$. The ILM-RNFL boundary does not fluctuate much vertically in macula centred B-scan images, hence the higher value for α_2. For computing the weight ψ^r (slope similarity to reference r) using (3.7), we define r to be a first order polynomial fitted to the *aprxRNFL* layer pixels. Next, layers' non-associativity weight (γ) is computed using two properties.

Property 1: The candidate pixels that are the closest and above the *aprxRNFL* layer along each A-scan with $p_1 = 2$.

Property 2: The candidate pixels above the *aprxONL* layer along A-scan with $p_2 = 2$.

Finally, the boundary is constructed using the shortest path algorithm as described in Sections 3.3.4 and 3.3.5.

3.4.2 Identification of RBC boundary

We know that the RBC boundary is below the ILM-RNFL, which we just located in the previous section, so we can restrict the search space for this boundary to between the ILM-RNFL and the the bottom of the B-scan. This smaller search space provides us higher confidence and accuracy on refining the *aprxTRL*, and allows more efficient computation. We can also use this reduced search space to refine estimates of the *aprxTRL*. The previous discovery of *aprxTRL* could have error as shown in Fig. 3.11 (a) and 3.11 (c) due to noise and pathology. Since these layers are the reference positions for the actual boundaries, the accuracy of *aprxTRL* directly influences the identification of boundaries. The refined output is shown in Fig. 3.11 (b) and 3.11 (d). This refinement procedure is the same as for the initial discovery, but one new limit condition on the index *rn* is added: $ILM\text{-}RNFL < rn < ILM\text{-}RNFL + \delta$, where δ is the approximate RNFL thickness which is set to 100μm (≈ 25 pixels) [166]. These refined *aprxTRL* are used for identification of the rest of the boundaries.

Select Edge pixels: The edge pixels are extracted using the Canny edge detection algorithm. Sometimes this boundary has low contrast due to pathology, and for this reason, a low standard deviation of 1.00 and a low threshold value of 0.01 are used for the Canny edge detection algorithm. *Select Candidate pixels:* The edge pixels with negative intensity gradient and located between the *aprxONL* layer and 500μm (≈ 125 pixels) below the ILM-RNFL boundary (since maximum retina thickness is 500μm [9]) become candidate pixels. *Select Nodes:* Each individual pixel forms a pixel group by itself. *Compute Edge Weight:* Since the RBC boundary is a relatively smooth line, the costs for the vertical (α_2) and diagonal distance (α_3) are given higher values than the horizontal distance (α_1) in the spatial distance weight computation. So, the coefficients of (3.6) are set to $\alpha_1 = 3, \alpha_2 = |a_y - b_y|$ and $\alpha_3 = 5$. Weight ψ (slope similarity to *r*) is computed using (3.7) and *r* set to a first order polynomial fitted line on the *aprxRPE* layer. A single property is used for computing the non-associativity weight (γ): the closest and below the *aprxRPE* layer along A-scan in the candidate pixels. Value p_1 is set to 2. Then the shortest path is computed and the boundary is constructed as previously described.
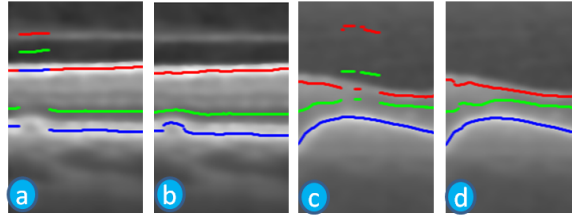
Figure 3.11: Two examples of *aprxTRL* refinement (shown in smoothed SD-OCT images). (a) and (c) are the *aprxTRL* before refinement; (b) and (d) are the refined *aprxTRL* of (a) and (c) respectively. Red, green and blue lines represent the RNFL, ONL and RPE layer positions respectively.

3.4.3 Identification of MZ-EZ boundary

Select Edge pixels: Since the MZ-EZ boundary has high contrast, the standard deviation and threshold values used for Canny edge detection are the same to those used for the ILM-RNFL boundary pixel detection. *Select Candidate pixels:* The search space for the identification of the MZ-EZ boundary is constrained above by the ILM-RNFL and below by the RBC boundaries. This small search space increases the efficiency of the method as well as the accuracy. The region of interest for the MZ-EZ boundary is defined under the *aprxONL* layer and above the RBC boundary. The edge pixels with positive vertical intensity gradient (along an A-scan) in that region of interest form the candidate pixels. *Select Nodes:* The contiguous pixels where $np = 15$ form the pixel-group, and end pixels of each pixel-group form the nodes of the graph. *Compute Edge Weight:* The coefficients of (3.6) are set to $\alpha_1 = log_2(|a_x - b_x|), \alpha_2 = 1$ and $\alpha_3 = 2$. The RBC boundary is used as r to compute the slope similarity weight (ψ^r). There are three properties that are used for computing the layers' non-associativity weight, and the power (p_i) is set to two for all of them. Using this weight, the shortest path is computed and boundary is constructed. The properties are as follows.

Property 1: Two nearest pixels along A-scan from the *aprxRPE* layers.

Property 2: Top most candidate pixels from Property 1 along A-scan.

Property 3: The pixels having the lowest intensity in each A-scan of the pixels from Property 1.

3.4.4 Identification of IZ-RPE boundary

Select Edge pixels: Since IZ-RPE boundary has low contrast, the parameters of Canny edge detection algorithm are set to those of the RBC boundary. *Select Candidate pixels:* The region of interest for the identification of IZ-RPE boundary is set using MZ-EZ as the upper limit and RBC as the lower limit. Then the edge pixels with positive vertical intensity gradient in that region of interest form the candidate pixels. *Select Nodes:* Each pixel of the candidate pixels is in its own pixel-group, and hence all are nodes. *Compute Edge Weight:* The coefficients of (3.6) are set to $\alpha_1 = (|a_x - b_x|), \alpha_2 = 3$ and $\alpha_3 = 2.5$. The RBC boundary is used as r to compute the slope similarity weight ψ^r. Then three properties are used for computing the layers' non-associativity weight. The power (p_i) for all of them is set to two. These three properties are as follows.

Property 1: The candidate pixels under the MZ-EZ boundary along A-scan. If no pixel is found in any A-scan then the pixels of the MZ-EZ boundary are chosen.

Property 2: The candidate pixels other than the pixels of the MZ-EZ boundary.

Property 3: The challenges for the abnormalities of drusen are addressed by this property. At first, the approximate drusen areas are discovered. If the distance between the MZ-EZ and the RBC along an A-scan is more than the distance of the average plus one standard deviation, then the A-scan is considered an approximate drusen area. The bottom candidate pixels in each A-scan other than the approximate drusen areas are selected for the third property. Then the average distance between those selected associated pixels and RBC along the A-scan are computed. The pixels closest to RBC boundary and above that average distance in the approximate drusen area are included into the third property.

Finally, shortest path is computed and boundary is constructed as shown in Fig. 3.7 (e), and 3.7 (f).

3.5   Validation method

For evaluation we compared the automatically produced output images against the manually segmented images (ground truth). We compute the precision of the boundary locations by computing the root mean square error (RMSE) between two different segmentations. The performances of six automatic methods are reported to justify the accuracy and robustness of the method.

RMSE is the average pixel distance of a single boundary between two different segmentations. It is the most well known and reported evaluation protocol for the segmentation of objects or boundary. Lower RMSE means better accuracy or performance for the method.

$$RMSE(B^{i,j_1}, B^{i,j_2}) = \sqrt{\frac{\sum_x (B^{i,j_1}(x) - B^{i,j_2}(x))^2}{\|A\text{-}scan\|}} \qquad (3.9)$$

where B^{i,j_1} is the ith boundary by the j method, $B^{i,j_1}(x)$ is the y-axis position of the ith boundary at x^{th} A-scan by the method j, $\|A\text{-}scan\|$ is the total number of A-scans, and x is taken over all A-scans.

3.6   Experimental setup

We evaluated our method on three datasets. Two of them are public datasets provided by Chiu et al. [78] and Tian et al. (OCTRIMA-3D) [63]. The third one is an image set obtained from Centre for Eye Research Australia (CERA). We have compared our method with five published automatic methods: AURA tools [101, 150], Iowa Reference Algorithm [8, 149], Dufour's Software [114, 151], OCTRIMA-3D [63] and Chiu et al. [78]. Among the published methods, AURA tools [150], Iowa Reference Algorithm [149] and Dufour's Software [114, 151] are publicly available. These methods need some additional information and predefine file types to process and identify the boundaries from SD-OCT images. For example, the Dufour software needs voxel size in mm, and AURA tools can only process vol and img file types which are proprietary file formats. The public datasets do not have many of those required parameters and file types. For this reason, we do not evaluate them on the two public data sets. This exclusion does not affect our performance evalua-

tion, as our aim is to show the robustness of our method on different datasets. Since, the two graph-based models, Chiu et al. and OCTRIMA-3D, are not available publicly, we have implemented their methods based on their published papers [77,78] and [63] respectively for a fair comparison with other methods by a common dataset (CERA dataset).

In our method, there are several constant coefficients to be defined. There are two window sizes ($w1x, w1y, w2x$, and $w2y$) for the Wiener filter, three parameters (K, two iteration values it_1 and it_2) for the anisotropic diffusion filter, four parameters ($\alpha_0, \alpha_1, \alpha_2$ and α_3) for (3.6), several p_i for the (3.8) and two values for np (number of maximum pixels in pixel-groups). For determining these coefficients, we have used a stochastic optimisation method for approximating the global optimum using Simulated Annealing (SA) [163]. This method works efficiently for finding discrete values for a large number of parameters. Since our method needs to determine 27 parameters for 4 boundaries, SA is used and the optimisation function used is root mean squared error. Table 3.1 shows the lower limit, upper limit, and step size (difference between two consecutive number) that are used for the parameter selection using SA. We have set two stopping criteria for the SA and they are *ErrorTolerance = 1e-6* and *MaxIterations = 5000*. The optimum values from the SA is also reported in Table 3.1. We have used 7 B-scans of four subjects from our local dataset for the optimisation of parameters and remaining 11 subjects are used for the performance of evaluation purposes.

Chiu's dataset includes 20 subjects; each one having 11 B-scans (220 B-scans in total) with various stages of drusen and OCT defined atrophy. The images are captured by the Bioptigen Envisu Spectral Domain Ophthalmic Imaging Systems from four different organisations under the A2A SD-OCT study [78]. This dataset contains manual segmentation of three retinal boundaries from two graders (MG1 and MG2) and their automatic segmentation output. These three boundaries are ILM-RNFL, IZ-RPE and RBC.

The second dataset is a dataset provided by Tian et al. [63]. The dataset contains 10 Spectralis SD-OCT (Heidelberg Engineering GmbH, Heidelberg, Germany) volume data sets from 10 healthy adult subjects in .mat file format. The original file contains 61 B-scans per subject, but only 10 B-scans per subject are available publicly. Each subject was scanned using IR+OCT scanning mode with a 30° area setting. The dimensions of the

Table 3.1: Parameter selection using the Simulated Annealing (SA).

Parameter Name	w1x	w1y	w2x	w2y	K	it_1	it_2	α_0
Lower Limit	1	1	1	1	10	0	0	1e-15
Upper Limit	30	40	30	40	60	40	30	1
Step Size	1	1	1	1	1	1	1	†
Optimum Value	3	15	3	17	32	8	3	1e-4

	For ILM-RNFL					For MZ-EZ					
Parameter Name	α_1	α_3	P_1	P_2	np	α_2	α_3	P_1	P_2	P_3	np
Lower Limit	0	0	0	0	0	0	0	0	0	0	0
Upper limit	8	8	8	8	80	8	8	8	8	8	80
Step Size	0.5	0.5	0.5	0.5	1	0.5	0.5	0.5	0.5	0.5	1
Optimum Value	1	2.5	2	2	25	2	2	2	2	1	15

	For IZ-RPE					For RBC					
Parameter Name	α_2	α_3	P_1	P_2	P_3	α_1	α_3	P_1	P_2	P_3	np
Lower limit	0	0	0	0	0	0	0	0	0	0	0
Upper limit	8	8	8	8	8	8	8	8	8	8	80
Step Size	0.5	0.5	0.5	0.5	0.5	0.5	0.5	0.5	0.5	0.5	1
Optimum Value	3	2.5	2	2	2	3	5	2	2	1	15

† It is chosen from $1, 10^{-1}, 10^{-2}, 10^{-3}, 10^{-4}, 10^{-15}$.

B-scan are 768×496 pixels (width $\times$ height). The axial resolution was 3.9μm and the transversal resolution varied from 10 to 12μm. To reduce the speckle noise and enhance the image contrast, every B-scan was the average of five aligned images. The dataset contains eight boundary positions selected by two expert graders (MG_1 and MG_2) and Tian et al.s' automatic segmentation output.

The third dataset has been collected locally from the Centre for Eye Research Australia (CERA) [159]. This dataset contains 15 subjects having varying stages of AMD. The dataset has various sizes of drusen complex in nearly all B-scan images. The images are macula centred and captured by a Heidelberg Spectralis SD-OCT scanner. Each subject has 49 B-scans with size 1024×496 pixels. Since manual segmentation is very time consuming, only the middle five B-scans for each subject has been manually segmented by an expert grader, and checked by a second expert grader. The grader used GIMP image editing software for delineating the targeted four retinal boundaries. The manual segmentation serves as the ground truth for this dataset The performances of the methods are discussed in the following section. Note that the bold texts in the tables show the best accuracy for the corresponding boundary. The p-values reported in the tables are computed using the paired sample t-test.

3.7 Results

We have computed the Root Mean Square Error (RMSE) on the results produced by our method and the ground truths (GT) that are provided in the dataset of Chiu et al. [78]. Similarly, we have produced the RMSE for the output of Chiu et al. [78] and the same GTs. They are reported in Table 3.2. The RMSE is also computed on Tians dataset for our proposed method and OCTRIMA-3D (Tian et al. [63]) against manual grading with the provided dataset and reported in Table 3.3. The tables (3.2 and 3.3) contain RMSE of their (Chiu et al. and Tian et al.) published segmentation, our implementation of their (Chiu et al. and Tian et al.) methods and our proposed method. The tables show that in each boundary that is produced by our proposed method has less RMSE than our implemented segmentation of the methods by Chiu et al. and OCTRIMA-3D, and the

differences are statistically significant. It is clear that the results of our implementation of the approaches of Chiu et al. and Tian et al. have lower accuracy compared with their reported results on the same data sets. We have made every attempt to try and reproduce their results by directly contacting the authors. Unfortunately, their software is not available due to their commercial interest, and so we could not replicate their experimental setup and any manual tuning of parameters that they may have applied to obtain their reported results. Although our proposed method has a slightly higher error than the published segmentation of Chiu et al. method for all boundaries, our proposed method is consistently low for all three datasets (reported in Table 3.2, 3.3, and 3.4). Moreover, the RMSE errors of two boundaries (ILM-RNFL and RBC) are not significantly different between our proposed method and inter grader in the Chiu's dataset. For Tians dataset, our proposed method has a slightly lower error than the published segmentation of Tian et al. method for two boundaries and slightly higher error for other two boundaries, but consistently low for each boundary of each of the datasets. Moreover, the RMSE errors of three boundaries are not significantly different between our proposed method and inter grader in the Tian's dataset. The error for the IZ-RPE boundary is high compared to all other boundaries because of its low contrast for both datasets and the distortion due to drusen and OCT defined atrophy, is larger than any other boundaries in the Chius dataset.

The CERA dataset is used to generate the RMSE for OCTRIMA-3D [63], Chiu et. al. [78], Dufour's Software [114, 151], Iowa Reference Algorithm [149], AURA tools [150] and our proposed method. The RMSEs are reported in Table 3.4 for each boundary (four). Chiu et al. does not identify MZ-EZ boundary and for this reason it is not reported (shown as NA in the table). The p-values from the paired-sample t-test of the RMSE between proposed and the other segmentation methods are always less than 0.001, reported in the Table 3.4. These results show that the overall RMSE for our proposed method is 1.57 ± 0.69 pixels where OCTRIMA-3D [63], Chiu et. al. [78], Dufour's Software [114, 151], Iowa Reference Algorithm [149], AURA tools [150] are 16.17 ± 22.64, 6.66 ± 9.11, 5.70 ± 10.54, 3.69 ± 2.04 and 2.29 ± 1.54 pixels respectively. For the ILM-RNFL boundary, AURA tools shows the best accuracy. For all other boundaries, our proposed

Table 3.2: The mean ± standard deviation of the RMSE in pixels for all boundaries on the Chiu et al. public dataset.

Boundary	Manual Segmentation by Grader 1 (MG$_1$) vs				Manual Segmentation by Grader 2 (MG$_2$) vs		
	MG$_2$	Chiu et al.		Our Method	Chiu et al.		Our Method
		Published	Our Imp.		Published	Our Imp.	
ILM-RNFL	1.66 ± 0.64 *	**1.39** ± **0.38** ‡	6.76 ± 13.29 †	1.54 ± 0.83	**1.61** ± **0.64** †	6.81 ± 13.38 †	1.91 ± 0.92
IZ-RPE	2.96 ± 1.04 †	**2.73** ± **1.02** †	6.22 ± 8.94 †	3.49 ± 1.46	**2.99** ± **1.21** †	5.88 ± 9.07 †	3.45 ± 1.54
RBC	1.93 ± 0.76 $^\bullet$	**1.66** ± **0.84** †	7.33 ± 9.74 †	2.07 ± 1.81	**2.03** ± **0.84** ‡	7.47 ± 9.78 †	2.33 ± 1.76
Overall	2.19 ± 1.00 $^\circ$	**1.93** ± **0.98** †	6.77 ± 10.81 †	2.37 ± 1.65	**2.21** ± **1.09** †	6.72 ± 10.91 †	2.56 ± 1.59

$^\star p = 0.07$, $^\bullet p = 0.26$, $^\circ p = 0.002$, $^\dagger p < 0.001$, $^\ddagger p = 0.006$, (paired t-test against Our Method).

Table 3.3: The mean ± standard deviation of the RMSE in pixels for all boundaries for Tian et al. (OCTRIMA-3D) data set of normal eyes.

Boundary	Manual Segmentation by Grader 1 (MG_1) vs				Manual Segmentation by Grader 2 (MG_2) vs		
	MG_2	OCTRIMA-3D Published	OCTRIMA-3D Our Imp.	Our Method	OCTRIMA-3D Published	OCTRIMA-3D Our Imp.	Our Method
ILM-RNFL	1.24 ± 0.28 ⊤	0.98 ± 0.24 ⊤	2.32 ± 6.49†	$\mathbf{0.97 \pm 0.24}$	$\mathbf{1.26 \pm 0.29}$‡	2.55 ± 6.36†	$\mathbf{1.26 \pm 0.29}$
MZ-EZ	0.98 ± 0.22 ⊥	0.79 ± 0.15†	5.52 ± 16.27†	$\mathbf{0.71 \pm 0.33}$	1.11 ± 0.32 *	5.92 ± 16.22†	$\mathbf{1.08 \pm 0.39}$
IZ-RPE	2.56 ± 0.98 ⊥	$\mathbf{1.88 \pm 1.11}$†	7.55 ± 14.53†	2.96 ± 1.42	$\mathbf{2.07 \pm 0.77}$†	6.19 ± 15.33†	2.82 ± 1.91
RBC	1.40 ± 0.39 *	$\mathbf{0.96 \pm 0.20}$†	6.43 ± 17.24†	1.01 ± 0.93	$\mathbf{1.30 \pm 0.35}$●	6.65 ± 17.24†	1.39 ± 0.95
Overall	1.55 ± 0.82 °	$\mathbf{1.15 \pm 0.72}$†	5.46 ± 14.35†	1.41 ± 1.25	$\mathbf{1.43 \pm 0.60}$†	5.33 ± 14.49†	1.64 ± 1.29

⊤ $p = 0.61$, ⊥ $p = 0.005$, ⊥ $p = 0.17$, * $p = 0.95$, ° $p = 0.09$, † $p < 0.001$, ‡ $p = 0.96$, * $p = 0.25$, ● $p = 0.29$ (against Our Method).

method shows the best accuracy.

In Fig. 3.12, we have delineated the ILM-RNFL, MZ-EZ, IZ-RPE and RBC boundaries using red, yellow, green and magenta lines respectively using all methods. We also put an original B-scan without any mark for the reference. The figure shows that our method performs the closest to the manually marked image. We note that Iowa Reference algorithm and AURA Tools work well for ILM-RNFL detection, but fail in detecting the other three boundaries. We observe that Dufour's software is better than the Iowa Reference approach in the detection of the ILM-RNFL, MZ-EZ and RBC boundaries, while it fails to detect IZ-RPE at the area of large drusen when the thickness of MZ decreases significantly. Also, Chiu's method works well on detecting ILM-RNFL and IZ-RPE, however, it completely fails to detect the RBC boundary. The OCTRIMA-3D algorithm fails to detect any of the boundaries for this image (Fig. 3.12) because of its dependency on the MZ-EZ boundary, which is disrupted by drusen in this image. Thus OCTRIMA-3D fails to detect the MZ-EZ boundary, and, consequently, the method fails to detect all other boundaries. Our method shows excellent performance for each of the boundaries compared to other methods.

3.8 Novelty of the proposed segmentation algorithm for detecting the retinal layers

Our proposed segmentation methods for detecting the boundaries of the retinal layers have the following novel features that help find layer boundaries very accurately.

- Narrowing the region of interest based on the approximate positions of three reference layers (TRL): The boundaries of the retinal layers are very close to each other. Within 350 μm retina, there are at most 12 boundaries. These dense areas of boundaries make detecting retinal layers boundaries very challenging. The detection of thin layers, for example, Myoid Zone (MZ) and External Limiting Membrane (ELM), are more challenging. The absence of layers due to the anatomical structure of the retina such as optic disc region and the effect of pathologies also make this detection more challenging. Narrowing the region of interest can provide a solution

Table 3.4: The mean ± standard deviation of the RMSE in pixels for various methods on the CERA data set.

Boundary	OCTRIMA-3D	Chiu et al.	Manual Segmentation vs			Our Method
			Dufour	Iowa	AURA tools	
ILM-RNFL	13.00 ± 20.91 †	5.96 ± 9.39 †	1.59 ± 0.22 †	3.13 ± 0.61 †	**1.02 ± 0.16** ‡	1.07 ± 0.17
MZ-EZ	16.90 ± 23.54 †	NA	4.34 ± 3.28 †	2.55 ± 0.50 †	2.11 ± 1.35 †	**1.21 ± 0.41**
IZ-RPE	16.83 ± 21.13 †		12.52 ± 18.88 †	3.44 ± 1.12 †	2.68 ± 1.20 †	**2.10 ± 0.54**
RBC	17.95 ± 25.03 †	6.84 ± 10.09 †	4.37 ± 3.84 †	5.64 ± 3.08 †	3.35 ± 1.84 †	**1.91 ± 0.81**
Overall	16.17 ± 22.64 †	6.66 ± 9.11 †	5.70 ± 10.54 †	3.69 ± 2.04 †	2.29 ± 1.54 †	**1.57 ± 0.69**

† $p < 0.001$, ‡ $p = 0.003$ (paired t-test against Our Method).
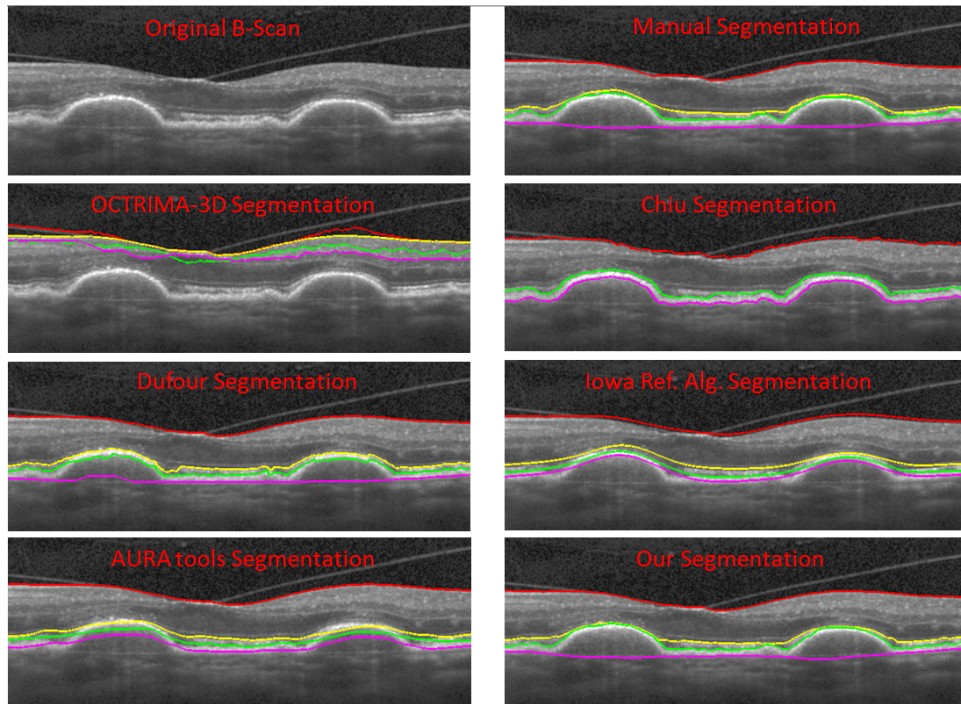
Figure 3.12: The segmentation outputs by manual, OCTRIMA-3D, Chiu et al., Dufour et al., Iowa Reference Algorithm, AURA Tools and our proposed method. The ILM-RNFL, MZ-EZ, IZ-RPE and RBC boundaries are delineated using red, yellow, green and magenta lines respectively.

to these challenges and increase the accuracy of detecting the boundaries. There are few methods that narrow the search space using already-detected boundaries and the estimated position of the RNFL and RPE [63]. The novelty of our robust method for detecting approximate positions lies in using three reference layers to narrow the region of interest. These three reference layers (TRL) are RNFL Layer, RPE Layer and ONL Layer. We have narrowed the region of interest so that our target boundary should be the highest contrast boundary in that region. We have also targeted the first high contrast boundaries such as ILM-RNFL. The detection of such boundaries first makes the method very accurate as it reduces the region of interest for low contrast boundaries which are generally difficult to locate. These narrowing operations increase accuracy as well as efficiency. Moreover, the detection approach using approximate positions of TRLs is another novelty. Currently, available methods have used only maximum intensity or clustering to find approx-

imate positions of layers for selecting the region of interest: this is prone to error due to the presence of noise and pathologies [52, 63]. We have used high smoothing using Gaussian filter on the image and both intensity and relative distance for detecting approximate position of TRL. Applying high smoothing increases accuracy to detect the approximate positions of these reference layers because it removes the presence of noise and the effect of pathologies. In addition, application of both the intensity and the position improves the accuracy of the determination of the three reference layers. Intensity-based detection alone is highly prone to error so the combination of intensity and relative position employed in our approximate TRL detection method helps to reduce false positions due to noise or pathologies.

- Computation of Edge Weight: The second novelty is computing robust edge weights where image information is obtained. This information includes intensity gradient, spatial distance between nodes, slope similarity to a reference line and association to the properties of layers (for example, the nearest two edge pixels in a vertical direction from the approximate RPE layer are more likely to be an MZ-EZ boundary). Some methods based on graph shortest path for detecting the boundaries have considered only the intensity gradient and spatial distance in edge weight computation [63, 77]. Our novel method of computing edge weight allows the shortest path algorithm to choose the nodes in its shortest path to be the part of the boundary. This means it can handle boundaries that are both straight and continuous or have parts that are non-straight such as macula, optic disc, and areas that have pathologies. The weighted Euclidean distance used in the edge weight influences the tracing direction such as a straight line or curved boundary. The slope similarity to a reference line helps to follow the curvature of the boundary when it is affected by pathologies such as drusen and OCT-defined atrophy. The layers non-associativity feature helps to trace the actual boundary of thin layers and prevents it from mixing with other boundaries.

- Selection of the graph nodes: The third novelty is selecting nodes for the graph of detecting the boundaries of the retinal layers. In available graph methods, nodes are formed either using all pixels or edge pixels in the region of interest for a bound-

ary. In our proposed method, we group the candidate pixels into pixel-groups and end pixels of the pixel-groups form the graph nodes. This process reduces the number of nodes and thus increases the efficiency of the algorithm and accuracy of the detection.

3.9   Conclusion

In the context of clinical practice and research in ophthalmology, we need to extract thin, elongated structures of retinal layers that can be visualised in SD-OCT images [115]. For AMD patients, it is common to see drusen and OCT defined atrophy in these images, and their presence increases the difficulties and challenges for correct identification of layer boundaries. In this chapter, we have presented a robust method for identifying four boundaries, ILM-RNFL, MZ-EZ, IZ-RPE and RBC, in the presence of pathology such as drusen and OCT defined atrophy. The approximate locations of three reference layers (RNFL, ONL and RPE) are used to define the region of interest for finding the boundaries. A weighted graph representation is used for precisely identifying the boundaries, with the weights including important features such as slope similarity to reference boundaries, and associativity to the region of interest. The intensity gradient of nodes, morphological properties of layers and spatial properties of the pathology are also incorporated into the edge weight computation. The edge weight computation proposed in our method has demonstrated robustness of the method in identifying the boundaries accurately even in the presence of pathology.

We evaluated our method on three different datasets from different sources. The results show a clear improvement in the identification of boundaries by our proposed method over the other five state-of-the-art methods. Our proposed boundary identification method can help finding the morphological changes such as the layer's thickness and also the layer intensity which will derive the presence, location and size of the pathology. Using this information, ophthalmologist can perform large-scale study for finding layer structures efficiently and accurately. This will eventually help the clinical studies with finding new and reliable biomarkers of severity and risk of progression for early

detection of the retinal diseases.

Chapter 4

2D Segmentation (2DS) Algorithm for the Detection of the Choroid-Sclera Interface

This chapter presents a novel 2D segmentation method for segmenting the choroid outer boundary i.e. Choroid-Sclera Interface from Enhanced Depth Imaging Optical Coherence Tomography (EDI-OCT) images. This chapter is based on the following publications:

Md Akter Hussain, Alauddin Bhuiyan, Hiroshi Ishikawa, R Theodore Smith, Joel S. Schuman and Ramamohanarao Kotagiri. *"An Automated Method for Choroidal Thickness Measurement from Enhanced Depth Imaging Optical Coherence Tomography Images"*, *Computerized Medical Imaging and Graphics. (Under review)*

Kokroo, Aushim, Alauddin Bhuiyan, Md Akter Hussain, Ramamohanarao Kotagiri, Meleha Ahmad and Theodore Smith. *"Validation of an Automated Software for Choroidal Thickness (CTh) Measurement." Investigative Ophthalmology and Visual Science 57, no. 12 (2016): 5954-5954.*

Md Akter Hussain, Alauddin Bhuiyan and Ramamohanarao Kotagiri. *"Automatic Detection of Choroid-Sclera Interface in EDI-OCT Images." 4th Annual Doctoral Colloquium, The University of Melbourne. 2016.*

4.1   Introduction

The choroid is a vascular plexus located between the retina and the sclera (Fig. 4.1). It provides oxygen and metabolic support to the Retinal Pigment Epithelium (RPE),

outer retina, and optic nerve and absorbs the excess light penetrating the retina [40, 167]. Anatomically, the choroid can be divided into two major components: choroidal vessels and stroma [168]. The choroidal vessels are further subdivided into five layers of increasing size: Bruch's membrane, Choriocapillaris, Sattler's layer, Haller's layers and Suprachoroidea (Sch) [40]. The Choriocapillaris (Cc) is adjacent to Bruch's membrane and is comprised of small fenestrated capillaries, whereas the outer Sattler's and Haller's layers feed the Cc network. The suprachoroid (Sch) is a transitional zone between choroid and sclera. The boundary between the choroid and the sclera is known as Choroid-Sclera Interface (CSI). The choroidal stroma is comprised of melanocytes, fibroblasts, immune cells, neurons, and ground substance that contribute to its thickness [40].

The qualitative and quantitative evaluation of the choroid is important in the study of glaucoma [169], Age-related Macular Degeneration (AMD) [170], choroidal melanoma [171], central serous chorioretinopathy [172], and many other retinal and systemic diseases [80, 173]. Quigley et al. [174] proposed that a mere $50\mu m$ choroidal expansion can increase the intraocular pressure to harmful levels in angle closure glaucoma patients. Some choroidal thinning occurs during normal aging, although, in some cases, a pathologic condition referred to as age-related choroidal atrophy can occur [31]. There has also been an increasing interest in investigating the correlation of choroidal thickness (CTh) with the age, gender, axial length and intra-ocular pressure in healthy human eyes [175–177]. However, lack of automation in this area makes large-scale studies challenging due to the time-consuming nature of manual measurement as well as significant inter- and intra-grader variability. A robust, reliable and cost-effective automatic method is essential for computing CTh in large population-based studies to better understand the implications of CTh in the retinal health. Here, we propose to develop an automatic method for segmenting the CSI and computing CTh from Enhanced Depth Imaging OCT (EDI-OCT) and Swept Source OCT (SS-OCT) images.

Figure 4.1 depicts four prominent retinal layers, the choroid and sclera. The choroidal vessels (CV) appear as the black regions surrounded by white pixels in choroidal region of the EDI-OCT image. The Bruch's membrane (BM) is a semi-permeable membrane located between the Cc and the RPE. The BM and Cc are typically not distinguishable
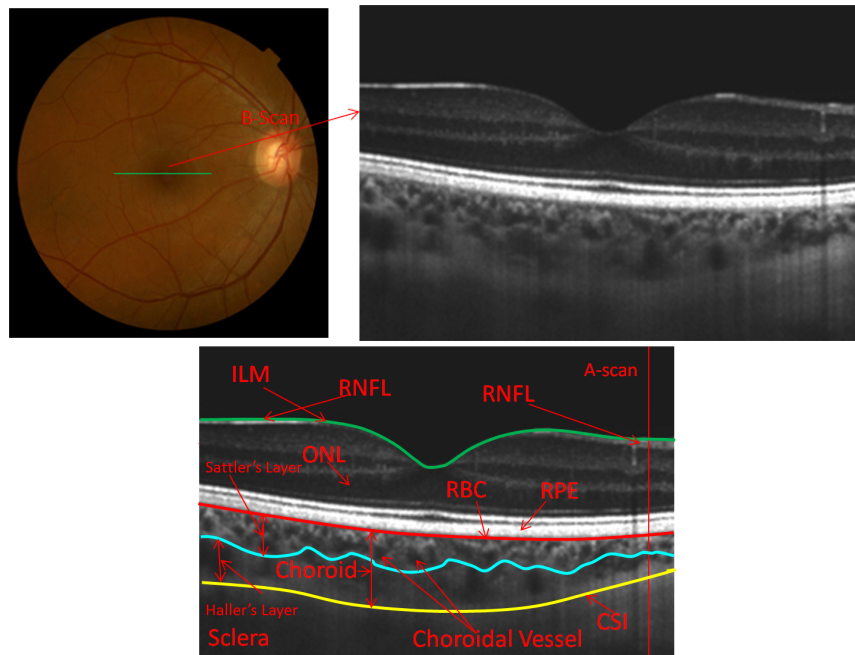
Retinal Layers: **ILM**: Internal Limiting Membrane; **RNFL**: Retinal Nerve Fiber Layer; **ONL**: Outer Nuclear Layer; **RPE**: Retinal pigment epithelium.
RBC: The outer border of the RPE/ Bruch's membrane (BM)/ Choriocapillaris Complex;**CSI**: Choroid Sclera Interface

Figure 4.1: Colour Fundus Photography image (left) and EDI-OCT image (middle) in a healthy eye. B-scan mode is demonstrated by the cross sectional image corresponding to the green line (left); A-scan mode is represented by red vertical line (right).

from the outer RPE except in pathologic state. Because of this, the term outer RPE-BM-Choriocapillaris complex (RBC) is typically used to demarcate the separation of the retina and choroid [145].

A number of studies have been reported semi-automatic and automatic methods of choroidal segmentation in OCT images [65, 80, 85, 145]. These methods utilise machine learning, graph shortest path, min-cut-max-flow, eigenvector analysis, tensor matrix and Gaussian mixture model for finding the CSI and/or CV borders from different types of OCT images such as polarization-sensitive OCT (PS-OCT), spectral domain OCT (SD-OCT) and EDI-OCT [65, 80, 83, 85, 145]. We have summarised these methods in Chapter 2 (Section 2.7.4). However, these methods have limitations for the unpredictable size of the choroid [80]. The lack of robustness and accuracy of the automatic choroid detection (choroid is defined by the RBC and CSI boundaries) and the need of automatic algorithm for monitoring and diagnosis of choroidal diseases motivated us to develop a robust,
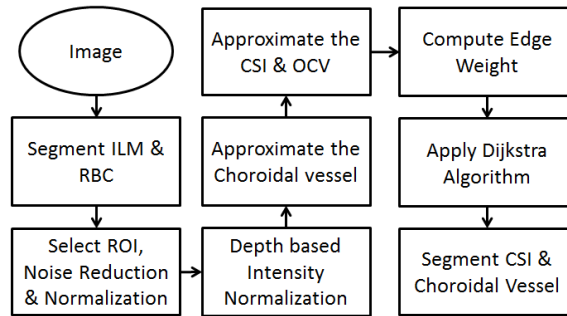
Figure 4.2: Flow diagram of the proposed method

reliable and more accurate automatic system for the measurement of CTh.

The rest of the chapter is organised as follows. The details of the proposed method is described in Section 4.2. Section 4.3, 4.4 and 4.5 comprises the validation methods, experimental setup and performance evaluation respectively. The novelty of our proposed algorithm is discussed in section 4.6. Finally, Section 4.7 concludes the chapter.

4.2   Proposed method

Figure 4.2 shows the flow diagram for our proposed method and Algorithm 2 provides the pseudo code. Since the choroid is located under RBC boundary and the maximum thickness of the choroid is approximately $350\mu m$ in healthy individuals [177], the Region Of Interest (ROI) for the choroid is defined $400\mu m$ underneath the RBC boundary. ILM segmentation is required for the segmentation of the RBC boundaries details in Chapter 3. The method of segmenting ILM and RBC boundaries is discussed in the same chapter. Depth-based Intensity Normalisation (DIN) methods are developed to achieve a continuous and stable pattern of intensity for CSI. Choroidal Vessels (CV) are located approximately using Otsu's clustering method [178]. An anatomical knowledge-based probability map from the DIN image is generated to find the approximate CSI. Following that, the approximate Outer Choroidal Vessels (OCV) boundary is detected using the approximate CV, approximate CSI and convex hull. The method of finding the RBC is explained in previous Chapter 3. The remaining steps for choroid detection and thickness measurement are described in the following subsections.

Algorithm 2 2DS Algorithm for the CSI

Input: B-scan Image.
Output: CSI boundary position.
  1: Detect ILM-RNFL and RBC boundaries using Algorithm 1.
  2: Select ROI using RBC boundary.
  3: Apply noise reduction filter.
  4: Apply Depth-based intensity normalisation (DIN) methods.
  5: Find approximate positions of the choroidal vessels.
  6: Find approximate positions of the CSI and outer choroidal vessels boundaries.
  7: Compute edge weights of the graph.
  8: Find the shortest path using Dijkstra's algorithm.
  9: Apply Gaussian filter for reducing zigzag from the shortest path and defined as CSI.

4.2.1 CSI boundary detection

The CSI boundary is determined by finding the ROI, followed by noise reduction and intensity normalisation To get a similar intensity for the surface of the choroid and sclera, depth-based intensity normalisation (DIN) is used. Choroidal vessel, the OCV and CSI are detected approximately to allow for more accurate detection of the CSI. Each pixel from the graph nodes and edge weight is computed using the normalised intensity and the approximate CSI and OCV boundary. Finally, shortest path defined the CSI boundary. The details of CSI detection are described below.

4.2.1.1 The ROI, Noise reduction & Normalisation:

Since the maximum thickness of the choroid is approximately $350 \mu m$ [177], the ROI is defined a slightly to be more, $400 \mu m$ from the RBC boundary. The red to yellow line in Fig. 4.1 is selected as ROI and Fig. 4.3 (a) shows the crop of the ROI.

The choroidal region contains many small vessels, creating edges that increase the difficulty of CSI detection. Noise can create additional false edges. The filters which are used to de-noise the image during the detection of the ILM-RNFL and RBC boundaries cannot resolve this type of noise. For this purpose, more smoothing operations are applied to reduce false edges, thus improving the accuracy of the identification of the CSI. Gaussian and Median filters are applied on the ROI in two steps. Before applying these filters, the intensities that are higher than a threshold due to imaging technology
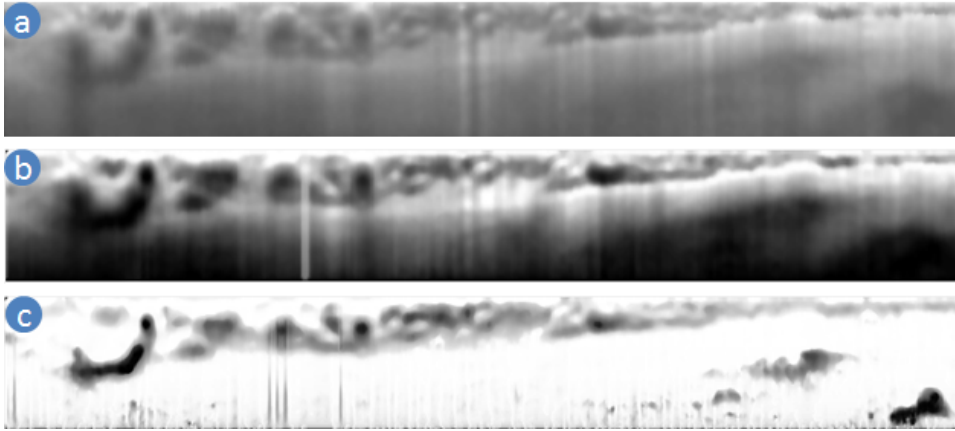
Figure 4.3: (a) The region of interest of the choroid, (b) The smooth image after intensity normalisation and (c) Depth- based intensity normalised (DIN) image

are replaced by that threshold using (4.1).

$$I(i,j) = \begin{cases} I(i,j) & \text{, if } I(i,j) < th_i \\ th_i & \text{, if } I(i,j) \geq th_i \end{cases} \tag{4.1}$$

Where th_i is the threshold value and $th_i = \mu(I_i) + 2 \times \alpha(I_i)$. $\mu(I_i)$ and $\alpha(I_i)$ are the mean intensity and standard deviation of the image I at i^{th} A-scan. Following this step, a median filter of 5×5 window is applied. The intensity of the image is normalised to values in the range 0 to 1 for each A-scan. Gaussian filter with the window size of 5×5 and standard deviation of 1 is then applied to further smoothen the image (Fig. 4.3 (b)).

4.2.1.2   Depth based Intensity Normalisation (DIN)

The intensities of the choroidal vessel and non-vessel pixels (referred to here as surface pixels) are not evenly distributed, and the intensity of the sclera region is similar to the choroidal vessel intensity (as shown in Fig. 4.3). The even distribution of the surface pixels of the choroid and sclera improved the identification of the CSI significantly. To allow for such normalisation, we propose a method that adapts the properties of the OCT image capturing technology to the anatomy of choroid and sclera. OCT imaging technology shows low intensity for the vessel and high intensity for the surface tissues. The intensity values also become lower as the depth increases. The goal of our proposed

depth based normalisation method is to make the intensity of the surface pixels of the choroid and sclera stable and to make the intensity of the choroidal vessels pixels lower than the surface pixels. Since the pixel intensity decreases with the increasing of depth, we use the depth information to normalise the image for the CSI detection. This simple and efficient method represents a significant novel step in our proposed method. This DIN method is shown by (4.2).

$$N(i,j) = \left(\sum_k \sum_l I(i,j) > I(k,l) \right) / n \qquad (4.2)$$

Where $I(i,j)$ is the intensity value of the pixel located at i^{th} row and j^{th} column. $i \leq k \leq$ # of row and $j - 1 \leq l \leq j + 1.n = |k| \times |l|$. $N(i,j)$ is the computed depth normalised intensity value.

The new intensity value of a pixel is the total number of lower intensity pixels located under that pixel. The value is divided by the number of pixels located under that pixel. This process uses multiple neighbour A-scans instead of single A-scan for the robustness of the method over noise which is formulated in (4.2) with k=2. This operation converts the surface pixels to a similar intensity. Figure 4.3 (c) shows an example of the output of the DIN process.

4.2.1.3 Choroidal Vessel (CV) approximation

The Depth based Intensity Normalisation (DIN) technique helps to differentiate the surface and vessel pixels, where the higher intensities are the surface and the lower intensities are the vessels. The vessel and surface pixels vary widely in the DIN image. We note that, we want an approximate result instead of an exact detection in this phase. Therefore, we consider the first six out of seven clusters using the Otsu method for initial approximation of CV as shown in Fig. 4.4 (a). To reduce false vessel pixels, two morphological operations (opening and closing) are applied to the initial approximation. The morphological opening operation removed noise based on the size of the blob as shown in Fig. 4.4 (b). The closing operation recovered deleted pixels from the border of the vessels for the opening operation as shown in Fig. 4.4 (c). These operations are applied by a disk as
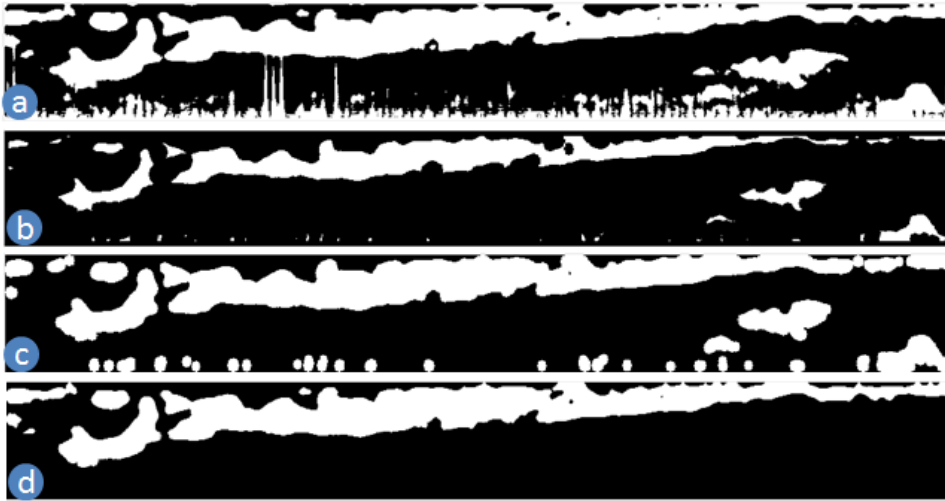
Figure 4.4: Vessel pixels after: (a) clustering; (b) morphological operation; (c) morphological closed operation; and (d) applying dynamic distance filter.

a blob with a radius of 5.

The initial approximation of the CV could, at times, have the sclera region as shown in Fig. 4.4 (c), represented by the white pixels in the lower part of the image. A dynamic distance filter is applied to the initial approximation for removing the sclera region as much as possible and output is shown in Fig. 4.4 (d). This dynamic distance filter selects pixels as vessels based on the distance of the already classified vessel pixels along A-scan. At first, the top $200\mu m$ initial approximated pixels are classified as approximated vessel pixels. If the distance between the classified pixels and next initial approximated pixels is less than a threshold value, then that next pixels are also classified as approximated vessel pixels and computation is continued iteratively until no pixels are found as approximated vessel pixels. That threshold value is defined dynamically based on the position of the current pixels. For example, suppose that the black pixels in Fig. 4.5 (a) are the initial approximated vessel pixels. There are two A-scans and each A-scan has two pixels. The red colour pixels in Fig. 4.5 (b) are classified as approximated pixels as they are located in the top $200\mu m$. The distances between two pixels in the A-scan are d_1 and d_2 where d_1 is less than the threshold value and d_2 is greater than the threshold value. Then the pixel located at d_1 is included in the approximated vessel but that at d_2 is not, as shown in Fig. 4.5 (c). The threshold is defined dynamically based on the position of the pixels that is
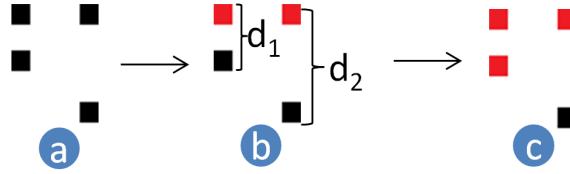
Figure 4.5: (a) Shows black colour pixels found after clustering, red pixels in (b) and (c) are selected as vessel after applying distance filter.

$th^d_{i,j} = \frac{100}{e^{i/400}}\mu m$ where $th^d_{i,j}$ is the distance threshold for the pixel at i^{th} row and j^{th} A-scan or column.

4.2.1.4 Approximate detection of CSI and OCV

The approximations of the CSI and OCV are used to manipulate the edge weight of the graph for selecting pixels as shortest path that is more likely to be the CSI. The approximated CSI line is identified based on prior information from localising the CSI and surface pixels. The cluster having the highest intensity by the Otsu method at the approximation of the choroidal vessel location is classified as surface pixels, shown in Fig. 4.6 (a). The approximated CSI is used to search $100\mu m$ (i.e., ≈ 25 pixels) away from the RBC. This explains why the pixels located in the top $100\mu m$ are removed from the surface pixels as shown in Fig. 4.6 (b). A probability matrix is computed based on the position of the pixels. The hypothesis behind computing the probability matrix is that the approximated CSI is more likely to be located near the maximum CTh ($350\mu m$ away from the RBC boundary). The probability value of a pixel decreases with the increasing distance from the position of the maximum CTh. This is formulated in (4.3) and shown in Fig. 4.6 (c) in the means of intensity (high intensity means high probability and low intensity means low probability).

$$P(i,j) = exp^{\frac{-|i-b|}{d}} \tag{4.3}$$

Where P(i,j) is the probability value of a pixel located at the ith row and j^{th} column, b is the hypothesised position of the CSI boundary which is $350\mu m$ and d is the normalised value which is set to $200\mu m$ empirically.
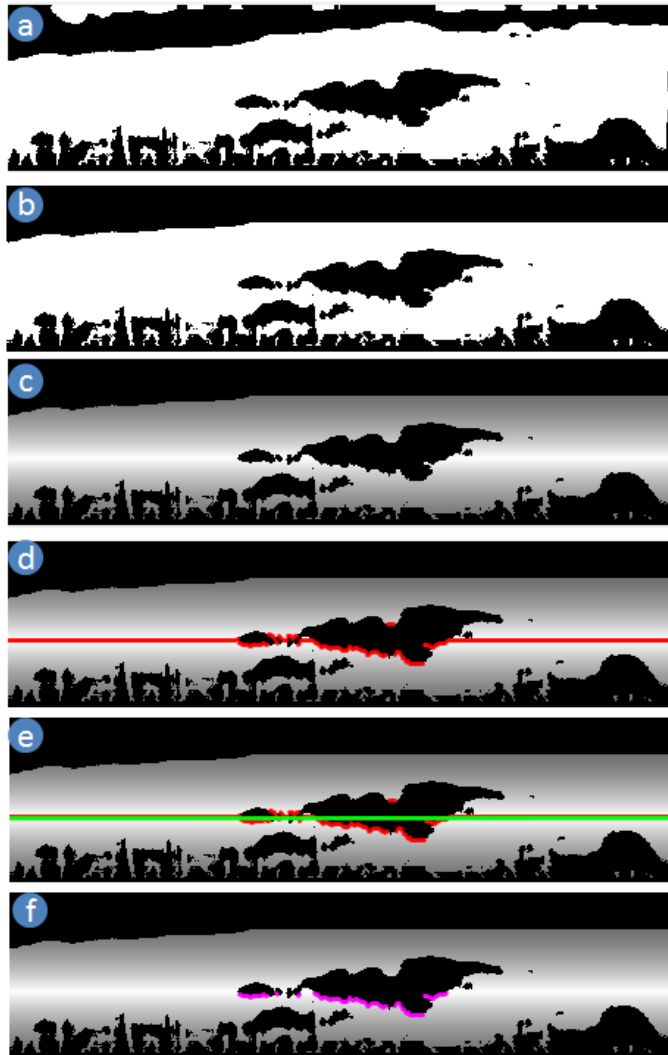
Figure 4.6: (a) Surface pixels, (b) following removal of top 100 μm surface pixels, (c) probability map for the surface pixels, (d) candidate pixels (pixels (red) with maximum probability in each A-scan), (e) first order polynomial line on the candidate pixels (green) (f) following removal of candidate pixels (magenta).

After computing the probability matrix, the next step is to find the approximated CSI line. The pixels having maximum probability value in each A-scan are selected as candidate pixels (red pixels in Fig. 4.6 (d) for CSI). A first order polynomial line is fitted (green line in Fig. 4.6 (e)) along these candidate pixels. Then the candidate pixels located under that fitted line by more than a threshold along A-scan are removed and their probability values are changed to zero so that they are not selected for the next iteration (magenta colour pixels in Fig. 4.6 (f)). The threshold value is defined by the standard deviation
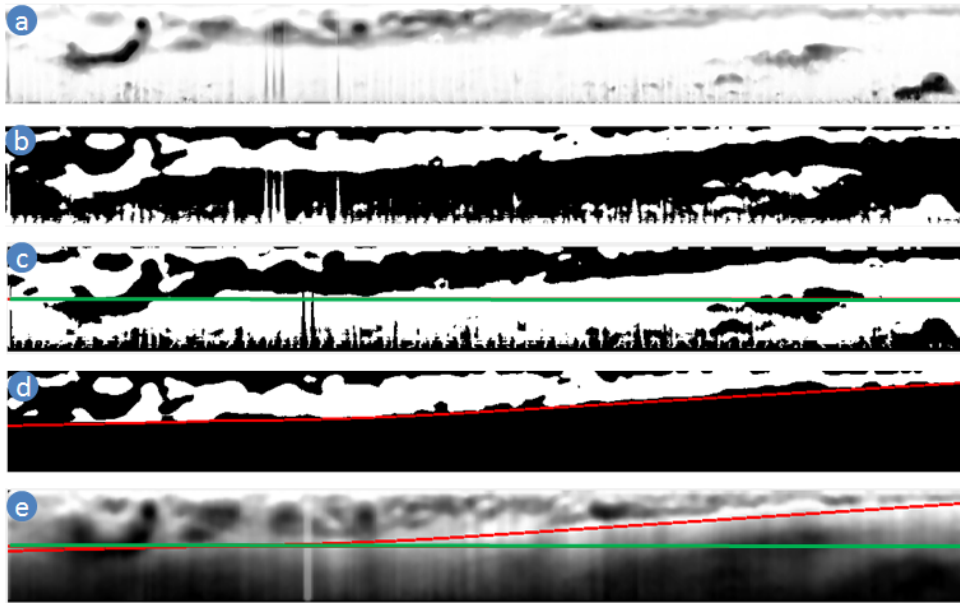
Figure 4.7: (a) The DIN image, (b) approximate vessel, (c) approximate CSI (green line) on the surface image (white colour), (d) approximate OCV boundary (red line), (e) approximated CSI (green line) and OCV boundary (red line) on the intensity normalised image.

of the distance between fitted line and candidate pixels under that fitted line. This procedure is applied iteratively until no pixels are found to remove. When the product of threshold value and the number of pixels removed is at a minimum, the first order polynomial fitted line on the candidate pixels at that iteration became the approximated CSI. Figure 4.7 shows an example of (a) the depth normalised image, (b) approximated vessel, (c) approximated CSI (green line) in the surface image (white colour).

After finding the approximated CSI line, approximated vessel pixels located under that approximated CSI line are removed to find a convex hull for the remaining pixels. The outer boundary of the convex hull is smoothed using average filter with window size of one fifth of the image width. This smooth line is defined as the OCV boundary. Figure 4.7 (d) shows an example of the approximated OCV boundary (red line) and vessels (white colour pixels). Figure 4.7 (e) shows the example of the approximated CSI (green line) and OCV boundary (red line) on the normalised image. The proposed method boosts the priority of those pixels located in between the approximated CSI and OCV for becoming the actual CSI by incorporating the edge weight computation.

4.2.1.5   Edge Weight Computation

The CSI detection problem is modelled as a graph shortest path problem where each pixel is the graph node. The nodes are connected with 8 neighbours The vertex weight is computed using (4.5) with the intensity of the smooth image and intensity and gradient of the DIN image. The approximated CSI and outer vessel boundary also incorporated with the weight computation as a distance factor. The weight of the nodes is decreased with increasing distance from the any of the boundaries. The distance factor of the approximate CSI and approximate choroidal vessel outer boundary from the pixels are computed using (4.4).

$$df_{i,j}^{r} = \alpha \times exp\left(-\frac{(r_j - i)^\beta}{\delta}\right) \tag{4.4}$$

Where $df_{i,j}^{r}$ is the distance factor of a node at the ith row and j^{th} column for the reference line (r). r_j gives the position of the row for the $j_t h$ column of r. α, β and δ are three coefficients to manipulate the equation as follows. The approximated CSI and outer boundary of choroidal vessel are used as r in (4.4). The coefficient values in (4.4) for approximated CSI (df^{CSI}) are $\alpha = 0.25, \beta = 1$ and $\delta = 100$. The coefficient value in (4.4) for approximated outer boundary of choroidal vessel (df^{OCV}) are assigned empirically and they are $\alpha = 0.5, \beta = 1$ and $\delta = 100$.

The DIN image is normalised in the range 0 to 1 for each A-scan. The vertex weight for the node is computed using the normalised intensity of the DIN image, gradient of that normalised value, distance factor for the approximated CSI and outer choroidal vessel boundary. This computation of the vertex weight is formulated by (4.5).

$$V \quad = \quad exp\left(-\left((N_{DIN} + G_{DIN}) \times (df^{CSI} + df^{OCV}) + 1\right) \times (I_s \times df^{pcsi})\right) \tag{4.5}$$

Where N_{DIN} and G_{DIN} are the depth normalised intensity and its vertical gradient value respectively, df^{CSI} and df^{OCV} are the distance factor of the approximated CSI and OCV respectively. I_s is the normalised image 0 to 1 of the after applying Gaussian and

median filter image and df^{pcsi} is the distance factor for normalise intensity of the image for increasing intensity near CSI boundary and decreasing the intensity of the pixel located away from CSI. This helps the method to detect higher intensity pixels as CSI and at the same time, avoiding pixels near the RBC that are generally higher in intensity. df^{pcsi} is computed using (4.4) where r is defined by the $(3 \times aprxOCV + aprxCSI)/4, \alpha = 0.25, \beta = 2$ and $\delta = 1000$. $aprxOCV$ is the approximated OCV and $aprxCSI$ is the approximated CSI.

The first and last column pixels are set to a predefined minimum cost so that the shortest path algorithm could choose the first and last vertical position freely or independently as the starting and ending of the boundary. This predefined minimum value is set to 0.001. The edge weight of the graph is computed by (4.6). Then the shortest path algorithm is applied where the start node is left top pixels, and the destination node is the bottom right node.

$$W_{u,v} = V_v \tag{4.6}$$

Where $W_{u,v}$ is the edge weight between node u and v; V_v is the vertex weight of node v that is computed by (4.6); u and v must be 8-connected neighbour.

The computed shortest path is formed to be the CSI. An average low-pass smoothing filter window size of one fifth of the width of b-scan image is applied on this shortest path for a smooth line instead of any zigzag line. This smooth line defined the CSI. Figure 4.8 shows (a) original image as a reference, (b) segmented output of the ILM-RNFL (green line), RBC (red line) and CSI (yellow line) by our proposed method.

4.2.2 Choroidal Vessel (CV) detection

After detecting the CSI, it can still be challenging to find the CV boundaries due to unstable shape and intensity distribution. Our proposed DIN method increases the accuracy of CV detection and increases efficiency. We have used the active contour method for detecting the CV boundaries where seed point is generated by applying clustering on the DIN image. The ROI for the CV boundary detection is the choroidal region that is from
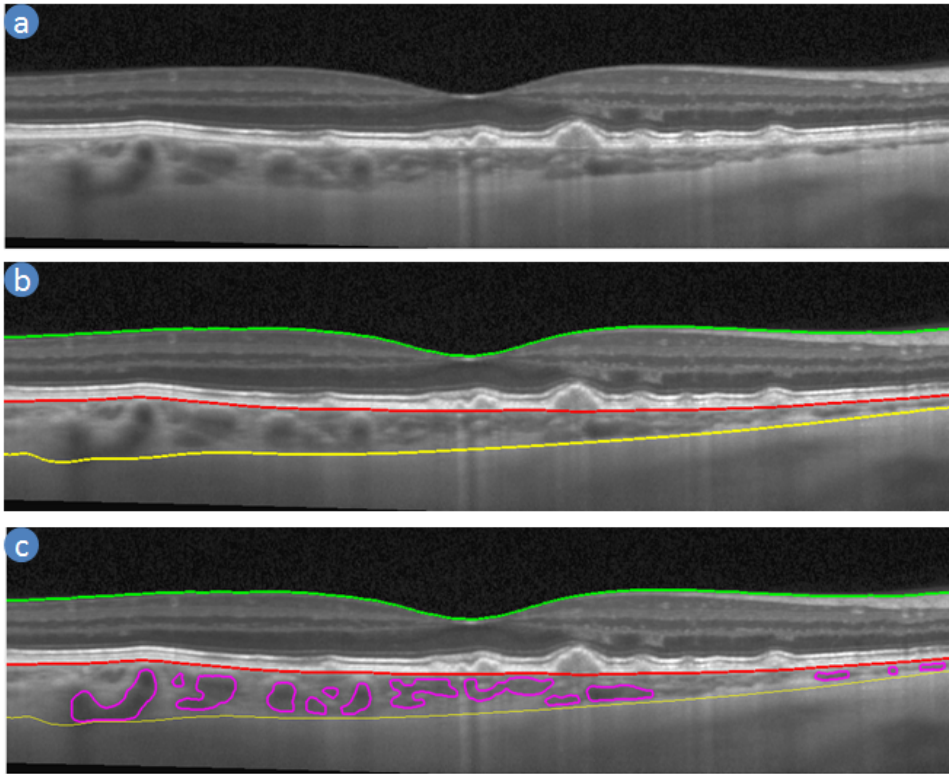
Figure 4.8: (a) Original image (b) segmented output of ILM-RNFL (green line), RBC (red line) and CSI (yellow line) (c) segmented output of choroidal vessels (magenta lines).

the RBC boundary to CSI. First, ROI in the DIN image is clustered into two regions by Otsu method. The cluster with the lowest intensity defined the initial CV that serves as the seed points of the active contour. Following that, due to uneven intensity distribution of the image, we divide the ROI into five parts along the width of the image. For each part, edge-based active contour is used to finalise the vessel area. The active contour is used from Matlab library function where it is iterated 300 times. Smooth factor and contraction bias are defined empirically by 0.1 and 0.01 respectively. Figure 4.8 (c) shows a segmented output of the CV boundaries.

4.3   Validation method

Validation is an important step for any automated methods because to assess the accuracy and usability of the method. We compared our method against the manually seg-

mented images (ground truth) and two state-of-the-art methods [80, 85]. Our assessment involves 1) Direct evaluation of the precision of the boundary locations by computing: the Root Mean Square Error (RMSE) between two different segmentations; 2) Dice Coefficient (DC) between two different segmentations for direct evaluation of the precision of the overlap of the choroidal border; 3) RMSE between two different segmentations for direct evaluation of the precision of the CTh measurement; 4) Pearson correlation coefficient and Interclass Correlation Coefficient (ICC) for the choroid thickness between two different segmentation methods. The performances of two automatic methods are reported using these four assessment methods to justify the accuracy and robustness of the method. The importance and computation process of the four evaluation protocols are described below.

4.3.1   Root Mean Square Error (RMSE):

RMSE is the average pixel distance of a single boundary between two different segmentations. It is well known and the most often reported way to compare segmentation of objects or boundaries by different methods. A lower RMSE error means better accuracy or performance for the method. The formula of computing the RMSE is (4.7).

$$RMSE(B^{i,j_1}, B^{i,j_2}) = \sqrt{\frac{\sum_x (B^{i,j_1}(x) - B^{i,j_2}(x))^2}{\|A\text{-}scan\|}} \qquad (4.7)$$

where B^{i,j_1} is the ith boundary by the j method, $B^{i,j_1}(x)$ is the y-axis position of the ith boundary at x^{th} A-scan by the method j, $\|A\text{-}scan\|$ is the total number of A-scans, and x is taken over all A-scans.

4.3.2   Dice Coefficient (DC):

This is a region-oriented analysis which provides more information about classification or identification errors. This allows us to assess whether the automatically-delineated layer is more prone to under-segmentation or over-segmentation in comparison to manual segmentation. The DC is sensitive to variations in shape, size and position. The

formula for DC is shown in (4.8) where i refers to a region, j_1 and j_2 refer to two methods of segmentation that they detect i^{th} region.

$$DC(Reg^{(i,j_1)}, Reg^{(i,j_2)}) = \frac{2|Reg^{(i,j_1)} \cap Reg^{(i,j_2)}|}{|Reg^{(i,j_1)}| + |Reg^{(i,j_2)}|} \qquad (4.8)$$

4.3.3   Interclass Correlation Coefficient (ICC):

ICC, also known as reliability coefficient, is an excellent parameter to evaluate an automatic method. A high-reliability coefficient of an automatic method represents high accuracy. Shrout et al. [179] proposed a method to compute reliability coefficient called ICC. Researchers have proposed six cases and our evaluation criteria are best satisfied by the third case, in which n targets are graded by k methods without any averaging. In this case, they proposed the ICC as follows.

$$ICC = \frac{BMS - EMS}{BMS + (k - 1) \times EMS} \qquad (4.9)$$

Where BMS is a between-targets mean square; EMS is a residual sum of squares. Let d is the data of $k \times n$ that is the ratings of n targets by k graders are stored in d. Then, BMS and EMS are computed by the following equations.

$$BMS = \frac{k \times \sum_i (\bar{d}_i - \bar{d})^2}{n - 1} \qquad (4.10)$$

$$EMS = \frac{\sum_j \sum_i (d_{i,j} - \bar{d}_i)^2 - n \times \sum_j (\bar{d}_j - \bar{d})^2}{(k - 1) \times (n - 1)} \qquad (4.11)$$

Where $\bar{d}$ is the mean of the ratings of all graders, $\bar{d}_i$ is the mean of the ratings of the ith target by all graders, $\bar{d}_j$ is the mean of the ratings of all targets by the jth grader and $d_{i,j}$ is the rating of the ith target by the jth grader.

4.4 Experimental setup

Our experimental setup consisted with 10 macular EDI-OCT volumes which are taken from 7 patients (each volume has 19 B-scan, Total 190 B-scans). All patients are imaged using EDI-OCT imaging on Heidelberg Spectralis HRA+OCT. Data is taken from patients without a history of retinal diseases seen at a large city hospital (average age 53 years, range 43-62). Each volume has $1021 \times 361 \times 19$ voxels with $3.9\mu m$ axial resolution and dB (image quality parameter) ranges are 20 to 39. Two expert graders from our institution manually traced the RBC and CSI boundaries using Photoshop CS3. In addition, images are run through CTh measurement software developed by Tian et al. [85] and Chen et al. [80] to allow for comparison of their methods to ours. Each of the three automatic methods is compared to the results of the two manual graders and their average. We used several methods to compare the performance of the three systems, including RMSE to compute error for the RBC, CSI and CTh, DC for the choroidal region, and correlation coefficient and interclass correlation coefficient for the CTh. We have also shown the DC for each volume for different signal strength in dB (see Fig. 4.9). We have also collected two random SS-OCT B-scans from [180] to show the robustness of our proposed method in diseased eye and different source of OCT imaging.

4.5 Results

Our results show better accuracy compare to the state-of-the-art automatic methods [80, 85]. RMSE for the two boundaries RBC and CSI are reported in Table 4.1. For the RBC boundary, our proposed method shows less error than other two state-of-the-art methods and inter-grader variability. The RMSE for the CSI shows that our proposed method is superior to the other automatic methods. Though our proposed method has a higher error than inter-grader variability, this difference is very small, as reported in Table 4.1. Our method has a DC of more than 92% where other two automatic methods have less than 65% and 70%. The RMSE, correlation coefficient (r) and ICC for the CTh also show our proposed method is superior to the methods of Tian et al. and Chen et al. The correlation coefficient (r) is more than 0.70 for our method but less than 0.51 for Tian et
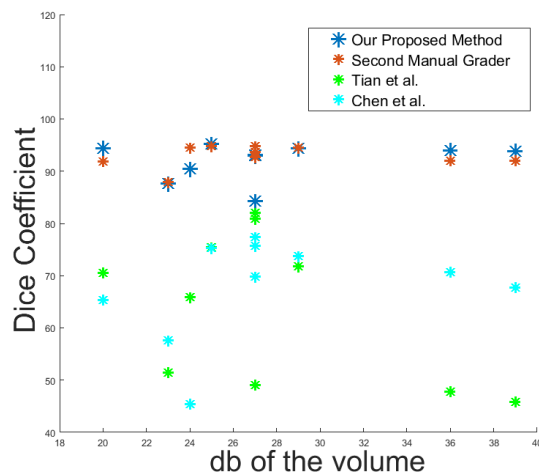
Figure 4.9: Dice Coefficient against dB of the volume between first manual grader and automatic methods.

al. and less than 0.70 for Chen et al. The interclass correlation coefficient is 0.65 for our proposed method, and less than 0.45 and 0.60 for Tian et al. and Chen et al. respectively.

In Fig. 4.9, we have shown DC of each volume where x-axis represent dB value of the volume and y-axis represents the DC of the image. The DC from second manual grader, Tian et al., Chen et al. and our proposed method are shown in the Fig. 4.9 where the grading of first manual grader is used as gold standard. This figure shows the DC of our proposed method is very near to inter grade compared to other automatic methods. It is also clear that our method performs consistently in different signal strength.

Two B-scans from SS-OCT have been used to evaluate the performance of our proposed method in different OCT type and pathology existed eyes as shown in Fig. 4.10. In Fig. 4.10, a) contains haemorrhage pathology from an AMD patient and b) is from neo-vascularisation patient [180]. Green, red and yellow line represent the ILM-RNFL, RBC and CSI respectively.

4.6 Novelty of the proposed segmentation algorithm for detecting the Choroid-Sclera Interface

Our proposed segmentation method for the detection of the CSI has the following novel features that help in finding CSI very accurately.

Table 4.1: The performance of the boundary of RBC and CSI, Choroid and CTh of the Tian et al., Chen et al. and our proposed methods. (units in pixel) .

Evaluation Method	M. Segmentation by Grader1 Vs				M. Segmentation by Grader2 Vs				Average M. Segmentation Vs		
	Grader2	Tian et al.	Chen et al.	Proposed	Grader1	Tian et al.	Chen et al.	Proposed	Tian et al.	Chen et al.	Proposed
RMSE for RBC	2.60 (1.34)	3.75 (1.79)	2.34 (1.33)	1.91 (1.24)	2.60 (1.34)	3.75 (1.50)	2.83 (1.00)	2.25 (0.89)	3.51 (1.58)	2.43 (0.87)	1.87 (0.75)
RMSE for CSI	7.08 (3.09)	35.45 (12.08)	45.79 (20.13)	8.64 (5.81)	7.08 (3.09)	37.05 (12.36)	43.22 (18.96)	8.68 (6.57)	36.17 (11.97)	44.19 (19.51)	7.71 (6.29)
DC for Choroid	92.87%	63.98%	67.87%	92.03%	92.87%	63.10%	69.59%	92.04%	63.62%	68.97%	92.91%
RMSE for CTh	6.90 (2.92)	34.81 (11.56)	46.03 (20.35)	8.79 (5.57)	6.90 (2.92)	35.99 (11.86)	43.96 (19.41)	8.98 (6.21)	35.27 (11.53)	44.85 (19.90)	8.08 (5.89)
r for CTh	0.79	0.5	0.62	0.74	0.79	0.49	0.62	0.71	0.51	0.66	0.76
ICC for CTh	0.76	0.43	0.53	0.69	0.76	0.41	0.54	0.65	0.43	0.56	0.72
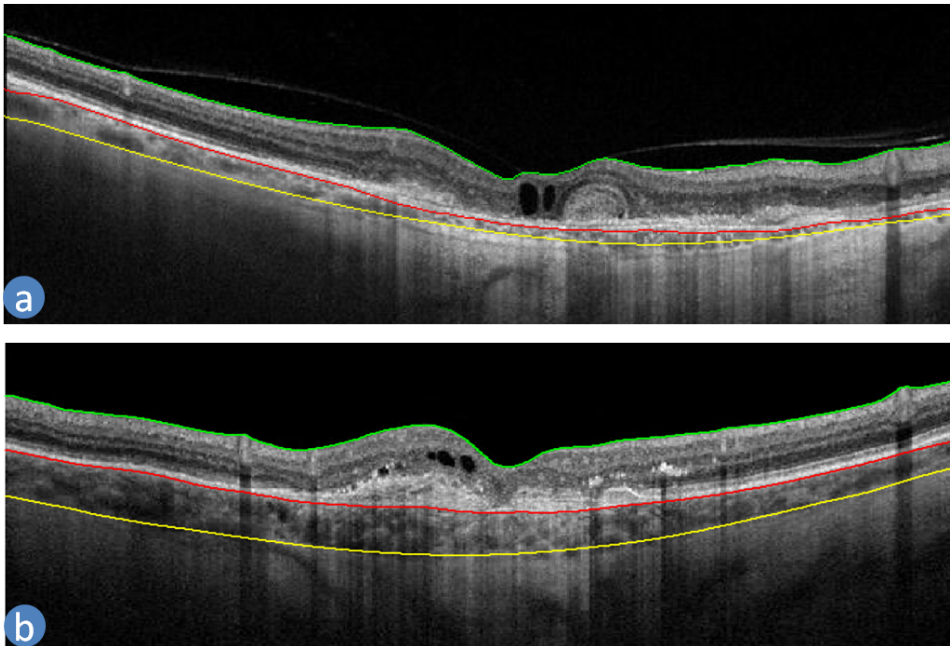
Figure 4.10: The output of our proposed method in the SS-OCT retinal scan presented with pathologies.

- Depth based Intensity Normalisation technique: The choroid is the noisiest area in the OCT image due to imaging technology and its anatomy. OCT technology is based on backscatter light from the tissues. As a result, it is sensitive to the depth of the tissue and loses sensitivity when increasing the depth of the tissue. Since the choroid is located under the retina, OCT cannot capture it with as high quality as the retina, although EDI-OCT and SS-OCT improve the quality of the image for the choroid. The images show high inconsistency in intensity even in the homogeneous area. The non-vessel regions of the choroid show high inconsistency in intensity and it is worse under the large choroidal vessel where the CSI boundary is located. Moreover, the presence of the large choroidal vessel increases such challenges as it has non-uniform distribution and shape. To solve this intensity variation and inconsistency, we have proposed a novel depth-based Intensity Normalisation technique which helps to make this uneven intensity distribution to even out the homogeneous area of the choroid and the sclera region.

- Computation of Edge weight: The second novelty in proposing the CSI detection is

a robust method of computing edge weight where the approximate position of the CSI and other structural information such as the outer boundary of the choroidal vessel are incorporated. Use of the normalised image and its intensity gradient in the edge weight computation instead of the original image has also improved the accuracy of the method in detecting the CSI due to reducing inconsistency of the intensities in the choroid. The combination of all these operations makes our method robust and accurate and outperforms the state-of-the-art methods.

4.7 Conclusion

We have proposed an automated, robust and highly accurate method for the detection of the CSI. We evaluate our method on the EDI-OCT images with different signal to noise ratio which has shown similar accuracy when compared with grader. We have also shown the robustness of our proposed method by showing segmentation output in the SS-OCT B-scans with pathologies. Our proposed method, which is simple and novel, is a depth-based intensity normalisation (DIN) method for analysing CTh in EDI-OCT image technology. The normalisation method reduces the challenges of low contrast and unstable or unpredictable changes of the choroid layer by converting high distorted intensity values to a stable for the surface and vessel pixels of the choroid and sclera. This approach provide a high robustness in the low contrast choroid. Then the Dijkstra shortest path algorithm has been applied to detect robustly the CSI where the edge-weights are chosen based on two approximate boundaries, the OCV and CSI. The edge weights has helped to detect the accurate boundary in a noisy and low-contrast image by reducing the search space and increasing the value of the probability of the pixels which are more likely to be the CSI. We have shown our method to be far superior to the state- of-the-art methods which has been established using several statistical tests including RMSE, DC and correlation coefficient. Our method has shown a performance similar to manual segmentation based on the inter-grader variability. The method of detecting ILM-RNFL and RBC has performed well even in the presence of pathology reported in Section 3.7 and here CSI detection method has performed well in the low-contrast and uneven thickness of the

choroid. Thus, the proposed method can be deployed for large-scale studies for tracking the progression and diagnosis of pathologies related to the choroid.

Chapter 5

3D segmentation (3DS) Algorithm for the detection of the retinal layers and the Choroid-Sclera Interface

This chapter presents a novel 3D segmentation method for segmenting the retinal layers through Spectral Domain Optical Coherence Tomography (SD-OCT) and Enhanced Depth Imaging Optical Coherence Tomography (EDI-OCT) volume images, and the Choroid-Sclera Interface from EDI-OCT images. This chapter is based on the following publication.

5.1 Introduction

With advanced imaging techniques such as 3D imaging much more information is available to analyse and assess the clinical relevance such as retinal layer and choroid thickness. In addition, 3D imaging can make use of more structural information of the tissues and pathologies than can 2D images, allowing better image analysis. 3D surfaces of a structure (e.g. retina) are scanned and segmented to detect the abnormalities for studying and diagnosing diseases. For example, retinal tissue layers are analysed for the more granular or precise grading or staging of disease, such as glaucoma and Age-related Mac-
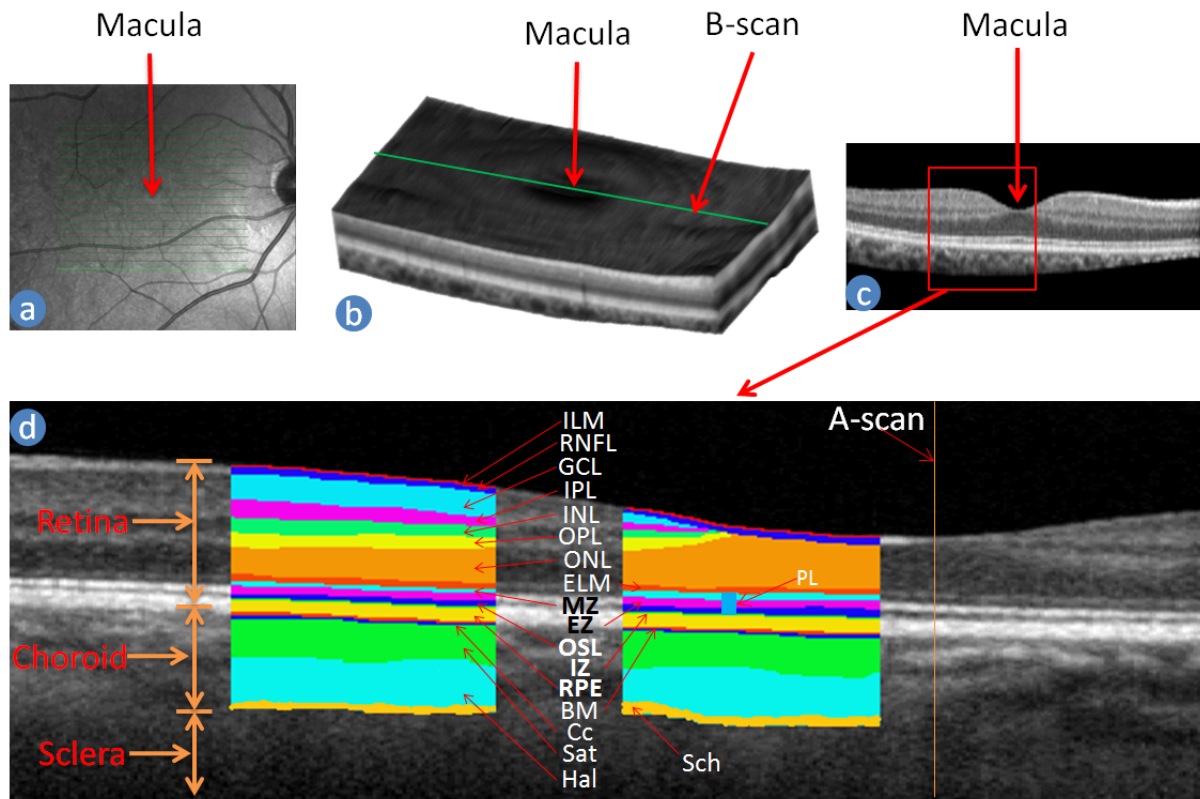
Ten Retinal Layers: **ILM**: Internal Limiting Membrane; **RNFL**: Retinal Nerve Fiber Layer; **GCL**: Ganglion Cell Layer;
IPL: Inner Plexiform Layer; **INL**: Inner Nuclear Layer; **OPL**: Outer Plexiform Layer; **ONL**: Outer Nuclear Layer; **ELM**:
External Limiting Membrane; **PL**: Photoreceptor Layer; **RPE**: Retinal pigment epithelium.
IZ: Interdigitation Zone, a layer which is not always distinguishable even in the normal eyes.
PL is divided into three segments: MZ + EZ + OSL; **MZ**: Myoid Zone; **EZ**: Ellipsoid Zone; **OSL**: Outer Segment Layer;
Five layers of the choroid: **BM:** Bruch's membrane; **Cc:**Choriocapillaris; **Sat:** Sattler's layer; **Hal:** Haller's layer and **Sch:**
Suprachoroidea.
The outer boundary of the choroid is known as the choroid-sclera interface (CSI).

Figure 5.1: Macula centred retinal image (a) Near infra-red image; (b) Volume or 3D
reconstruction of the retina from OCT scans; (c) A B-scan image (cross-section of the
retina through the green line in Fig. a and b) and (d) Retinal Layers are delineated in a
B-scan image.

ular Degeneration (AMD), to more precisely or accurately determine the risk that some-
one has in progressing to vision loss [7,8]. A near infrared fundus image of the reitna, 3D
view of a macula centred retina from Spectral Domain Optical Coherence Tomography
(SD-OCT) B-scans, a SD-OCT B-scan and layers of the retina and the choroid are shown
in Fig. 5.1. In this chapter, we have proposed a 3D segmentation algorithm to segment
all layers of the retina and the Choroid-Sclera Interface (CSI).

There have been many attempts to obtain robust and accurate retinal image anal-

ysis systems. Current automatic methods for retinal OCT image analysis can be categorised into three classes based on the dimensions, and they are 1) 1-Dimension (1D); 2) 2-Dimensions (2D); and 3) 3-Dimensions (3D). Hee et al. [123] have proposed an automatic method of computing retinal thickness on finding peaks in 1D using kernel and threshold in 1995. Then many other methods considered 2D and 3D segmentation. Simple thresholding schemes to more complex machine-learning approaches have been used to detect layers in 2D and 3D [7,8,116]. The literature review of the detection of the retinal layers and the choroid was discussed in Chapters 2 (Sections 2.7.3 and 2.7.4). However, those methods still need improvement in terms of the accuracy of the segmentation and detection. Our goal in this chapter is to present a robust algorithm to segment the retina with more accuracy than the state-of-the-art methods in 3D images which can also work for the 2D images (B-scans) if required. The benefit of using 3D over 2D segmentation is that it increases accuracy and shows a full structure of the retina that can be visualised effectively. Though 3D segmentation can potentially increase the complexity of the algorithm, computing in parallel multiple 2D-scans can reduce the need for larger Regions Of Interest (ROI) that is required in 2D segmentation. Already-detected boundaries in the same or adjacent B-scans help to decrease ROI and therefore segmentation can be achieved in real time. In addition, for clinical purposes, it is essential that retinal OCT image analyses should be able to segment accurately even in the presence of pathology in the image. By considering these, in this chapter, our focus is to develop a robust and automatic 3D segmentation method for determining the boundaries of the retinal layers and the CSI in the presence of pathology. In this chapter, we do not consider parallel computation; however, the methods amenable to parallel processing would be a goal of future work.

The main advantages of our approach which leads to increased accuracy, speed and robust 3D retinal layer and CSI segmentation are as follows.

- Improved accuracy through using the neighbourhood information from adjacent B-scans

- Improved computational efficiency through finding and using ROI from adjacent B-scans which enables a smaller search space

- Improved robustness of the segmentation algorithm through employing information from adjacent B-scans even if any of the B-scans have low contrast, presence of noise or pathology which can mislead the segmentation algorithm.

Our proposed 3D Segmentation (3DS) method relies on the notion of a Stable Reference (SR) boundary and two segmentation methods: 2D-Segmentation (2DS) and Greedy 3D Segmentation (G3DS). There are two 2DS algorithms for the retinal layers and Choroid-Sclera Interface (CSI). They have been explained in Chapters 3 and 4. The 2DS algorithm does not use adjacent B-scan information and the G3DS algorithm uses the adjacent B-scan information which will be discussed in Section 5.2.2. In Chapter 3, we discussed parameters of the graph generation for the detection of four boundaries of the retinal layer. In this chapter, we will discuss all 12 boundaries of the retinal layer in Section 5.2.1.

If boundaries in a B-Scan determined by 2DS and G3DS are very similar, then we refer to them as a Stable Reference (SR) boundary, which is explained in detail in Section 5.2.3. After finding the SR boundaries, a 3DS algorithm detects the boundaries in all volumes. The proposed method of boundary tracing is achieved by solving the graph shortest path problem using Dijkstra's Algorithm, where the nodes of the graph are the edge pixels of the image found using a Canny Edge Detection (CED) algorithm and with a robust edge weight computation for overcoming pathological disruptions in layers. The approximate positions of three reference layers (RNFL, ONL and RPE) are used to determine ROI for the first few retinal layer boundaries and their exact positions using the graph method discussed in Section 5.2. Once the exact boundary of a layer is detected, this boundary is also used to choose small ROI for determining the other boundaries. In a similar way, when a boundary of a B-scan is detected, this boundary is used as further reference to choose ROI for the boundaries in the adjacent B-scans for 3D segmentation. The edge pixels found by a CED detection algorithm are formed into pixel groups based on the length and neighbourhood of the edge pixels. The end points of each pixel group form two graph nodes. The spatial distance between the nodes, slope similarity with respect to the reference boundary and non-associativity (pixels not satisfying the associated layer property) to a layer are used to estimate the graph edge weight. Then Dijkstra's shortest

path algorithm is used to find the shortest path that determines the boundary of the layer. The main aspects of our 3D segmentation method are as follows.

- Mapping 3D segmentation problems as a shortest path problem in a graph.

- Avoiding complexity of 3D graph, by reducing the ROI using the adjacent B-scans as 3D information. This is achieved by reducing the 3D problem to a 2D problem using neighbouring pixels in the 3rd dimension simultaneously.

- Adjacent B-scans help to reduce the size of ROI for improving efficiency without compromising accuracy.

- Graph edge weights are estimated based on the following criteria.

  - The slope similarity to the reference line should decrease the cost of edge which is more likely to be the target boundary, since reference lines are selected which have the best correlation to the target boundary.

  - Non-associativity of pixel group should increase the edge weight as it is less likely to be the target boundary.

The main contributions of our method are as follows.

- An automated method for 3D segmentation of retinal layers for SD-OCT images which is also applicable for OCT images such as EDI-OCT and SS-OCT due to similar or higher quality of image.

- A segmentation method based on Graph algorithm that is robust despite the presence of various retinal pathologies in the images.

- Highly accurate segmentation of highest numbers of the retinal boundaries which includes all retinal layers and subdivision of the PL layer such as MZ, EZ and OSL which are sub-layers.

- Experiments conducted on 250 images of 10 different subjects with two subjects of various retinal pathologies showing highly accurate segmentation.

- Proposed segmentation is compared with five state-of-the-art retinal image segmentation methods and the results show it out-performs all those methods.

The rest of the chapter is organised as follows. The proposed algorithm is explained in Section 5.2. This section has several subsections explaining the proposed method step-by-step. In the subsections 5.2.1, the 2D segmentation method for a B-scan for the retinal layers' boundaries is discussed as it is the basis of the 3D segmentation. The Greedy 3D Segmentation method and the SR Boundary Detection, a condition for using the 3D segmentation in our proposed method, are discussed in Sections 5.2.2 and 5.2.3 respectively. The 3D segmentation algorithm is explained in Section 5.2.4. Sections 5.3, 5.4 and 5.5 provide the validation method, experimental setup and results of the performance respectively. Additional novelty of our proposed 3D segmentation algorithm over using the proposed 2D is discussed in Section 5.6. The last section, 5.7 concludes the chapter.

5.2 The proposed boundary detection method

The tissue of the retina are continuous in adjacent B-scans when the distance between the adjacent scans are very close. Therefore, we expect very small changes of a boundary from one B-scan to the next. This information helps to get correct boundaries where 2D automatic segmentation fails for the noise or tissue structure or pathologies, but 3D segmentation would be correct by using this neighbourhood information. This is the main advantage of 3D segmentation over 2D segmentation for our proposed method. That is why we have attempted to detect 12 boundaries of the retinal layers in 3D. The boundaries are detected sequentially which is based on the anatomical structure of the retinal layers. The method first detects the highly distinguishable boundaries compared to the other boundaries. This approach helps to detect the low contrast boundaries in a small ROI, since we define ROI using the already detected boundaries and adjacent B-scans. The reduction of the ROI helps improving the accuracy and efficiency of the detection even in the presence of pathologies. The sequence of the detection of boundaries is 1) ILM-RNFL, 2) RBC, 3) MZ-EZ 4) IZ-RPE 5) OPL-ONL, 6) ONL-ELM, 7) EZ-OSL, 8) ELM-MZ, 9) INL-OPL, 10) IPL-INL, 11) RNFL-GCL and 12) GCL-IPL. Finally the CSI is

detected.

Our proposed 3D Segmentation (3DS) method relies on the notion of a stable bound-
ary and two segmentation methods: 2D-Segmentation (2DS) and Greedy 3D segmenta-
tion (G3DS). The finding of a SR boundary is explained in details in section 5.2.3. There
are two 2DS algorithms and they are for retinal layers (Algorithm 1) and Choroid-Sclera
Interface (Algorithm 2). They have been discussed in Chapter 3 and 4 respectively. Here,
we only discussed about the parameters of the graph generation for all 12 boundaries
as they are not discussed in Chapter 3. G3DS algorithm are discussed in the following
section 5.2.2. The 3DS algorithm is discussed in section 5.2.4.

5.2.1   2D Segmentation (2DS) algorithm for detecting the boundaries of the retinal layers

The boundaries of the retinal layers have a smooth and similar gradient except for re-
gion where there is pathology. However, our assumption is that each boundary must
have similar gradient at most of the position in the boundary. For this reason, we use
the Canny edge detection (CED) algorithm for detecting the edge pixels of the bound-
aries with the different threshold values and standard deviation depending on the prior
knowledge of the boundary-contrast. The ROI for the boundaries is narrowing using
three reference layers (TRL: RNFL, ONL and RPE) and already detected boundaries. The
edge pixels from CED in the ROI are defined as the candidate pixels for the target bound-
ary. The candidate pixels are split into small connected parts called pixel groups. End
pixels of the pixel groups are the nodes of the graph. The edge weights between all
nodes are determined using spatial distance, slope similarity to the reference boundary
and pixels non-associativity to the layer. Finally, the Dijkstra's shortest path algorithm is
used to define the boundary.
Since an SD-OCT image has noise from the accusation process of the image, we apply
the Anisotropic Diffusion (AD) and Wiener filters to reduce image noise with minimum
distorting the edge of boundaries. Then we will discover the TRL and following this
we will detect the boundaries. Figure 5.2 shows the flow diagram of the boundaries of
the retinal layers detection in an individual B-scan (i.e. 2DS Algorithm). First, a B-scan
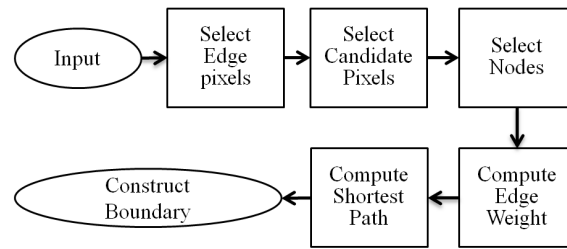
Figure 5.2: The basic flow diagram of the 2DS algorithm for the boundaries of the retinal layers.

image is taken as input. The second step is to detect pixels which have higher gradient intensity exceeding the given threshold value. We call these pixels edge pixels. We can find edge pixels using CED algorithm with the threshold value and standard deviation for smoothing the image. Since retinal boundaries have different contrast labels, we use different threshold values and standard deviations for the different boundaries, Table 5.1 shows optimum threshold values determined using Simulated Annealing (SA) over two subjects (details in Section 3.6). The third step is one of the most important operations in our proposed method where we select edge pixels that are in the ROI. The pixels are called candidate pixels. The candidate pixels are grouped into small connected parts called pixel groups. The maximum number pixels allowed in a pixel group is determined using SA. The minimum can be one pixel. Therefore, contiguous candidate pixels could be divided into several pixel groups due to the restrictions of the pixel-group size. End points of the pixel-groups are defined as the nodes of the graph. We then form a fully connected graph using these nodes. The next step is the computation of the edge weights based on three features, which are described in the following paragraphs. After computing edge weight, the shortest path is discovered using Dijkstra's shortest path algorithm. Start and end nodes are added automatically and treated them specially so that shortest path would be independent of the start and end of the boundary. The start and end nodes are removed in the reconstruction phase of the boundaries. The pixel groups of the corresponding shortest path nodes are used to fit a continuous line. Gaussian smoothing is applied to find a smooth line and removes noisy effect which may still exist after noise reduction.

We utilise three features to compute edge weights using (5.1) for the boundaries: spa-

tial distance, slope similarity to a reference boundary and nodes non-associativity to the boundary. For computing spatial distance, slope similarity to a reference boundary and nodes non-associativity to the boundary, we use (5.2), (5.3) and (5.4), respectively.

$$\omega_{a,b} = \phi_{a,b} + \psi^r_{a,b} + \gamma_{a,b} \tag{5.1}$$

Where $\omega_{a,b}$ is the edge weight of node a to node b that is the sum of $\phi_{a,b}$, the weight for the spatial distance; $\psi^r_{a,b}$, the weight for the slope discontinuity with reference line r and $\gamma_{a,b}$, the weight for the relevance to the layer's boundary. Each node (a and b) represents one two-coordinate value - (a_x, a_y) and (b_x, b_y).

$$\phi_{a,b} = \begin{cases} 0 & \text{, if } a = b \\ \alpha_0 & \text{, if } a \text{ \& } b \text{ in the same pixel-group} \\ \alpha_1|a_x - b_x|^2+ \\ \alpha_2|a_y - b_y|^2+ & \text{, otherwise} \\ \alpha_3|\frac{a_y - b_y}{a_x - b_x}|^2 \end{cases} \tag{5.2}$$

where α_1, α_2, and α_3 are three coefficients , and a_x, a_y, b_x and b_y are the coordinate position of nodes a and b.

$$\psi^r_{a,b} = |(r(a_x) - a_y) - (r(b_x) - b_y)| \tag{5.3}$$

where $r(x)$ is the y value of the reference boundary r at x-coordinate x.

$$\gamma_{a,b} = \sum_i (1 + E_b - f_{b,i})^{p_i} \tag{5.4}$$

where E_b is the number of pixels in the pixel-group containing node b, i is 1 to total number of property, $f_{b,i}$ is the number of associated pixels for i^{th} property in the pixel group containing node b, and p_i is a parameter to control the influence of each property.

In Table 5.1, we have reported the parameters for detecting the boundaries of the retinal tissue layers in the order of their detection. The constant values are defined using SA over two subjects. The first column contains the boundary name and the second column contains the parameter for detection of Edge pixels: Standard deviation (SD) and

threshold (Th) for the Canny edge detection. Candidate pixels detection is reported in the third column which is sub-divided into three columns: direction of the vertical gradient (dg), top border and bottom border. Top and bottom border are used to define the region of interest (ROI). Most of the times, they are simply two boundaries and sometimes they are defined by multiple boundaries. The forth column contains the parameter of the maximum pixel number (np) to form the pixel groups whose end points are the nodes. The last (fifth) column is the parameter for the computation of the edge weight. It is mainly divided into three based on their respective weights: spatial distance ($\phi_{a,b}$), slope similarity to a reference line ($\psi^r_{a,b}$) and layer non-associativity ($\gamma_{a,b}$). The column of spatial distance ($\phi_{a,b}$) is subdivided into three for three coefficient values. The column for the slope similarity to a reference line ($\psi^r_{a,b}$) contains the name of the reference line (r). Most of the times, the reference line is the detected boundary or approximately detected layer position. Sometimes they are derived line from other boundaries; in these cases, we explain them in the footnote under the table. The column of the layer non-associativity ($\gamma_{a,b}$) holds the number of properties that are considered to compute $\gamma_{a,b}$ and in all cases p_i is two, unless it is mentioned. While we find top or bottom pixels from any of the boundaries, it is computed along A-scan.

Table 5.1: The parameters for detecting the boundaries of the retinal tissue layers.

Boundary Name	Edge Pixels		Candidate Pixels			Node	Compute Edge weight				
	SD	Th	dg	Top Border	Bottom Border	np	$\phi_{a,b}$			$\psi^r_{a,b}$	$\gamma_{a,b}$
							α_1	α_2	α_3		
ILM-RNFL	$\sqrt{2}$	0.1	+	f_1	f_1	25	1	ly	2.5	f_1	2, f_1
RBC	1	0.01	-	$aprxONL$	f_2	1	3	dy	5	f_2	1, f_2
MZ-EZ	$\sqrt{2}$	0.1	+	$aprxONL$	RBC	15	lx	1	2	RBC	3, f_3
IZ-RPE	1	0.01	+	MZ-EZ	RBC	1	dx	3	2.5	RBC	3, f_4
OPL-ONL	1	0.01	-	ILM-RNFL	f_5	5	1	1	ry	f_5	1, f_5
ONL-ELM	0.1	0.01	+	OPL-ONL	f_6	1	1	1	1	MZ-EZ	2, f_6
EZ-OSL	1	0.01	-	MZ-EZ	IZ-RPE	5	1	1	ry	MZ-EZ	1, f_7
ELM-MZ	0.5	0.01	-	ONL-ELM	MZ-EZ	5	1	1	ry	ONL-ELM	1, f_8

INL-OPL	0.5	0.01	+	f_9	f_9	5	1	1	ry	ILM-RNFL	1, f_9
IPL-INL	1	0.01	-	f_{10}	INL-OPL	5	1	1	ry	ILM-RNFL	1, f_{10}
RNFL-GCL	2	0.01	-	ILM-RNFL	INL-OPL	5	1	1	ry	f_{11}	2, f_{11}
GCL-IPL	2	0.01	+	RNFL-GCL	IPL-INL	5	1	1	ry	ILM-RNFL	1, f_{12}

Footnote is numbered by f_n, where n is a number and all explanation of a boundary is explained in same footnote. dy = $|a_y - b_y|$, dx = $|a_x - b_x|$, ry = $|\frac{a_y}{b_y}|$, $lg_2 = log_2$

f_1, Candidate pixels: The closest and above the approximate RNFL layer and connected with them. r: the first order polynomial fitted line at the approximate RNFL layer pixels. Property 1: the closest and above the approximate RNFL layer. Property 2: above the approximate ONL (*aprxONL*, an approximate layer in TRL layers) layer.

f_2, Bottom border is 500μm below the ILM-RNFL boundary. r: the first order polynomial fitted to the *aprxRPE* (an approximate layer in TRL layer) layer pixels. Property 1: the closest and below the approximate RPE layer.

f_3, Property 1: Two nearest pixels from the approximate RPE layers. Property 2: Top most pixels from Property 1 along A-scan. Property 3: The pixels having the lowest intensity in each A-scan from Property 1.

f_4, Property 1: The pixels under the MZ-EZ boundary and pixels of MZ-EZ in case of no pixels under it. Property 2: The pixels except the pixels of the MZ-EZ boundary. Property 3: The challenges for the abnormalities of drusen are addressed by this property. If the distance between the MZ-EZ and the RBC along an A-scan is more than the distance of the average plus one standard deviation, then the A-scan is considered an approximate drusen area. The bottom candidate pixels in each A-scan except the approximate drusen areas are selected for the third property. Then the average distance between those selected associated pixels and RBC are computed. The pixels closest to RBC boundary and above that average distance in the approximate drusen area are included into the third property.

f_5, Candidate pixels: we refine by removing the top most pixels where there is more than one pixels for any A-scan as they are belongs to RNFL-GCL. The *aprxONL* layer position is refined by finding the pixel position of the minimum intensity in the ROI (ILM-RNFL to MZ-EZ) and applying a moving average filter to remove noises, referred as refONL. The top and closest pixels from refONL in the remained candidate pixels and connected pixels with them are formed the final candidate pixels for the OPL-ONL. Property 1: The candidate pixels above and closest to the refONL.

f_6, Bottom border is 0.5 μm below the MZ-EZ boundary. Property 1: Last candidate pixels in each A-scan. Property 2: First candidate pixels in each A-scan.

f_7, f_8: Property 1: First candidate pixels in each A-scan.

f_9, The negative gradient edge pixels which are located under and closest to ILM-RNFL are defined as the approximate RNFL-GCL. The Candidate pixels is those positive gradient edge pixels which are located approximate RNFL-GCL to OPL-ONL boundary. After that, a smooth averaging filter is applied on approximate RNFL-GCL with window size of the one tenth of the width of the B-scan for removing noises. If any A-scan in the candidate pixels has no pixels then add pixels from the ILM-RNFL to approximate RNFL-GCL region for those A-scans. If there is still no pixels for any A-scan then add OPL-ONL boundary pixels for those A-scans. Property 1: Last candidate pixels in each A-scan.

f_{10}, Top Border is the approximate RNFL-GCL from f_9. Property 1: Last candidate pixels in each A-scan.

f_{11}, Two reference lines are used for this boundary to compute $\psi_{a,b}^{r}$ and $\psi_{a,b}^{r} = \psi_{a,b}^{r_1} + \psi_{a,b}^{r_2}$ where r_1 is ILM-RNFL and r_2 is INL-OPL. Property 1: Last candidate pixels in each A-scan. Property 2: First candidate pixels in each A-scan.

f_{12}, Property 1: Last candidate pixels in each A-scan.

5.2.2 Greedy 3D Segmentation (G3DS) algorithm: Boundary detection using adjacent B-scans

In 3D detection, adjacent B-scan (one of the immediate left or the right scans of the current B-scan) information is used to detect the boundary in the current B-scan. The adjacent

B-scan is called base B-scan, and the boundary is called base boundary. Pseudo code for G3DS is presented in *Algorithm 3*. G3DS algorithm is similar to 2DS but it uses of base boundary and is more efficient and accurate. The parameter used for G3DS for Canny detection, pixel groups, noise reduction method, the detection of the edge pixels, the use of vertical gradient, the defining of the pixel group and nodes, the spatial distance ($\phi_{a,b}$) for computing edge weight and the boundary construction for a boundary are same as used in 2D detection. However, the ROI for the candidate pixels, slope continuity to a reference ($\psi_{a,b}^{r}$) and layer non-associativity to a layer ($\gamma_{a,b}$) for computing edge weight which are different and these are described below. We have used some constant values for selecting the ROI, those values are chosen based on the resolution of the image.

Algorithm 3 G3DS Algorithm

Input: B-scan image, required already detected Boundary, base boundary.
Output: Boundary position.
  1: Find the ROI using already detected boundary and base boundary.
  2: **If** *TargetBoundary = The boundary of the retinal layer* **then**
  3:      Detect the boundary using Algorithm 1 by replacing the ROI by the current ROI.
  4: **EndIf**
  5: **If** *TargetBoundary = The CSI* **then**
  6:      Detect the boundary using Algorithm 2 by replacing the ROI by the current ROI and a new cost function equation 5.5.
  7: **EndIf**

Some Notation that is used to explain the G3DS method

$B_{current}$: The B boundary at the current B-scan.

B_{base} : The B boundary at the base B-scan.

$WR(x) = x/mean(x)$

$B_1 - B_2$: subtraction between two boundaries along A-scan.

CEW : Compute Edge Weight

ILM-RNFL

ROI : $5\mu m$ top and bottom from the base boundary.

CEW: r for $\psi_{a,b}^{r}$ is the base boundary and $\gamma_{a,b} = 0$.

RBC

$\delta = max(3\mu m, |\text{ILM-RNFL}_{current} - \text{ILM-RNFL}_{base}|)$

ROI : δ pixels top to 5μm bottom from the base boundary.

CEW: r for $\psi_{a,b}^r$ is the base boundary and $\gamma_{a,b}$ is the vertical distance from the base boundary and nodes with $p = 2$;

MZ-EZ

Since this boundary shows big change due to drusen, that is why, selection of ROI is different from other boundaries.

$\delta = max(|RBC_{current} - RBC_{base}|)$

$aprxONL$ = the pixel position of the minimum intensity between ILM-RNFL and δ pixels beneath the base boundary.

$aprxRPE$ = the pixel position of maximum intensity between $aprxONL$ and RBC.

ROI = two nearest pixels from $aprxRPE$ and under $aprxONL$.

$R = WR(RBC_{current} - aprxRPE_{current})$

$refBaseBoundary$ = min(base boundary, R x ($RBC_{current}$ - base Boundary)).

CEW: r for $\psi_{a,b}^r$ is the $refBaseBoundary$ and $\gamma_{a,b}$, one property (top candidate pixels);

IZ-RPE

ROI: Top two edge pixels between 1μm top of the MZ-EZ boundary and RBC boundary.

CEW: r for $\psi_{a,b}^r$ is the base boundary and $\gamma_{a,b}$=0;

OPL-ONL

$\delta = max(|RBC_{current} - RBC_{base}|)$

ROI = Top and bottom closest pixels from the $aprxONL$ in between the ILM-RNFL and MZ-EZ.

CEW: r for $\psi_{a,b}^r$ is the base boundary and $\gamma_{a,b}$, one property (nearest candidate pixels from the base boundary plus δ);

ONL-ELM

$D = max(|ONL\text{-}ELM_{base} - MZ\text{-}EZ_{base}|)$

$\delta = max(|RBC_{current} - RBC_{base}|)$

$topBorder$ = min(base boundary - δ, MZ-EZ - D).

ROI: topBorder to 0.5μm top the MZ-EZ.

CEW: r for $\psi_{a,b}^r$ is the MZ-EZ boundary and $\gamma_{a,b}$, two properties (Property-1: top nearest candidate pixels from the MZ-EZ boundary and Property 2: top candidate pixels);

EZ-OSL, ELM-MZ, INL-OPL, IPL-INL, RNFL-GCL, GCL-IPL

Since ROI for these boundaries is small, we use same method of the individual B-scan except r of $\psi_{a,b}^r$ which is used the corresponding base boundary.

CSI

$\delta = max(|RBC_{current} - RBC_{base}|)$

$D = max(|RBC_{current} - Base_{Boundary}|) + \delta + 4\mu m$

ROI1 = RBC to RBC+D

NI = Apply the noise reduction and normalisation of the CSI detection in *ROI1* same as individual B-scan method.

$N = 0.5 * exp(-(Base_{Boundary} + \delta)/(\delta * 10))$

$ROI = \delta + 3\mu m$ top to $\delta + 4\mu m$ bottom the base boundary. Then straighten the image so that top pixels of the ROI become a straight line.

DIN = Apply Depth-based intensity normalisation (DIN) methods and normalise the pixels value 0 to 1.

Surfline = middle of the ROI minus δ

Vsl = intensity less than 0.5 in the DIN and located top to *surfline*.

Vslfactor = set the pixels value for vessel pixels and its top pixels to 0.5, non-vessel pixels but top of surfline to 0.9 and all other pixels 1. For smoothing these values along A-scan, we apply Gaussian filter trice one after another where window size is δ and standard deviation is 1.

$$Cost = DIN_{gradient} + NI + vslFactor. \tag{5.5}$$

5.2.3 Stable Reference (SR) boundary selection

The SR boundary is a boundary which is the same or similar and that tolerates some deviation using the detection of algorithms 2DS and G3DS. We assume that if 2DS and G3DS algorithms detect a boundary at the same position (or very close to each other) then it is an accurate boundary. As a consequence, we can use that boundary for G3DS algorithm

as a reference boundary for detecting the boundary in the adjacent B-scans. Since accurate reference boundary leads to accurate detection and inaccurate reference boundary leads to inaccurate detection for full volume of image. Pseudo Code for SR boundary detection is presented in *Algorithm 4*. To determine SR boundary in set of continuous B-Scans, we first compute boundary in the first B-scan using 2DS. The boundaries of the retinal layers are detected using Algorithm 1 and the choroid-sclera interface is detected using Algorithm 2. Then we compute same boundary in the 2nd B-Scan using 2DS and G3DS where 1st scan's boundary from 2DS algorithm is used as adjacent B-scan's boundary. If the percentage of absolute pixel difference between the boundaries of 2DS and G3DS at 2nd B-scan less than *ETh* along A-scan is greater than *PTh* and standard deviation of absolute pixel difference is less than *STh*, then they are defined as same boundaries and 2nd B-scan is the stable boundary B-scan with the boundary from G3DS algorithm. If the two boundaries found by 2DS and G3DS of 2nd B-Scan are not similar we repeat the process using 2nd and 3rd B-Scans where 2nd scan's boundary from 2DS algorithm is used as adjacent B-scan's boundary in G3DS algorithm for detecting the boundary at 3rd B-scan. If the boundaries at 3rd B-scan are same then 3rd B-scan is used as SR boundary B-scan. If such SR boundary is not found until the Kth (K = 10, gave good results) B-Scan, we compute the root mean square error (RMSE) between each of the K boundaries detected by 2DS and formed a graph where every boundary is a node and RMSE values are edge weight. Now we find the minimum RMSE value using binary search algorithm as a threshold, so that by applying the threshold value more than half of the nodes stay connected. The lowest B-scan from the connected group is defined as the SR boundary B-scan's and its boundary from G3DS uses as the SR boundary.

The three threshold values in the decision of same boundary are $ETh = 3, PTh = 85$ and $STh = 3$ for the boundaries of the retinal layers. Since CSI is not detected using edge pixels and it could have a higher variation than the retinal layers that we need to accept. That is why we allow more deviation between the boundaries to be decided as same boundary and they are $ETh = 6, PTh = 60$ and $STh = 6$.

Algorithm 4 Stable Reference (SR) Boundary Selection Algorithm for A Boundary

---

Input: Volume image.
Output: B-scan and boundary Position of the SR Boundary.
1: Detect the boundary for 1st B-scan using 2DS Algorithm. **For** $i = 1$ to 10
2: $b2DSi$ = Detect the boundary for i^{th} using 2DS Algorithm
3: $bG3DSi$ = Detect the boundary for i^{th} using G3DS Algorithm
4: **If** percentage of $|b2DSi - bG3DSi| \leq ETh$ is greater than PTh and standard deviation of $|b2DSi - bG3DSi|$ is less than STh **then**
5:     SR boundary is found for i^{th} B-scan, return i and $bG3DSi$.
6: **EndIf**
7: $Ebnd = RMSE(bnd_i, bnd_j)$, where $i, j = 1$ to 10 and bnd are the boundaries of first 10 B-scans from 2DS Algorithm.
8: $CNode$ = Find the minimum value in the $Ebnd$ for which more than half of the nodes (cell of the $Ebnd$) are connected.
9: Return the lowest B-scan position and its detected boundary position from G3DS Algorithm from $CNode$.

5.2.4 3D Segmentation (3DS) algorithm

Our 3D segmentation algorithm relies on the notion of a stable boundary and two segmentation methods: 2D-Segmentation (2DS) and Greedy 3D segmentation (G3DS). Pseudo code for 3DS is presented in *Algorithm 5*. First, we find the position of the B-scan containing the current target SR boundary using *Algorithm 4* where 2DS (*Algorithm 1 and 2*) and G3DS (*Algorithm 3*) algorithms are used. Then the target boundary is segmented using G3DS algorithm in the previous and succeeding B-scans from the B-scan consisting stable boundary. Figure 5.3 shows the basic flow diagram of our proposed 3D method for detecting retinal layers. In 3D, a boundary from an adjacent B-scan (in stable system that is after detecting SR boundary) is used to detect the ROI for the target B-scan for segmenting the boundary. After detecting a boundary for the 3D cube/volume, we start detecting other boundaries.

5.3 Validation method

For validation, we compared the results obtained by our proposed method against the manually segmented images (ground truth). We also compared our method against six state-of-the-art methods (includes two CSI segmentation methods) [62,80,85,101,114,116]

Algorithm 5 3DS Algorithm

Input: Volume Image.
Output: Boundary position.
1: **For** each of the boundaries of the retina and the choroid
2:     *StP* = find the Stable Boundary Position for the current Boundary.
3:     **For** i =*StP*-1 to 1 (decreasing)
4:         Bnd = Find boundaries using G3DS where adjacent B-scan is i+1.
5:     **EndFor**
6:     **For** i =*StP*+1 to end of the B-scan
7:         Bnd = Find boundaries using G3DS where adjacent B-scan is i-1.
8:     **EndFor**
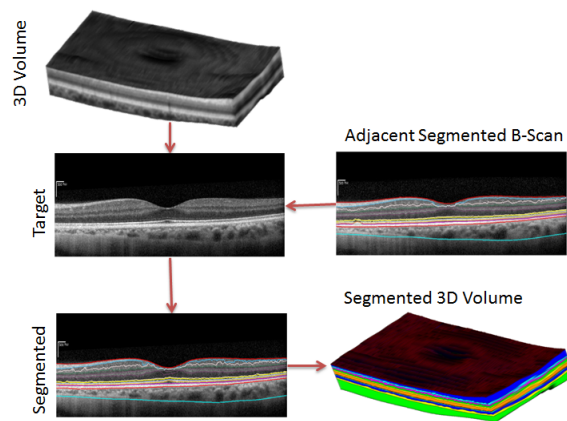
Figure 5.3: The basic flow diagram of our proposed 3D segmentation.

and our proposed 2D methods of the retinal layer and CSI detection. The three automatic segmentation methods for the retinal layer boundaries are publicly available, one method [116] is collected from the authors and fifth automatic method is our 2D Segmentation method. In chapter 3, we have used two more methods Chiu et al. [78] and Tian et al. [63] as well as their dataset for the evaluation. The implementation of their methods do not show satisfactory performance in other dataset (see Section 3.7). Hence, we ignore them in this evaluation process and consider current five state-of-the-art methods are sufficient for the evaluation. There is no method for the choroid segmentation publicly available, thus we have implemented Tian et al. [85], and Chen et al. [80] for the evaluation process of the choroid. We have also shown the result of our 2D method for CSI segmentation. Our assessment involves direct evaluation of the precision of the boundary locations by computing: the root mean square error (RMSE) between two dif-

ferent segmentations. The performances of six state-of-the-art methods, our proposed 2D segmentation methods and our proposed 3D method are reported using this assessment method to compare and justify the accuracy and robustness of the methods over two datasets (details are in next section).

5.4 Experimental setup

Our experimental setup consisted of two datasets of eight subjects' i.e., eight macular EDI-OCT volumes of healthy subjects and two subjects i.e., two macular SD-OCT volumes of participants with intermediate AMD. Two subjects used in SA optimisation computation are excluded from the evaluation process. Each volume of healthy subjects has 19 B-scans ($1021 \times 361 \times 19$ voxels), therefore we had a total of 152 B-scans and AMD subjects have 49 B-scans ($1024 \times 496 \times 49$ voxels) per volume (total 98 B-scans) with 3.9 μm axial resolution. All Subjects are imaged using Heidelberg Spectralis HRA+OCT in two different organisations. We have 250 manually graded B-scans of 10 subjects for evaluation the methods. This data is used as our Gold Standard for comparing our method with the state-of-the-art methods. In addition, images are run through segmentation software developed by Dufour et al. [114, 151], Iowa Reference Algorithm [62, 149], AURA tools [101, 150], Duan et al. [116], Tian et al. [85], and Chen et al. [80]. Since the choroid is not capture properly in the SD-OCT images of the AMD subjects, they are excluded from the evaluation of the choroid detection. Each of the automatic methods is generated segmentation results and computed RMSE against the manual grader. These computations allow comparing each of the method between them. The details are presented in the result section.

5.5 Results

Our results show high accuracy compared to the currently available state-of-the-art automatic methods [62,80,85,101,114,116] and our 2D segmentation methods in the means of RMSE. The RMSE of the retinal layers boundaries of the four state-of-the-art methods, our 2D segmentation method and our proposed 3D method are reported in Table 5.2 and

5.3. The RMSE The p-values from the paired-sample t-test of the RMSE between proposed and the other segmentation methods are statistically significant i.e. less than 0.001 for all cases. The mean and standard deviation of the corresponding metric are reported in the Tables. Some cells of the table are empty because the corresponding methods do not detect those corresponding boundaries.

The RMSE of the boundary positions in Table 5.2 shows our proposed method has significantly lower error than any other state-of-the-art methods. The overall mean of the RMSE of the boundaries positions of the retinal layers for the Dufour et al., Iowa Reference Algorithm, AURA Tools, Duan et al. and Hussain et al. methods are $3.05, 5.50, 2.19, 4.08$, and 0.64 in pixels respectively where our proposed method has achieved 0.20, a clear improvement in the accuracy. We also performed interclass correlation coefficient (ICC) for layer thicknesses. The average ICC score from our proposed method is 0.92 for all layers where as the best ICC score achieve by the state-of-the-art methods is 0.58.

The RMSE of the boundary positions of AMD subjects are reported in Table 5.3. In general, the result shows our proposed 3D method has better than the state-of-the-art methods even in the presence of pathologies. The overall mean score of RMSE for our proposed method for AMD subjects is 0.69 pixels whereas for Dufour et al., Iowa Reference Algorithm, AURA Tools, Duan et al. and Hussain et al. methods the RMSE values are $2.03, 2.89, 1.49, 3.67$, and 0.76 pixels respectively. Finally, our 3D method is three times faster than our 2D method as 3D method needs to select much smaller ROI from adjacent B-scans for building 3D structure.

The performance of proposed 3D method for the choroid detection is reported in Table 5.4. Two state-of-the-art methods, Tian et al. [85] and Chen et al. [80] , and our previous 2D method for the choroid detection are also reported against manual grading. The lower mean and standard deviation of the RMSEs of the CSI and CTh represent the reliability and robustness of our proposed over two state-of-the-art methods and our previous 2D method. The mean of the RMSE of the CSI and CTh for the Tian et al. and Chen et al. methods is more than 30 pixels, our previous 2D method has more than 10 pixels where our proposed 3D method has less than 1.50 pixels.

Figure 5.4 and 5.5 show the segmentation results by state-of-the-art methods and our

Table 5.2: The mean and standard deviation in pixels of the RMSE for boundary position on normal subject's dataset.

Boundary	Dufour	Iowa	AURA	Duan	Hussain	Proposed
ILM-RNFL	1.62 (0.99)	3.14 (0.25)	1.87 (1.15)	0.93 (0.32)	0.95 (0.32)	**0.55 (0.34)**
RNFL-GCL	4.84 (3.11)	5.71 (4.08)	4.02 (1.01)	17.13 (12.01)		**0.59 (0.43)**
GCL-IPL		4.94 (3.45)				**0.17 (0.17)**
IPL-INL	3.21 (1.50)	3.95 (2.73)	2.11 (1.55)	9.36 (0.91)		**0.19 (0.24)**
INL-OPL		3.10 (1.17)	2.31 (1.49)	2.31 (0.50)		**0.44 (0.58)**
OPL-ONL	4.72 (5.22)	3.35 (0.41)	2.32 (1.61)	1.67 (0.40)		**0.06 (0.10)**
ONL-ELM			2.45 (1.66)	1.65 (0.70)		**0.04 (0.10)**
ELM-ISL						**0.03 (0.04)**
ISL-EZ	1.15 (0.19)	2.34 (0.17)	1.36 (1.94)	0.71 (0.14)	0.43 (0.11)	**0.16 (0.22)**
EZ-OSL		5.75 (0.29)		1.26 (0.62)		**0.01 (0.02)**
IZ-RPE		8.69 (1.24)	1.89 (1.84)		0.82 (0.09)	**0.16 (0.22)**
RBC	2.76 (2.91)	14.03 (1.51)	1.38 (1.91)	1.74 (0.78)	0.37 (0.15)	**0.01 (0.03)**
Overall	3.05 (3.04)	5.50 (3.87)	2.19 (1.68)	4.08 (6.51)	0.64 (0.31)	**0.20 (0.32)**

The best performance are marked by bold letter. Standard deviation is enclosed in parenthesis.

proposed 3D automatic method on normal and pathology existed subject respectively. The 3D render image of a volume in Fig. 5.7 is generated by our segmented output and Fiji, an open source image processing tools [181]. Figure 5.7(a) is a 3D render image of the segmented 3D volume; 5.7 (b) is a 3D render image of the segmented RNFL, ONL and RPE layers; and 5.7 (c) is a 3D render image of the segmented RNFL and Choroid. The segmentation output on different pathology (i.e. Cyst, Lesion in the inner retina etc.) are shown in Fig. 5.6.

In many instances, SD-OCT or EDI-OCT images may not have B-Scans as close as we have used in our evaluation. In order to evaluate robustness of the proposed method we removed some of the B-scans and measured estimated volume differences from the manually graded images of the AMD subjects. The original resolution of the images is $1024 \times 49 \times 496$ pixels in $6 \times 6 \times 2$ mm area at the macula centred retina. There is $122\mu m$ difference between two B-scans. We detect the layer in the volume by reducing the number of B-scans and reconstruct the original volume using interpolation. We compute the RMSE of the detected boundaries of layers against the manual grading and reported in Table 5.5. Generally, errors are increased in low-resolution image, which is expected

Table 5.3: The mean and standard deviation in pixels of the RMSE for boundary position on AMD subject's dataset.

Boundary	Dufour	Iowa	AURA	Duan	Hussain	Proposed
ILM-RNFL	0.95 (0.00)	2.12 (0.09)	0.79 (0.04)	0.79 (0.02)	0.12 (0.03)	**0.09 (0.02)**
RNFL-GCL	1.91 (0.25)	2.85 (0.05)	1.18 (0.06)	8.93 (1.96)		**0.37 (0.19)**
GCL-IPL						**0.01 (0.02)**
IPL-INL	2.06 (0.00)	3.11 (0.03)	1.13 (0.04)	10.88 (0.11)		**0.34 (0.12)**
INL-OPL		1.98 (0.32)	1.21 (0.11)	3.31 (0.75)		**0.46 (0.04)**
OPL-ONL	3.41 (0.28)	3.91 (0.09)	1.75 (0.04)	2.83 (0.47)		**0.85 (0.06)**
ONL-ELM			2.09 (0.06)	1.23 (0.13)		**1.05 (0.34)**
ELM-ISL						**0.92 (0.55)**
ISL-EZ	1.95 (0.94)	2.45 (0.03)	1.41 (0.46)	1.08 (0.02)	**0.86 (0.44)**	0.90 (0.50)
EZ-OSL		2.53 (0.21)		1.54 (0.56)		**1.27 (0.61)**
IZ-RPE		2.30 (0.26)	1.93 (0.65)		**1.62 (0.49)**	1.73 (0.64)
RBC	1.90 (0.51)	4.13 (1.62)	1.89 (1.28)	2.46 (1.21)	0.44 (0.58)	**0.33 (0.42)**
Overall	2.03 (0.83)	2.89 (0.83)	1.49 (0.57)	3.67 (3.61)	0.76 (0.68)	**0.69 (0.57)**

The best performance are marked by bold letter. Standard deviation is enclosed in parenthesis.

Table 5.4: The means and standard deviation of the evaluation protocols for CSI positions and the thickness of the choroid.

Metric	Tian et al. [85]	Chen et al. [80]	Our 2D method	Proposed 3D method
RMSE for CSI	31.13 (16.71)	34.34 (20.98)	10.81 (15.62)	**1.40 (2.08)**
RMSE for CTh	29.09 (15.73)	33.53 (20.66)	10.70 (15.62)	**1.40 (2.07)**

The best performance are marked by bold letter. Standard deviation is enclosed in parenthesis.

Table 5.5: The mean and standard deviation in pixels of the RMSE for boundary position on AMD subject's dataset for different resolution (number of B-scans per $6\mu m$) .

	Number of B-Scans chosen				
	49 (all)	33	25	17	10
Overall RMSE	0.69 (0.57)	2.14 (1.53)	2.77 (1.95)	2.67 (1.28)	3.71 (1.30)
ILM-RNFL	0.09 (0.02)	0.88 (0.25)	1.27 (0.48)	1.66 (0.14)	2.71 (0.04)
RBC	0.33 (0.42)	0.79 (0.05)	0.85 (0.08)	0.95 (0.09)	1.31 (0.23)

(see Table 5.5). Though errors are worsening with decreasing the resolution of the image, still error is low compared to the state-of-the-art methods (see Table 5.3 and 5.5).
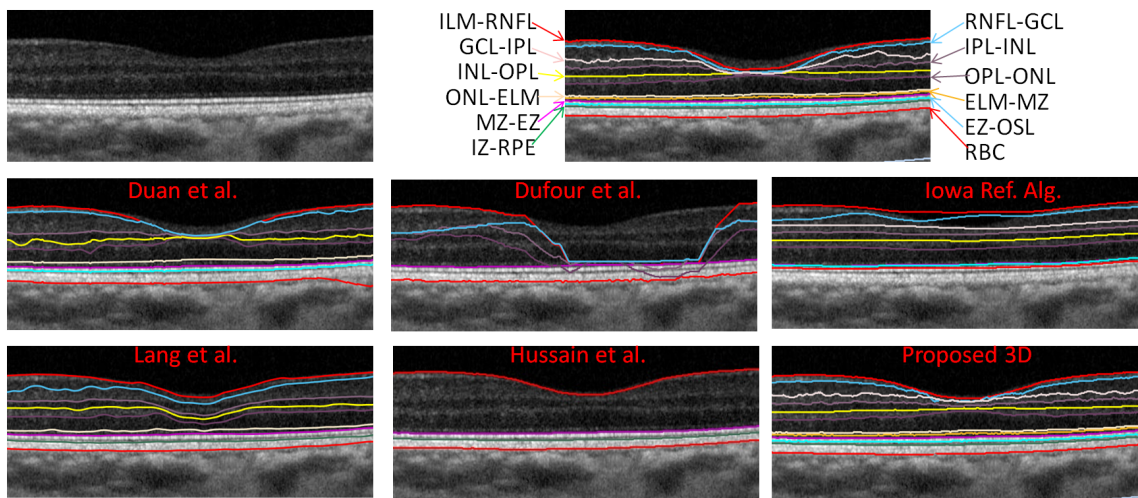
Figure 5.4: Segmentation result by state-of-the-art and our proposed 3D automatic methods on normal subject.
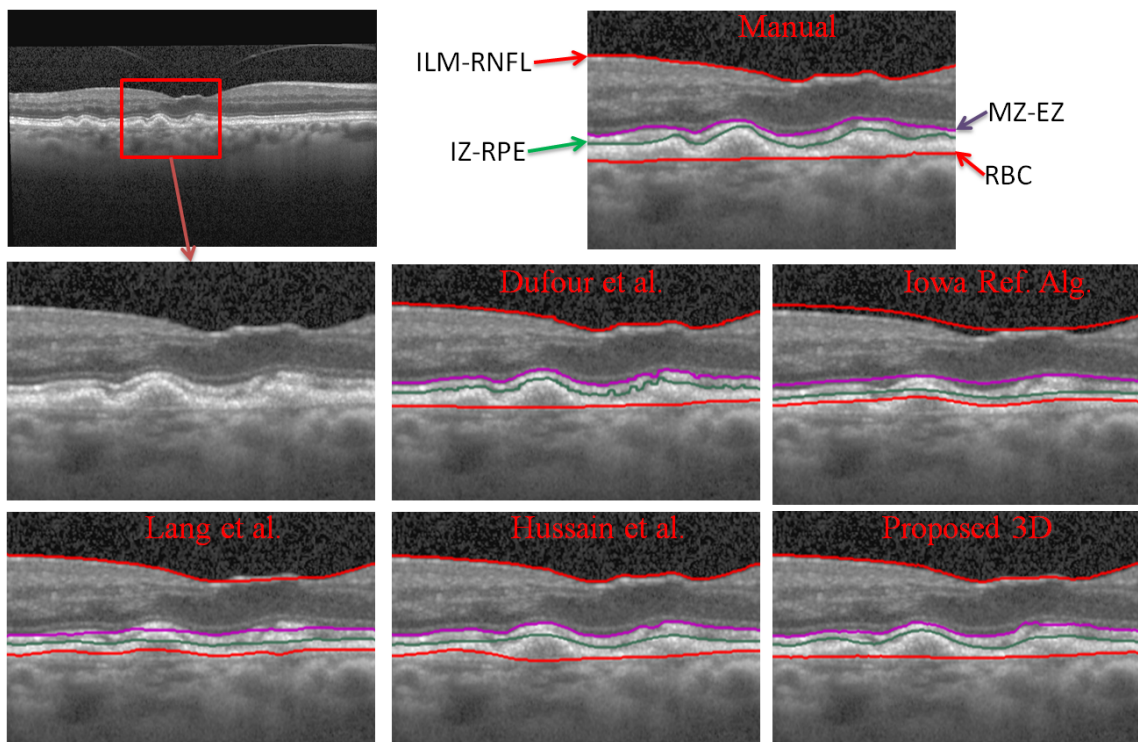
Figure 5.5: Segmentation result by state-of-the-art and our proposed 3D automatic methods on a subject with AMD.
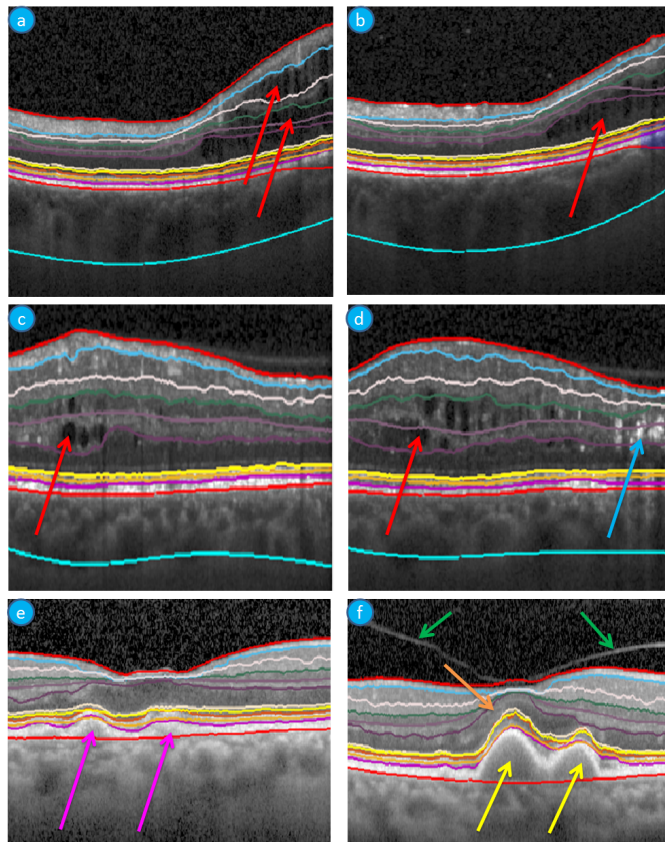
Figure 5.6: Some examples of detection in the presence of different pathologies using our proposed method. The CSI is not detected in (e) and (f) due to not captured properly. (a) and (b) In the presence of large Cyst (red arrow signs) of DME patient (c) In the presence of small Cyst (red arrow signs) of DME patient;; (d) In the presence of small Cyst (red arrow sign) and lesion at the inner retina (blue arrow signs) of DME patient; (e) and (f) In the presence of vitreomacular traction (green arrow sign), drusen (pink arrow sign) and RPE detachment (yellow arrow sign) of AMD patients. In some places of the image (f) have lost the ONL layer properties (orange arrow sign) as well. (a, b, c, and d) Images are collected from a public dataset (DUKE university) [1].

5.6   Novelty of the proposed 3D segmentation algorithm

In this section, we discuss the reasons why our proposed method performs well in detecting the boundaries. Its main advantages are its robustness in the presence of pathologies and high accuracy. The novelty of the proposed 2D segmentation methods of detecting retinal layers and CSI are described in Chapter 3 and 4 respectively. Our 3D segmentation algorithm inherits those 2D segmentation algorithm advantages. In addition, our proposed 3D segmentation algorithm has more novelty. They are described below.
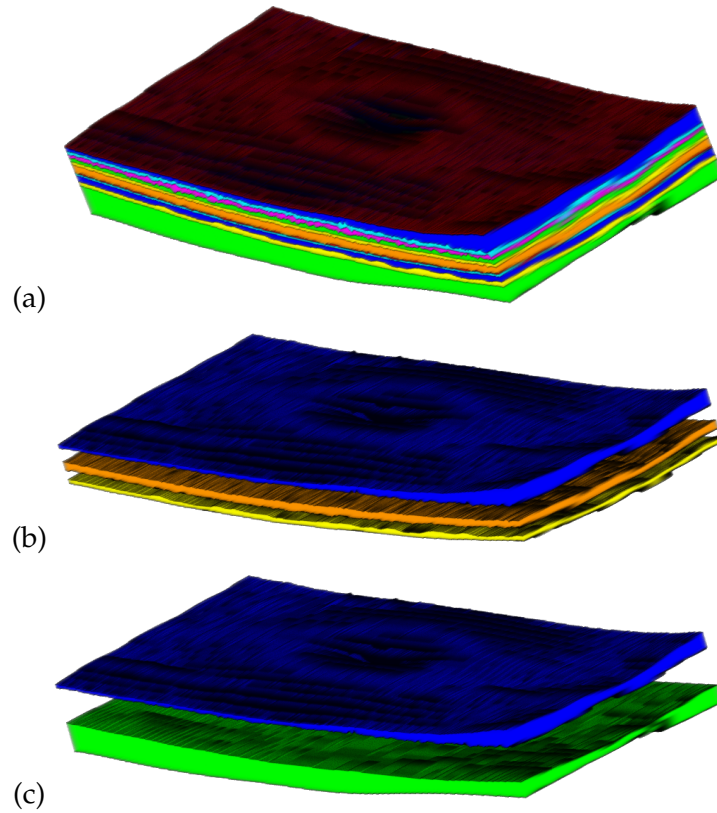
Figure 5.7: A pictorial example of our proposed method segmentation. (a) 3D render of a volume; (b) A 3D render image of RNFL (blue), ONL (magenta) and RPE (yellow) Layers; and (c) A 3D render image of RNFL (blue), and Choroid (green).

- Targeting first high contrast boundaries to low contrast boundaries. For example, our first target is ILM-RNFL, one of the high contrast boundaries of the retinal layer, and last target is GCL-IPL, one of the low contrast boundaries. The identified high contrast boundaries are used to reduce the region of interest (ROI) for the low contrast boundaries. This increases the accuracy as well as the efficiency of the proposed method.

- One of the novelties of 3D segmentation algorithm is in using the stable reference boundary. It provides an accurate reference boundary for reducing the ROI at the adjacent B-scans for detecting the boundaries to the full volume of the OCT images. The use of a stable reference boundary in 3D segmentation is one of the significant operations that increases efficiency by reducing the ROI for detecting the

boundaries more than does our 2D Segmentation algorithm. For this reason, 3D segmentation algorithm is more efficient than the 2D segmentation algorithm. At the same time, this operation selects precise ROI in the adjacent B-scans. As a result, if the B-scans suffer from heavy noises or effect of pathologies, our proposed 3D segmentation method is still able to detect the boundaries accurately.

- The use of stable reference boundary in the edge weight computation as a reference line for slope similarity is another novelty of our 3D segmentation algorithm. This allows the shortest path algorithm to choose the nodes in its shortest path to be that part of the boundary which is nearly parallel to the reference boundary. As a result, boundaries of the current B-scan can be detected as nearly parallel as possible with the boundaries of adjacent B-scans which can handle the effect of non-straight substructures such as macula, optic disc and areas that have pathologies.

5.7   Conclusion

We have proposed an automated, robust and highly accurate method for the detection of the all boundaries of the retinal layers and the Choroid-Sclera Interface (CSI). We have developed 3D segmentation method by extending our previous 2D segmentation methods for efficient segmentation without compromising the accuracy. No other methods has attempted to discover as many boundaries as ours for the retinal layers. The region of interest selection based on adjacent B-scans and robust cost function definition makes our proposed method efficient and accurate than the state-of the-art methods. The utilisation of approximate three reference layers for the detection of retinal layers improves efficiency and accuracy. On the other hand, depth based intensity normalisation helps to find the accurate the CSI robustly. We have shown our method is superior to the state of-the-art methods using RMSE and paired sample t-test. The lower RMSE for the boundaries positions of the retina even in the presence of pathologies indicate the robustness of our method. The mean RMSE for the boundaries of the retinal layers is less than 1 pixels for our proposed method where the state-of-the-art methods have nearly 5 pixels in the normal subjects. The overall RMSE for the pathology existed images is increased for our

proposed method but still much better than state-of-the-art methods. The RMSE for the CSI position of our proposed 3D method is less than 2 pixels where two state-of-the-art methods have more than 30 pixels. This excellent performance of our method on normal and AMD subjects indicates its suitability for identifying and tracking pathology in a longitudinal manner and able to be used in large-scale clinical studies.

Chapter 6

The Optic Nerve Head Detection and Eight Prominent Biomarkers Extraction

This chapter presents a novel method for segmenting the retinal layers in the presence of the Optic Nerve Head (ONH)/macula; detecting the ONH border and the extraction of eight biomarkers of interest to ophthalmologists from Spectral Domain Optical Coherence Tomography (SD-OCT) volume images. This chapter is based on the following publications.

Md Akter Hussain, Alauddin Bhuiyan, Chi D. Luu, Robyn H. Guymer, Hiroshi Ishikawa, Joel S. Schuman and Ramamohanarao Kotagiri. *"Novel Automatic Approach of Computing Eight Biomarkers for Retinal and neuropathy Diseases in Macula and ONH Centred SD-OCT Imaging". (To be submitted)*

Md Akter Hussain, Alauddin Bhuiyan and Ramamohanarao Kotagiri. *"Disc segmentation and BMO-MRW measurement from SD-OCT image using graph search and tracing of three bench mark reference layers of retina." Image Processing (ICIP), 2015 IEEE International Conference on. IEEE, 2015.*

Md Akter Hussain, Alauddin Bhuiyan and Ramamohanarao Kotagiri. *"Automatic Retinal Minimum Distance Band (MDB) Computation from SD-OCT Images." Digital Image Computing: Techniques and Applications (DICTA), 2015 International Conference on. IEEE, 2015.*

6.1   Introduction

Research and development of novel interventions at the early stages of eye diseases, such as Age-related Macular Degeneration (AMD), glaucoma and Diabetic Macular Edema (DME), are currently hampered by the lack of measurable/quantifiable biomarkers of early diseases and their progression [16]. Such biomarkers are required to provide an assessment of disease severity level and to serve as early screening or outcome measures of its progression. As a result, many research studies have been performed and found some biomarkers on different kinds of imaging modalities such as Colour Fundus Photography (CFP) and Optical Coherence Tomography (OCT) [8]. For example, cup-disc ratio and RNFL thickness are useful for glaucoma diagnosis; retina thickness and the reflectivity value of Ellipsoid Zone (EZ) layer are useful for identifying AMD. OCT can obtain the cross-sectional as well as 3-Dimensional (3D) structural information of the retina with microscopic resolution in a non-contact and non-invasive fashion that any other imaging modalities cannot do. The identification of early structural changes in high-resolution OCT and its correlation with functional changes can provide novel biomarkers of early disease [16]. To utilise the strengths of OCT such as 3D volumetric image data, substantial efforts have been made to find more clinically useful biomarkers for the retinal (e.g. AMD and DME) and neuropathy (e.g. glaucoma) diseases. Traditional methods involving human graders (qualitative or manual/semi-automatic quantitative grading) are no longer feasible or cost-effective on large-scale datasets as they are prone to inaccuracy, more grading variability and subjective bias. Automatic grading will allow more accurate, consistent and effective measurements, and consequently give an opportunity to gain new insight into many retinal diseases. Considering this imminent requirement, we propose an automatic approach for extraction of retinal SD-OCT image-based biomarkers which are described in this chapter.

These biomarkers' computation relies on the position, shape and intensity of the layers of the retinal tissues. Therefore, we have proposed an automatic segmentation method for detecting retinal layers and pathologies from the Optic Nerve Head (ONH) and macula-centred OCT images. Fig. 6.1 (a) shows: Scanning Laser Ophthalmoscopy (SLO) of a portion of the macula-centred retina with green lines indicating where OCT

scanning is taking place; (b) a volumetric OCT image rendering of the retina, and (c) which is a B-scan, a slice of the cross-section of the retina along a yellow line on Fig. 6.1 (b). Each column in a B-scan (vertical orange line in Fig. 6.1 (d)) is called A-scan. Ten layers and sub layers of the retina and the layers of the choroid are shown in Fig. 6.1 (d). The centre of the macula, called the fovea, shows a depression in the OCT image as shown in Fig. 6.1 (c) due to the absence of the inner retinal cells [76]. The optic disc, also known as ONH, shows a sharp fall in Fig. 6.1 (f) due to the absence of the retinal tissues. In the optic disc, there is a pink rim with a pale centre containing nerve fibres. This is called the neuro-retinal rim and that pale centre, devoid of neuroretinal tissue, is called the cup. This is shown in the enface image (2D coronal projection of 3D OCT image data) in Fig. 6.1 (e) and (f). The Hyper-Reflective intra-retinal Spots (HRS), and drusen in OCT images are shown in Fig. 6.1 (g) and (h).

Previous OCT-based studies provided some biomarkers such as retinal layer thickness, volumetric quantification of the pathologies (e.g. HRS and drusen) cup-disc ratio, Bruch Membrane Opening Minimum Rim Width (BMO-MRW) and Minimum Distance Band (MDB) [15–18]. The studies reported the association of the biomarkers with specific retinal or eye diseases. For example, a cup-to-disc ratio more than 0.5 is a risk factor for glaucoma [15]. Table 6.1 summarises the association of the biomarkers with DME, AMD and glaucoma.

We have extended our 3D Segmentation (3DS) algorithm to detect boundaries of the retinal layers in the presence of ONH. The graph edge-weight (spatial distance, slope continuity and layers' non-associativity) is modified if there is a presence of ONH. The results show that our proposed method is the better than seven other state-of-the-art methods. We detect the ONH region automatically using the knowledge of a priori anatomical patterns. Three patterns of the ONH are used to locate the ONH correctly. We have also proposed a method for detecting the drusen in the OCT volumes using the abnormal thickness of a composite layer called Hyper-Reflective Complex (HRC) constructed from MZ-EZ boundary to RBC [112]. This detection of drusen allows quantifying the volume and visualising drusen in 3D. In this chapter, we have also demonstrated novel techniques for computing eight biomarkers introduced by the researchers and which are
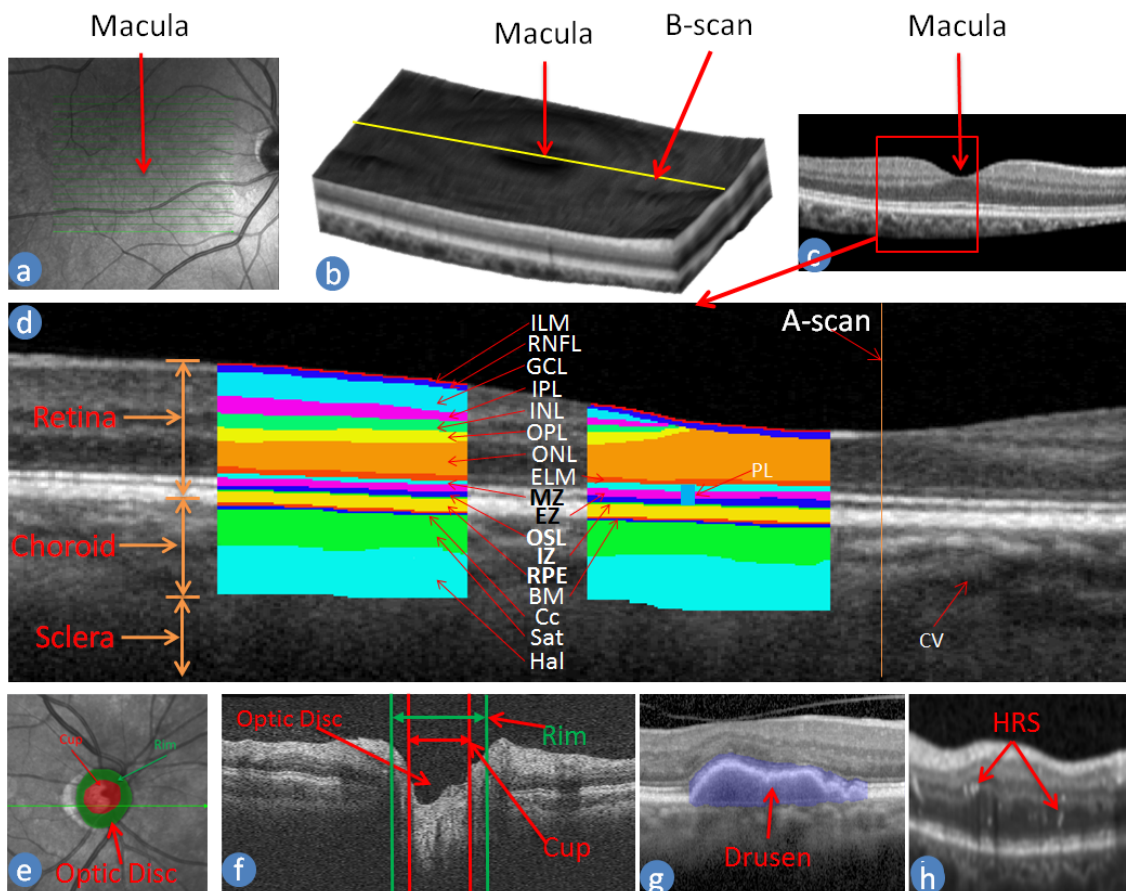
Figure 6.1: Macula centred retinal image. (a) SLO image; (b) A 3D or volume of the retina from OCT image; (c) A B-scan image (cross-section of the retina through the green and yellow lines in Fig. (a) and (b) respectively) and (d) Retinal Layers are delineated in a B-scan image (e) Optic disc centred Enface image (Cup: red area; Rim: green area) (f) A B-scan of Optic Disc centred Retina (g) A B-scan showing drusen (blue) (h) A B-scan showing Hyper-Reflective intra-retinal Spots (HRS) (pointed by red arrow).

relevant in DME, AMD and glaucoma. To the best of our knowledge, this is the first time a report presents a framework for computing these biomarkers automatically in the presence of pathology.

The contributions of the chapter can be summarised as follows.

1. The reflectivity value of the EZ layer is attempted by computing automatically for the first time.

2. The first automatic method of detecting HRS.

Table 6.1: The association of the biomarkers with DME, AMD and glaucoma.

Biomarkers	Threshold level & Disease Correlation
Biomarker 1: Layer Thickness	Retinal Nerve Fiber Layer (RNFL), Ganglion Cell Layer (GCL) and Inner Plexiform Layer (IPL) layers were significantly thinner in glaucoma eye, approximately 20% less width than age-matched normal eyes ($p < 0.001$) [17]. Mean retinal thickness was reduced significantly in early AMD patients, approximately $10\%(p = 0.008)$ than age-matched normal eyes [19].
Biomarker 2: Quantification value of the HRS	The presence of HRS is a characteristic finding various stages of DME and is a key risk factor for the development of more advanced stages of DME [2, 18].
Biomarker 3: Quantification value of drusen	The presence of macular large drusen ($> 125\mu$m) is a characteristic finding of early stages of AMD and is a key risk factor for the development of more advanced stages [20].
Biomarker 4: Cup-disc ratio	Cup-disc ratio more than 0.5 is a risk sign of glaucoma [15].
Biomarker 5: BMO - Minimum Rim Width (BMO-MRW)	The visual sensitivity of Glaucoma patients is significantly correlated to the BMO-MRW ($r = 0.32, p < 0.001$), which has higher correlation than RNFL Thickness [21]. BMO-MRW in normal patients is $307 \pm 84.3\mu m$ whereas early glaucoma patients have $211 \pm 60.5\mu m$ [22].
Biomarker 6: Minimum distance Band (MDB)	The correlation coefficient between the MDB and cup-disc ratio are -0.88 and -0.56 for MDB value and area respectively with $p < 0.05$ which means MDB is highly correlated to glaucoma like cup disc ratio [12].
Biomarker 7: Attenuation Coefficient of the RNFL	The severity label of the glaucoma increases with decreasing the RNFL's attenuation coefficient [23]. Schoot et al. [23] found that a significant structure-function relationship between the attenuation coefficient and the visual field's mean defect.
Biomarker 8: Reflectivity value of EZ layer	Early AMD patients have an average value of 1.73 and the control patients have an average value of 2.27 [16].

3. Fully automated retinal segmentation that works on both macular and ONH-centred OCT volumes seamlessly.

4. Fully automated system which computes eight biomarkers.

The rest of the chapter is organised as follows. In Section 6.2, we describe the proposed method and performance of the ONH border and layer detection in the ONH-centred image. Section 6.3 describes the extraction of eight biomarkers including the segmentation method of HRS and drusen, and performance measurements of the proposed method. Finally, Section 6.4 concludes the chapter.

6.2   The ONH segmentation and Layers detection in the presence of ONH

The ONH region is very different from other regions of the retina (Fig. 6.1 (e) vs. (c) and (f)). There are no retinal tissue layers in the ONH region and consequently there is a sharp fall (valley) in the ILM (Fig. 6.1 (e)). The presence of the different sizes of the vessels makes an unpredictable pattern of the ONH region. These properties make it difficult to segment ONH. A number of methods have been proposed for the ONH and layer segmentation in the presence of the ONH from SD-OCT images. Among the prominent techniques adaptive threshold techniques, graph search such as the shortest path finding, and machine-learning approaches such as K-NN classifier, have been used to detect the ONH [82, 148]. Some methods also utilise CFP by registering them with OCT for detecting ONH [82]. The literature reviews of the ONH detection are presented in Chapter 2 (Section 2.7.5). Our proposed method is based on the graph shortest path finding for detecting the ILM layer from where we have detected the ONH by finding inconsistencies in the RNFL, ONL and RPE layers; and intensity distribution in the enface image of the SD-OCT B-scans of the retina.

6.2.1   Proposed segmentation method

Our proposed ONH and layer detection method works in three steps: 1) ILM-RNFL boundary detection; 2) ONH detection, and 3) detection of other boundaries of the reti-

nal layers. The ILM-RNFL boundary and three patterns (such as the absence of layers, dissimilar layer positions, and intensity pattern) of the ONH in the SD-OCT image are utilised to detect the ONH. The other boundaries of the retinal layers are then detected without changing the original method (explained in Chapter 5) but applying the method separately in each part of the retina - divided by the ONH region. We described the boundaries of the retinal layers detection in Chapter 5. In this chapter, we describe the detection method of the ILM-RNFL boundary in the presence of ONH region and the ONH.

6.2.1.1   ILM-RNFL boundary detection in the presence of the ONH

We use the approximate positions of the three reference layers along A-scans for defining some A-scans as inconsistent positions of the layers where the differences between two layers are three standard deviations away from the mean of their position. These inconsistent A-scans are used to define the potential area of the ONH. Otherwise, if a ILM-RNFL boundary in the adjacent B-scans is detected, then A-scans having ILM-RNFL boundary position less than 200 μm (half of the maximum retinal thickness) of its 1st order polynomial line are defined as a potential ONH region. The edge pixels in this potential ONH region are detected by applying a high smoothing parameter ($SD = 3$) in a canny edge detection algorithm. The spatial distance weight ($\phi_{(a,b)}$) in the graph edge weight is modified for this region using 6.1 where $\phi^o_{(a,b)}$ is the original computation in 5 and $\phi^m_{(a,b)}$ is computed with $\alpha_1 = 1, \alpha_2 = 1$ and $\alpha_3 = 0$. Other weight parameters of the graph edge weight remain the same. Fig. 6.2 shows an example of the procedure for detecting the ILM-RNFL boundary.

$$\phi_{(a,b)} = 0.3 \times \phi^o_{(a,b)} + 0.7 \times \phi^m_{(a,b)}, \tag{6.1}$$

6.2.1.2   ONH detection

After detecting the ILM-RNFL boundary of the volume, the ONH is detected at the OCT image volumes using three patterns of the ONH. The patterns are: the absence of the
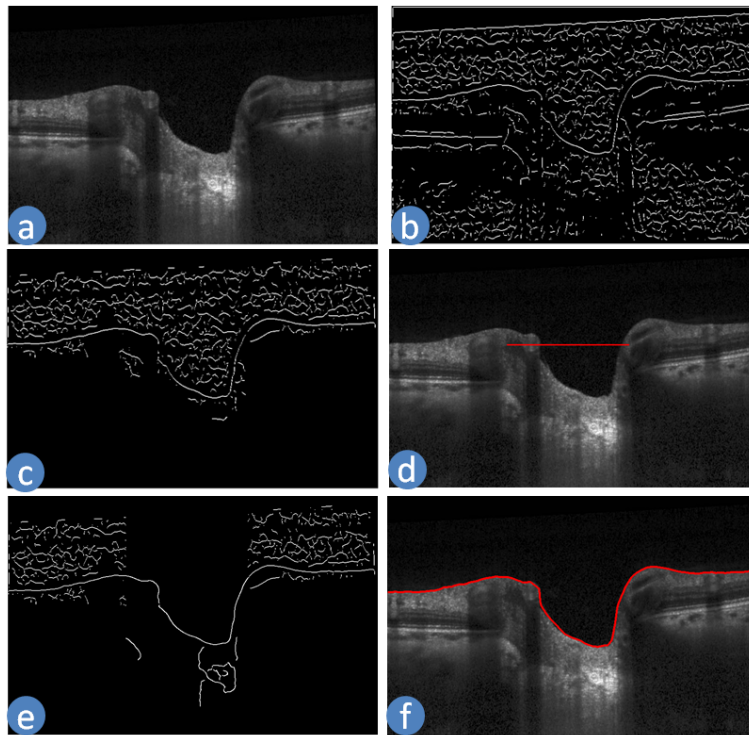
Figure 6.2: ILM-RNFL boundary detection in the presence of ONH. (a) an ONH-centred B-scan; (b) positive gradient edge pixels; (c) Candidate pixels for the ILM-RNFL boundary; (d) potential ONH region (red colour A-scans); (e) modified candidate pixels in the potential ONH region after applying more smoothing operations during edge detection; (f) The ILM-RNFL boundary at the ONH-centred SD-OCT B-scans the red line.

retinal layers; dissimilar layer positions, and dissimilar intensity pattern at the ONH region with respect to the other areas of the retina. Fig. 6.3 shows the effect of processing steps of the ONH detection in an OCT image. Fig. 6.3 (a) is the enface image of a portion of the retina with ONH centre. Fig. 6.3 (b) is an OCT B-scan with ILM-RNFL boundary delineated of the cross-section of the retina across the green line on the enface image.

The first pattern, the absence of the retinal layers, is found by the sharp fall of the ILM-RNFL boundary. A-scans where the ILM-RNFL boundary position is less than $200\mu m$ of the 1st order polynomial line of the ILM-RNFL boundary along A-scans, and is considered as a potential ONH region (Fig. 6.3 (d), green). If a B-scan has potential ONH region then the other two patterns are applied to detect the exact position of the ONH.

The second pattern, dissimilar layer positions, is detected by finding the abrupt positions of the approximate ONL and RPE layers positions. There is no layers in ONH
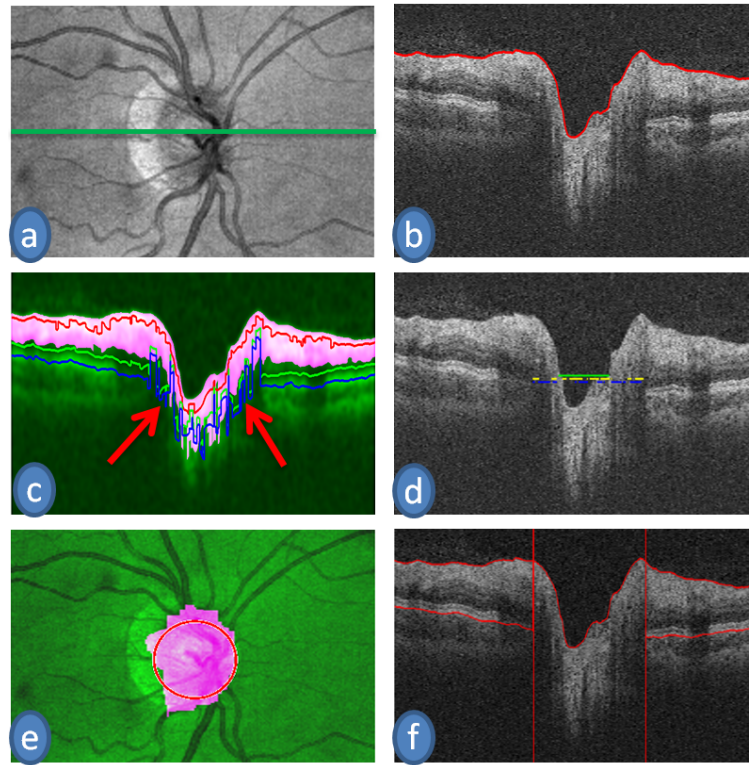
Figure 6.3: ONH detection. (a) Enface image of a portion of the ONH centred retina; (b) A cross section of the retina (B-scan, along green line in (a)) with delineating ILM-RNFL (red line); (c) Approximate RNFL layer (pink)and approximate three layers positions (RNFL: red line, ONL: green line, RPE: blue line) (d) Potential ONH regions: green line for distance between polynomial line and ILM-RNFL boundary, yellow line for the pattern of the unlike position of the approximate ONL and RPE, blue line for the intensity disorder between the approximate ONL and RPE; (e) Detected initial positions of the ONH (pink) and the best circle (red) fit; (f) ONH boundary(red vertical line), ILM-RNFL (top continuous red line) and BM boundary (bottom red lines at the left and right of the ONH).

region other than the ganglion cells and hence finding approximate ONL, and RPE layers positions gives a noisy output at the ONH region as shown in Fig. 6.3 (c - red arrow signed regions). The A-scans where the approximate ONL and RPE layers' position are located at the RNFL layer are considered as abrupt positions and added to the potential ONH region, the yellow positions in Fig. 6.3 (d). The RNFL layer is detected approximately at this stage (the area of pink in Fig. 6.3 (c)) using the intensity greater than a threshold value, computed using (2).

$$th_{aprxRNFL} = \mu\left(Bscan(b_1, b_2)\right), \qquad\qquad (6.2)$$

Where $th_{aprxRNFL}$ is the threshold value for computing approximate RNFL, b_1 and b_2 are two boundaries (b_1 is the ILM-RNFL and b_2 is the $5\mu m$ below of ILM-RNFL), Bscan(b_1, b_2) gives the area of the current B-scan inside of the b_1 and b_2; and $\mu(x)$ gives the mean value of the x.

The third pattern, dissimilar intensity pattern, is detected using the ratio of the intensities of the approximate ONL and RPE layer- positions. Generally, the intensities of the ONL and RPE layers should be more than 50%, but at the ONH region these are not consistent due to absence of those layers. We use this inconsistency for detecting the A-scans in potential ONH. If the ratio is less than 10% they are added to the potential ONH region as shown in Fig. 6.3 (d) in blue. After determining the potential locations of ONH for all B-scans of a volume, as shown in Fig. 6.3 (e) in pink on the enface image, we find the largest and the best-fitted circle using Hough transformation, as shown in Fig. 6.3 (e), in red, and defined as the ONH region. Fig. 6.3 (f) shows the ONH position in the B-scan (red vertical line) with delineating ILM-RNFL (red horizontal continuous line in the top) and BM (two separated red horizontal lines in the bottom).

6.2.2   Results on ONH boundary detection

Dataset: We have used two macula-centred SD-OCT volumes of AMD patients with $512 \times 1024 \times 49$ voxels per volume (total 98 B-scans) for the evaluation process. We have also used one ONH-centred SD-OCT volume scan from a glaucoma patient with $512 \times 1024 \times 200$ voxels (total 200 B-scans). The third dataset is collected from [1] of one macula-centred SD-OCT volumes of DME patients with $496 \times 512 \times 97$ voxels (total 97 B-scans). A grader has manually detected all the boundaries of the retinal layers, and drusen from two AMD patients that serve as a gold standard. The same grader has also manually detected ONH, ILM-RNFL, IZ-RPE and RBC boundaries for the glaucoma patient that also serves as a gold standard. The same grader has also manually marked the HRS from DME patients and these also serve as a gold standard for measuring the accu-

racy of the automatic method for HRS detection. We have named the dataset as AMD, glaucoma and DME dataset in the remainder of this chapter.

We have used a glaucoma dataset for evaluating the accuracy of the boundaries of the layer and ONH detection. As this dataset has only ILM-RNFL, IZ-RPE and RBC boundaries as provided by the grader, we have computed accuracy for them only and found the means of Root Mean Square Error (RMSE) of the boundary positions are $0, 0.21$ and 0.11 pixels respectively with a standard deviation 0. No other methods can automatically detect the ONH-centred OCT volumes to segment the boundaries. For computing the ONH boundary accuracy, we have created an enface image from the manual and automatic segmentation of the OCT images. We have found sensitivity is 0.97, Specificity 0.99, Precision 0.99, Recall 0.97, Accuracy 0.99, and F1-score 0.98. We have also computed the thickness accuracy of the layers over AMD dataset which was discussed earlier. Fig. 6.4 shows three B-scans by delineating boundaries of the retinal layers with automatic segmentation of our proposed method. In the glaucoma patients image (Fig. 6.4 (c)), there are undetectable layers such as ONL-ELM and for this reason, they are not shown in the image. The vertical line shows the boundary of the ONH.
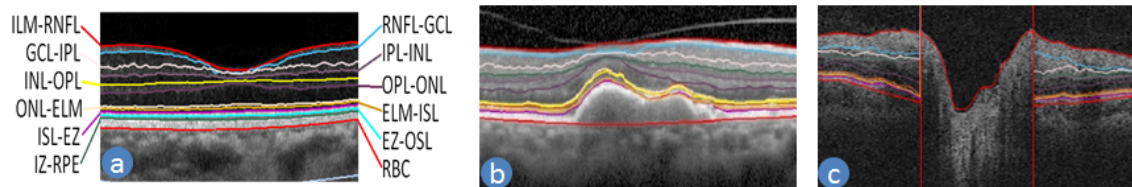
Figure 6.4: Automated segmentation output. Segmented (a) macula centred normal subject, (b) AMD subject in the presence of drusen and (c) ONH centred glaucoma subjects.

6.3 Extracting the biomarkers from OCT image

Ophthalmologists have found some biomarkers from the OCT images for early diagnosis and progression of the ocular diseases such as DME, AMD and glaucoma. However, it is still necessary to find new biomarkers to improve the accuracy of early detection and prediction of retinal diseases [16]. In this chapter, we focus on showing the extraction of eight OCT-based biomarkers defined by the ophthalmology researchers. In the following

sections we will discuss these biomarkers along with their computation methods.

6.3.1   Biomarker-1: Layer Thickness

The thicknesses of the retinal layers are potentially an important biomarker of interest to ophthalmologists for retinal and other diseases such as diabetes, AMD, glaucoma, CNS diseases and cardiovascular diseases. The significance of the layer thickness can be summarised as follows.

- The visual sensitivity is significantly correlated to the RNFL layer thickness ($r = 0.23, P < 0.001$) and RNFL layer volume ($r = 0.21, P < 0.001$) [21].

- It has been estimated that up to 40% of the nerve fibre layer can be destroyed before significant vision loss occurs from glaucoma [93].

- The RNFL, GCL and IPL layers were significantly ($p < 0.001$) thinner in glaucoma eye approximately 20% than normal eyes [17].

- Mean retinal thickness was reduced significantly ($p = 0.008$) in the group of participants with early AMD compared with the control group approximately 10% at multiple locations within $2.0mm$ of the fovea [19].

6.3.1.1   Detection process and Evaluation of Biomarker-1

We have computed the distance between two boundaries of the corresponding layers as the thicknesses of the corresponding retinal layers. Four state-of-the-art methods (three of them are publicly available [114, 119, 150] and other one is collected from the author on request [116]) are used to compare the proposed method performance. The result shows that our proposed method has significantly lower error than any other state-of-the-art methods. The mean percentages of absolute difference error of the layer thickness is reported in Table 6.2. The errors also indicate it is reliable for disease progression and diagnosis due to low error than the distortion in the layer thickness for the diseases. Fig. 6.5 shows the manual and automatic retinal thickness.
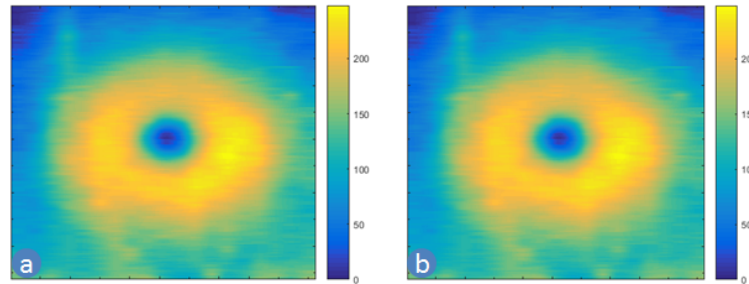
Figure 6.5: Quantification output of layer thickness (Biomarker-1). (a) Manual and (b) automatic thickness map of the macula centred retina from a subject of the AMD dataset.

Table 6.2: The mean percentage of absolute error between manual and automatic detection of layers thickness (Biomarker-1).

Layer	Dufour et al. [114]	Iowa Ref. [119]	AURA tools [150]	Duan et al. [116]	Proposed
RNFL	9.79	10.84	7.14	56.76	2.75
GCL		17.82			2.76
IPL		18.35			3.10
INL		20.21	11.50	120.01	4.92
OPL		24.90	13.83	16.07	7.67
ONL			12.20	10.89	5.74
ELM					25.66
ISL					14.26
EZ		17.87		20.49	16.34
OSL		31.41			21.94
RPE		21.94	11.32		11.65

6.3.2 Biomarker-2: Hyper-Reflective intra-retinal Spots (HRS) segmentation & quantification

The appearance of the Hyper-Reflective intra-retinal Spots (HRS) is a sign of diabetic retinopathy [2]. These HRSs are located in the inner retina, mostly between the INL and ONL layers [2, 18]. Although a number of automatic methods exist for detecting these HRSs from the CFP images [7, 68], to the best of our knowledge there is no automatic method available from the retinal SD-OCT images. Fig. 6.6 shows the examples of HRS appearance in the SD-OCT images and segmented manually, using our automated method.
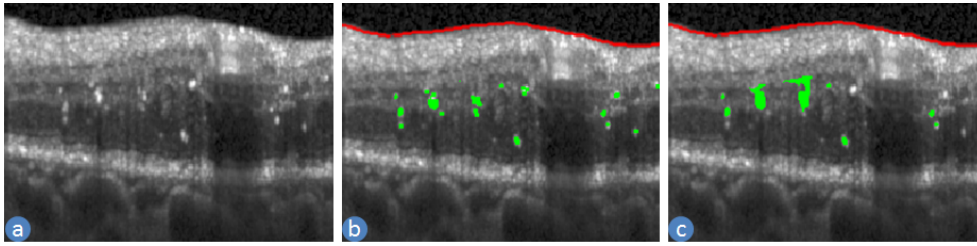
Figure 6.6: Hyper-Reflective intra-retinal Spots (HRS) in the retinal SD-OCT (Biomarker-2). (a) SD-OCT B-scan (b) manual ILM-RNFL boundary (red line) and HRSs (green) (c) automatically detected ILM-RNFL boundary (red line) and HRSs (green).

6.3.2.1   Detection process and Evaluation of Biomarker-2

HRSs are brighter and located in the inner retina, mostly between the INL and ONL layers [18] as shown in Fig. 6.7. Since we have segmented layers, ROI for detecting the HRSs are limited to the area between the INL and the ONL layers. In general, these layers are darker than RNFL and RPE layers. So, the pixels which are between the INL and ONL layers have intensity values more than the mean intensity of the RNFL and RPE layers. The pixels are defined as HRS pixels.

We have used the DME dataset for evaluating the accuracy of the HRS detection between manual and automatic methods. Fig. 6.6 shows the automatic and manual detections of the HRS in a B-scan. We have achieved sensitivity 0.82, Specificity 0.99, Precision 0.77, Recall 0.82, Accuracy 0.99 and F1-score 0.79.

6.3.3   Biomarker-3: Drusen segmentation & quantification

Drusen are the accumulation of extracellular material (proteins and lipids) between the RPE and BM layers: see Fig. 6.1 (g) and 9. The morphological features such as distinctness, individual size, total area, volume and number of drusen are used as important biomarkers of early AMD and signify a risk of progression. The presence of macular large (greater than 125 μm) drusen is a characteristic finding of early intermediate AMD and is a key risk factor for the development of more advanced dry AMD [20]. For decades, CFP has been used to image the in vivo drusen as gold standard. Due to 3D information such as volumes, depth position of the drusen motivated ophthalmic practitioners are using OCT imaging to find new biomarkers of risk of diagnosis and progression of

diseases [130]. Drusen detection in CFP and SD-OCT images has good agreement, and each imaging modality has its own advantages [132]. Most of the OCT imaging-based drusen detection methods used polynomial line fitting on RPE or finding the abnormality in thickness of the RPE. The recent methods of detecting drusen have been reported in Chapter 2 (Section 2.7.6).

6.3.3.1   Detection process and Evaluation of Biomarker-3

Drusen detection is done by prior MZ-EZ to RBC thickness knowledge which should be around 20 μm. If there are regions where the thickness of the ISL-EZ to RBC is 50% more than the 20 μm then this region is regarded as the seed points of the drusen. Then the region with 5% more than 20 μm and connected with those seed points are included as drusen.
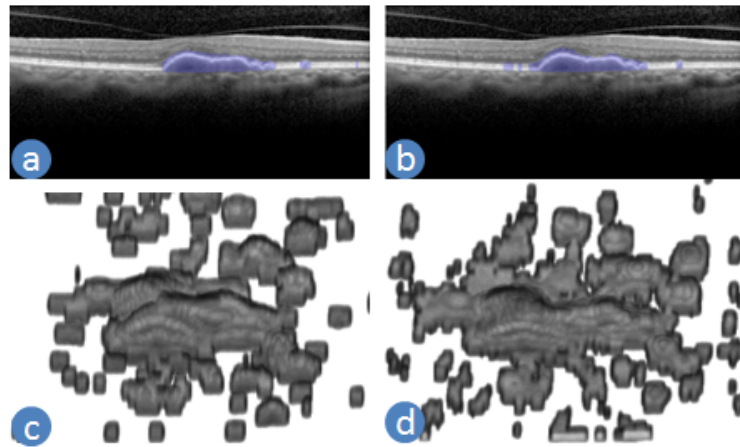
Figure 6.7: 2D and 3D drusen visualisation (Biomarker-3). (a) Manual and (b) automatic detection of drusen, blue in the B-scan (top) and 3D view of drusen (bottom).

We have used an AMD dataset for evaluating the accuracy of drusen detection between manual and automatic measures. Fig. 6.7 shows the automatic and manual detection of drusen in a B-scan and a 3D view of the drusen. We have achieved sensitivity 0.70, Specificity 0.99, Precision 0.70, Recall 0.70, Accuracy 0.99 and F1-score 0.70.

6.3.4   Biomarker-4: Cup-Disc ratio

The ratio between optic disc cup and neuroretinal rim surfaces is called the cup-disc ratio [6]. It is a very important structural indicator for assessing the presence and progression of glaucoma. If this ratio increases by more than 0.5, it is a risk sign for glaucoma. Increasing cup means decreasing the nerve fibre tissues in the rim area and worsening glaucoma.

In an OCT image, the terminal point of the BM, called BM Opening (BMO) gives the boundary of the disc that is also rim and the intersection points of the 120 μm top to the BM plane, and ILM-RNFL gives the boundary of the cup [6]. Fig. 6.1 (e) and 6.8 show cup and disc in an enface image and B-scan of the OCT image respectively. To quantify the ratio, glaucoma specialists generally used CFP of the optic disc. In OCT images, there is also a good correlation with the fundus image [68].

There are many automatic methods for detecting the optic disc or ONH from OCT images. Only a few extend their work towards cup detection and cup-disc ratio computation. The first work found by Boyer et al. [90] who shows the correlation coefficient between manual and their algorithm are 0.8 for cup diameter and 0.9 for disc diameter. Abramoff et al. [68] detects ONH using graph search and computes the cup-disc ratio with 0.93 correlation coefficient between manual and automatic detection. Hu et al. [148] found 0.85 correlation coefficient. Lee et al. [81] used K-NN classifier for a cup and disc detection and found an unsigned error for the optic disc cup of $0.076 \pm 0.026mm$ and the neuroretinal rim of $0.061 \pm 0.026mm$.

6.3.4.1   Detection process and Evaluation of Biomarker-4

We have developed the ONH detection method as described earlier. The cup detection is a simple mathematical calculation using the position of the ILM-RNFL, RBC and ONH boundaries. A reference line in parallel to the BM line is set at the height of 120 μm, and the intersection points between the ILM-RNFL and reference line define the boundary of the cup.

The glaucoma dataset is used to evaluate the accuracy of the cup-disc ratio. A cup
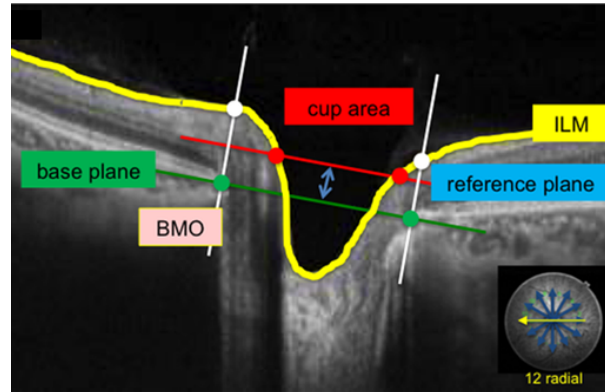
Figure 6.8: Cup and Rim in a SD-OCT B-scan [6]. BMO points (green dots) indicate the disc area. The reference plane (red line) was set above the base plane (BMO plane, green line) at a height 120 μm. Intersections of the ILM-RNFL and the reference plane indicated the cup area (green dot).

is detected using the formula described earlier for both of the automatic and manual detection. We have found manual cup-disc ratio is 0.1453 and automatic 0.1406 where the difference of error is 0.005. The accuracy of the disc as earlier reported is the same for the rim as the disc border is the rim border. The Sensitivity of the cup detection is 0.95, Specificity 0.99, Precision 0.99, Recall 0.95, Accuracy 0.99, and F1-score 0.97.

6.3.5 Biomarker-5: Bruch's Membrane Opening Minimum Rim Width (BMO-MRW)

Fig. 6.9 shows an example of a retinal B-scan with delineating BMO-MRW. It is an optic disc parameter and associated with glaucoma. The minimum distance between BMO and ILM-RNFL is called the BMO-Minimum Rim Width (BMO-MRW) [21]. It represents a geometrically accurate estimate of rim width. This biomarker detection is possible only in ONH-centred OCT images. The visual sensitivity of glaucoma patients is significantly correlated to the BMO-MRW ($r = 0.32, p < 0.001$), which is a higher correlation then RNFL Thickness [21]. The BMO-MRW in normal patients is $307 \pm 84.3 \mu m$ whereas early glaucoma has $211 \pm 60.5 \mu m$ [22].

OCT imaging allows the extraction of this biomarker. Our study found only Antony et al. [119] computes this parameter automatically and reported that their measurements were not significantly different from the manual computation.
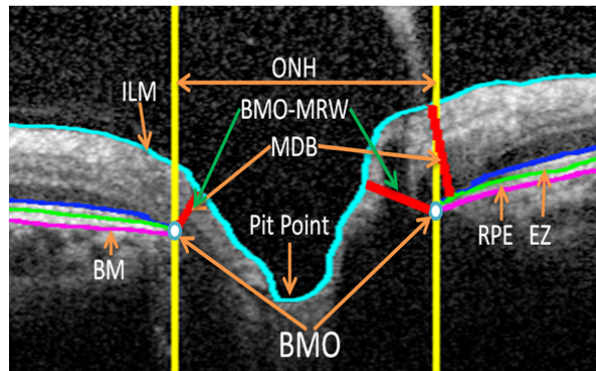
Figure 6.9: A retinal B-scan in optic disc region with BMO-MRW and MDB.

6.3.5.1   Detection process and Evaluation of Biomarker-5

The BMO-MRW is computed by the minimum arithmetic distance between BMO and ILM-RNFL.

We have used a glaucoma dataset for computing performance and have found the mean $\pm$ standard deviation of the absolute difference was 2.3 ± 5.1 pixels.

6.3.6   Biomarker-6: Minimum Distance Band (MDB)

The MDB is the circular band and a quantitative OCT-based metric of neuro-retinal rim tissue [12]. It is computed by the minimum distance between the ONH surface and RPE layers. MDB is a biomarker for glaucoma and can compute only in ONH-centred OCT images. MDB is inversely proportional to the cup-disc ratio. Fig. 6.9 shows an ONH-centred retinal B-scan with delineating the MDB. The correlation coefficient between the MDB and cup-disc ratio are -0.88 and -0.56 for MDB value and area respectively with $p < 0.05$ which means MDB is highly correlated to the glaucoma-like cup-disc ratio [12]. To the best of our knowledge, only we are the first computed MDB automatically.

6.3.6.1   Detection process and Evaluation of Biomarker-6

MDB is computed by the minimum distance between the top boundary of the RPE and ILM-RNFL boundary in the ONH region which serve as the surface of the ONH.

We have used a glaucoma dataset for computing performance and found the mean $\pm$

standard deviation of the absolute difference was 2.1 ± 4.6 pixels.

6.3.7 Biomarker-7: Attenuation coefficient of the RNFL

The strength of the OCT signal provides information about the retinal layers. This strength of the signal is not only related to the scattering properties of the tissue but also depends on many other factors such as media opacities, strength of the incident light beam and the intermediate tissue before reaching the deeper tissues. As a consequence, the OCT signal needs to be further analysed by taking these factors into account to reduce artefacts and errors in accuracy and precision. Ignoring these factors shows a difference between the signal strength of healthy and glaucomatous RNFL tissue. Schoot et al. [23] found by increasing the severity label of glaucoma, RNFL's attenuation coefficient is decreased and a significant structure-function relationship between the attenuation coefficient and the visual field's mean defect.

Schoot et al. suggested the attenuation coefficient of the RNFL from the RNFL and the RPE signal of OCT, which latter is not affected by the aforementioned factors and represents a tissue property, can be quantitatively analysed. The attenuation coefficient is computed for each A-scan by using the following formula [23].

$$\mu_{RNFL} = \frac{log\left(\frac{R}{\beta} + 1\right)}{2d} \tag{6.3}$$

Where R denotes the ratio of the integrated OCT signal of the RNFL over the integrated OCT signal of the RPE, d denotes the thickness of the RNFL, and β is a constant and estimate value is 2.3.

Vermeer et al. [5] are the only research article where attenuation coefficient of the RNFL layer has been computed. They detect RNFL and RPE using Support vector machine with eight features constructed by the intensity and gradient distribution. They have shown that the attenuation coefficients for glaucomatous eyes were much lower and showed local defects. Normal and glaucomatous average RNFL attenuation coefficients were highly significantly different ($p < 0.0001$) and fully separable.

6.3.7.1   Detection process and Evaluation of Biomarker-7

We have computed the attenuation coefficient of the RNFL layer using its definition along each A-scan.

We have computed the attenuation coefficient of the RNFL layer for each A-scan. For the purpose of comparison, we have computed the unsigned difference of the attenuation coefficient for each A-scan between manually segmented layers and automatically segmented layers. We have used the SD-OCT volumes of AMD patients for evaluation purposes and found the mean unsigned difference of the attenuation coefficient is 0.0008.

6.3.8   Biomarker-8: Reflectivity of The EZ layer

The ratio between the peak intensity of the EZ and ELM is defined as the relative intensity or reflectivity value of the EZ layer [16]. There have been reports of correlations between the intensity of the second reflective band and early AMD. The control patients had an average of 2.27 reflectivity value for the EZ layer whereas early AMD patients had an average of 1.73. This value also reduces with age [16]. To the best of our knowledge, we are the first to compute the reflectivity value of the EZ layer automatically.

6.3.8.1   Detection process and Evaluation of Biomarker-8

The ratios between the peak intensity of the EZ and ELM along each A-scan are computed as the reflectivity value of the EZ layer.

We have computed the attenuation coefficient of the RNFL layer for each A-scan. For a comparison, we have computed the unsigned difference of the attenuation coefficient for each A-scan between manually segmented layers and automatically segmented layers. We have used the SD-OCT volumes of AMD patients for evaluation purposes and found the mean unsigned difference of the attenuation coefficient is 0.06.

Table 6.3: The summary of performance evaluation of the Biomarker 2 to 7.

Biomarker	Manual Vs Automatic quantification
Biomarker-2: Quantification value of HRS	Sensitivity = 0.82, Specificity = 0.99, Precision = 0.77, Recall = 0.82, Accuracy = 0.99, and F1-score = 0.79
Biomarker-3: Quantification value of Drusen	Sensitivity = 0.70, Specificity = 0.99, Precision = 0.70, Recall = 0.70, Accuracy = 0.99, and F1-score = 0.70
Biomarker-4: Cup-Disc ratio	Manual cup-disc ratio is 0.1453 and automatic 0.1406 where the difference of error is 0.005.
Biomarker-5: BMO-MRW	Mean $\pm$ standard deviation of the absolute difference was 2.3 $\pm$5.1 pixels.
Biomarker-6: Minimum Distance Band (MDB)	Mean $\pm$ standard deviation of the absolute difference was 2.1 $\pm$ 4.6 pixels.
Biomarker-7: Attenuation Coefficient of the RNFL	Mean unsigned difference of the attenuation coefficient is 0.0008.
Biomarker-8: Reflectivity value of the EZ layer	Mean unsigned difference of the attenuation coefficient is 0.06.

6.4 Conclusion

Retinal diseases such as DME, AMD and neuropathy diseases such as glaucoma cause vision loss. They are both common and devastating. With the advanced SD-OCT imaging techniques, we now have much more information available for interpretation, measuring and potentially tracking the progression of these diseases. In this chapter, we have proposed an automatic segmentation method for detecting ONH and layers in the presence of the ONH which also equally works in other OCT images such as macula-centred OCT images. To the best of our knowledge, this is the first automatic method to segment layers in any area of the retina without human intervention. In this chapter, we have also proposed a highly accurate segmentation method for the HRS and drusen from the retinal SD-OCT images. The high accuracy of the automatic method in estimating eight biomarkers demonstrates its potential usefulness in large-scale studies for early retinal disease screening.

Chapter 7

Classification model of Diseased patients

This chapter presents a novel method for classifying the diseased eye into Age-related Macular Degeneration (AMD)) and Diabetic Macular Edema (DME) from Spectral Domain Optical Coherence Tomography (SD-OCT) volumetric images. This chapter is based on the following publication.

> Md Akter Hussain, Alauddin Bhuiyan, Chi D. Luu, Robyn H. Guymer, Hiroshi Ishikawa, R Theodore Smith, Joel S. Schuman and Ramamohanarao Kotagiri. *"Classification of Healthy and Diseased Retina Using SD-OCT Imaging and Random Forest Algorithm"*. *(To be submitted)*

7.1 Introduction

Eye diseases such as Age-related Macular Degeneration (AMD) and Diabetic Macular Edema (DME) are amongst the most common causes of vision loss in our communities. The number of people with AMD is expected to increase by $\sim$1.5 fold over the next ten years due to an increase in aging population [7]. Similarly cases of DME are expected to grow exponentially affecting over 300 million people worldwide in the next few years [14]. In this chapter, we have proposed an automatic classification method for people with AMD, DME, and people with normal retina using Random Forest classifier, a highly robust and efficient machine-learning algorithm. The classification method might be able to used to determine the severity level of the diseases for patients based upon their risk of progression and potentially serve as a prediction tool. A total of ten features based

161

upon current clinical knowledge have been extracted automatically from the Spectral Domain Optical Coherence Tomography (SD-OCT) images of the retina of patients. We have tested several machine learning algorithms such as Support Vector Machine (SVM), Decision Tree, and Random Forest. Among them, Random Forest has shown the best performance (more than 97% accuracy) overall.

There has been few work on the automatic segmentation of the retinal layers, but only a few methods are available for the classification of the SD-OCT volumes [26, 153, 154]. Among those classification methods, most of them are binary classifier that is classified into diseased or normal cases, not specific diseased such as AMD and DME. The features for classification purposes are mostly on texture information of the image and are created using Local Binary Pattern (LBP), a histogram of oriented gradient and other texture analysis. These features are filtered using Principle Component Analysis (PCA), Bag-of-word, and k-means cluster, etc. The disadvantage of the texture information is that it is more susceptible to noises and device oriented due to different intensity variation among them. On the other hand, retinal structure information does not depend on the device and is less susceptible to noise. That is why the classification method based on retinal structure information is more reliable than the texture-based classification. Fraccaro et al. [26] developed a classification method using retinal pathology information, but they were manually extracted features. He showed that Random Forest algorithm has superior performance when compared to One-rule, Decision Tree, Logistic Regression, AdaBoost, and Support vector machine for the classification of the diseases. To the best of our knowledge, there is no classification method based on automatically segmented the retinal structure and pathology information. A brief survey of the classification methods used in eye disease is discussed in chapter 2 (section 2.7.7).

In this chapter, we have proposed a classification method of AMD, DME and normal individuals. The system has also been tested for the binary classification case that has also shown excellent performance. There are a total of ten retinal features extracted from the SD-OCT images, and all of these are considered clinically important features based on the changes of the retinal structure and pathology due to AMD and DME. The retinal layers are automatically segmented using our method explained in Chapter 5. We

have proposed a quantification method for pathology with the help of segmented layer. The features constructed with two parameters each from the retinal thickness, the complex of ELM to RPE layer, and the RPE layer; two parameters from the boundary curviness of the retinal layers (OPL-ONL and MZ-EZ), and two parameters for the volume of the drusen and Hyper-Reflective intra-retinal Spots (HRS). Several machine-learning approaches have been used to test the performance of the feature selection as well as a comparison between them. Evaluation is performed on two datasets including a public dataset[1] with fifteen-fold cross validation such that each test includes one case of each for the data set containing 45 individuals and also leave one out cross validation test. The results show high accuracy on both datasets (45 and 72 SD-OCT volumes) and higher than the original work on the public dataset [1].

Contributions of the chapter are as follows.

- Automatic classification of SD-OCT volumes of patients into AMD, DME, and normal.

- Automatic feature extraction from the SD-OCT volumes that are related to the changes of the retinal structure due to AMD and DME (such as thickness of the retina and retinal layers, drusen).

This chapter is organised as follows. Section 7.2 describes the methodology of classification including the features extraction and the classification approach. Experimental method and results are discussed in section 7.3 and 7.4 respectively. Finally, section 7.5 concludes the chapter.

7.2   Methodology

The methodology of classification of the diseased eyes is formulated as a standard classification procedure as shown in Fig. 7.1. Since the proposed method uses the segmentation output of the retinal layer boundaries (explained in chapter 3 and 5), there is no requirement for pre-processing or noise reduction. The noise reduction has already been employed in the segmentation phase. After the segmentation, ten retinal features are extracted as described in section 7.2.1. The difference between boundaries of a layer along

the A-scan is considered as the thickness of the layers and retina. The pathologies such as drusen and HRS are identified using position and intensity profiling of the image (explained in Chapter 6). Layer segmentation is used to identify the position and hence the type of pathology. For example, drusen are identified using the non-uniformity of thickness of RPE layer and by simply counting the number of pixels in the drusen gives the volume of the drusen. Training and testing are two steps of the machine learning algorithm where training is used to create the classification model, and testing is used to evaluate the performance of the model. In the next subsection, the method of extracting the features is discussed.
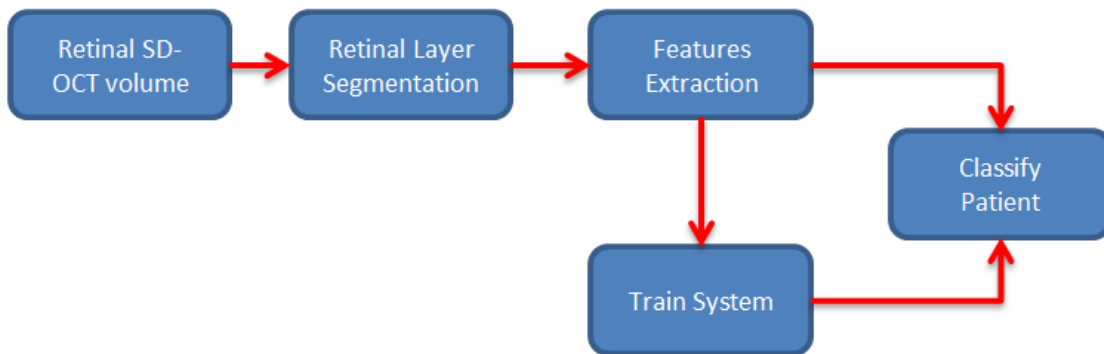
Figure 7.1: The flow diagram of the proposed classification method.

7.2.1 The feature extraction process

Ophthalmologists have defined a set of signs from the changes of the retinal structural information for the retinal diseases such as AMD and DME [2, 19, 182]. The signs include abnormality of the retina and its layer thickness and reflectivity such as OSL thickness was reduced significantly in early AMD patients [183]. Ophthalmologists have also defined presence of pathologies as retinal diseases such as drusen and RPE detachments for AMD; cysts for DME. As a consequence, the proposed method has used these signs of the DME and AMD as features for the classification method. A total of ten features are extracted via a process as follows.

7.2.1.1   Feature 1: Volume of the Hyper-Reflective intra-retinal Spots (HRS)

The presence of the HRS in the retinal SD-OCT volumes present in diabetic eyes even when clinical retinopathy is undetectable [2]. For this reason, we have chosen the volume of the HRS as a feature. It is characterised by the brighter intensity and located in the inner retina mostly in INL to ONL layer. Since we have segmented the layers, we search HRS only in those layers. In general, those layers are darker than RNFL and RPE layers except those HRS pixels. So the pixels, which are located in INL to ONL layer and have intensity value more than the mean intensity of the RNFL and RPE layers, are defined as HRS pixels. The total number of pixels multiplied by the resolution of the image is considered as the volume of the HRS. Figure 7.2 shows an example of the automatic segmentation of HRS by our proposed method.
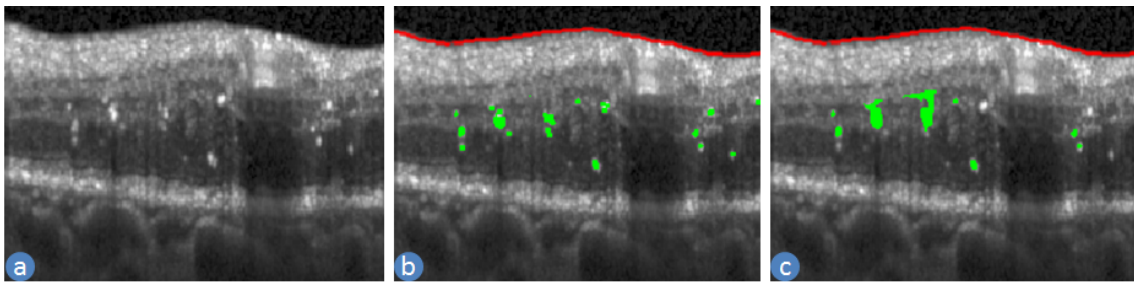
Figure 7.2: (a) A SD-OCT B-scan (b) manual ILM-RNFL boundary (red line) and HRS (green) (c) automatically detected ILM-RNFL boundary (red line) and HRS (green).

7.2.1.2   Feature 2: Volume of the drusen

The presence of drusen in the retinal SD-OCT images are a key risk factor for AMD and DME patients [19,182]. For this reason, we have chosen the volume of a druse as a feature for the classification method. They are characterised by RPE layer detaching from the BM create an enlarged and intensities in the enlarged area are lower than the RPE layer. This enlargement is also found in the upper few layers all the way to ELM layer. The thicknesses of ELM to BM layer are computed and a first order polynomial is used to fit the thickness with respect to horizontal position. If the value of the thickness deviates from the fitted value of the polynomial is considered as potential drusen area. If the intensity ratio between upper and lower few pixels in the potential drusen area is greater

than 1.3 are considered as drusen. The total number of pixels multiplied by the resolution of the image is considered as the volume of the drusen. Figure 7.3 shows an example of the automatic segmentation of the drusen area by our proposed method and a 3D view of drusen in the SD-OCT volume.
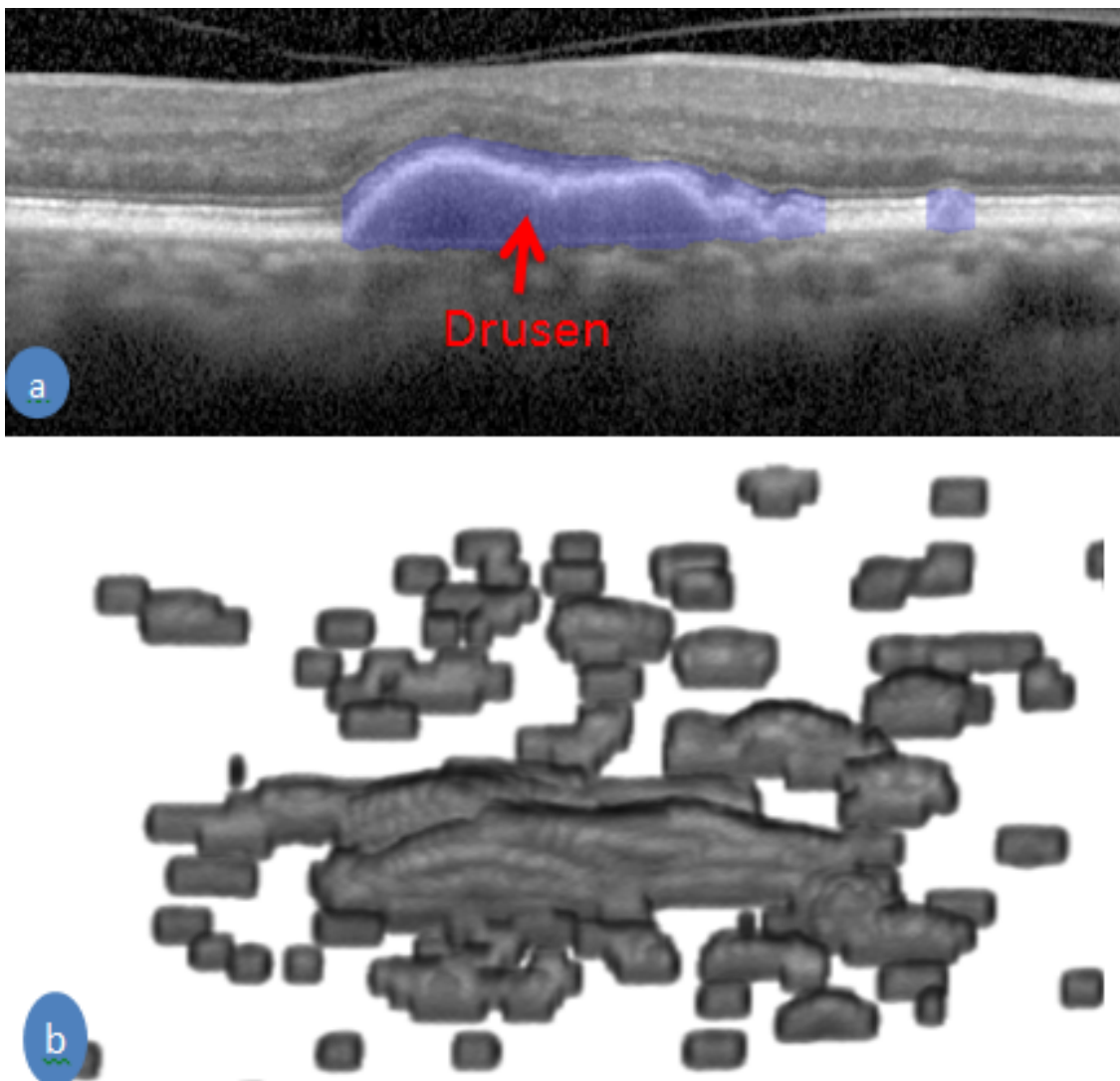
Figure 7.3: (a) A SD-OCT B-scan with delineating drusen by the blue colour (b) Drusen in 3D view of an SD-OCT volume of an AMD patient.

7.2.1.3   Feature 3: Curviness of the MZ-EZ boundary

The curviness of the MZ-EZ boundary is an effect of RPE detachment and drusen for the retinal diseases AMD. We have proposed a method to compute the curviness of a boundary that is shown in Algorithm 1. In step 1, the position of the RBC boundary is subtracted from the given boundary to normalize line the position. A constant value ($\alpha = 3$) is used to penalize a position of the boundary as curviness. For example, if deficiency of the boundary from the first order polynomial value is more than α, we consider them as curvy and penalize otherwise they are not penalized. Another constant value ($\delta = 5$) is used to find the peak of the boundary. For example, a position of the boundary is defined as peak, if it has at least δ difference between the local maxima and the local minima. A value is considered local maxima if that value is more than one of the neighbours but not less than any of the neighbours. Similarly, a value is considered local minima if that value is less than one of the neighbours but not greater than any of the neighbours. This will ensure there is one local maxima between two local minima and vice versa. The nearest two local maxima and minima are removed if the difference between them is less than δ. This step is repeated for removing all neighbour local minima and maxima with difference less than δ. Figure 7.4 shows the curviness of different boundaries.

Algorithm 6 Curviness of a given boundary

Input: The boundary of RBC (B_{RBC}) and given (B_{Given}).
Output: The value of curviness (C).
  1: NL = B_{RBC} - B_{Given}.
  2: Compute first order polynomial P_{NL}^1 using NL
  3: Df = $|NL - P_{NL}^1|$
  4: $C_1 = \Sigma_{i\epsilon(Df>\alpha))} Df_i$
  5: LMM=$localMaxMin$(NL)
  6: Repeat until there is at least one $minDiffNeigh$(LMM)$< \delta$
  7:         Remove Smallest Difference Pair in LMM
  8: End Loop
  9: C_2 = Number of Local Maxima in LMM
 10: C= $C_1 \times C_2$.
α is the maximum deficiency value for not a curve. $localMaxMin$(NL) is a function that gives the local maxima and minima in the NL and stored into LMM; $minDiffNeigh$(LMM) is a function which gives minimum difference between neighbour minima and maxima.
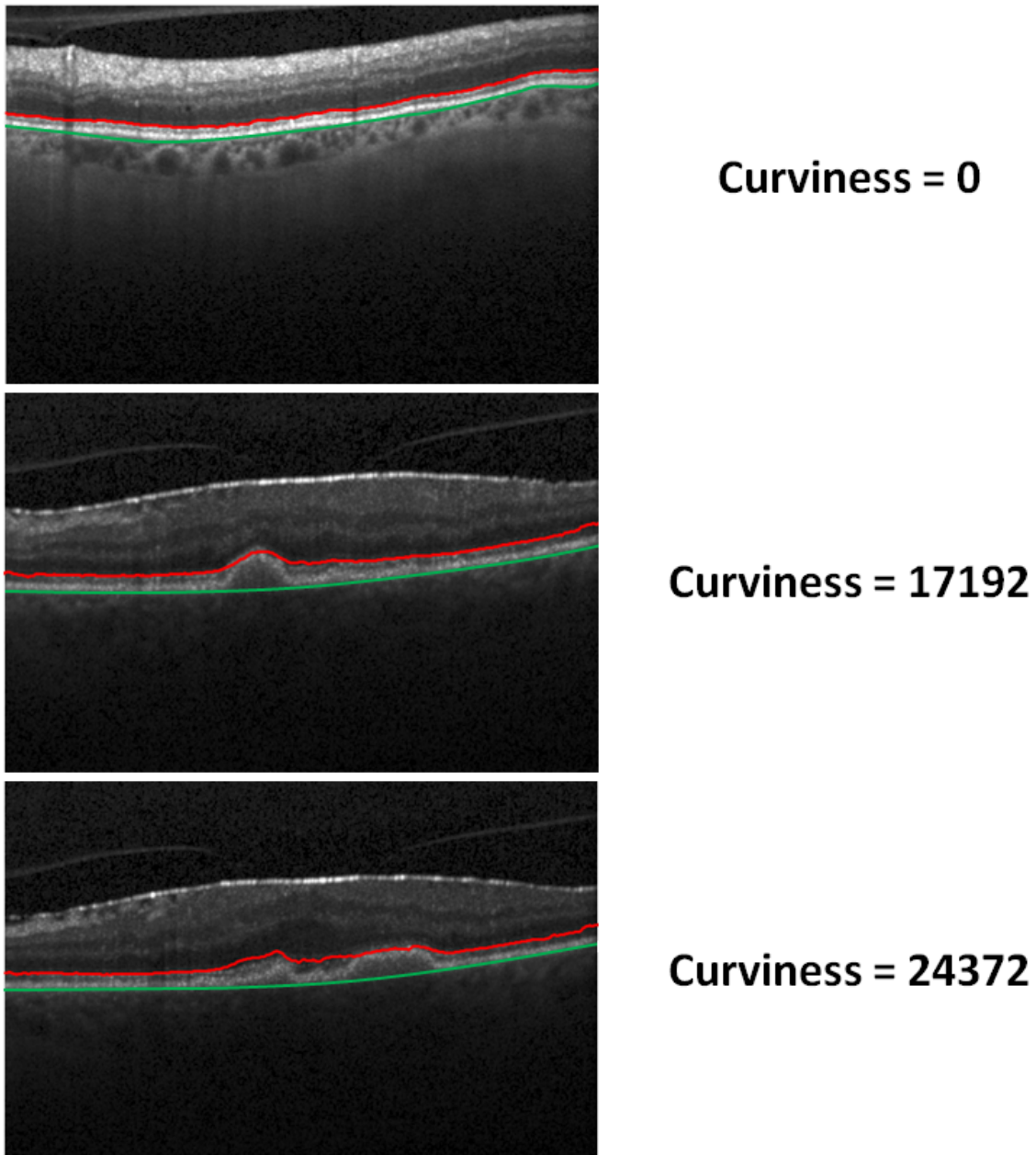
Figure 7.4: The curviness of different MZ-OZ boundaries (red) with a different curve using our proposed method. RBC boundary is in green.

7.2.1.4   Feature 4: Curviness of the OPL-ONL boundary

The curviness of the OPL-ONL boundary is an effect due to the Cyst and HRS exist for retinal disease DME. The curviness of this boundary is computed using Algorithm 1 with

the same constant values as MZ-OZ curviness (Feature 3).

7.2.1.5   Feature 5-10: Thickness parameters of the structures

Six more features from three structures, Retina, Complex of EZ to RBC layers, and RPE layer are quantified as features shown in Fig. 7.5. Two features from each of the structure are added to the feature list. The thicknesses of these structures of the retina have changed significantly due to the retinal diseases of the AMD and DME [26, 183]. For this reason, we have added mean and 70th percentile of the thickness value of these structures as features for the classification method. The thickness of the structure is computed by the difference of the position of the enclosed boundaries such as the thickness of the retina is computed by ILM-RNFL and RBC boundaries. Similarly, the thickness of the complex of EZ to RBC layer is computed by ONL-EZ and RBC boundaries, and the thickness of the RPE layer is computed by IZ-RPE and RBC boundaries. The thickness is then smoothed for reducing the possible error in the segmentation by applying the Gaussian filter. Then these smooth thickness values are used for computing the features.

7.3   Dataset and Experiment setup

We obtained SD-OCT images from three sources: DUKE University [1], Centre for Eye Research Australia (CERA) and New York University. The Duke University provided 45 images consisting of 15 normal, 15 AMD and 15 DME. CERA provided 14 AMD images and New York University provided 13 normal images. Using these three sources of images we constructed two datasets one entirely based on DUKE image data (D-1) and the second by combining all the three sources with 72 images consisting of 29 normal, 28 AMD and 15 DME (D-2). CERA images have $512 \times 1024 \times 49$ voxels per subjects of SD-OCT volumes acquiring from Spectralis SD-OCT (Heidelberg Inc., Heidelberg, Germany). New York University images have $512 \times 1024 \times 19$ voxels per subjects of EDI-OCT volumes acquiring from Spectralis SD-OCT (Heidelberg Inc., Heidelberg, Germany).

Several machine-learning algorithms are used to compare the accuracy of the classifi-
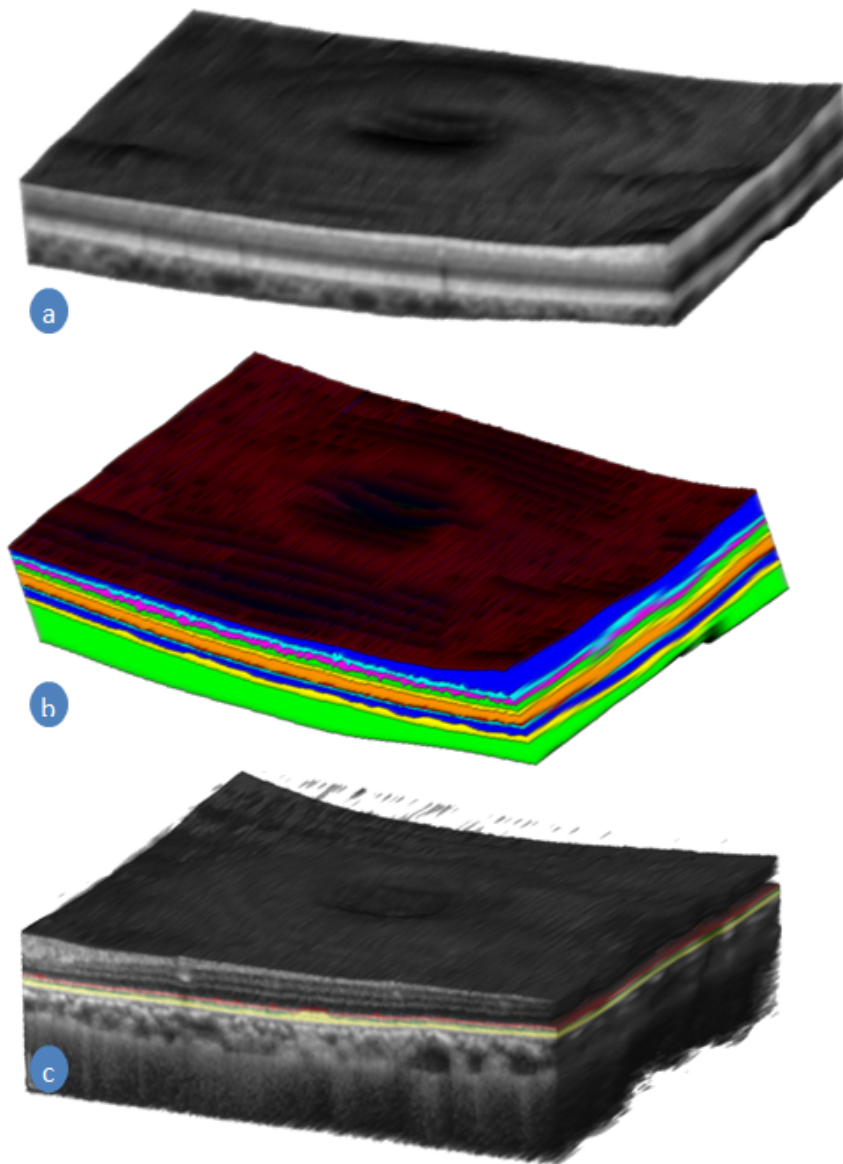
Figure 7.5: (a) A 3D render image of the retina with the choroid constructed from an SD-OCT volume; (b) Segmented layers of the retina and choroid; (c) The complex of the EZ, IZ, and RPE in a different colour in the gray-scale retinal SD-OCT image.

cation model for two and three class classifications of eye patients. The machine-learning algorithm are Logistic Regression Model; Support Vector Machine with two kernel functions, Linear and Radial basis function; AdaBoost, Nave Bayes Model, Decision Tree with Regression and classification model; and Random Forest; two class classification model

categorizes the subjects into normal and diseased, while three class classification model categorizes into AMD, DME and normal. We have used Matlab [1] default library function for each of the machine learning algorithms' implementation. We have performed k-fold cross validation with k=15 for all machine learning algorithms on both datasets, this way we make sure that each test fold has at least one instance of each case tested as in [1]. In k-fold cross validation test, a given dataset is randomly divided into k parts (fold) where (k-1) folds of subjects are used for training the classification model and the remaining one fold of subjects are used to test the model. The system is executed k times so that each fold of the subjects must be used once for testing the model. Since the given dataset is divided randomly into folds and the performance of the classification model depends on the training data, the performance of the model varied in each iteration. For this reason, we have repeated the k-fold cross validation test 10 times and the average accuracy (total number of successfully classified subjects divided by the total number of subjects) is defined as the model's accuracy. The optimal parameters of the classification algorithms are selected for each fold using a portion of training data as validation data. Once the optimal parameters for the fold are chosen the model is learned using the whole training data and the model is tested using the test data. The optimal parameters chosen are number of trees for Random Forest and Kernel scale for SVM. We have further examined Random Forest algorithm with leave one out test. The results are shown as the percentage of successfully classifying the subjects of a dataset as accuracy.

7.4   Results and Discussion

Our classification model for the eye diseases patients is designed using the Random Forest Algorithm. Table 7.2 shows the average confusion matrix for 10 k-fold cross validation tests where k = 15 using Random Forest classification method. It is the best way to evaluate the performance as each test fold contains one instance of each class. The accuracy for our proposed method is better than Srinivisan et al. (the owner of the dataset D-1) on dataset D-1 where we have achieved average accuracy 97.11% with standard deviation

---

Table 7.1: Performance of four state-of-the-art and proposed methods on partial DUKE dataset (D-1) considering only normal and DME patients (because Venhuizen et al., Lemaitre et al., and Sidibe et al. used to classify only them).

Metric	Srinivisan et al. [1]	Venhuizen et al. [155]	Lemaitre et al. [14]	Sidibe et al. [25]	Proposed method
Sensitivity	100	71.42	86.67	80	97.33
Specificity	86.67	68.75	100	100	100
Accuracy	93.33%	70.00%	93.33%	90.00%	98.67%
AUC value	-	-	-	-	0.99

1.07 for ten iterations of 15-fold cross validation tests while Srinivisan et al. [1] achieved 95.56%. The comparison between state-of-the-art methods in terms of sensitivity and specificity on partial DUKE dataset is shown in Table 7.1. Since Lemaitre et al. [14] and Sidibe et al. [25] have reported the performance of the classification model for two classes (Normal and DME) using sensitivity and specificity on the partial data of DUKE dataset (only normal and DME patients), we have also follow the same approach for comparison purpose between Srinivisan et al. [1], Venhuizen et al. [155], Lemaitre et al. [14], Sidibe et al. [25] and our proposed method on partial DUKE dataset (only DME and Normal patients) (see Table 7.1). An Area Under the receiver operator characteristics Curve (AUC) value does not report by the other researchers that is why the corresponding cells in Table 7.1 contain dash sign (-). The accuracy values show our proposed method outperforms these four state-of-the-art methods.

For three-class classification model, normal patients are classified with 100% accuracy in both of the datasets (D-1 and D-2). AMD patients are classified with 92.7% and 98.9% accuracy on dataset D-1 and D-2 respectively. We can observe that the classification accuracy increases when the AMD subjects are increased. DME patients are classified with 98.7% and 94.0% accuracy on dataset D-1 and D-2 respectively. Total accuracy for the dataset D-1 and D-2 are 97.1% and 98.3%. For two-class classification model, the classification for normal subjects shows 100% accuracy on both datasets but the diseased cases are classified correctly more in dataset D-1 than D-2. We have tested Random Forest algorithm with leave one out test where three and two class classification model shows 97.78% accuracy in each case on dataset D-1 that is better than the accuracy (95.83% and 97.22%) on dataset D-2. The confusion matrix of Random Forest classification model is

reported in table 7.2. In addition, we have achieved the AUC values for each case (for example, normal patients as positive class in three and two class classification method; AMD patients as positive class; DME as positive class; etc.) 0.99 with a standard deviation of 0.001.

Table 7.2: Average of 10 confusion matrixes on 15-fold cross-validation test for the proposed classification model using Random Forest.

# of class in classification	Random Forest			
	D1		D2	
2	**Target Class**		**Target Class**	
	N: 15.00 (0.00) | 0.80 (0.63)		N: 29.00 (0.00) | 1.80 (0.79)	
	D: 0.00 (0.00) | 29.20 (0.63)		D: 0.00 (0.00) | 41.20 (0.79)	
	N | D		N | D	
3	**Target Class**		**Target Class**	
	N: 15.00 (0.00) | 1.00 (0.00) | 0.20 (0.42)		N: 29.00 (0.00) | 0.30 (0.48) | 0.90 (0.57)	
	A: 0.00 (0.00) | 13.90 (0.32) | 0.00 (0.00)		A: 0.00 (0.00) | 27.70 (0.48) | 0.00 (0.00)	
	D: 0.00 (0.00) | 0.10 (0.32) | 14.80 (0.42)		D: 0.00 (0.00) | 0.00 (0.00) | 14.10 (0.57)	
	N | A | D		N | A | D	
N, A and D are category of the patients; N is for Normal; A for AMD; and D for DME in three class classification and diseased in two class classification;				

We have examined the classification model using several machine learning approaches. The average accuracy with 15-fold cross validation test applied ten times in both dataset is reported in Table 7.3 with mean accuracy and standard deviation for ten iterations. Logistic regression model shows the worst performance that demonstrates unsuitability as classification model for the patients based on the proposed features from SD-OCT images. SVM with linear and RBF kernel functions show better result in dataset D-2 but not as good as AdaBoost, Nave Bayes Model, Decision Tree with Regression and classification model; and Random Forest based classification model. AdaBoost based classification model shows similar performance as SVM. Nave Bayes Model shows good accuracy for the binary classification where it shows 100% accuracy on dataset D-1. Regression

Table 7.3: The accuracy for different machine-learning algorithms for the classification model based on the proposed features.

# of class	Data-sets	LR Model	SVM		Ada-Boost	NB Model	Decision Tree		Random Forest
			Linear	RBF			Reg.	Class.	
2	D-1	76.44 (3.18)	87.33 (1.50)	88.67 (1.26)	95.56 (1.48)	100.00 (0.00)	92.22 (2.40)	94.00 (1.50)	98.22 (1.41)
	D-2	80.42 (2.12)	96.81 (0.67)	95.97 (1.02)	96.94 (1.94)	97.50 (1.43)	99.72 (0.88)	99.86 (0.44)	97.50 (1.10)
3	D-1	49.56 (2.58)	87.56 (1.55)	86.22 (1.75)	88.44 (3.89)	91.11 (1.81)	93.33 (0.00)	93.56 (0.70)	97.11 (1.07)
	D-2	65.97 (3.83)	94.03 (1.74)	91.11 (1.99)	98.89 (0.59)	92.36 (1.18)	97.22 (0.00)	98.47 (0.44)	98.33 (0.88)

LR: Logistic Regression; SVM: Support Vector Machine; RBF: Radial basis function; NB: Naive Bayes; Reg.: Regression; Class.: classification.

and Classification based decision tree shows better accuracy in dataset D-2 compares to dataset D-1. Though classification based decision tree has better accuracy than regression based decision tree, the difference is not big. Random Forest shows accuracy more than 97% in all tests with low standard deviation for each iteration of 15-fold cross validation test. Though, Random Forest based classification model is not the best in accuracy in all cases that is true for others as well, its consistency in each test makes it superior for acceptance over others.

7.5 Conclusion

In this chapter, we have proposed a novel method of eye disease classification using automatically quantified hand-crafted clinical driven features of AMD, DME and normal patients using Random Forest algorithm. We have also examined a number of machine learning algorithms but Random Forest performs best on accuracy than others in both datasets. The AUC value is also high (0.99) with a small standard deviation 0.001 for the classification method. This high accuracy with several machine algorithms demonstrates the features extracted can model the disease. Moreover, this is the first method where automatic segmentation of the layers and extraction of pathologies are employed for classification of AMD, DME using SD-OCT images. The results show as predicted

since diseases are highly correlated with the layer thickness and pathologies. The score of the classifiers might be used as the severity level of the disease. Since we have no data of severity level of the disease, we are unable to compute the system performance against severity level of the diseases. This research of severity can be investigated in the future when there is an available dataset with a severity level. This score of severity might also used as prediction for the eye diseases. Other layers information can also be considered as features for designing the classification model or the prediction model. As a consequence, early detection of the diseases is possible which allow preventing blindness significantly as well as the system can provide a score value as a condition of the eye.

Chapter 8

OCTInspector: A Complete Automated System for OCT Image Analysis

A user-friendly Graphical User Interface (GUI) has been developed for segmenting Optical Coherence Tomography (OCT) images using the proposed method as shown in Fig. 8.1. A semi-automated module for the correction of the automatic segmentation of the boundaries of the retinal layers and the choroid has also been included. The optic disc border and pathologies (i.e. drusen and hyper-reflective intra-retinal spots) can be corrected by a manual module. This manual correction can be used for further improving the automatic segmentation by learning the parameters of the proposed method. The flow diagram of the OCTInspector system is shown in Fig. 8.2.

8.1 The features of the OCTInspector

The features of the system are as follows.

- Automatic segmentation of the boundaries of the retinal layers and Choroid-Sclera Interface.

- Automatic segmentation of the pathologies (for example, hyper-reflective intra-retinal spots and drusen).

- Automatic segmentation of cup and disc.

- Automatic extraction of Biomarkers such as cup-disc ratio, minimum distance band.
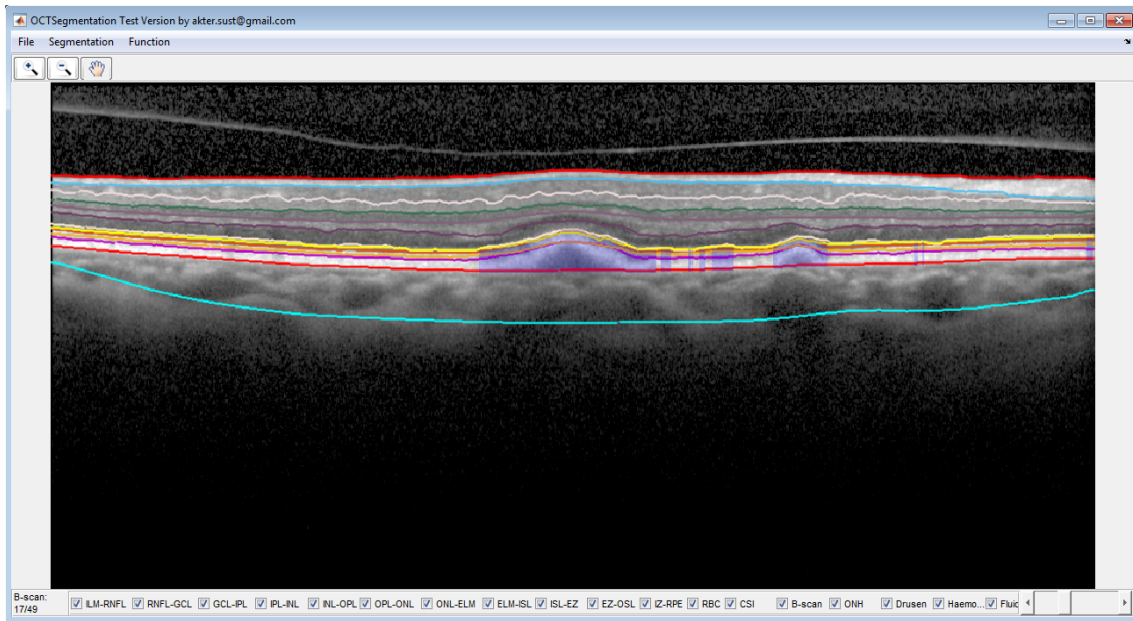
Figure 8.1: The graphical user interface of the developed system using proposed method.
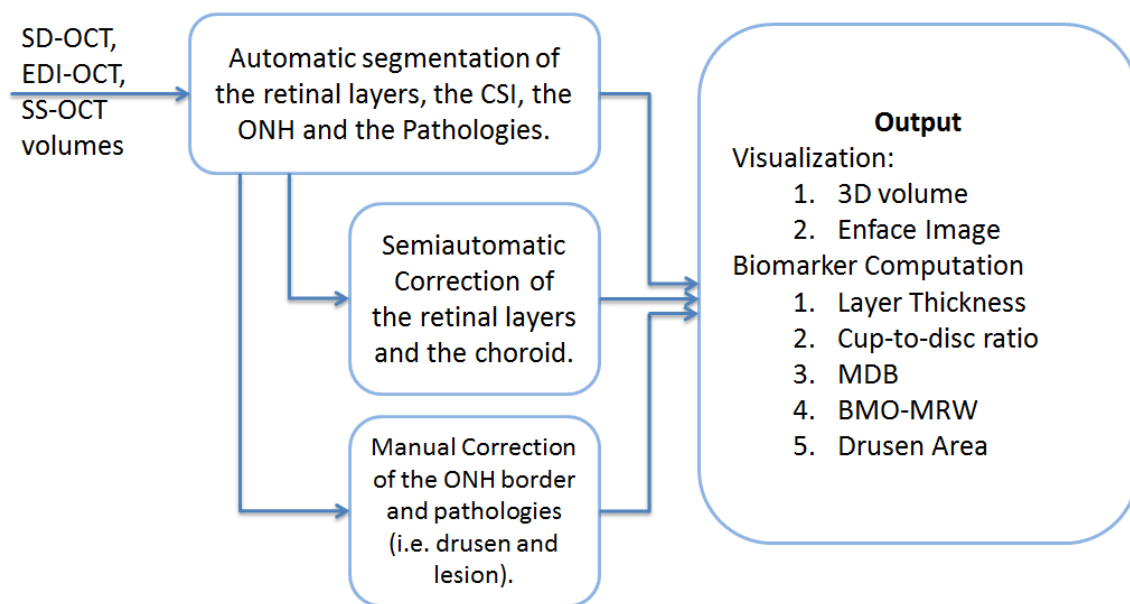
Figure 8.2: The flow diagram of the OCTInspector System.

MDB: Minimum Distance Band; BMO-MRW: Bruch's Membrane Opening Minimum Rim Width.

- Manual correction of the automatic segmented structures as shown in Fig. 8.3.

- Produce 3D view of any combination of the layers and pathologies shown in Fig. 8.4.

- Produce enface image of any combination of the layers and pathologies shown in Fig. 8.4.

- Can read all kinds of OCT files such as image files (.png, .jpeg, .tif, etc.), Cirrus OCT files (.img) and Spectralis OCT (Heidelberg Engineering) files (.vol).

- Allows saving of the automatic segmentation which can also be re-examined for future analysis and/or modification.
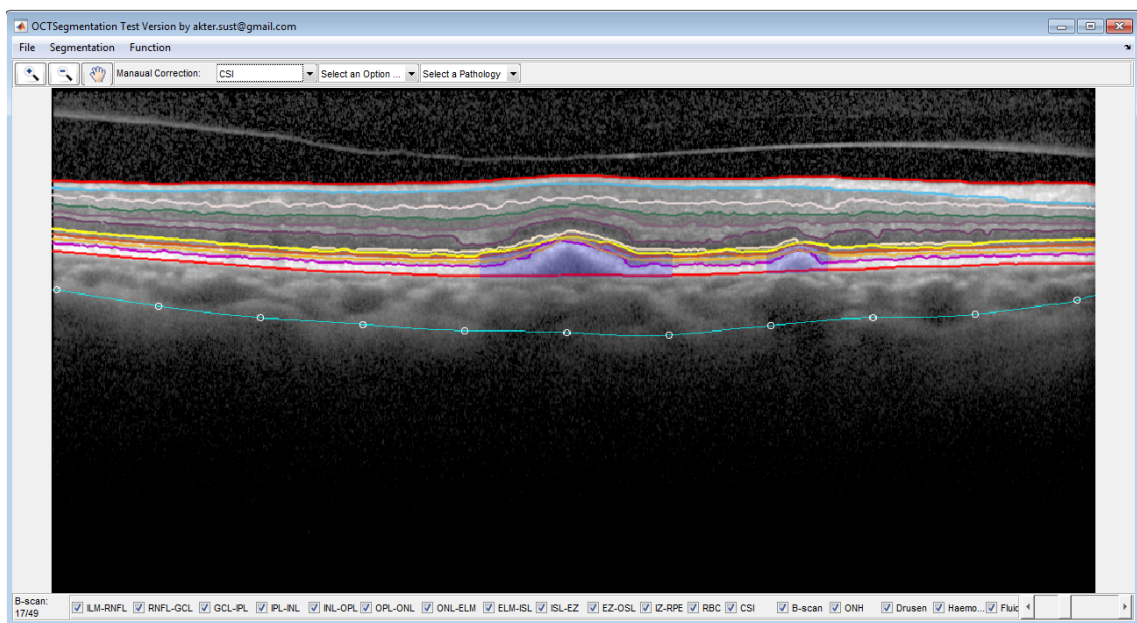
Figure 8.3: The correction mode where Choroid-Sclera Interface (CSI) is selected for correction.

8.2 The functionalities of the OCTInspector

For automatic segmentation, the system only needs to open an OCT image volume or file and then a single click will do automatic segmentation. The system automatically shows the segmented boundaries and pathologies in the interface as shown in Fig. 8.1. The
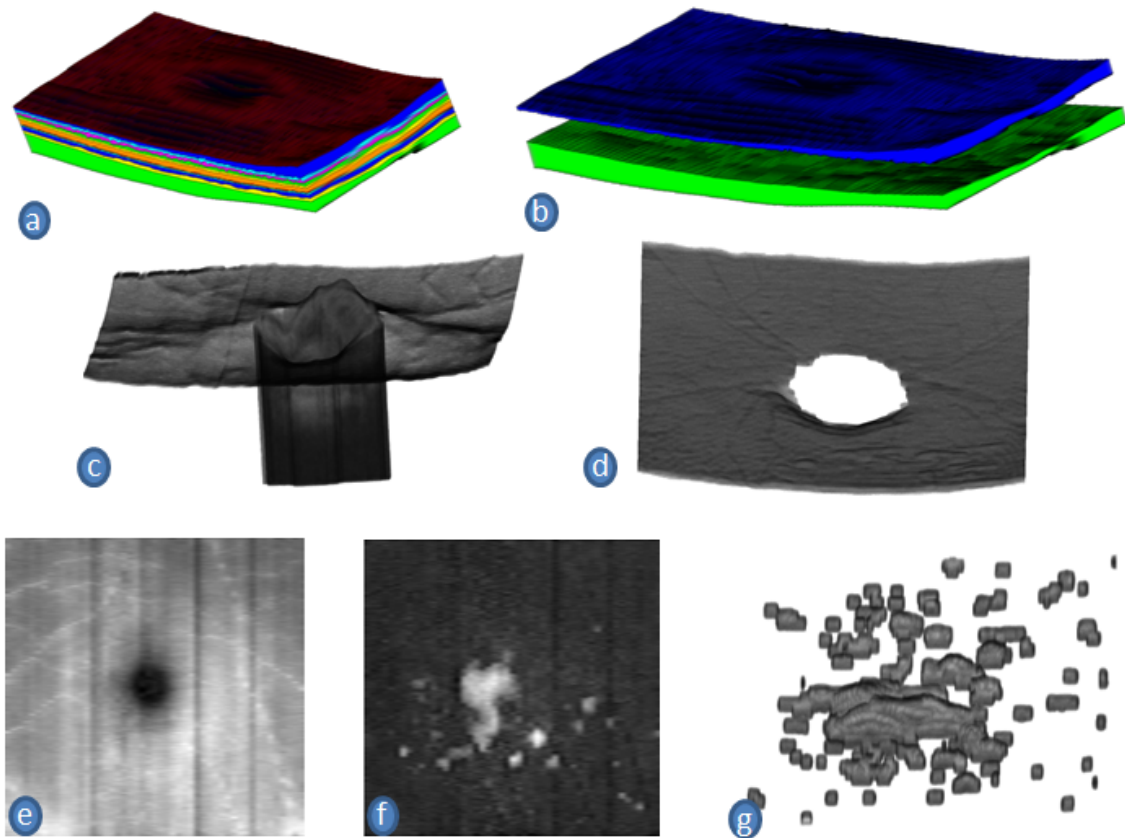
Figure 8.4: (a) 3D View of a segmented macula centred OCT image; (b) 3D view of a segmented RNFL and Choroid in macula centred OCT image; (c) 3D view of a segmented ILM surface and ONH; (d) 3D view of the RPE in ONH centred OCT image; (e) Enface image of the RNFL, GCL, IPL from Macula Centred OCT Image; (f) Enface image of the RPE Layer from macula-centred OCT image that shows the drusen by brighter intensity; and (g) 3D view of drusen from a macula-centred SD-OCT volume.

RNFL: Retinal Nerve Fiber Layer ; ILM: Internal Limiting Membrane; RPE: Retinal Pigment Epithelium ; GCL: Ganglion Cell Layer; IPL: Inner Plexiform Layer.

information about current steps in a loading bar is displayed. The user can change the colour of the boundaries as well as choose which boundaries should be visible or hidden.

When a user selects the manual correction mode, it will show the options of a correction menu as shown in Fig. 8.3. The boundaries of the retinal layers and the choroid are corrected by a semi-automated method. When a user selects a boundary from the drop-down menu, the system will highlight the boundary by drawing a circle on the boundary. The user needs to click on the correct position of the boundary; then the sys-

tem will run the automated method of the selected boundary, but this time, a region of interest is restricted by the boundary and the click points. If a single click cannot detect the correct boundary, then multiple clicks are required to correct that boundary. The optic disc border and pathologies can also be corrected by clicking.

The system is able to produce a 3D view of any combination of the layers and pathologies as well as their 2D enface image, using automatic segmentation or manually correct segmentation as shown in Fig. 8.4. The system utilises Fiji [181], an open source module for image processing, for visualising the structures in 3D.

The system can also compute various biomarkers such as cup-disc ratio, Bruch's membrane opening minimum rim width, minimum distance band using the segmented output. The list of biomarkers and procedure of computing them are discussed in Chapter 6.

Chapter 9

Conclusion and Future Research Direction

9.1 Summary of contributions

This thesis described the development and validation of a set of novel medical image analysis methods for the automated segmentation of the retinal layers and the choroid that work well even in the presence of drusen, geographic atrophy and Hyper-Reflective intra-retinal Spots (HRS). The methods also perform well at the Optic Nerve Head (ONH) and/or macula regions and can extract and quantify eight significant biomarkers accurately. A system named as OCTInspector has been developed using the algorithms developed in this thesis for automatic segmentation of Optical Coherence Tomography (OCT) images. The system also provides additional manual/semi-automatic functionality to correct any segmentation errors of the automated process. The quantification of biomarkers by the systems provides more detail and precise information about the severity of eye diseases. A classification model of eye diseases based on the biomarkers has been developed using machine-learning algorithms, which has given an accuracy of more than 98%. A summary of these contributions is demonstrated in Fig. 9.1.

9.1.1 Automated 3D Segmentation algorithm for the retinal layer and the choroid

A robust and effective automatic 3D Segmentation method is proposed to identify the retinal layers and the choroid from the Spectral Domain Optical Coherence Tomography (SD-OCT) images or higher-resolution OCT images such Enhanced Depth Imaging
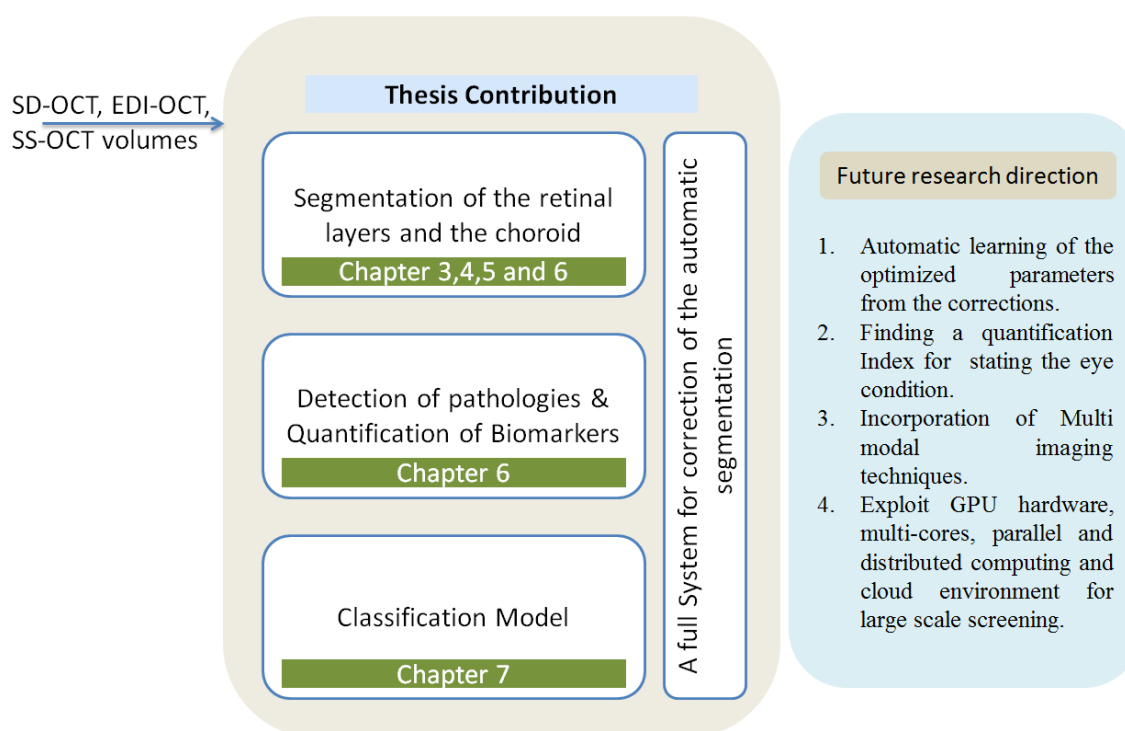
Figure 9.1: A brief summary of the thesis contribution and the future research direction.

OCT (EDI-OCT) and Swept Source OCT (SS-OCT). 3D segmentation utilises more information than 2D segmentation that leads to high accurate and reliable segmentation than 2D segmentation. The proposed method also works in the presence and absence of pathologies and morphological changes due to disease. This method is also seamlessly applicable to any regions of the retina-centred OCT images. These contributions are described in Chapter 3 to 5. In Chapter 3, the first attempt at 2D segmentation of four prominent boundaries of the retinal layers is explained. These layers are most affected and distorted due to drusen and OCT defined geographic atrophy. This method has enabled the development of the proposed 3D segmentation algorithm. The problem of finding a boundary from the SD-OCT images is solved by mapping the problem into a graph shortest-path problem such that finding the shortest path using Dijkstra's algorithm is equivalent finding the boundaries of layers in the retina. The edge pixels of the image derived from canny edge detection form the nodes of the graph instead of all pixels of the image. That improves the efficiency of the algorithm by reducing the nodes of the graph. A novel method has been proposed for approximately detect-

ing the three reference layers that are used to reduce the Region Of Interest (ROI): this improves the efficiency and accuracy of the detection of the boundary. The graph edge weight is designed using spatial distance, slope similarity to a reference line and node's non-associativity (pixels not satisfying associated layer property) with the layer are used for obtaining an accurate boundary as the shortest path. The method can be adapted or generalised for other images with other kinds pathologies (although not handled in the proposed method) by adding more properties for a node's non-associativity weight. In Chapter 4, an automatic 2D method for identifying the Choroid-Sclera Interface (CSI) has been proposed. Since the choroid is different from the retina, the graph construction and edge weight are designed by addressing the particular challenges regarding the choroid, and the shortest path becomes the CSI. Due to small changes from one B-scan to another, a 3D segmentation algorithm can exploit information from adjacent B-scans for getting the boundaries of the retina and the CSI, described in Chapter 5. The adjacent B-scans allow the method to reduce the ROI substantially and to improve the efficiency and accuracy of finding the boundaries. The method first detects the boundaries sequentially in the order of high contrast and the maximum gradient intensity to low contrast and minimum gradient intensity of the boundaries. This approach helps to detect the low contrast boundaries in a small ROI. In Chapter 6, the boundary detection algorithm has been extended to work in the presence of the ONH. Due to the absence of layers in the ONH, it requires different computations for finding the boundaries accurately. The edge weight of the ILM-RNFL boundary is adjusted in the ONH region so that the boundary is detected accurately by falling in that region. After detection of the ILM-RNFL boundary, ONH is detected by using enface image and three patterns (such as the absence of layers, dissimilar layer positions and intensity pattern) of the ONH in the SD-OCT image. At this stage, the proposed method can detect all boundaries in the absence/presence of the ONH and macula even in the presence of pathologies. Five datasets (two of which are public) from four sources have been evaluated in a different stage of the method. The total dataset contains 56 subjects among them 36 subjects with pathologies- and contains images of varying resolutions. There is an ONH-centred volume with 200 B-scans from one glaucoma patient. Manual grading of the images serves as the gold standard to com-

pare the accuracy of the automatic method. A total of six state-of-the-art methods for the retinal layer and two for the CSI produces the output from the dataset. In every dataset, the proposed method performs best. The overall mean of the root mean square error of the boundaries positions of the retinal layers in the macula and ONH-centred images from the proposed method are 0.20 and 0.11 pixels respectively, which is significantly better than the state-of-the-art methods. This performance demonstrates the potential effectiveness of the proposed 3D automated method for monitoring the progression and early diagnosis of retinal diseases by conducting studies on a large-scale. A system for processing, segmenting, and viewing the SD-OCT, EDI-OCT, and SS-OCT volumes has been developed which also includes the semi-automatic correction of the segmentation. The system can also produce 3D views of the volumes of any combination of the retina layers and choroid; the pathologies, etc.

9.1.2   Biomarkers quantification

In this study, methods for segmenting pathologies such as drusen and Hyper-Reflective intra-retinal Spots (HRS), and a computation method for quantifying the clinically-derived biomarkers have been proposed as described in Chapter 6. A novel framework is proposed for measuring eight biomarkers of interest to ophthalmologists related to retinal structural thickness, ONH, the morphological parameters of ONH, the volume of the pathologically altered tissue (lesions of the inner and outer retina), the reflectivity of the Ellipsoid Zone and attenuation coefficients of the Retinal Nerve Fiber Layer for early screening of glaucoma, Diabetic Macular Edema (DME) and Age-related Macular Degeneration (AMD). An automatic method for detecting the retinal layers in the presence of pathologies or distorted layers due to diseases, is the primary requirement for automatically quantifying the biomarkers. The pathologies are detected using intensity profiling and thickness of the retinal layers computed using the proposed automatic 3D segmentation. Finally, these eight clinically-useful biomarkers of the retinal and neuropathy diseases are quantified automatically using the same protocol as defined by the ophthalmologists' research. The evaluation process found a low margin of error between manual and automatic grading of the biomarkers. An automatic method for detecting

HRS and drusen achieved a F1-score of 0.79 and 0.70 respectively compared with the manual quantification. The eight biomarkers have also achieved high accuracy matching the manually quantified values where the mean error is as low as 0.06. The high accuracy of the automated quantification identifies its potential use for early diagnosis and monitoring the progression of retinal diseases in large-scale studies.

9.1.3   Develop classification model for the eye diseases

In this study, a first classification model has been built based on automatically-quantified clinically driven features. The method can classify eye disease patients from OCT images into Diabetic Macular Edema (DME), Age-related Macular Degeneration (AMD) and normal. The proposed classification method is designed with ten clinically driven features based on the thickness of the retina and retinal layers, and the volume of the pathologies such as drusen and HRS as features using the machine-learning algorithm, such as Random Forest (as detailed in Chapter 7). Two datasets comprising a public dataset (15 DME, 15 AMD and 15 normal) and a local dataset (combining the public and local datasets, 15 DME, 28 AMD and 29 normal) of 45 and 72 SD-OCT volumes respectively, are used to evaluate the classification method that achieved high classification accuracy. Ten-fold and leave one out cross validation tests for Random Forest with three classes (DME, AMD and normal) and two classes (disease and normal) on both datasets are performed. The proposed method has achieved a success rate of more than 98% by Random Forrest that is better than four state-of-the-art methods. We have evaluated the performance of classification model using the same ten features with many machine-learning algorithms such as AdaBoost, Decision tree, and support vector machine. Each method has achieved excellent accuracy. This first method of a multi-classification model of eye diseases based on the automatically-quantified clinically driven features indicates that a quantified value of the eye status is achievable that can be used to monitor the progression or severity of eye diseases.

9.1.4   OCTInspector A fully automated system based on the proposed methods

In this study, we have developed a fully automated software system for OCT image analysis using developed methods of retinal layer segmentation, CSI detection and biomarkers extraction. A user-friendly Graphical User Interface (GUI) has been developed from where any kind of OCT image files such as image files (.png, .jpeg, .tif, etc.), Cirrus OCT files (.img) and Spectralis OCT (Heidelberg Engineering) files (.vol) can be opened and automatically segment the retinal layers, CSI and pathologies. In addition, it can compute biomarkers such as cup-disc ratio, Bruch's membrane opening minimum rim width, minimum distance band. The options of manual correction for retinal layers, CSI, pathologies and cup-disc are provided in the system. This manual correction can be used for further improvement of the automatic segmentation by learning the parameters of the proposed method. These features and functionalities of the system have been described in Chapter 8 .

9.2   Future Research Direction

This section briefly describes some possible future research directions, which may come out of this research work. The main and interesting problems are described in detail in the following section.

9.2.1   Improving the algorithm addressing more pathological distortion by automatically modifying the parameters of the edge weight from the manual correction

The proposed method has adapted the pattern of the layers in non-associativity edge weight, one of three parameters of graph edge weights. This parameter can be used for adapting new challenges due to a change of the dataset or presence of pathologies. In the future, an automatic method can be defined for modifying the method by adding new properties when there is an error, in conjunction with a semi-automatic method used for the correction. Furthermore, a technique can be used to learn and adjust the coefficients of the edge weight parameters from corrections of the incorrect segmentation produced

from the proposed segmentation. This acquired edge weight would be useful for finding the accurate boundary in the next execution and will be improved successively. This can be achieved by using machine-learning methods or a parameter optimisation technique such as simulated annealing. This would improve the image processing and segmentation of the retinal layers and the choroid.

9.2.2 Finding quantification value as a parameter about the condition of the eye and finding new information about the disease progression and diagnosis

The proposed method has been used in quantification of eight biomarkers. This is an initial work towards quantifying other biomarkers. This can be extended to quantify other biomarkers available in the SD-OCT images. In the future, large-scale studies can be conducted for finding a quantification value for representing the eye condition which would be a significant area of work in the field of ophthalmology. This digitised value of the eye condition would be used for future research for finding the diagnosis of the eye disease by analysing the progression of the diseases and medication. Currently, researchers in the field of eye research face a lack of parameters to represent the eye status. This research can improve the medical field specially ophthalmology.

9.2.3 Improving the segmentation algorithm by using multi-modal imaging

Multi-modal imaging is a method that uses more than one type of imaging in any particular task. For example, if Colour Fundus Photography (CFP) and SD-OCT imaging are used to segment the ONH or blood vessel or pathologies, then that method is called multi-modal segmentation model. Each kind of image has advantages in its field; for example, blood vessels have a clearer contrast in CFP than SD-OCT B-scans: however, SD-OCT images have depth information of the blood vessels. Therefore, for blood vessel detection, the multi-modal technique would provide more information and improve the accuracy. There are few methods that utilise a multi-modal technique for finding blood vessels and ONH. In the future, pathologies or other substructures of the retina and the choroid may be segmented by utilising multi-modal imaging. For example, angiography

imaging with OCT imaging could be used for blood vessel segmentation and thus provide 3D mesh information correctly since angiography images show blood vessels more clearly even in the presence of the pathologies.

9.2.4 Improving efficiency by exploiting Graphics Processing Unit (GPU) implementation, Parallel Segmentation and deployed in the Cloud Environment real-time application

Automatic methods must be highly efficient when targeting real-time usage on the general population mass. Recent improvements in computer hardware offer very fast computations, for example, Graphics Processing Unit (GPU) and parallel computing. GPU systems would take a few seconds to make a computation that would otherwise have taken several minutes in a normal system. Similarly, parallel computing also boosts the efficiency of the algorithm. Since there are multiple layers and B-scans in OCT imaging, the design of a segmentation algorithm in parallel computing with GPU implementation would be a useful area of future research. Another future direction in the field of OCT technology is developing a portable OCT device for image acquisition, in order to reach people in remote areas without degrading the image quality (resolution) [8]. Therefore, the automatic method should also be developed to be compatible with such a system to promote large scale use. Since a segmentation algorithm needs a large amount of resources (storage and computation), recent cloud computing technology can be exploited to address this issue. Moreover, that technology is a suitable and practical platform for providing services of retinal layer segmentation in smartphone-based systems, which are limited in their memory capacities. Consequently, this is a future research topic: how to use GPU, Parallel Computing and Cloud environment to serve as a mass screening system.

Finally, the system can be utilised in future investigations not only for large-scale eye disease studies but also in longitudinal studies to evaluate/discover new biomarkers that can help early detection of eye diseases and in monitoring eye disease progression. The system can also be used to study drug response in large-scale studies as it can provide

automatic analysis of disease progression.

Bibliography

[1] Pratul P Srinivasan, Leo A Kim, Priyatham S Mettu, Scott W Cousins, Grant M Comer, Joseph A Izatt, and Sina Farsiu. Fully automated detection of diabetic macular edema and dry age-related macular degeneration from optical coherence tomography images. *Biomedical optics express*, 5(10):3568–3577, 2014.

[2] Stela Vujosevic, Silvia Bini, Giulia Midena, Marianna Berton, Elisabetta Pilotto, and Edoardo Midena. Hyperreflective intraretinal spots in diabetics without and with nonproliferative diabetic retinopathy: an in vivo study using spectral domain oct. *Journal of diabetes research*, 2013, 2013.

[3] Caio V. Regatieri, Lauren Branchini, and Jay S. Duker. The role of spectral-domain oct in the diagnosis and management of neovascular age-related macular degeneration. *Ophthalmic surgery, lasers & imaging : the official journal of the International Society for Imaging in the Eye*, 42:S56–S66, 2011.

[4] Renata Portella Nunes, Giovanni Gregori, Zohar Yehoshua, Paul F Stetson, William Feuer, Andrew A Moshfeghi, and Philip J Rosenfeld. Predicting the progression of geographic atrophy in age-related macular degeneration with sd-oct en face imaging of the outer retina. *Ophthalmic Surgery, Lasers and Imaging Retina*, 44(4):344–359, 2013.

[5] Koenraad A Vermeer, Josine van der Schoot, Hans G Lemij, and Johannes F de Boer. Rpe-normalized rnfl attenuation coefficient maps derived from volumetric oct imaging for glaucoma assessmentrnfl attenuation coefficient maps for glaucoma. *Investigative ophthalmology & visual science*, 53(10):6102–6108, 2012.

[6] Naoko Takada, Kazuko Omodaka, Tsutomu Kikawa, Airi Takagi, Akiko Mat-
    sumoto, Yu Yokoyama, Yukihiro Shiga, Kazuichi Maruyama, Hidetoshi Takahashi,
    Masahiro Akiba, et al. Oct-based quantification and classification of optic disc
    structure in glaucoma patients. *PloS one*, 11(8):e0160226, 2016.

[7] Yogesan Kanagasingam, Alauddin Bhuiyan, Michael D Abràmoff, R Theodore
    Smith, Leonard Goldschmidt, and Tien Y Wong. Progress on retinal image analysis
    for age related macular degeneration. *Progress in retinal and eye research*, 38:20–42,
    2014.

[8] Michael D Abràmoff, Mona K Garvin, and Milan Sonka. Retinal imaging and image
    analysis. *Biomedical Engineering, IEEE Reviews in*, 3:169–208, 2010.

[9] David Huang, Eric A Swanson, Charles P Lin, Joel S Schuman, William G Stinson,
    Warren Chang, Michael R Hee, Thomas Flotte, Kenton Gregory, Carmen A Puli-
    afito, et al. Optical coherence tomography. *Science*, 254(5035):1178–1181, 1991.

[10] Delia Cabrera DeBuc. *A review of algorithms for segmentation of retinal image data
    using optical coherence tomography*. INTECH Open Access Publisher, 2011.

[11] Wikipedia. Fundus photography — Wikipedia, the free encyclopedia. `https:
    //en.wikipedia.org/wiki/Fundus_photography`, 2004. [Online; accessed
    18-Jan-2017].

[12] Teresa C Chen. Spectral domain optical coherence tomography in glaucoma: quali-
    tative and quantitative analysis of the optic nerve head and retinal nerve fiber layer
    (an aos thesis). *Transactions of the American Ophthalmological Society*, 107:254, 2009.

[13] P. Bettin and F. Di Matteo. Glaucoma: Present challenges and future trends. *Oph-
    thalmic Research*, 50(4):197–208, 2013.

[14] Guillaume Lemaìtre, Mojdeh Rastgoo, Joan Massich, Carol Y Cheung, Tien Y
    Wong, Ecosse Lamoureux, Dan Milea, Fabrice Mriaudeau, and Dèsirè Sidibè. Clas-
    sification of sd-oct volumes using local binary patterns: Experimental validation
    for dme detection. *Journal of Ophthalmology*, 2016, 2016.

[15] Andrew J Tatham, Robert N Weinreb, Linda M Zangwill, Jeffrey M Liebmann, Christopher A Girkin, and Felipe A Medeiros. The relationship between cup-to-disc ratio and estimated number of retinal ganglion cellscdr and retinal ganglion cell number. *Investigative ophthalmology & visual science*, 54(5):3205–3214, 2013.

[16] Zhichao Wu, Lauren N Ayton, Robyn H Guymer, and Chi D Luu. Relationship between the second reflective band on optical coherence tomography and multifocal electroretinography in age-related macular degeneration. *Invest Ophthalmol Vis Sci*, 54(4):2800–2806, 2013.

[17] Ou Tan, Gisèle Li, Ake Tzu-Hui Lu, Rohit Varma, David Huang, Advanced Imaging for Glaucoma Study Group, et al. Mapping of macular substructures with optical coherence tomography for glaucoma diagnosis. *Ophthalmology*, 115(6):949–956, 2008.

[18] Laxmi Gella, Rajiv Raman, Padmaja Kumari Rani, and Tarun Sharma. Spectral domain optical coherence tomography characteristics in diabetic retinopathy. *Oman journal of ophthalmology*, 7(3):126, 2014.

[19] Ashley Wood, Alison Binns, Tom Margrain, Wolfgang Drexler, Boris Považay, Marieh Esmaeelpour, and Nik Sheen. Retinal and choroidal thickness in early age-related macular degeneration. *American journal of ophthalmology*, 152(6):1030–1038, 2011.

[20] Allan A Hunter, Eric K Chin, David RP Almeida, and David G Telander. Drusen imaging: A review. *Journal of Clinical & Experimental Ophthalmology*, 5(327):2, 2014.

[21] Kyoichi Mizumoto, Masahiko Gosho, and Masahiro Zako. Correlation between optic nerve head structural parameters and glaucomatous visual field indices. *Clinical ophthalmology (Auckland, NZ)*, 8:1203, 2014.

[22] Jonas MD Gmeiner, Wolfgang A Schrems, Christian Y Mardin, Robert Laemmer, Friedrich E Kruse, and Laura M Schrems-Hoesl. Comparison of bruch's membrane opening minimum rim width and peripapillary retinal nerve fiber layer thickness

in early glaucoma assessment bmo-mrw and rnflt in early glaucoma assessment. *Investigative Ophthalmology & Visual Science*, 57(9):OCT575–OCT584, 2016.

[23] Josine Van Der Schoot, Koenraad A Vermeer, Johannes F de Boer, and Hans G Lemij. The effect of glaucoma on the optical attenuation coefficient of the retinal nerve fiber layer in spectral domain optical coherence tomography images light attenuation in glaucomatous rnfl. *Investigative ophthalmology & visual science*, 53(4):2424–2430, 2012.

[24] Peter M Brennen, Larry Kagemann, and Thomas R Friberg. Comparison of stratusoct and cirrus hd-oct imaging in macular diseases. *Ophthalmic Surgery, Lasers and Imaging Retina*, 40(1):25–31, 2009.

[25] Dèsirè Sidibè, Shrinivasan Sankar, Guillaume Lematre, Mojdeh Rastgoo, Joan Massich, Carol Y. Cheung, Gavin S. W. Tan, Dan Milea, Ecosse Lamoureux, Tien Y. Wong, and Fabrice Mriaudeau. An anomaly detection approach for the identification of dme patients using spectral domain optical coherence tomography images. *Computer Methods and Programs in Biomedicine*, 139:109–117, 2017.

[26] Paolo Fraccaro, Massimo Nicolo, Monica Bonetto, Mauro Giacomini, Peter Weller, Carlo Enrico Traverso, Mattia Prosperi, and Dympna OSullivan. Combining macula clinical signs and patient characteristics for age-related macular degeneration diagnosis: a machine learning approach. *BMC Ophthalmology*, 15(1):10, 2015.

[27] Andrew Cameron, Dorothy Lui, Ameneh Boroomand, Jeffrey Glaister, Alexander Wong, and Kostadinka Bizheva. Stochastic speckle noise compensation in optical coherence tomography using non-stationary spline-based speckle noise modelling. *Biomedical optics express*, 4(9):1769–1785, 2013.

[28] T Ojala and M Pietikainen. Texture classification — machine vision and media processing unit, university of oulu, finland. `http://homepages.inf.ed.ac.uk/rbf/CVonline/LOCAL_COPIES/OJALA1/texclas.htm`. [Online; accessed 25-Feb-2017].

[29] Wikipedia. Choroid — Wikipedia, the free encyclopedia. `https://en.wikipedia.org/wiki/Choroid`, 2004. [Online; accessed 18-Jan-2017].

[30] C Qiu, MF Cotch, S Sigurdsson, PV Jonsson, MK Jonsdottir, S Sveinbjrnsdottir, G Eiriksdottir, R Klein, TB Harris, and MA van Buchem. Cerebral microbleeds, retinopathy, and dementia the ages-reykjavik study. *Neurology*, 75(24):2221–2228, 2010.

[31] Richard F Spaide, Hideki Koizumi, and Maria C Pozonni. Enhanced depth imaging spectral-domain optical coherence tomography. *American journal of ophthalmology*, 146(4):496–500, 2008.

[32] Helga Kolb. Simple anatomy of the retina. *Webvision: The Organization of the Retina and Visual System*, 2005. [In: Kolb H, Fernandez E, Nelson R, editors. University of Utah Health Sciences Center; 1995; Online; accessed 18-Jan-2017].

[33] David Hubel and Jonathan D Fratkin. Eye, brain, and vision. *Journal of Neuropathology and Experimental Neurology*, 55(2):257, 1996.

[34] Steven C. Gabaeff. Challenging the pathophysiologic connection between subdural hematoma, retinal hemorrhage and shaken baby syndrome. *Western Journal of Emergency Medicine*, 12(2), 2011.

[35] Giovanni Staurenghi, Srinivas Sadda, Usha Chakravarthy, Richard F Spaide, et al. Proposed lexicon for anatomic landmarks in normal posterior segment spectral-domain optical coherence tomography: the in oct consensus. *Ophthalmology*, 121(8):1572–1578, 2014.

[36] Juan Xu, D. A. Tolliver, Hiroshi Ishikawa, Gadi Wollstein, and JoelS Schuman. *3D OCT retinal vessel segmentation based on boosting learning*, volume 25/11 of *IFMBE Proceedings*, chapter 48, pages 179–182. Springer Berlin Heidelberg, 2009.

[37] E Dittrich, R Neji, T Schmoll, S Schriefl, C Ahlers, R Leitgeb, and G Langs. Detection of capillary vessels in optical coherence tomography based on a probabilistic ker-

nel. In *Proc. 13th Annual Meeting, Medical Image Understanding and Analysis*, pages 37–41. Kingston University UK, 2009.

[38] Andrew A Dahl. Retina anatomy. `http://emedicine.medscape.com/article/2019624-overview`, 2015. [Online; accessed 18-Jan-2016].

[39] Jay Chhablani, Ian Y. Wong, and Igor Kozak. Choroidal imaging: A review. *Saudi Journal of Ophthalmology*, 28(2):123–128, 2014. S1319-4534(14)00033-2[PII]24843305[pmid]Saudi J Ophthalmol.

[40] Debora L Nickla and Josh Wallman. The multifunctional choroid. *Progress in retinal and eye research*, 29(2):144–168, 2010.

[41] Brandon J. Lujan. Cotton-wool-spot — octmd. `http://www.octmd.org/findings/ischemia/cotton-wool-spot/`, 2017. [Online; accessed 21-Jan-2017].

[42] Lee Vien. Optical coherence tomography scans. `http://www.octscans.com/`. [Online; accessed 01-Feb-2017].

[43] National Eye Institute [Internet]. Bethesda (md): National institutes of health (us);. `https://www.nei.nih.gov/`. [Online; accessed 18-Jan-2017].

[44] Bernhard Baumann, Erich Götzinger, Michael Pircher, Harald Sattmann, Christopher Schütze, Ferdinand Schlanitz, Christian Ahlers, Ursula Schmidt-Erfurth, and Christoph K Hitzenberger. Segmentation and quantification of retinal lesions in age-related macular degeneration using polarization-sensitive optical coherence tomography. *Journal of biomedical optics*, 15(6):061704–061704, 2010. 10.1117/1.3499420.

[45] Anat London, Inbal Benhar, and Michal Schwartz. The retina as a window to the brainfrom eye research to cns disorders. *Nature Reviews Neurology*, 9(1):44–53, 2013.

[46] Rana Sorkhabi, Somaiyeh Mostafaei, Mohammadhosein Ahoor, and Mahnaz Talebi. Evaluation of retinal nerve fiber layer thickness in migraine. *Iranian Journal of Neurology*, 12(2):51–55, 2013.

[47] F. Spaide Richard, P. Ehlers Justis, and Yiu Glenn. Imaging the choroid: Pearls from the experts. http://retinatoday.com/2013/09/imaging-the-choroid-pearls-from-the-experts/, 2013. [Online; accessed 31-Jan-2017].

[48] Vedran Kaji, Marieh Esmaeelpour, Carl Glittenberg, Martin F. Kraus, Joachim Honegger, Richu Othara, Susanne Binder, James G. Fujimoto, and Wolfgang Drexler. Automated three-dimensional choroidal vessel segmentation of 3d 1060 nm oct retinal data. *Biomedical Optics Express*, 4(1):134–150, 2013.

[49] Qiang Chen, Luis de Sisternes, Theodore Leng, Luoluo Zheng, Lauren Kutzscher, and Daniel L. Rubin. Semi-automatic geographic atrophy segmentation for sd-oct images. *Biomedical Optics Express*, 4(12):2729–2750, 2013. 195911[PII]24409376[pmid]Biomed Opt Express.

[50] Maurice H Luntz, Samuel Boyd, and Benjamin F Boyd. *Innovations in the Glaucomas: Etiology, Diagnosis, and Management*. Slack, 2002.

[51] Qi Song, Junjie Bai, Mona Kathryn Garvin, Milan Sonka, John M Buatti, and Xiaodong Wu. Optimal multiple surface segmentation with shape and context priors. *Medical Imaging, IEEE Transactions on*, 32(2):376–386, 2013.

[52] Raheleh Kafieh, Hossein Rabbani, and Saeed Kermani. A review of algorithms for segmentation of optical coherence tomography from retina. *Journal of medical signals and sensors*, 3(1):45–60, 2013.

[53] Delia Cabrera Fernndez, Harry M Salinas, and Carmen A Puliafito. Automated detection of retinal layer structures on optical coherence tomography images. *Optics express*, 13(25):10200–10216, 2005.

[54] Hiroshi Ishikawa, Scott Piette, Jeffrey M Liebmann, and Robert Ritch. Detecting the inner and outer borders of the retinal nerve fiber layer using optical coherence tomography. *Graefe's archive for clinical and experimental ophthalmology*, 240(5):362–371, 2002.

[55] Alfred R Fuller, Robert J Zawadzki, Stacey Choi, David F Wiley, John S Werner, and Bernd Hamann. Segmentation of three-dimensional retinal image data. *Visualization and Computer Graphics, IEEE Transactions on*, 13(6):1719–1726, 2007.

[56] Christian Ahlers, Christian Simader, Wolfgang Geitzenauer, Geraldine Stock, Paul Stetson, Shawn Dastmalchi, and Ursula Schmidt-Erfurth. Automatic segmentation in three-dimensional analysis of fibrovascular pigmentepithelial detachment using high-definition optical coherence tomography. *British Journal of Ophthalmology*, 92(2):197–203, 2008.

[57] Azadeh Yazdanpanah, Ghassan Hamarneh, Benjamin Smith, and Marinko Sarunic. *Intra-retinal layer segmentation in optical coherence tomography using an active contour approach*, pages 649–656. Springer, 2009.

[58] Tapio Fabritius, Shuichi Makita, Masahiro Miura, Risto Myllylä, and Yoshiaki Yasuno. Automated segmentation of the macula by optical coherence tomography. *Optics express*, 17(18):15659–15669, 2009.

[59] Qi Yang, Charles A Reisman, Zhenguo Wang, Yasufumi Fukuma, Masanori Hangai, Nagahisa Yoshimura, Atsuo Tomidokoro, Makoto Araie, Ali S Raza, Donald C Hood, et al. Automated layer segmentation of macular oct images using dual-scale gradient information. *Optics express*, 18(20):21293–21307, 2010.

[60] KA Vermeer, J Van der Schoot, HG Lemij, and JF De Boer. Automated segmentation by pixel classification of retinal layers in ophthalmic oct images. *Biomedical optics express*, 2(6):1743–1756, 2011.

[61] Raheleh Kafieh, Hossein Rabbani, Michael D Abramoff, and Milan Sonka. Intra-retinal layer segmentation of 3d optical coherence tomography using coarse grained diffusion map. *Medical image analysis*, 17(8):907–928, 2013.

[62] Bhavna J Antony, Michael D Abràmoff, Matthew M Harper, Woojin Jeong, Elliott H Sohn, Young H Kwon, Randy Kardon, and Mona K Garvin. A combined machine-learning and graph-based framework for the segmentation of retinal surfaces in sd-oct volumes. *Biomedical optics express*, 4(12):2712–2728, 2013.

[63] Jing Tian, Boglàrka Varga, Gàbor Màrk Somfai, Wen-Hsiang Lee, William E Smiddy, and Delia Cabrera DeBuc. Real-time automatic segmentation of optical coherence tomography volume data of the macular region. *PloS one*, 10(8):e0133908, 2015.

[64] Li Zhang, Kyungmoo Lee, Meindert Niemeijer, Robert F Mullins, Milan Sonka, and Michael D Abramoff. Automated segmentation of the choroid from clinical sd-octautomated segmentation of choroid from sd-oct. *Investigative ophthalmology & visual science*, 53(12):7510–7519, 2012.

[65] Zhihong Hu, Xiaodong Wu, Yanwei Ouyang, Yanling Ouyang, and Srinivas R Sadda. Semiautomated segmentation of the choroid in spectral-domain optical coherence tomography volume scanssemiautomated choroid segmentation in sd-oct. *Investigative ophthalmology & visual science*, 54(3):1722–1729, 2013.

[66] Martin Dolejsi, Michael D Abràmoff, Milan Sonka, and Jan Kybic. Semi-automated segmentation of symptomatic exudate-associated derangements (seads) in 3d oct using layer segmentation. In *Biosignal*, 2010.

[67] Zhihong Hu, Gerard G Medioni, Matthias Hernandez, Amirhossein Hariri, Xiaodong Wu, and SriniVas R Sadda. Segmentation of the geographic atrophy in spectral-domain optical coherence tomography and fundus autofluorescence images. *Investigative Ophthalmology & Visual Science*, 54(13):8375–8383, 2013.

[68] Michael D Abràmoff, Kyungmoo Lee, Meindert Niemeijer, Wallace LM Alward, Emily C Greenlee, Mona K Garvin, Milan Sonka, and Young H Kwon. Automated segmentation of the cup and rim from spectral domain oct of the optic nerve head. *Investigative ophthalmology & visual science*, 50(12):5778–5784, 2009.

[69] Zhihong Hu, Meindert Niemeijer, Michael D Abramoff, Kyungmoo Lee, and Mona K Garvin. *Automated Segmentation of 3-D Spectral OCT Retinal Blood Vessels by Neural Canal Opening False Positive Suppression*, pages 33–40. Springer, 2010.

[70] Zhihong Hu, M Niemeijer, MD Abramoff, and Mona K Garvin. Automated multimodality concurrent classification for segmenting vessels in 3-d spectral oct and

color fundus images. In *Proc. of SPIE Medical Imaging: Image Processing*, volume 7962, page 796204, 2011.

[71] Zhihong Hu, Meindert Niemeijer, Michael D Abramoff, and Mona K Garvin. Multimodal retinal vessel segmentation from spectral-domain optical coherence tomography and fundus photography. *Medical Imaging, IEEE Transactions on*, 31(10):1900–1911, 2012.

[72] Raheleh Kafieh, Hossein Rabbani, Fedra Hajizadeh, and Mohammadreza Ommani. An accurate multimodal 3-d vessel segmentation method based on brightness variations on oct layers and curvelet domain fundus image analysis. *Biomedical Engineering, IEEE Transactions on*, 60(10):2815–2823, 2013.

[73] Vedran Kajiċ, Marieh Esmaeelpour, Carl Glittenberg, Martin F Kraus, Joachim Honegger, Richu Othara, Susanne Binder, James G Fujimoto, and Wolfgang Drexler. Automated three-dimensional choroidal vessel segmentation of 3d 1060 nm oct retinal data. *Biomedical optics express*, 4(1):134–150, 2013.

[74] Hajar Danesh, Raheleh Kafieh, Hossein Rabbani, and Fedra Hajizadeh. Segmentation of choroidal boundary in enhanced depth imaging octs using a multiresolution texture based modeling in graph cuts. *Computational and mathematical methods in medicine*, 2014, 2014.

[75] Yijun Huang, Artur V Cideciyan, Georgios I Papastergiou, Eyal Banin, Susan L Semple-Rowland, Ann H Milam, and Samuel G Jacobson. Relation of optical coherence tomography to microanatomy in normal and rd chickens. *Investigative Ophthalmology & Visual Science*, 39(12):2405–2416, 1998.

[76] Hiroshi Ishikawa, Daniel M Stein, Gadi Wollstein, Siobahn Beaton, James G Fujimoto, and Joel S Schuman. Macular segmentation with optical coherence tomography. *Investigative ophthalmology & visual science*, 46(6):2012–2017, 2005.

[77] Stephanie J Chiu, Xiao T Li, Peter Nicholas, Cynthia A Toth, Joseph A Izatt, and Sina Farsiu. Automatic segmentation of seven retinal layers in sdoct images congruent with expert manual segmentation. *Optics express*, 18(18):19413–19428, 2010.

[78] Stephanie J Chiu, Joseph A Izatt, Rachelle V O'Connell, Katrina P Winter, Cynthia A Toth, and Sina Farsiu. Validated automatic segmentation of amd pathology including drusen and geographic atrophy in sd-oct images. *Investigative ophthalmology & visual science*, 53(1):53–61, 2012.

[79] Alexander Ehnes, Yaroslava Wenner, Christoph Friedburg, Markus N Preising, Wadim Bowl, Walter Sekundo, Erdmuthe Meyer zu Bexten, Knut Stieger, and Birgit Lorenz. Optical coherence tomography (oct) device independent intraretinal layer segmentation. *Translational Vision Science and Technology*, 3(1), 2014.

[80] Qiang Chen, Wen Fan, Sijie Niu, Jiajia Shi, Honglie Shen, and Songtao Yuan. Automated choroid segmentation based on gradual intensity distance in hd-oct images. *Optics express*, 23(7):8974–8994, 2015.

[81] Kyungmoo Lee, Meindert Niemeijer, Mona K Garvin, Young H Kwon, Milan Sonka, and Michael D Abràmoff. Segmentation of the optic disc in 3-d oct scans of the optic nerve head. *Medical Imaging, IEEE Transactions on*, 29(1):159–168, 2010.

[82] Mohammad Saleh Miri, Kyungmoo Lee, Meindert Niemeijer, Michael D Abràmoff, Young H Kwon, and Mona K Garvin. Multimodal segmentation of optic disc and cup from stereo fundus and sd-oct images. In *SPIE Medical Imaging*, pages 86690O–86690O. International Society for Optics and Photonics, 2013.

[83] Teresa Torzicky, Michael Pircher, Stefan Zotter, Marco Bonesi, Erich Götzinger, and Christoph K Hitzenberger. Automated measurement of choroidal thickness in the human eye by polarization sensitive optical coherence tomography. *Optics express*, 20(7):7564–7574, 2012.

[84] Lian Duan, Masahiro Yamanari, and Yoshiaki Yasuno. Automated phase retardation oriented segmentation of chorio-scleral interface by polarization sensitive optical coherence tomography. *Optics express*, 20(3):3353–3366, 2012.

[85] Jing Tian, Pina Marziliano, Mani Baskaran, Tin Aung Tun, and Tin Aung. Automatic segmentation of the choroid in enhanced depth imaging optical coherence tomography images. *Biomedical optics express*, 4(3):397–411, 2013.

[86] David Alonso-Caneiro, Scott A Read, and Michael J Collins. Automatic segmentation of choroidal thickness in optical coherence tomography. *Biomedical Optics Express*, 4(12):2795–2812, 2013.

[87] A George, JL Dilienseger, M Weber, and A Pechereau. Optical coherence tomography image processing. In *Investigative Ophthalmology & Visual Science*, volume 41, pages S173–S173. Assoc Research Vision Ophthalmology Inc 9650 Rockville Pike, Bethesda, MD 20814-3998 USA, 2000.

[88] Dara Koozekanani, Kim Boyer, and Cynthia Roberts. Retinal thickness measurements from optical coherence tomography using a markov boundary model. *IEEE transactions on medical imaging*, 20(9):900–916, 2001.

[89] Mahnaz Shahidi, Zhangwei Wang, and Ruth Zelkha. Quantitative thickness measurement of retinal layers imaged by optical coherence tomography. *American Journal of Ophthalmology*, 139(6):1056–1061, 2005.

[90] Kim L Boyer, Artemas Herzog, and Cynthia Roberts. Automatic recovery of the optic nervehead geometry in optical coherence tomography. *Medical Imaging, IEEE Transactions on*, 25(5):553–570, 2006.

[91] Maurizio Baroni, Pina Fortunato, and Agostino La Torre. Towards quantitative analysis of retinal features in optical coherence tomography. *Medical engineering & physics*, 29(4):432–441, 2007.

[92] Pengxiao Zang, Simon S Gao, Thomas S Hwang, Christina J Flaxel, David J Wilson, John C Morrison, David Huang, Dengwang Li, and Yali Jia. Automated boundary detection of the optic disc and layer segmentation of the peripapillary retina in volumetric structural and angiographic optical coherence tomography. *Biomedical Optics Express*, 8(3):1306–1318, 2017.

[93] Artemas Herzog, KimL Boyer, and Cynthia Roberts. *Robust Extraction of the Optic Nerve Head in Optical Coherence Tomography*, volume 3117 of *Lecture Notes in Computer Science*, chapter 34, pages 395–407. Springer Berlin Heidelberg, 2004.

[94] Vivek J Srinivasan, Bryan K Monson, Maciej Wojtkowski, Richard A Bilonick, Iwona Gorczynska, Royce Chen, Jay S Duker, Joel S Schuman, and James G Fujimoto. Characterization of outer retinal morphology with high-speed, ultrahigh-resolution optical coherence tomography. *Investigative Ophthalmology & Visual Science*, 49(4):1571–1579, 2008.

[95] DA Tolliver, I Koutis, H Ishikawa, JS Schuman, and GL Miller. Automatic multiple retinal layer segmentation in spectral domain oct scans via spectral rounding. *Investigative Ophthalmology & Visual Science*, 49(13):1878–1878, 2008.

[96] Ou Tan, Vikas Chopra, Ake Tzu-Hui Lu, Joel S Schuman, Hiroshi Ishikawa, Gadi Wollstein, Rohit Varma, and David Huang. Detection of macular ganglion cell loss in glaucoma by fourier-domain optical coherence tomography. *Ophthalmology*, 116(12):2305–2314. e2, 2009.

[97] Alexandre R Tumlinson, Boris Hermann, Bernd Hofer, Boris Povaay, Tom H Margrain, Alison M Binns, and Wolfgang Drexler. Techniques for extraction of depth-resolved in vivo human retinal intrinsic optical signals with optical coherence tomography. *Japanese journal of ophthalmology*, 53(4):315–326, 2009.

[98] Robert Koprowski and Zygmunt Wrobel. *Layers recognition in tomographic eye image based on random contour analysis*, pages 471–478. Springer, 2009.

[99] Shijian Lu, Carol Yim-lui Cheung, Jiang Liu, Joo Hwee Lim, Christopher Kai-shun Leung, and Tien Yin Wong. Automated layer segmentation of optical coherence tomography images. *IEEE Transactions on Biomedical Engineering*, 57(10):2605–2608, 2010.

[100] Markus A Mayer, Joachim Hornegger, Christian Y Mardin, and Ralf P Tornow. Retinal nerve fiber layer segmentation on fd-oct scans of normal subjects and glaucoma patients. *Biomedical optics express*, 1(5):1358–1383, 2010.

[101] Andrew Lang, Aaron Carass, Matthew Hauser, Elias S Sotirchos, Peter A Calabresi, Howard S Ying, and Jerry L Prince. Retinal layer segmentation of macular oct images using boundary classification. *Biomedical optics express*, 4(7):1133–1152, 2013.

[102] Kyungmoo Lee, Michael D. Abràmoff, Meindert Niemeijer, Mona K. Garvin, and Milan Sonka. 3-d segmentation of retinal blood vessels in spectral-domain oct volumes of the optic nerve head. In *Proc. SPIE 7626, Medical Imaging 2010: Biomedical Applications in Molecular, Structural, and Functional Imaging,*, volume 7626, pages 76260V–76260V–8, 2010. 10.1117/12.844330.

[103] Delia Cabrera Fernandez. Delineating fluid-filled region boundaries in optical coherence tomography images of the retina. *IEEE transactions on medical imaging*, 24(8):929–945, 2005.

[104] Pedro Guimares, Pedro Rodrigues, Dirce Celorico, Pedro Serranho, and Rui Bernardes. Three-dimensional segmentation and reconstruction of the retinal vasculature from spectral-domain optical coherence tomography. *Journal of Biomedical Optics*, 20(1):016006–016006, 2015.

[105] Javier Mazzaferri, Luke Beaton, Gisle Hounye, Diane N. Sayah, and Santiago Costantino. Open-source algorithm for automatic choroid segmentation of oct volume reconstructions. *Scientific Reports*, 7:42112, 2017.

[106] G Gregori and RW Knighton. A robust algorithm for retinal thickness measurements using optical coherence tomography (stratus oct). *Investigative Ophthalmology & Visual Science*, 45(13):3007–3007, 2004.

[107] Mona Haeker, Michael Abramoff, Randy Kardon, and Milan Sonka. Segmentation of the surfaces of the retinal layer from oct images. In *International Conference on Medical Image Computing and Computer-Assisted Intervention*, pages 800–807. Springer, 2006.

[108] Mona K Garvin, Michael D Abràmoff, Randy Kardon, Stephen R Russell, Xiaodong Wu, and Milan Sonka. Intraretinal layer segmentation of macular optical coherence tomography images using optimal 3-d graph search. *Medical Imaging, IEEE Transactions on*, 27(10):1495–1505, 2008.

[109] Mircea Mujat, Raymond C Chan, Barry Cense, B Hyle Park, Chulmin Joo, Taner Akkin, Teresa C Chen, and Johannes F de Boer. Retinal nerve fiber layer thick-

ness map determined from optical coherence tomography images. *Optics express*, 13(23):9480–9491, 2005.

[110] Mona Kathryn Garvin, Michael David Abràmoff, Xiaodong Wu, Stephen R Russell, Trudy L Burns, and Milan Sonka. Automated 3-d intraretinal layer segmentation of macular spectral-domain optical coherence tomography images. *Medical Imaging, IEEE Transactions on*, 28(9):1436–1447, 2009.

[111] Bhavna J Antony, Michael D Abràmoff, Kyungmoo Lee, Pavlina Sonkova, Priya Gupta, Young Kwon, Meindert Niemeijer, Zhihong Hu, and Mona K Garvin. Automated 3d segmentation of intraretinal layers from optic nerve head optical coherence tomography images. In *SPIE Medical Imaging*, pages 76260U–76260U–12. International Society for Optics and Photonics, 2010.

[112] Itebeddine Ghorbel, Florence Rossant, Isabelle Bloch, Sarah Tick, and Michel Paques. Automated segmentation of macular layers in oct images and quantitative evaluation of performances. *Pattern Recognition*, 44(8):1590–1603, 2011.

[113] Bhavna J Antony, Michael D Abràmoff, Milan Sonka, Young H Kwon, and Mona K Garvin. Incorporation of texture-based features in optimal graph-theoretic approach with application to the 3d segmentation of intraretinal surfaces in sd-oct volumes. In *SPIE Medical Imaging*, pages 83141G–83141G. International Society for Optics and Photonics, 2012.

[114] Pascal A Dufour, Lala Ceklic, Hannan Abdillahi, Simon Schroder, Sandro De Dzanet, Ute Wolf-Schnurrbusch, and Jens Kowal. Graph-based multi-surface segmentation of oct data using trained hard and soft constraints. *Medical Imaging, IEEE Transactions on*, 32(3):531–543, 2013.

[115] Florence Rossant, Isabelle Bloch, Itebeddine Ghorbel, and Michel Paques. Parallel double snakes. application to the segmentation of retinal layers in 2d-oct for pathological subjects. *Pattern Recognition*, 48(12):3857–3870, 2015.

[116] Jinming Duan, Christopher Tench, Irene Gottlob, Frank Proudlock, and Li Bai. Automated segmentation of retinal layers from optical coherent tomography images using geodesic distance. *arXiv preprint arXiv:1609.02214*, 2016.

[117] Xinjian Chen, Meindert Niemeijer, Li Zhang, Kyungmoo Lee, Michael D Abràmoff, and Milan Sonka. Three-dimensional segmentation of fluid-associated abnormalities in retinal oct: probability constrained graph-search-graph-cut. *Medical Imaging, IEEE Transactions on*, 31(8):1521–1531, 2012.

[118] Kayoung Yi, Mircea Mujat, Wei Sun, Daina Burnes, Mark A. Latina, Derrick T. Lin, Daniel G. Deschler, Peter A. D. Rubin, B. Hyle Park, Johannes F. de Boer, and Teresa C. Chen. Imaging of optic nerve head drusen: Improvements with spectral domain optical coherence tomography. *Journal of glaucoma*, 18(5):373–378, 2009. 19525727[pmid]J Glaucoma.

[119] Bhavna J Antony, Mohammed S Miri, Michael D Abràmoff, Young H Kwon, and Mona K Garvin. *Automated 3D Segmentation of Multiple Surfaces with a Shared Hole: Segmentation of the Neural Canal Opening in SD-OCT Volumes*, pages 739–746. Springer, 2014.

[120] Meindert Niemeijer, Mona K. Garvin, Bram van Ginneken, Milan Sonka, and Michael D. Abràmoff. Vessel segmentation in 3d spectral oct scans of the retina. In *Proc. SPIE 6914, Medical Imaging 2008*, volume 6914, pages 69141R–69141R–8, 2008. 10.1117/12.772680.

[121] Lian Duan, Young-Joo Hong, and Yoshiaki Yasuno. Automated segmentation and characterization of choroidal vessels in high-penetration optical coherence tomography. *Optics express*, 21(13):15787–15808, 2013.

[122] Ahmet Murat Bagci, Mahnaz Shahidi, Rashid Ansari, Michael Blair, Norman Paul Blair, and Ruth Zelkha. Thickness profiles of retinal layers by optical coherence tomography image segmentation. *American Journal of Ophthalmology*, 146(5):679–687. e1, 2008.

[123] Michael R Hee, Joseph A Izatt, Eric A Swanson, David Huang, Joel S Schuman, Charles P Lin, Carmen A Puliafito, and James G Fujimoto. Optical coherence tomography of the human retina. *Archives of ophthalmology*, 113(3):325–332, 1995.

[124] Akshaya Mishra, Alexander Wong, Kostadinka Bizheva, and David A Clausi. Intra-retinal layer segmentation in optical coherence tomography images. *Optics express*, 17(26):23719–23728, 2009.

[125] Vedran Kajič, Boris Považay, Boris Hermann, Bernd Hofer, David Marshall, Paul L Rosin, and Wolfgang Drexler. Robust segmentation of intraretinal layers in the normal human fovea using a novel statistical model based on texture and shape analysis. *Optics express*, 18(14):14730–14744, 2010.

[126] Fei Shi, Xinjian Chen, Heming Zhao, Weifang Zhu, Dehui Xiang, Enting Gao, Milan Sonka, and Haoyu Chen. Automated 3-d retinal layer segmentation of macular optical coherence tomography images with serous pigment epithelial detachments. *IEEE transactions on medical imaging*, 34(2):441–452, 2015.

[127] Kyungmoo Lee, Michael D Abràmoff, Milan Sonka, and Mona K Garvin. Automated segmentation of intraretinal layers from spectral-domain macular oct: reproducibility of layer thickness measurements. In *SPIE Medical Imaging*, pages 796523–796523–8. International Society for Optics and Photonics, 2011.

[128] Sijie Niu, Qiang Chen, Luis de Sisternes, Daniel L. Rubin, Weiwei Zhang, and Qinghuai Liu. Automated retinal layers segmentation in sd-oct images using dual-gradient and spatial correlation smoothness constraint. *Computers in Biology and Medicine*, 54:116–128, 2014.

[129] Markus A Mayer, Ralf P Tornow, Joachim Hornegger, and Friedrich E Kruse. Fuzzy c-means clustering for retinal layer segmentation on high resolution oct images. *Analysis of Biomedical Signals and Images*, pages 160–166, 2008.

[130] Sina Farsiu, Stephanie J Chiu, Joseph A Izatt, and Cynthia A Toth. Fast detection and segmentation of drusen in retinal optical coherence tomography images. In

Biomedical Optics (BiOS) 2008, pages 68440D–68440D. International Society for Optics and Photonics, 2008.

[131] Gwènolè Quellec, Kyungmoo Lee, Martin Dolejsi, Mona Kathryn Garvin, Michael D Abràmoff, and Milan Sonka. Three-dimensional analysis of retinal layer texture: identification of fluid-filled regions in sd-oct of the macula. *Medical Imaging, IEEE Transactions on*, 29(6):1321–1330, 2010.

[132] Qiang Chen, Theodore Leng, Luoluo Zheng, Lauren Kutzscher, Jeffrey Ma, Luis de Sisternes, and Daniel L Rubin. Automated drusen segmentation and quantification in sd-oct images. *Medical image analysis*, 17(8):1058–1072, 2013.

[133] Jing Wu, Bianca S. Gerendas, Sebastian M. Waldstein, Christian Simader, and Ursula Schmidt-Erfurth. Automated vessel shadow segmentation of fovea-centered spectral-domain images from multiple oct devices. In *Medical Imaging: Image Processing*, volume 9034, pages 903403–903403–8, 2014. 10.1117/12.2044034.

[134] Matthus Pilch, Yaroslava Wenner, Elisabeth Strohmayr, Markus Preising, Christoph Friedburg, Erdmuthe Meyer zu Bexten, Birgit Lorenz, and Knut Stieger. Automated segmentation of retinal blood vessels in spectral domain optical coherence tomography scans. *Biomedical Optics Express*, 3(7):1478–1491, 2012.

[135] Hassan Wehbe, Marco Ruggeri, Shuliang Jiao, Giovanni Gregori, and Carmen A. Puliafito. Automatic retinal blood vessel parameter calculation in spectral domain optical coherence tomography. In *Proc. SPIE*, volume 6429, pages 64290D–64290D–7, 2007. 10.1117/12.702513.

[136] L Beaton, J Mazzaferri, F Lalonde, M Hidalgo-Aguirre, D Descovich, MR Lesk, and S Costantino. Non-invasive measurement of choroidal volume change and ocular rigidity through automated segmentation of high-speed oct imaging. *Biomedical Optics Express*, 6(5):1694–1706, 2015.

[137] Kiran Kumar Vupparaboina, Srinath Nizampatnam, Jay Chhablani, Ashutosh Richhariya, and Soumya Jana. Automated estimation of choroidal thickness dis-

tribution and volume based on oct images of posterior visual section. *Computerized Medical Imaging and Graphics*, 46:315–327, 2015.

[138] Marco Ruggeri, Hassan Wehbe, Shuliang Jiao, Giovanni Gregori, Maria E Jockovich, Abigail Hackam, Yuanli Duan, and Carmen A Puliafito. In vivo three-dimensional high-resolution imaging of rodent retina with spectral-domain optical coherence tomography. *Investigative ophthalmology & visual science*, 48(4):1808–1814, 2007.

[139] Maciej Szkulmowski, Maciej Wojtkowski, Bartosz Sikorski, Tomasz Bajraszewski, Vivek J Srinivasan, Anna Szkulmowska, Jakub J Kaluzny, James G Fujimoto, and Andrzej Kowalczyk. Analysis of posterior retinal layers in spectral optical coherence tomography images of the normal retina and retinal pathologies. *Journal of Biomedical Optics*, 12(4):041207–041207–11, 2007.

[140] I. Moupagiatzis, M. Mayer, J. Hornegger, R. Tornow, and C. Mardin. Application of morphological operators for optic nerve head segmentation in optical coherence tomography images. In *Systems, Signals and Image Processing (IWSSIP), 2012 19th International Conference on*, pages 572–575, 2012.

[141] Erich Gotzinger, Michael Pircher, Wolfgang Geitzenauer, Christian Ahlers, Bernhard Baumann, Stephan Michels, Ursula Schmidt-Erfurth, and Christoph K Hitzenberger. Retinal pigment epithelium segmentation by polarization sensitive optical coherence tomography. *Optics express*, 16(21):16410–16422, 2008.

[142] CA Toth, S Farsiu, SJ Chiu, AA Khanifar, and JA Izatt. Automatic drusen segmentation and characterization in spectral domain optical coherence tomography (sdoct) images of amd eyes. *Investigative Ophthalmology & Visual Science*, 49(13):5394–5394, 2008.

[143] Giovanni Gregori, Fenghua Wang, Philip J Rosenfeld, Zohar Yehoshua, Ninel Z Gregori, Brandon J Lujan, Carmen A Puliafito, and William J Feuer. Spectral domain optical coherence tomography imaging of drusen in nonexudative age-related macular degeneration. *Ophthalmology*, 118(7):1373–1379, 2011.

[144] Daisuke Iwama, Masanori Hangai, Sotaro Ooto, Atsushi Sakamoto, Hideo Nakanishi, Takashi Fujimura, Amitha Domalpally, Ronald P Danis, and Nagahisa Yoshimura. Automated assessment of drusen using three-dimensional spectral-domain optical coherence tomography. *Investigative Ophthalmology & Visual Science*, 53(3):1576–1583, 2012.

[145] Vedran Kajìc, Marieh Esmaeelpour, Boris Považay, David Marshall, Paul L Rosin, and Wolfgang Drexler. Automated choroidal segmentation of 1060 nm oct in healthy and pathologic eyes using a statistical model. *Biomedical optics express*, 3(1):86–103, 2012.

[146] Mona K Garvin, Wenxiang Deng, Bhavna Josephine Antony, Elliott H Sohn, and Michael David Abramoff. Machine-learning-based retinal vessel segmentation in spectral-domain optical coherence tomography volumes of mice. *Investigative Ophthalmology & Visual Science*, 55(13):2091–2091, 2014.

[147] Zhihong Hu, Meindert Niemeijer, Kyungmoo Lee, Michael D Abramoff, Milan Sonka, and Mona K Garvin. Automated segmentation of the optic disc margin in 3-d optical coherence tomography images using a graph-theoretic approach. In *SPIE Medical Imaging*, pages 72620U–72620U–11. International Society for Optics and Photonics, 2009.

[148] Zhihong Hu, Michael D Abràmoff, Young H Kwon, Kyungmoo Lee, and Mona K Garvin. Automated segmentation of neural canal opening and optic cup in 3d spectral optical coherence tomography volumes of the optic nerve head. *Investigative ophthalmology & visual science*, 51(11):5708–5717, 2010.

[149] Kyungmoo Lee, Michael D Abràmoff, Mona Garvin, and Milan Sonka. The iowa reference algorithms (retinal image analysis lab, iowa institute for biomedical imaging, iowa city, ia). `https://www.iibi.uiowa.edu/`, 2014. [Online; accessed 20-Feb-2015].

[150] Andrew Lang. Aura tools : Automated retinal analysis tools. `http://www.nitrc.org/projects/aura_tools/`, 2015. [Online; accessed 18-Apr-2016].

[151] Pascal A Dufour, Lala Ceklic, Hannan Abdillahi, Simon Schroder, Sandro De Dzanet, Ute Wolf-Schnurrbusch, and Jens Kowal. Oct segmentation application. `http://pascaldufour.net/Research/software_data.html`, 2012. [Online; accessed 18-Feb-2014].

[152] Hirotaka Tanabe, Yasuki Ito, and Hiroko Terasaki. Choroid is thinner in inferior region of optic disks of normal eyes. *Retina*, 32(1):134–139, 2012.

[153] Yu-Ying Liu, Hiroshi Ishikawa, Mei Chen, Gadi Wollstein, Jay S Duker, James G Fujimoto, Joel S Schuman, and James M Rehg. Computerized macular pathology diagnosis in spectral domain optical coherence tomography scans based on multiscale texture and shape features. *Investigative Ophthalmology & Visual Science*, 52(11):8316–8322, 2011.

[154] Abdulrahman Albarrak, Frans Coenen, and Yalin Zheng. Age-related macular degeneration identification in volumetric optical coherence tomography using decomposition and local feature extraction. In *Proceedings of 2013 International Conference on Medical Image, Understanding and Analysis*, pages 59–64, 2013.

[155] Freerk G Venhuizen, Bram van Ginneken, Bart Bloemen, Mark JJP van Grinsven, Rick Philipsen, Carel Hoyng, Thomas Theelen, and Clara I Snchez. Automated age-related macular degeneration classification in oct using unsupervised feature learning. In *SPIE Medical Imaging*, pages 94141I–94141I–7. International Society for Optics and Photonics, 2015.

[156] Teresa C Chen, Barry Cense, Mark C Pierce, Nader Nassif, B Hyle Park, Seok H Yun, Brian R White, Brett E Bouma, Guillermo J Tearney, and Johannes F de Boer. Spectral domain optical coherence tomography: ultra-high speed, ultra-high resolution ophthalmic imaging. *Archives of Ophthalmology*, 123(12):1715–1720, 2005.

[157] CATT Research Group et al. Ranibizumab and bevacizumab for neovascular age-related macular degeneration. *The New England journal of medicine*, 364(20):1897, 2011.

[158] Juliana Bottòs, Javier Elizalde, J Fernando Arevalo, Eduardo B Rodrigues, and Maurìcio Maia. Vitreomacular traction syndrome. *Journal of ophthalmic & vision research*, 7(2):148–161, 2012.

[159] Zhichao Wu, Chi D Luu, Lauren N Ayton, Jonathan K Goh, Lucia M Lucci, William C Hubbard, Jill L Hageman, Gregory S Hageman, and Robyn H Guymer. Optical coherence tomography–defined changes preceding the development of drusen-associated atrophy in age-related macular degeneration. *Ophthalmology*, 121(12):2415–2422, 2014.

[160] John Canny. A computational approach to edge detection. *Pattern Analysis and Machine Intelligence, IEEE Transactions on*, PAMI-8(6):679–698, 1986.

[161] Pietro Perona and Jitendra Malik. Scale-space and edge detection using anisotropic diffusion. *Pattern Analysis and Machine Intelligence, IEEE Transactions on*, 12(7):629–639, 1990.

[162] Norbert Wiener. *Extrapolation, interpolation, and smoothing of stationary time series*, volume 2. MIT press Cambridge, MA, 1949.

[163] Scott Kirkpatrick, C Daniel Gelatt, Mario P Vecchi, et al. Optimization by simmulated annealing. *science*, 220(4598):671–680, 1983.

[164] Chourmouzios Tsiotsios and Maria Petrou. On the choice of the parameters for anisotropic diffusion in image processing. *Pattern recognition*, 46(5):1369–1381, 2013.

[165] Edsger W Dijkstra. A note on two problems in connexion with graphs. *Numerische mathematik*, 1(1):269–271, 1959.

[166] Tarek Alasil, Kaidi Wang, Pearse A Keane, Hang Lee, Neda Baniasadi, Johannes F de Boer, and Teresa C Chen. Analysis of normal retinal nerve fiber layer thickness by age, sex, and race using spectral domain optical coherence tomography. *Journal of glaucoma*, 22(7):532–541, 2013.

[167] Ron Margolis and Richard F Spaide. A pilot study of enhanced depth imaging optical coherence tomography of the choroid in normal eyes. *American journal of ophthalmology*, 147(5):811–815, 2009.

[168] Michael John Hogan, Jorge A Alvarado, and Joan Esperson Weddell. Histology of the human eye: an atlas and textbook. *Philadelphia,: Saunders. xiii*, 1971.

[169] Zheng Qin Yin, Tom J Millar, Paul Beaumont, Shirley Sarks, et al. Widespread choroidal insufficiency in primary open-angle glaucoma. *Journal of glaucoma*, 6(1):23–32, 1997.

[170] Richard F Spaide. Age-related choroidal atrophy. *American journal of ophthalmology*, 147(5):801–810, 2009.

[171] Virginia LL Torres, Nicole Brugnoni, Peter K Kaiser, and Arun D Singh. Optical coherence tomography enhanced depth imaging of choroidal tumors. *American journal of ophthalmology*, 151(4):586–593, 2011.

[172] M Gemenetzi, G De Salvo, and AJ Lotery. Central serous chorioretinopathy: an update on pathogenesis and treatment. *Eye*, 24(12):1743–1756, 2010.

[173] Hasan Altinkaynak, Necip Kara, Nihat Sayın, Hasan Güneş, Şahin Avşar, and Ahmet Taylan Yazıcı. Subfoveal choroidal thickness in patients with chronic heart failure analyzed by spectral-domain optical coherence tomography. *Current eye research*, 39(11):1123–1128, 2014.

[174] Harry A Quigley. What's the choroid got to do with angle closure? *Archives of Ophthalmology*, 127(5):693–694, 2009.

[175] Yasushi Ikuno, Kana Kawaguchi, Takeyoshi Nouchi, and Yoshiaki Yasuno. Choroidal thickness in healthy japanese subjects. *Investigative ophthalmology & visual science*, 51(4):2173–2176, 2010.

[176] Xiaoyan Ding, Jiaqing Li, Jing Zeng, Wei Ma, Ran Liu, Tao Li, Shanshan Yu, and Shibo Tang. Choroidal thickness in healthy chinese subjects. *Investigative ophthalmology & visual science*, 52(13):9555–9560, 2011.

[177] Varsha Manjunath, Mohammad Taha, James G Fujimoto, and Jay S Duker. Choroidal thickness in normal eyes measured using cirrus hd optical coherence tomography. *American journal of ophthalmology*, 150(3):325–329, 2010.

[178] Nobuyuki Otsu. A threshold selection method from gray-level histograms. *Automatica*, 11(285-296):23–27, 1975.

[179] Patrick E Shrout and Joseph L Fleiss. Intraclass correlations: uses in assessing rater reliability. *Psychological bulletin*, 86(2):420, 1979.

[180] Topcon Europe Medical B.V. Topcon dri oct triton, swept source oct. `http://www.sweptsourceoct.eu/images.html`, 2016. [Online; accessed 20-Dec-2015].

[181] Johannes Schindelin, Ignacio Arganda-Carreras, Erwin Frise, Verena Kaynig, Mark Longair, Tobias Pietzsch, Stephan Preibisch, Curtis Rueden, Stephan Saalfeld, Benjamin Schmid, et al. Fiji: an open-source platform for biological-image analysis. *Nature methods*, 9(7):676–682, 2012.

[182] Early Treatment Diabetic Retinopathy Study Group. Early treatment diabetic retinopathy study group: photocoagulation for diabetic macula edema. *Arch Ophthalmol*, 106:1796–1806, 1985.

[183] Jennifer H. Acton, R. Theodore Smith, Donald C. Hood, and Vivienne C. Greenstein. Relationship between retinal layer thickness and the visual field in early age-related macular degeneration. *Investigative Ophthalmology & Visual Science*, 53(12):7618–7624, 2012.

Author/s:
Hussain, Md Akter

Title:
Automatic optical coherence tomography imaging analysis for retinal disease screening

Date:
2017

Persistent Link:
http://hdl.handle.net/11343/196413

File Description:
Automatic optical coherence tomography imaging analysis for retinal disease screening